Alma Mater Studiorum – Università di Bologna

DOTTORATO DI RICERCA IN

Scienze della terra, della vita e dell’ambiente

Ciclo XXX

Settore Concorsuale: 04/A2

Settore Scientifico Disciplinare: GEO/01

The origin and significance of carbonaceous matter within Palaeoarchaean marine environments of the Barberton Greenstone Belt, South Africa

Presentata da: Francesco Greco

Coordinatore Dottorato

Prof. Giulio Viola

Supervisore

Dr.ssa Barbara Cavalazzi

Co-Supervisore

Prof. Axel Hofmann

Esame finale anno 2018

Abstract

Palaeoarchaean (3.6-3.2 Ga) cherts are commonly associated with hydrothermal activity and retain evidence for an early biosphere. They are rich in disordered carbonaceous matter (CM) whom origin cannot be readily associated to biological activity. This project investigate CM-rich material from the BARB3 core obtained from the c. 3.4 Ga old Buck Reef Chert (BRC) of South Africa, one of the best preserved volcano-sedimentary succession on Earth. CM from the core is characterized through a multiple analytical approach based on *in situ* complementary techniques. The aim was to reconstruct the CM origin and evaluate its biogenicity. Samples from the BARB3 shallow-platformal lithofacies, are rich in CM occurring within: (i) crinkly laminated chert; (ii) massive black chert; (iii) laminated black chert; and (iii) granular carbonaceous chert. These four facies bear a specific CM microtextures related to their depositional history. The crinkly laminated chert has a planar stromatolitic-like fabric and include CM mat-like laminae and grains. The massive black chert is structureless and include “cloudy” diffuse CM, CM grains and bitumen-interstitial CM originated as a fluid phase. The laminated black chert include CM grains and the granular carbonaceous chert is a mixture of carbonaceous detritus generated by the hydrothermal brecciation of soft crinkly laminated sediments and it is associated to botryoidal-quartz stratiform veins. The structural characterization of such CM microtextures by means of Raman spectroscopy and HRTEM analyses have confirmed their consistency with the BGB regional metamorphic imprint. However a between-facies and, more importantly, a between-microtexture structural heterogeneity occur guiding the reconstruction of the CM and of the depositional facies history. The result is a revisited picture of the BRC as a shallow-water hydrothermal field characterized by complex microbial communities and carbon remobilization now expressed by multiple CM generations.

Table of Contents

Chapter 1

General introduction

1.1 Origin of carbonaceous matter in modern and ancient sediments

Since life has become well established on Earth it has played a leading role in the global carbon cycle as every known organism needs carbon for its structure or metabolic processes. Photosynthesis, aerobic and to minor extent anaerobic respiration represent the principal pathways by which carbon is processed on the modern Earth (Ellis-Evans, 2011). The biological fixation of carbon greatly affect the element global budget as the remains of dead organisms get buried within sediments resulting into carbon being sequestered in the geosphere where it can be found in the form of amorphous carbonaceous matter (CM).

In meta-sedimentary rocks CM is a typical component and occurs as discrete particles, laminae, clots, or, more often, as diffusely distributed matter within the hosting mineral matrix (Walsh, 1992; Walsh and Lowe, 1999). It consists mainly of sp^2-bonded carbon structures containing minor amounts of hydrogen and other heteroatoms including oxygen, nitrogen, sulphur and phosphorus, and it originates from both, albeit rare, non-biological carbon precursors and biological organic matter (OM) (Olcott Marshall et al., 2014). Heating of inorganic compounds, inorganic precipitation from hydrothermal fluids, serpentinization, Fischer-Tropsch-type synthesis and siderite decomposition are among the processes which account for abiotic formation of CM in rocks (Olcott Marshall *et al.*, 2014; Delarue *et al.*, 2016). In contrast, the maturation of biological organic matter and organic debris within sediments during burial, diagenesis and metamorphism accounts for the vast majority of CM in meta-sedimentary rocks (Wopenka and Pasteris, 1993). Such evolution, including early carbonization and later graphitization (Jehlička *et al.*, 2003; Delarue *et al.*, 2016), represents a "defect removal" process during which amorphous organic compounds are gradually deprived of hydrogen, nitrogen, oxygen and other heteroatoms, while the formation of sp^2-carbon bonds and hexagonal aromatic rings is promoted (Pasteris and Wopenka, 1991; Ferrari and Robertson, 2000; Jehlička *et al.*, 2003). The original OM is thus progressively reorganized into graphene-like layers, which become stacked together in a trend that, from completely amorphous material, moves towards an ideally pure, crystalline graphite lattice. Because this evolution depends largely on the pressure-temperature (P-T) metamorphic conditions and on the original carbon precursor (Yui *et al.*, 1996; Beyssac *et al.*, 2002), the degree of disorder and the heterogeneity of incompletely reacted CM species in meta-sedimentary rocks can give us insights into the metamorphic history of CM-bearing strata and help to identify the carbonaceous precursor (Yui *et al.*, 1996; Ferrari and Robertson, 2000; Marshall *et al.*, 2012).

On the modern Earth the connection between CM production and biological activity can be readily inferred. This become less obvious for the early Earth CM fossil record because our understanding on the impact of life during the Archaean, between 4 and 2.5 Ga ago, is still hazy. This is for several principal reasons: (i) unequivocal evidence for Archaean life is scarce (Schopf *et al.*, 2007) and both the rate and pathways of ancient OM matter production remain poorly understood; (ii) ancient CM is frequently strongly altered during metamorphic overprints; and (iii) diffuse hydrothermalism through an ultramafic substrate, a suitable setting for the abiotic production of CM, appears to have been widespread on the early Earth (Brasier *et al.*, 2006; Hofmann, 2011). Furthermore, impactors in the form of both carbonaceous chondrites and micrometeorites would have delivered much exogenous CM to the Earth (Maurette *et al.*, 2006). Therefore the assumption for a biological origin of CM in ancient rocks requires caution. Still, most of the earliest evidence for life on Earth occur as microbial carbonaceous remains or as microbialites within Archaean meta-sedimentary rocks generally enriched in CM (Altermann and Kazmierczak, 2003; Schopf *et al.*, 2007; Wacey, 2009; Tab.1.2). Verifying the biogenicity of such CM has long represented a crucial target for the early life investigators and much energy has been directed to reconstruct possible connections between ancient CM production and the early microbial biosphere.

1.2 The earliest geological and fossil record on Earth

When directly investigating the most ancient microbial life, geologists and geobiologists find their first obstacle in retrieving suitable rocks where the early evolution can be studied and reconstructed faithfully. This problem rises as billions of years of plate tectonics have inevitably affected our planet earliest rocks resulting into a scattered, deformed and often highly-metamorphosed ancient geological record. The oldest rocks found on Earth today belong to the Eoarchaean Era (~4-3.6 Ga ago) and consist of high-grade gneiss terranes which have experienced at least amphibolite facies regional metamorphic grade (Nutman *et al.*, 2001; Kranendonk *et al.*, 2007; Ogg *et al.*, 2016). They include primarily plutonic complexes of TTGs (Tonalite–Trondhjemite-Granodiorite) and minor successions of volcanic and meta-sedimentary units, such as those found in Canada and Greenland (Tab. 1.1). Although tangible, this very first geological window of early Earth processes is problematic especially with concerns to life investigation as the volcano-sedimentary successions, often of dubious interpretation, are scarce, deformed and metamorphosed to a grade at which individual units are difficult to trace and primary evidences of life would be altered beyond recognition.

Table 1.1 - Principal locations of the Earth oldest supracrustal rocks. Eoarchaean rocks are represented mainly by plutonic rocks and scarce meta-sedimentary rocks of dubious origin. Field correlations and depositional reconstructions are particularly difficult in these highly metamorphosed and deformed terrains. This results in the claims for Eoarchaean life to be very contradictory. References for each locality: (1) (Iizuka *et al.*, 2007); (2) (Komiya *et al.*, 2015); (3) Harley and Kelly, 2007; (4) (Nutman *et al.*, 1993); (5) Mojzsis and Harrison, 2002; (6) Nutman *et al.*, 2007; (7) O'Neil *et al.*, 2012; (8) Lowe and Tice, 2007.

Name	Area	Lithologies	Age (Ga)	Metamorphic grade
Acasta gneisses(1)	NW Canada	TTGs, volcanic and sedimentary rocks	4.03 - 3.94	Amphibolite
Nulliak supracrustal rocks(2)	NE Labrador (Canada)	volcanic and sedimentary rocks	>3.95	Granulite-Amphibolite
Uivak gneisses(2)	NE Labrador (Canada)	granitic rocks	>3.95	Granulite
Napier complex(3)	Antartica	TTGs, volcanic and sedimentary rocks	3.95 - 3.8	Granulite
Amitsoq complex(4)	SW Greenland	TTGs and granitic rocks	3.9 - 3.6	Amphibolite
Akilia island(5)	SW Greenland	TTGs, volcanic and sedimentary rocks	3.83	Amphibolite
Isua belt(6)	SW Greenland	TTGs, volcano-sedimentary successions	3.8 - 3.7	Amphibolite
Nuvvuagittuq belt(7)	Northern Quebec (Canada)	TTGs, volcano-sedimentary successions	3.8	upper Amphibolite
Pilbara craton greenstone belts(8)	Western Australia	TTG, volcano-sedimentry successions	3.53 - 3.31	Greenschist
Barberton greenstone belt(8)	South Africa and Swaziland	TTG, volcano-sedimentry successions	3.5 - 3.2	Greenschist

Table 1.2 - Principal claims for life in Palaeoarchaean cherts or highly silicified deposits from the Pilbara Craton (Australia) and the Barberton Greenstone Belt (South Africa and Swaziland). All listed deposits are rich in CM however not always carbonaceous body fossils (CM microfossils) have been reported. Environments have been typically interpreted as shallow-marine; often hydrothermalism is involved. The age of the claims is expressed in millions of years. Fm: Formation; PS: Pilbara Supergroup; BGB: Barberton Greenstone Belt.

Age	Geological unit	Environment	Claims for life	References
3496	Dresser Fm, Warrawoona Group, PS	shallow-marine hydrothermal	domical microbialites CM microfossils	Ueno *et al.*, 2001; Van Kranendonk, 2006; Noffke *et al.*, 2013
3470	Mount Ada Basalt, Warrawoona Group, PS	shallow-marine	planar microbialites CM microfossils	Awramik *et al.*, 1983; Schopf *et al.*, 2007
3465	Apex chert, Warrawoona Group, PS	marine hydrothermal	CM microfossils	Schopf, 1993
3460	Hooggenoeg Fm, Onverwacht Group, BGB	shallow-marine	planar microbialites CM microfossils	Walsh, 1992; Hofmann, 2000; Westall *et al.*, 2006; Glikson *et al.*, 2008
3450	Josefdal Chert, Onverwacht Group, BGB	shallow-marine hydrothermal	planar microbialites	Westall et al., 2006, 2015
3440	Panorama Fm, Warrawoona Group, PS	shallow-marine hydrothermal	conical microbialites CM microfossils	Hofmann, 2000; Westall et al., 2006
3426	Strelley Pool Chert, Kelly Group, PS	shallow-marine	planar microbialites CM microfossils	Sugitani *et al.*, 2015; Duda *et al.*, 2016
3400	Strelley Pool Chert, Kelly Group, PS	shoreline	CM microfossils	Allwood *et al.*, 2006; Wacey, 2010
3388	Strelley Pool Chert, Kelly Group, PS	shallow-marine	planar microbialites CM microfossils	Schopf et al.2007
3320	Kromberg Fm, Onverwacht Group, BGB	shallow-marine	planar microbialites CM microfossils	Walsh, 1992; Westall *et al.*, 2001; Kremer and Kaźmierczak, 2017
3316	Buck Reef Chert, Onverwacht Group, BGB	shallow-marine	planar microbialites	Tice and Lowe, 2004, 2006a,b
3260	Swartkoppie Fm, Onverwacht Group, BGB	shallow-marine	CM microfossils	Knoll and Barghoorn, 1977
3245	Sheba Fm, Fig Tree Group, BGB	shallow-marine	columnar microbialites CM microfossils	Schopf and Barghoorn, 1967; Byerly *et al.*, 1986
3240	Kangaroo Caves Fm, Sulphur Spring Group, PS	deep-marine hydrothermal	CM microfossils	Rasmussen, 2000
3225	Clutha Fm, Moodies Group, BGB	shallow-marine	CM microfossils	Javaux *et al.*, 2010
3200	Dixon Island Fm, Cleaverville Group, PS	deep-marine hydrothermal	planar microbialites CM microfossils	Kiyokawa *et al.*, 2006

This means that even if signs of microbial activity were originally present those are now prone to equivocal interpretations. Moreover it has been demonstrated that hydrothermal activity, widely diffused on the early Earth (Van Kranendonk, 2006; Hofmann, 2011), and metamorphic processes may generate morphological or chemical features possibly misinterpreted as biological in their origin (García-Ruiz *et al.*, 2003; Brasier *et al.*, 2006; Wacey, 2009; Gargaud *et al.*, 2013). As a result, claims for life from the very first geological record are extremely controversial and putative biological evidence tend to be weakly supported, failing in passing several biogenicity criteria (García-Ruiz *et al.*, 2003; Brasier *et al.*, 2006; Wacey, 2009; Gargaud *et al.*, 2013). This suggests that extreme caution should be taken when interpreting such ancient material. The problem is well exemplified by the process of the "run" for the oldest microfossil, that may results into claims for life, which, in spite of "making it" to the public news, are far from a scientific consensus, providing insufficient support to justify such ancient and important claims (Nutman *et al.*, 2016; Dodd *et al.*, 2017; Tashiro *et al.*, 2017).

Although the biogenicity dilemma recurs constantly in the search for early life, this can be better tested in the Palaeoarchaean (3.6-3.2 Ga ago) record. From this Era well-preserved supracrustal successions of low-metamorphic grade can be found in the cratons of Kaapvaal and Pilbara (Hofmann and Bolhar, 2007; Kranendonk *et al.*, 2007; Wacey *et al.*, 2009; Arndt and Nisbet, 2012; Tab.1.1).Those represent the ideal geological record for a reliable reconstruction of the early Earth processes including life.

1.2.1 The Pilbara and Kaapvaal cratons

Representing the oldest terrains of true continental size in the geological record, the coeval cratons of Pilbara in Western Australia and Kaapvaal in southern Africa share a suite of lithologies and structural affinities which make geologists believe they were once part of a single supercontinent called Vaalbara (Zegers *et al.*, 1998). Formed between about 3.6 and 3.1 Ga ago, they consist of three principal structural components: (I) granitoid-gneiss terrains composed mainly of TTG magmatic complexes; (II) volcano-sedimentary supracrustal successions both pre- and post-dating different phases of TTGs; and (III) late intrusive granitoids (Gargaud *et al.*, 2013). Of those main structural constituents, the volcano-sedimentary sequences from both cratons represent the most celebrated cradles of life on Earth (Altermann, 2001; Altermann and Kazmierczak, 2003; Schopf *et al.*, 2007). They make up elongated structures, wrapped and intruded by earlier and later granitoids, which, in reason of their characteristic greenschist low-metamorphic grade, are called Greenstone Belts. These true[1] Archaean Greenstone Belts preserve a range of depositional settings which goes from deep-basin and shallow-marine environments characterized by intense extrusive ultramafic-mafic magmatism, hydrothermal activity, silicification and by the precipitation of authigenic sediments such as cherts and banded iron formations (BIFs), to shallower, coastal-deltaic, fluviatile sub-aerial environments observed typically in the upper part of the belts and typified by less abundant, more acidic volcanic rocks and detrital, siliciclastics deposits (Lowe and Byerly, 1999a; Eriksson and Simpson, 2000; Bolhar *et al.*, 2005; Van Kranendonk, 2006; Kranendonk *et al.*, 2007; Hofmann and Bolhar, 2007b; Hofmann and Harris, 2008a). Multiple habitats where chemosynthetic and photosynthetic microbial life could have evolved and flourished are thus represented in this ancient geological record.

In Western Australia the oldest sedimentary rocks are found in the 3.5-3.16 Ga old East Pilbara Terrane (Hickman, 2012). Here vestiges of life in the form of possible microfossils, microbial mats and recurring microbialites have been reported from the numerous greenstone belts grouped in the Pilbara Supergroup (Van Kranendonk, 2007) (Tab. 1.2). Of those fossils, stromatolites and microbial mats occurring in the 3.49 Ga old Dresser Formation and in the 3.45 Ga old Strelley Pool Formation represent some of the most convincing, best preserved and widely accepted proofs for an about 3.5 Ga old Archaean biosphere (Wacey, 2010; Wacey, 2012; Bontognali *et al.*, 2012; Kranendonk, 2011; Noffke *et al.*, 2013; Sugitani *et al.*, 2013; Sugitani *et al.*, 2015; Duda *et al.*, 2016). Similarly, evidence for Palaeoarchaean microbial activity has been reported from the "twin" craton of Kaapvaal, in southern Africa (Tab. 1.2). Here the oldest microbial fossils occur in the greenstone belt of Barberton, one of the classic location for early Life studies and also the geological setting investigated during this work.

The Pilbara Supergroup and the Barberton area offer undoubtedly the geological record where the early microbial evolution can be retraced most faithfully. However this doesn't imply any ease in such reconstruction. At this stage, in fact, another fundamental challenge emerge as researchers are called to disclose cryptic palaeoenvironments developed under an oxygen depleted and highly reducing atmosphere and in oceans deeply affected by diffusive seafloor hydrothermal systems. Such non-actualistic conditions provided us with peculiar

[1]The term greenstone belt, which has a metamorphic-grade connotation, is commonly misused when referred to Eoarchaean volcano-sedimentary successions like the Isua Greenstone Belt or the Nuvvuagittuq Greenstone Belt, as those terrains have undergone amphibolite-grade regional metamorphism and thus do not represent true greenstone belts.

enigmatic rocks characteristic of the early Earth geological history. Within those, Archaean sedimentary cherts, with their incredible preservational potential and CM content, represents the preferential deposits where the early biosphere is investigated.

1.2.2 Origin and biological significance of Archaean cherts

Cherts are deposits composed almost entirely by silica (> 75%) in the form of microcrystalline quartz and represent a recurrent component in the Archaean marine volcano-sedimentary successions. On the modern Earth, since the beginning of the Proterozoic, the oceanic silica concentration has been kept extremely low mainly by the activity of organisms constructing Si-skeletons. With no evidence for such biological control, the abundance of chert deposits in the Archaean record is thought to reflect the non-actualistic conditions in which the early Earth environments developed, whereas abiotic quartz precipitation occurred out of a Si-rich seawater (Maliva *et al.*, 2005). However, the factors and processes which controlled cherts formation are still unclear and the object of a longstanding scientific debate.

Archaean cherts are representative of a variety of depositional facies including bedded, stratiform horizons, crosscutting and stratiform veins, dykes and massive layered rocks (Lowe and Knauth, 1977; Lowe and Fisher Worrel, 1999; Van Kranendonk et al., 2003; Hofmann et al., 2007). In reason of such heterogeneity and after the occurrence of textural, mineral and elemental relicts, evidence for pre-existing rocks, cherts are largely considered the result of secondary silicification[2] on a wide range of lithologies including volcanic and volcaniclastic rocks, terrigenous sediments, mud, silts, chemical deposits such as carbonates or evaporites and biogenic sediments (Lowe and Knauth, 1977; Paris *et al.*, 1985; Lowe and Worrell, 1999; Walsh and Lowe, 1999; Van Kranendonk, 2006; Hofmann and Bolhar, 2007). Mechanisms for primary chert precipitation as a colloidal gel, out of Si-saturated seawater and/or hydrothermal fluids, have been also proposed (Boorn *et al.*, 2007; Ledevin *et al.*, 2014) and may better explain occurrences of pure translucent sedimentary cherts or chert veins, such as the botryoidal quartz-filled veins described in the chapters 2 and 4 of this work.

Different models have been proposed for the genesis of secondary cherts and these vary in terms of source, setting and timing of the silicification process. In many investigations chert deposition has been interpreted to have happened very early in the sediments history, possibly syn-depositionally or during the early diagenesis; this is the case of the fossiliferous

[2] The process of pervasive replacement of the original rock by Si-rich minerals

Archaean cherts whereas silicification probably occurred prior to compaction resulting into the preservation of the original microbial structures. Other occurrences have resulted instead from a much later alteration of rocks. In general the same deposits could have been interested by multiple processes of silicification occurred at various stages during the rocks history. Similarly, several settings and triggers have been suggested.

Considering the presence of an hot Si-rich Archaean ocean some authors have interpreted the silicification as the result of direct interaction between sediments and low-temperature seawater at the sediment-water interface in the absence of hydrothermal activity (Lowe and Knauth, 1977; Lowe and Worrell, 1999; Tice and Lowe, 2006b). Other models proposed instead serpentinization of the oceanic rocks as the source for silica (Wit *et al.*, 1982) or also the devetrification of volcanic rocks (Paris *et al.*, 1985). However, the formation of chert, especially in the Palaeoarchaean record, has been most commonly associated to the circulation of Si-rich hydrothermal fluids, whereas hydrothermal activity was widely diffused on the early Earth (Wit *et al.*, 1982; Paris *et al.*, 1985; Van Kranendonk, 2006; Hofmann and Bolhar, 2007c; Hofmann and Harris, 2008b; Ledevin *et al.*, 2015). This would have resulted into the silicification at the seafloor due to the mixing between hydrothermal fluids and cooler seawater, but also in the subsurface by fracturing, veining or fluid convection through the sediments column.

Although distinct investigations may support contrasting silicification models even for the very same geologic unit, as illustrated in the following section for the geological settings studied in this work, and the origin and exact timing of Si-precipitation may remain shadowy, cherts represent the most informative deposits for the reconstruction of the early Earth surface processes. Particularly, Palaeoarchaean carbonaceous cherts, which are microcrystalline quartz deposits rich in carbonaceous matter, preserving a wide variety of ancient viable habitats are the key lithology in search for Life and provide evidence for the most ancient microbial remains in the form of putative carbonaceous microfossils.

However although carbonaceous morphologies suggest for a widespread Palaeoarchaean biological organic production, abiotic processes occurring on the early Earth are known to result into carbonaceous morphologies and chemistry reminiscent of life without the actual necessity of biological activity (García-Ruiz *et al.*, 2003; Brasier *et al.*, 2006). It results that detailed investigations on the origin and evolution of carbonaceous matter within the Palaeoarchaean cherts are fundamental to improve our understanding of the early Life evolution.

1.3 Regional geology and fossil record of the Barberton Greenstone Belt

Situated at the eastern boundary of the Kaapvaal Craton, the Barberton Greenstone Belt (BGB) of South Africa and Swaziland (Fig. 1.1) is a succession of volcano-sedimentary rocks termed the Swaziland Supergroup (Viljoen and Viljoen, 1969; Ronde *et al.*, 1994; Lowe and Byerly, 1999) which have experienced regional lower greenschist facies grade metamorphism that reached the amphibolite grade in proximity to the surrounding and intruding granitoid domes (Lowe and Byerly, 1999; Tice *et al.*, 2004). The belt is a NE-SW elongated structure which reaches about 150 km in length and 50 km in maximum width and can be divided into northern and southern domains separated by the major Inyoka Fault system. It consists of almost vertically dipping strata tightly folded into a number of synclines and anticlines which offer a journey through the whole Palaeoarchaean time by a simple N-S walk in the field. The Barberton Greenstone Belt is composed of three major stratigraphic units (Lowe and Byerly, 1999; Hofmann and Bolhar, 2007): (I) the basal ultramafic-volcanic dominated Onverwacht Group; (II) the overlying Fig Tree Group, made mainly of argillaceous shales and volcaniclastic sediments; and (III) the youngest siliciclastic Moodies Group.

Dated between about 3.57 and 3.30 Ga, the Onverwacht Group is the most basal unit of the belt and consists of a series of submarine volcano-sedimentary successions representative of intense extrusive activity alternating with periods of volcanic quiescence. Each sequence consist typically of a basal thick volcanic unit highly silicified at its top, an overlying highly silicified volcaniclastic deposit and finally a minor thickness of capping sedimentary chert often enriched in CM (Lowe and Byerly, 1999; Hofmann and Bolhar, 2007). Silica-filled dykes, vein systems and cavities observed especially at the top the sequences, in the upper magmatic sections and sedimentary cherts, have been interpreted as the result of hydrothermal activity possibly related to the residual energy trapped within and escaping from the cooling underlying ultramafic-rocks (Hofmann and Bolhar, 2007; Hofmann and Harris, 2008; Ledevin *et al.*, 2015). South of the major Inyoka Fault system, the Onverwacht Group has been subdivided into six formations, the basal highly metamorphosed Sandspruit and Theespuit formations, the Komati, Hooggenoeg, Kromberg and Mendon formations (Viljoen and Viljoen, 1969; Ronde *et al.*, 1994; Lowe and Byerly, 1999b). North of the fault, rocks have been grouped in the Weltevreden Formation. Overlying the Onverwacht Group, the 3.26 to 3.23 Ga old Fig Tree is composed of distinctive northern and southern domains (Hofmann, 2005).The northern facies consist mainly of turbiditic greywacke, shale and felsic volcanic rocks representative of deep-marine environments. The southern facies instead formed in a

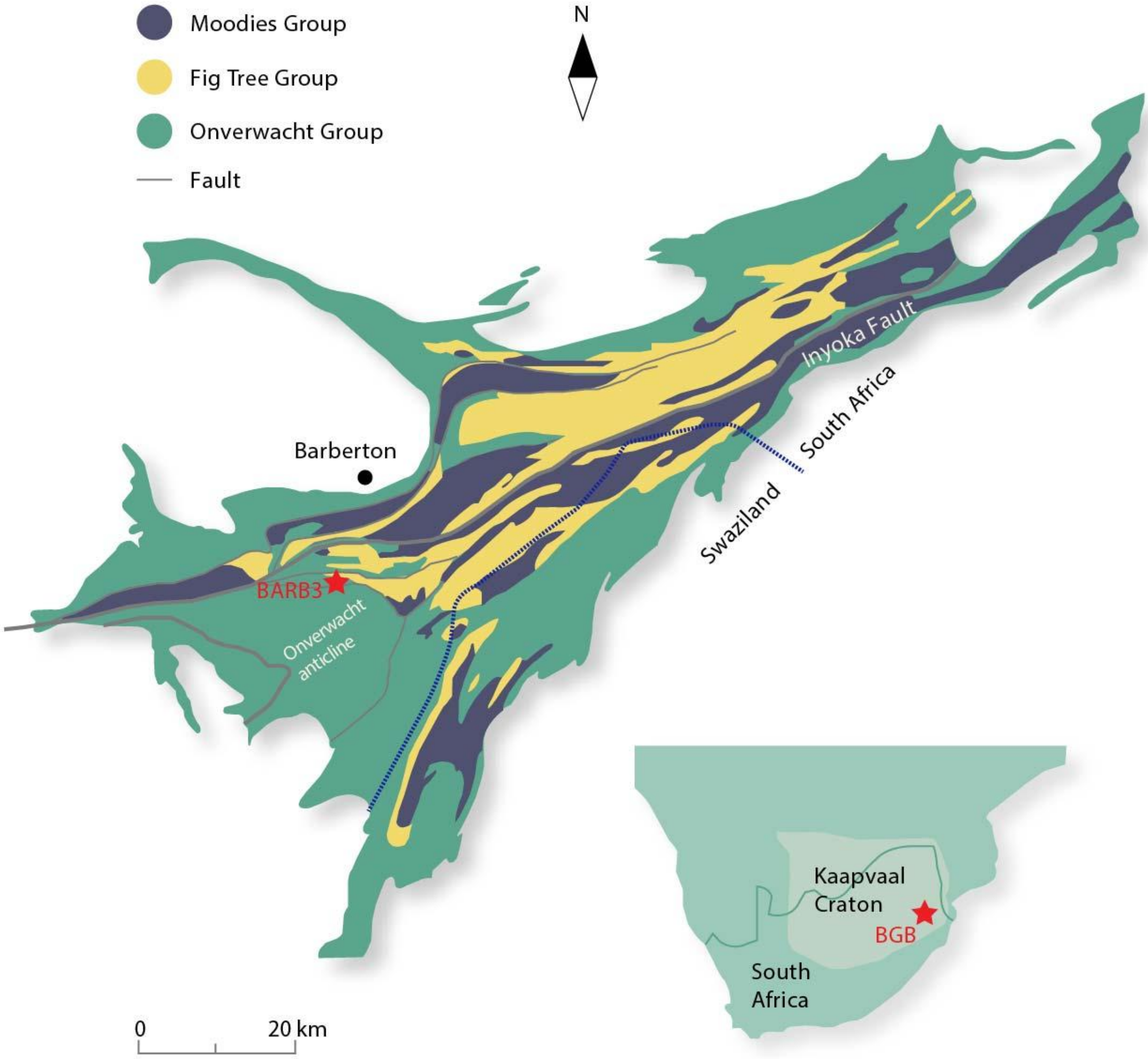

Figure 1.1 - Geological map of the Barberton greenstone belt in South Africa and Swaziland within the Kaapvaal Craton, showing the location of the BARB3 drilling hole (star). After Homann et al. (2015).

shallower setting and include beside shale and greywacke also a variety of coarse siliciclastic sedimentary rocks, minor conglomerates, cherts and jaspilitic banded iron formations. Horizons of impact spherules have also been recognized at the base of both the Fig Tree domains (Lowe *et al.*, 2003; Hofmann *et al.*, 2006). Completing the BGB succession is the youngest Moodies Group which was deposed in a shallow-marine to fluvial environment about 3.22 Ga ago (Hessler and Lowe, 2006). This include thick sandstones, conglomerates, minor shales and banded iron formation.

The BGB represents a classic location to investigate the early record of life. Cherts of the Swaziland Supergroup are rich in sedimentary carbonaceous material which has been interpreted as the remains of microbially produced organic matter (Walsh, 1992; Walsh and

Lowe, 1999; Tice and Lowe, 2006c). A wide range of putative microbial features has been reported, including filamentous, coccoidal, spindle-shaped and spheroidal microfossils (Knoll and Barghoorn, 1977; Walsh and Lowe, 1985; Walsh and Lowe, 1999; Walsh, 1992; Javaux *et al.*, 2010; Homann *et al.*, 2016; Kremer and Kaźmierczak, 2017), stromatolite-like structures (Byerly *et al.*, 1986; Walsh and Westall, 2003) and fossilised carbonaceous mats (Walsh and Lowe, 1999; Tice and Lowe, 2004a; Tice and Lowe, 2006c; Noffke *et al.*, 2006; Westall *et al.*, 2011; Westall *et al.*, 2015; Homann *et al.*, 2015). Within this fossil record, microbial mats from the 3.4 Ga sedimentary succession of the Buck Reef Chert (BRC) represent one of the oldest claims for life on Earth (Walsh, 1992; Tice *et al.*, 2011).

1.3.1 The Buck Reef Chert: a cradle for early microbial life

1.3.1.1 Stratigraphy

Located in the Barberton Greenstone Belt along the western limb of the Onverwacht Anticline at the contact between the Hoggenoegg and Kromberg formations the Buck Reef Chert represent one of the few well-preserved, low- grade metamorphic (lower greenschist facies; (Tice *et al.*, 2004) Palaeoarchaean sedimentary units on Earth. Its age is constrained by 3416 ± 3 Ma old zircons (Krüner *et al.*, 1991) from a thin detrital layer at the succession's base and the 3334 ± 5 Ma old Footbridge Chert situated at the top of the Kromberg Formation 1.3 km above the sequence (Byerly *et al.*, 1993; Byerly *et al.*, 1996).

The BRC consists of an unusually thick (up to 400 m) sequence of mainly black-and-white banded sediments composed almost entirely of microcrystalline quartz (chert) enriched in carbonaceous material and other accessory minerals. Minor silicified banded units are a recurring feature of the Palaeoarchaean volcano-sedimentary successions (de Vries *et al.*, 2010). Three main lithofacies have been recognized in the succession (Fig. 2.1) (Lowe and Worrell, 1999; Tice and Lowe, 2004, 2006a;b):

I. A basal evaporitic facies which includes silicified ripple laminations (Fig. 1.2a) and chert lenses interfingering with underlying silicified volcaniclastic sandstones of the Hoggenoegg Formation. Pseudomorphs after nahcolite, silica-replaced evaporitic crystals and botryoidal quartz-filled cavities (Fig. 1.2b) have been also reported (Lowe and Worrell, 1999; Tice and Lowe, 2004, 2006b). Locally, at the top of the evaporitic and botryoidal chert, a 50-100 cm thick pseudo-conglomerate consists of banded and evaporitic chert fragments in a quartz and botryoidal quartz matrix (Hofmann and Bolhar, 2007) (Fig. 1.2b);

II. A platformal facies of black, carbonaceous, and white banded chert. This is characterized especially in the lower part by disrupted or brecciated banded chert units and by the occurrence of megaquartz-filled cavities (Lowe and Worrell, 1999; Tice and Lowe, 2004,2006b);

III. A basin facies of more compacted and finely laminated ferruginous banded chert. Here bands disruption, brecciation and quartz-filled cavities are rare or absent (Lowe and Worrell, 1999; Tice and Lowe, 2004, 2006b).

A further upper platformal division is found locally on the west limb of the Onverwacht anticline. The succession is finally capped by a thick ultramafic sill which separate the BRC from the ultramafic lapillistone of the overlying Kromberg Formation.

The BRC facies have been interpreted as deposited in a coastal-lagoonal to open marine environment, based on stratigraphic progression from evaporites to homogeneous banded units, which traditionally reflect a transition from shallow to deeper marine conditions (Lowe and Worrell, 1999; Tice and Lowe, 2006b). However, some aspects of the environment, with pivotal implications for the ecosystem reconstruction, remain cryptic, such as the influence of hydrothermal activity on the BRC deposition (Hofmann, 2011).

1.3.1.2 The role of hydrothermalism in the Buck Reef Chert

Hydrothermal activity during BRC deposition has been suggested by de Vries (2004) and de Vries et al.(2006) in relation to syn-depositional normal faulting which according to those authors may have driven the formation of the Buck Ridge volcano-sedimentary complex. On the other hand, Tice and Lowe (2004, 2006a,b) considered the BRC to represent sediments deposited in a non-hydrothermal environment. They pointed at the absence of exhalites, fluid conduits and hot springs and suggested silicification of the deposits trough the interaction with hot marine water supersaturated in amorphous silica directly at the sediment-water interface. Nevertheless, cross-cutting and planar vein networks interpreted as the remains of hydrothermal systems have been reported below the basal chert horizons of the BRC and support active syn-depositional hydrothermal venting at least for the lower part of the succession (Hofmann and Bolhar, 2007). Hofmann and Bolhar (2007) and Hofmann and Harris (2008), based on such structural evidence and geochemical data, provided a model for

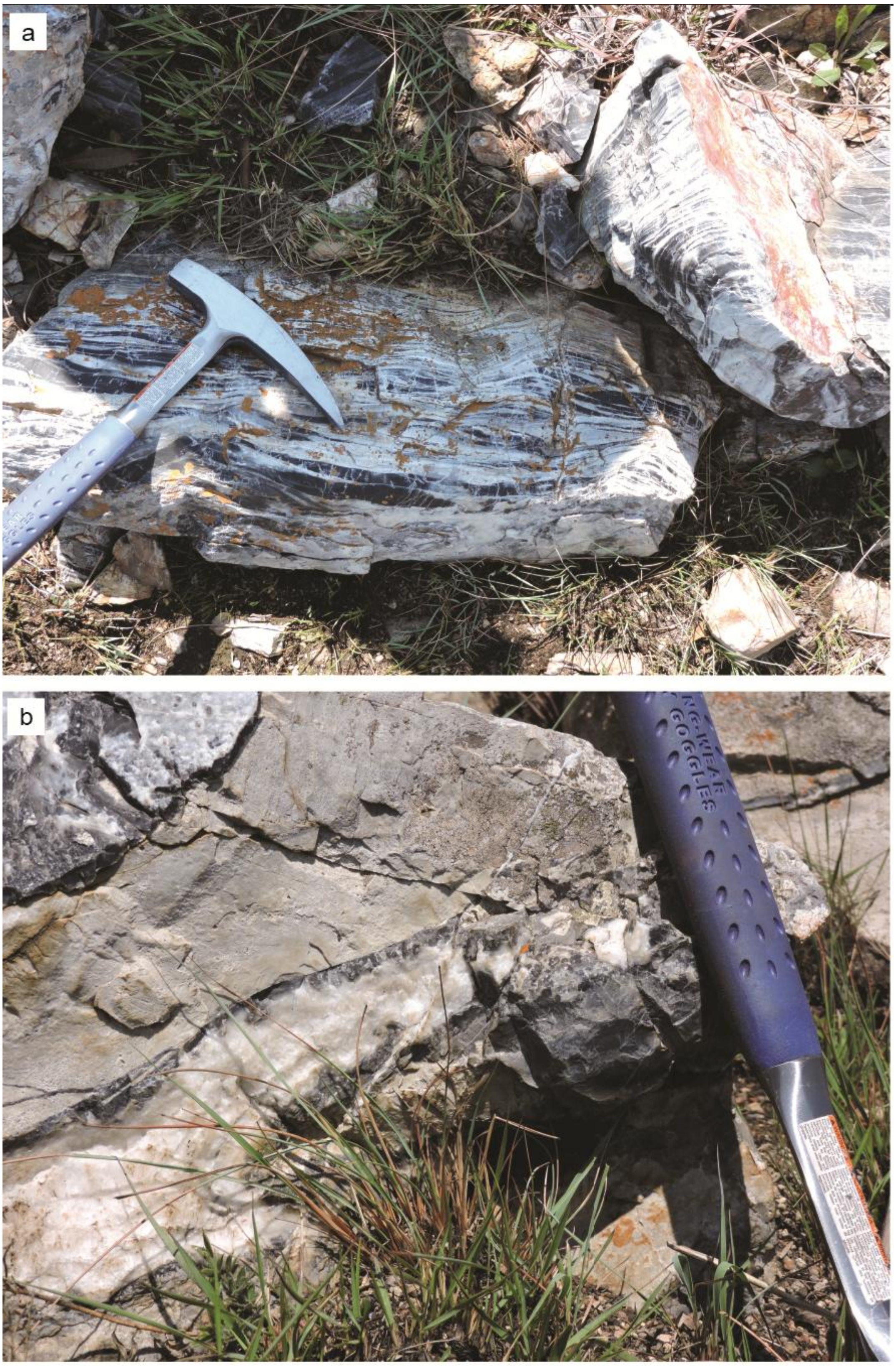

Figure 1.2 – Evaporitic section of the BRC outcrop. a) wavy laminated white and translucent chert from the basal BRC evaporitic facies interpreted to represent Paleoarchean ripples formed in coastal-lagoonal environment (Tice and Lowe, 2006b). b) botryoidal quartz-filled cavity or vein at the top of the BRC basal evaporitic facies occurring in the conglomerate (Tice and Lowe, 2006b) or pseudo-conglomerate, chert breccia (Hofmann and Bolhar, 2007) section. Such features recur frequently also in the ripple section and in the overlying platformal facies, they have been interpreted differently depending if hydrothermalism has been supported or not during the BRC deposition.

the development of chert veins, silica alteration zones and the origin of overlying stratified cherts horizons. According to this model convection of Si-saturated seawater, driven by the high regional heat flow caused sediments silicification at the sediment-water interface as the hydrothermal fluids were cooling after mixing with seawater. Such process formed impermeable silicified caps inducing overpressure in the hydrothermal system and eventually hydrothermal brecciation and branching of stratiform veins. Finally, unsilicified carbonaceous sediments would have entered the conduits resulting into carbonaceous veins observed today in the field. Similar processes have been previously proposed in a general model for the silicification of volcanic rocks and the formation of veining systems within the BGB (Paris *et al.*, 1985).

A compelling aspect of the debate is the significance of the botryoidal quartz-filled cavities (Fig. 1.2b) found in both the evaporitic and platformal facies of the BRC. In the non-hydrothermal settings (Tice and Lowe 2004, 2006) they are regarded as dissolution cavities formed in the phreatic zone, in the evaporitic facies, and as fluid escape structures resulting from soft-sediment disruption after storm events, in the platformal facies. In the hydrothermal model (de Vries *et al.*, 2006; de Vries and Touret, 2007; Hofmann and Bolhar, 2007; Hofmann and Harris, 2008) the same structures have been described as the result of veining, brecciation and precipitation of colloform silica after upwelling and pervading silica-rich fluids. However both interpretations rely on the depositional settings supported by the respective authors and the botryoidal quartz-filled cavities haven’t been directly investigated yet.

1.3.1.3 Carbonaceous matter and traces of life in the Buck Reef Chert

The BRC has long been appealing for early life researchers, as the succession is rich in sedimentary carbonaceous material, which, as described in the previous chapter, brings implications with concern to possible ancient microbial organic production. In fact, CM from the BRC, similarly to the rest of the BGB, has been suggested to be largely, if not entirely, of biological origin (Walsh, 1992; Walsh and Lowe, 1999; Tice and Lowe, 2006b). This view is supported by morphological evidences of diffuse carbonaceous laminations interpreted as the remains of seafloor microbial communities and by the occurrence of such laminations and other CM-rich textures in cherts deposited during periods of volcanic quiescence, in environmental settings suitable to life (Walsh, 1992; Walsh and Lowe, 1999; Tice and Lowe, 2006b). Isotopic composition of the carbonaceous matter has been also used to invoke different microbial metabolic pathways and in general the BRC CM has been placed in textural, compositional, depositional and abundance continuity with sedimentary kerogens of the younger Precambrian geological record, implying thus a similar microbial origin (Walsh, 1992; Walsh and Lowe, 1999; Tice and Lowe, 2006b). Furthermore the same investigators (Walsh, 1992; Walsh and Lowe, 1999; Tice and Lowe, 2006b) have precluded possibilities of carbonaceous remobilization or hydrothermal inputs as hydrothermalism during BRC deposition has been excluded.

Previous workers have been focusing mainly on the BRC shallow-platformal facies as in this lithofacies CM is particularly rich, texturally diverse and preserves morphological evidences for a Palaeoarchaean microbially active environment. Here, anastomosing, bifurcating and cohesive carbonaceous-rich laminations have been recognized as well-preserved microbial mats (Walsh, 1992; Tice and Lowe, 2006b). Tice and Lowe (2004, 2006a,b) and Tice (2009, 2011) provided extensive and detailed investigations on such structures which they classified into three major morphotypes possibly reflecting different populations of mat-constructors. Excluding hydrothermal activity from the BRC, hence from the possible sources for microbial sustenance, those authors evaluated the intact laminations focusing on their exclusive distribution within the platformal facies. Such restriction to estimated depth between 15 and 200 m was regarded as a microbial confinement to the euphotic zone. Accordingly, in spite of the aforementioned morphotypes distinction, all mats were seen as produced by photosynthetic communities, with the BRC $\delta^{13}C$ isotopic composition falling between -35‰ and -30‰ (Tice and Lowe, 2006b), consistent with carbon fixation through the Calvin cycle by autotrophic microorganisms.

The view of the BRC mats as the remains of photosynthetic microbial communities largely rely on the environmental constraints proposed. However, as reported above, hydrothermalism has also been supported (de Vries *et al.*, 2006; de Vries and Touret, 2007; Hofmann and Bolhar, 2007; Hofmann and Harris, 2008) so that pathways of CM production and maturation and the trophic identity of microbial communities at the BRC are at the centre of a controversy thus in need of further elucidation.

1.4 This study

Much has been written in recent years concerning the biogenicity dilemma of ancient CM and two principal approaches can be recognized. The first, namely the “list of criteria approach” (Awramik *et al.*, 1983; Buick, 1984), propose a list of positive (bio-affine) and negative (abio-affine) tests against which CM should be verified to identify possible biogenic rather than abiotic features. The second, the “falsification approach” (Brasier *et al.*, 2002, 2004), suggest a more systematic test against possible abiotic hypotheses; in this way the “falsification approach” appear to be an implementation of the “list of criteria” whereas more abiotic hypotheses are tested. However, as wisely pointed out by Tice and Lowe (2006b), both approaches, at the state of our current knowledge, fail in defining a finite set of criteria to clearly establish the biogenicity of ancient CM and both procedures rather set the stage for an infinite list of possible null hypothesis. On the other hand researchers have noted how many Archaean CM properties such as its structure, composition, depositional and preservational environments and abundance are basically in continuity with the younger Precambrian record (Tice and Lowe, 2006b). At the same time recent increasing evidence for a Palaeoarchaean microbial biosphere have in many cases already opened discussions about ecological behaviour of ancient microbial remains (Tice *et al.*, 2011). In this way much of the CM from the Pilbara Supergroup and Barberton Greenstone Belt, following the Occam’s razor principle, appear more reasonably comparable with younger biogenic deposits rather than tested against an infinite set of “null hypothesis”.

Following such philosophy in this project investigated CM-rich drill core (BARB3) material from the c. 3.4 Ga old Buck Reef Chert of the Barberton greenstone belt of South Africa, one of the best preserved, less metamorphic Archaean volcano-sedimentary succession on Earth and a classic location for the early Life research. A multiple analytical approach, based on *in situ* complementary techniques, is here used to characterize the BRC shallow-platformal CM within its mineralogical context, from the core down to the atomic scale, to investigate its origin and evolution in the perspective of the BRC depositional environment open debate (Hofmann, 2011)

The aim of this study has been to: (I) recognize evidence of biological activity within the core through the morpho-chemical characterization of potential microbial fossils; (II) investigate the provenance and relationships between CM in the different lithofacies to test theories for CM origin and evolution; (III) search for biosignatures, if any, and techniques for early life detection; (IV) contribute to the Paleoarchean environmental reconstruction.

Chapter 2

From the outcrop to the Ångstrom: materials and techniques for the characterization of carbonaceous matter from the BARB3 drill core in its mineralogical context

2.1 Peering into the cradle of life

In May 2012, aiming to improve our understanding of geological and biogeochemical processes on the early Earth through the investigation of extraordinarily well-preserved Palaeoarchaean material, the ICDP-sponsored Barberton drilling project completed piercing at four sites in the Barberton Greenstone Belt obtaining five continuous and relatively unaltered sections through the southern African volcano-sedimentary succession (Arndt *et al.*, 2013). The main targets of the drilling were: (I) sedimentary sequences, with the intent to provide insights into the early Earth surface processes, including modes of sedimentation, geochemical cycles, marine/hydrothermal conditions and the evolution of the early biosphere; (II) ultramafic to felsic volcanic rocks to reconstruct the dynamics and rate of extrusive, crustal and mantel processes.

Responding to the first purpose, a single core, the BARB3 drill core (Hofmann et al., 2013a), was obtained from the ~3.4 Ga old Buck Reef Chert sedimentary unit which, as showed in the previous chapter, represents an excellent location for ancient biological and depositional processes investigation. Focusing on traces of microbial activity and possible early life environments preserved in the BARB3 material, this study is a contribution to the Barberton drilling project early life investigation.

2.1.1 Stratigraphy of the BARB3 core

The BARB3 core consist of a total length of ~899 m drilled at an angle of 45° to the BRC sedimentary plane (Hofmann et al., 2013a). About 200 m of the serpentinized peridotite sill at the base of the Kromberg Formation was first intersected while the majority of the core (618 m) consists of sedimentary carbonaceous and ferruginous banded cherts intruded by two minor sills, mafic and felsic respectively (Fig. 2.1). Based on their textures and degree of compaction, sedimentary cherts, which are estimated to represent an actual stratigraphic section of about 337 meters (618 *sin* 45°), can be divided into a lower, an intermediate and a top division, corresponding to the succession of two main lithofacies along the core. The lower and top sections (I) consist mainly of interspersed ferruginous, carbonaceous and white chert mesobands[3] and are both characterized by the occurrence of frequent stratiform

[3]In reason of their bedded nature on a multiple range of scales and of their iron-rich content, the terms mesobands (centimetre-thick bands) and microbands (millimetre and sub-millimetre thick bands), typically used for Precambrian banded iron formations(Ayres, 1972; Konhauser *et al.*, 2002; Rasmussen *et al.*, 2013), appear particularly suited to the description of the BARB3 chert divisions.

botryoidal quartz-filled veins, granular carbonaceous chert layers and brecciated white chert slabs conferring an overall heterogeneous aspect to the core especially at its base (Fig. 3.1). The intermediate division (II) is largely a banded iron formation (BIF) composed of an alternation of notably more homogenous and compacted mesobands of siderite and white chert characterized by sparse bright-red jasper mesobands and by the reduction and loss of those attributes distinctive of the lower and upper sections including black chert, granular carbonaceous chert and botryoidal quartz-filled veins. The overall BARB3 chert sequence can be readily correlated with the BRC stratigraphy (Fig. 3.1) proposed by Lowe and Fisher Worrell (1999), Lowe and Byerly (2003) and Tice and Lowe (2004), particularly to the so called platformal-basinal-platformal lithofacies succession observed on the west limb of the Onverwacht anticline (Tice and Lowe, 2004), with the main core lithofacies described above corresponding respectively to the BRC shallow-platformal facies (I) and deeper basin facies (II). The basal evaporites of the BRC succession are not represented in the BARB3 core as they were not traversed during the drilling.

2.1.2 Sampling from the BARB3

All the samples analyzed during this investigation derive from the BARB3 core (Fig. 2.1) which at the time of this study was housed at the Department of Geology, University of Johannesburg. The BARB3 drill core was systematically sampled to provide 26 quarter core specimens representative of stratiform chert horizons corresponding to the Buck Reef Chert shallow-water platformal facies and 5 specimens from the deep-water basin facies. Although some preliminary mineralogical data was obtained from the basin samples, this study focus on the upper and lower platformal deposits. Core cutting was performed at the Department of Geology, University of Johannesburg, using an Almonte Automatic Core Cutter. 42 polished petrographic 40 μm thin sections[4] was prepared for analyses at the thin section preparation lab of the Department of Biological, Geological and Environmental Science (BiGeA), University of Bologna and 20 more sections were produced at the Central Analytical Facility of the Faculty of Science (Spectrum), University of Johannesburg. During

[4]Due to the optical translucent quartz-rich composition of the analyzed material, the in-depth working techniques used during this study, except for transmitted infrared spectroscopy that required a special preparation (see the vibrational spectroscopy section), are not affected by the original section thickness. Considering this, thin sections thicker than the usual 30 μm were prepared in order to increase the volume of analyzed material and the chances of including possible traces of life.

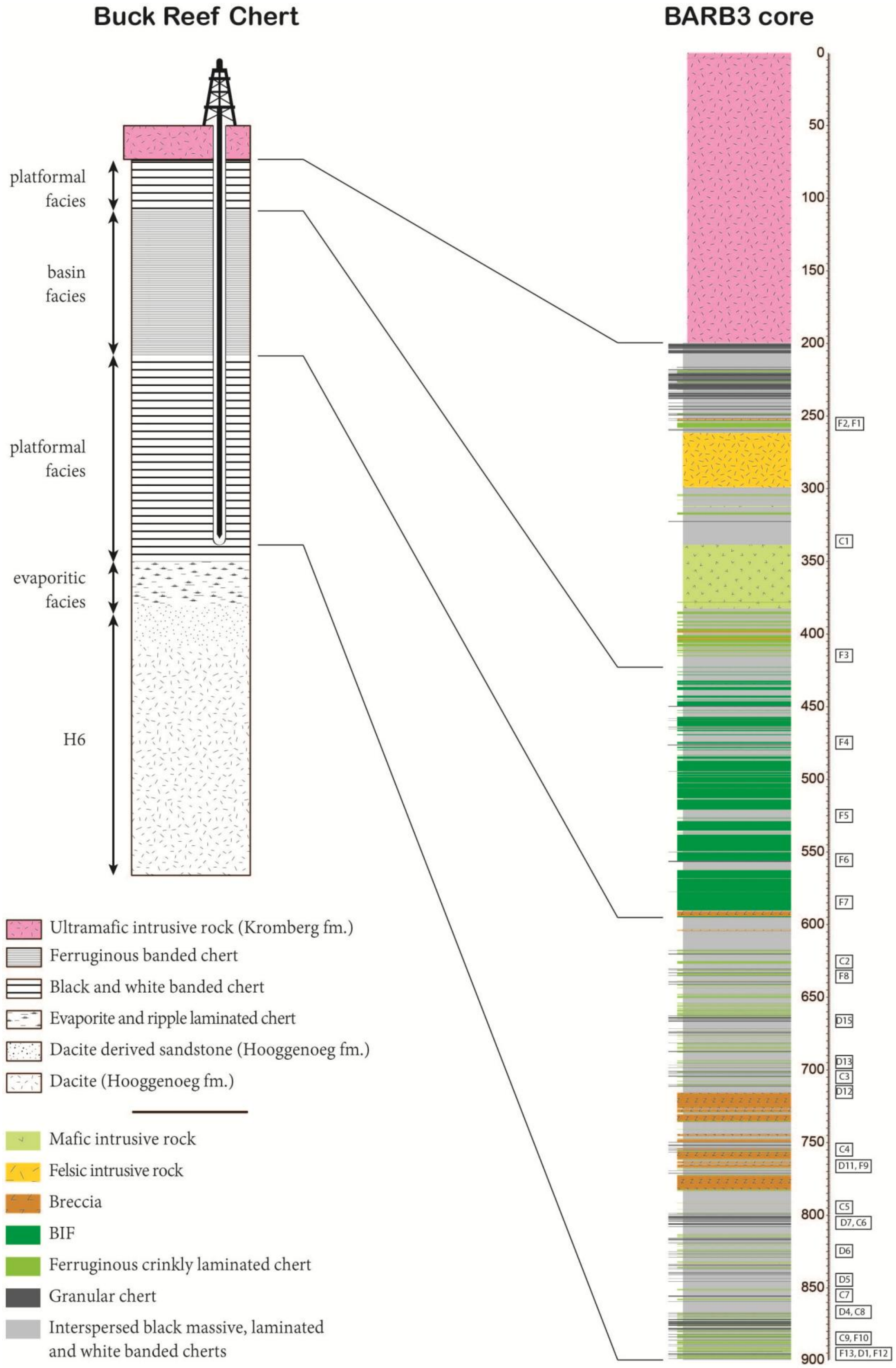

Figure 2.1–Stratigraphic logs of BARB3 core (Hofmann, unpubl.), with sampling vs the Buck Reef Chert.

this study most of the analyses were conducted on such prepared standard polished petrographic thin sections, in the cases where further preparation was needed this will be illustrated as part of the analytical method for which it was required. For details concerning samples provenance along the core, represented facies and employed techniques refer to S1 supplementary material.

2.2 A multiple analytical approach

In the absence of “smoking guns” (Tice and Lowe, 2006b) providing unequivocal evidence for life, investigators of the ancient geological record are called to face the ambiguity between abiotic and biotic signatures. Moreover, biogenicity and syngenicity of possible microbial traces need to be tested within rocks which even when weakly metamorphosed may not easily allow the identification of primary rather than post-depositional features, especially considering that our understanding of depositional processes on the early Earth is still shadowy. Such complications require extreme caution and an investigative approach to be applied at different scales in order to obtain multiple lines of evidences for life (Wacey, 2009). Particularly one should be able to recognize an environment compatible with life from the outcrop down to the micro-scale of the mineralogical context embedding the hypothetical biosignature. An exhaustive approach would than verify evidences of biological morphology, including possible indicators of microbial behaviour, a carbonaceous rich composition in the case of direct microbial remains (including EPS and mat remains) or bio-affine elemental enrichments in the case of indirect biosignatures, and finally metabolic pathways consistent with the reconstructed environment possibly supported by suitable isotopic fractionations (Brasier and Wacey, 2012; Brasier *et al.*, 2015; Wacey *et al.*, 2017).

Similar steps need to be followed when retracing the origin of Palaeoarchaean CM and its possible relation to microbial activity (Oehler and Cady, 2014). The depositional environment needs to be clarified in order to understand which abiotic and biotic pathways may have been possibly responsible for the CM production and the extent of their respective contributions to the rocks carbonaceous content. CM should be also chemically and structurally characterized at different scales within its mineralogical context to provide insights about the nature of its possible original precursor and about the processes of maturation which have led to its actual form. Particularly, by means of several analytical techniques, CM can be investigated at its multiple levels of organization corresponding to its texture, microtexture, structure and nanotexture.

In this work multiple and complementary analytical tools operating at different scales have been applied to the BARB3 drill core material. The investigation has been focused on the BRC shallow-platformal lithofacies and their carbonaceous content. The experimental approach has been carried out following two parallel interdependent lines of investigation: (I) the examination of the depositional and mineral-petrographic context in which the BARB3 CM occur through direct core observations, optical microscopy, Raman spectroscopy, scanning and transmitted electron microscopy; (II) the characterization of the BARB3 CM at its various level of organization through direct core observations for its textures, optical microscopy for the microtextures, infrared and Raman spectroscopy for the carbonaceous structure and high resolution transmitted microscopy for the nanotexture.

The study of the BARB3 material was also supported by observations made directly from the BRC outcrop in the field and some field evidences will be presented in the form of photographic material.

2.2.1 Core survey and optical microscopy

The whole BARB3 chert succession was inspected during the sampling process, however direct observations were focused on the shallow-platformal facies. Observations with the unaided eye and the hand lens took place at the core storage facility, while further inspections were done on hand specimens and with the assistance of a Zeiss Discovery Stereo Microscope, Spectrum facilities. Optical petrography and fabric mapping were performed on polished thin sections using a Zeiss Axioplan Microscope equipped with a Nikon HS DS-Vi1 colour camera at BiGeA and a Zeiss Axioplan 2 Compound Microscope equipped with an AxioCam HR colour CCD camera at Spectrum facilities.

2.2.2 Vibrational spectroscopy

Spectroscopy investigates the interactions between the electromagnetic radiation and matter and it can be classified depending on the energy of the radiation employed and on the type of interaction promoted. In vibrational spectroscopy low-frequency radiations, typically in the infrared or visible spectra, interact with the molecular vibrational modes inducing low-energy quantum transitions. As vibrations happen at specific frequencies depending on the atomic masses involved, their bonds and spatial arrangement, the detection of such interactions provide insights into the structure of the analyzed substance.

The two most commonly used vibrational spectroscopic techniques are infrared (IR or more commonly FTIR, Fourier Transform Infrared spectroscopy) and Raman spectroscopy. In both of these processes when light interacts with the matter vibrations, exchanges in energy occur and result in a difference between the original and the collected radiation. Such difference can be detect and visualized on a graphic spectrum in the form of peaks appearing at specific frequencies which are diagnostic for the chemical structure of the investigated sample. It follows that IR and Raman spectroscopy can be used for the identification and the structural/chemical characterization of minerals, but also amorphous materials like the organics buried within sediments or other CM. Particularly, for reasons of the energy involved, IR is more sensitive and thus more suited for strongly polarized bonds typical of functional groups such as C-N, C-O, C=O, N-H and O-H, while neutral or weakly polarized bonds composing the molecular frameworks such as C-C, C-H, S-H, C=S, and C=C produce stronger Raman scattering (Olcott Marshall and Marshall, 2015). The two methods thus provide complementary information about the structural characteristic of the investigated substances. During this work Raman and FTIR-microspectroscopy, representing both non-destructive *in situ* techniques have been applied to structurally characterize meta-sedimentary BARB3 CM. However during the IR analytical work several difficulties have been encountered which can be related to the employed experimental method. In reason of such difficulties a proper IR characterization of CM, also due to the limited analytical time available, has not been possible. However believing this technique has a great potential interested researcher are suggested to read the fundamental work of Igisu and collaborators (Igisu et al., 2006, 2009, 2011, 2014) and Preston et al.(2011) but also to the more recent and very interesting studies by Qu et al. (2015, 2017).

2.2.2.1 Raman spectroscopy

During the interaction of visible light with matter discrete amounts of energy can be exchanged between the incoming radiation and the vibrational modes of crystals or molecules composing the irradiated substance. Such transfer may results in an inelastic scattering of light known as Raman scattering (or Raman light), named after the physicist C.V. Raman who first observed and described the phenomenon (Raman, 1928). As the shift in energy between the incoming and scattered radiation reflects the frequencies of specific vibrational modes, related to specific atomic masses and bonding, detecting and interpreting the Raman light can "[...]enable us to obtain insights into the ultimate structure of the scattering substance." (from C.V. Raman Nobel lecture, 1930). Raman spectroscopy represent a unique technique to investigate vibrational properties of materials and it can be used to characterize the chemical structure of a sample by mean of a low-energy, non-destructive radiation.

In Raman spectroscopy the substance under investigation (solid, liquid or gas) is most commonly irradiated with a laser light having a wavelength ranging between 514 and 785 nm (Andò and Garzanti, 2014). However other radiations, like near-infrared light (NIR-Raman spectroscopy, Schrader et al., 1999), are also employed depending on the specific case necessity. Interacting with the sample a component of the incident laser light can be scattered elastically (Rayleigh effect) and, in a minor portion, inelastically as a result of two type of events, a gain of energy (anti-Stokes Raman scattering) or a loss of energy (Stokes Raman scattering). Those energy transfers results into discrete shifts of the original radiation frequency towards higher (anti-Stokes) or lower (Stokes) frequencies. In Raman spectroscopy, by mean of a CCD collector and specific software, the scattering events can be quantified in terms of their frequencies and counts which can then be plotted as Raman spectra. Here the inelastic scattering is visualized in the form of peaks whose shapes and positions in relation to the original frequency (represented by the Rayleigh line) are diagnostic for peculiar atomic vibrational modes and thus for the sample chemical structure. Particularly a specific Raman-active mode will produce a Stoke and a symmetric anti-Stoke counterpart, however, as the gain in energy by the incoming radiation happen with less probability (low counts), only the Stoke part of the spectra is usually considered. Therefore, by convention, the Stokes shifts are expressed with positive wavenumber values starting from the Rayleigh signal which represent the zero Raman shift. In this way the Raman spectrum pattern gives us insights into the structural characteristics of the investigated sample.

The association of the above described methodology to standard or confocal optical microscopes, namely Raman micro-spectroscopy and Confocal Raman spectroscopy (Dieing *et al.*, 2011), results into an efficient and versatile analytical technique which allows the characterization of materials in-situ at the micron scale. The application of automated stages to such instruments have further improved research opportunities introducing Raman imaging facilities (Salzer and Siesler, 2009). In such technique selected areas of the studied sample are automatically scanned by lines of punctual Raman measurements. From the obtained dataset the operator can than select a specific wavelength to map its intensity through the analyzed area. The result is an image where each pixel, corresponding to each analyzed point, have a brightness (on a preset colour) reflecting the intensity of the selected wavelength in that specific position of the map. In this way Raman imaging highlight the distribution of specific molecular vibrations and maps can be compared to optical images of the same area. In reason of such possibilities and of the non-destructive energies employed Raman microspectroscopy is now applied to a wide range of research fields including geology.

Raman Spectroscopy in mineral-petrographic investigations

Allowing the characterization of the chemical structure in crystalline materials, Raman spectroscopy finds its first geological application in mineral identification. Common rock-forming minerals can be recognized with great precision as their vibrational modes produce diagnostic bands at characteristic wavelengths with specific relative intensities, making this technique an excellent fingerprinting mineralogical-petrographic tool (Fig. 2.2). Furthermore, Raman analyses present some important advantages over other routinely mineralogical-petrographic techniques. Raman micro-spectroscopy can identify directly observed grains and crystals, with a resolution down to a few microns, independently from their orientation in the sample. Also the method doesn't require any specific preparation and it can be applied to both hand-specimens and normal petrographic thin sections in contrast to SEM-EDX which usually involve some invasive sample preparation. Additionally if electron-beam based measurements provide the bulk elemental content of the analyzed volume through the Raman scattering we can directly discriminate the different occurring mineral phases in the investigated spot. Finally, while SEM-EDX or EMPA are both working at the sample surface, Confocal Raman spectroscopy allows investigation at depth finding its ideal application in mineral inclusion studies (Beran and Libowitzky, 2004; Frezzotti *et al.*, 2012).

A second crucial benefit of Raman spectroscopy is its sensitivity to amorphous materials and non-crystalline molecules, other than just mineral phases, which allows the detailed characterization of carbonaceous materials and other non–crystalline organic or inorganic compounds buried within rocks. By Raman imaging the interrelationships between both crystalline and amorphous phases can thus be explored so that carbonaceous and organic materials are characterized within their mineralogical context. The sensitivity of Raman spectroscopy to amorphous materials finds an important application in the analysis and characterisation of carbonaceous materials from throughout the geological record and the

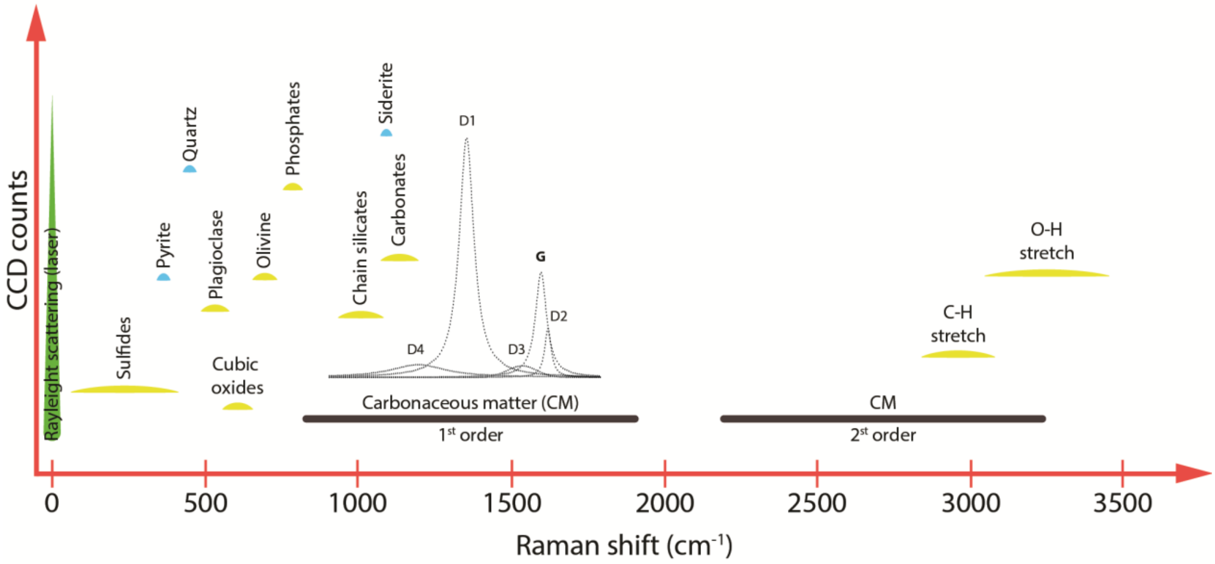

Figure 2.2 – Diagnostic regions for Raman mineral fingerprinting. Diagnostic peaks of specific mineral groups occur within specific wavelength ranges. The first-order Raman spectrum of disordered carbonaceous materials (CM) can result from the combination of up to 5 different bands (D1, D2, D3, D4, G) as shown by a decomposed representative CM spectrum. The G band corresponds to the diagnostic peak of graphite. Weak bands at higher wavenumbers appear in the CM second-order range. Rayleigh scattering results in a zero Raman shift. Modified from Dieing et al. (2010).

technique has been used to investigate the chemical and mineral composition of a variety of fossil assemblages including ancient carbonaceous microfossils (Kudryavtsev *et al.*, 2001; Schopf and Kudryavtsev, 2009) and stromatolites (Allwood *et al.*, 2006).The following section illustrates how the decomposition of Raman spectra by fitting modelling provides a tool to investigate the carbonaceous provenance and to reconstruct the geothermal history of the hosting formation.

Characteristics and evolution of the CM Raman spectrum

The Raman spectrum of carbonaceous material (Fig. 2.2) is composed of two regions: (1) a first-order region (~800-1900 cm^{-1}) which includes frequencies of the CM fundamental vibrations, and (2) a second-order region (~2200-3300 cm^{-1}) with Raman bands corresponding to overtones and combinations of the fundamental modes. It is usually the first-order region which accounts for the features more sensitive to CM structural variations and which, once deconvoluted, is best suited to obtain peak parameters and to characterize the CM disorder (e.g., Marshall et al., 2010).

The evolution of the Raman spectrum of CM is best illustrated by tracing back the carbonaceous maturation from fully-crystalline graphite to completely amorphous CM. In the first-order region of crystalline graphite only a single line, at ~1580 cm^{-1}, is present. This band, termed the G-band (graphitic), results from the ideal graphitic lattice E_{2g}-symmetry and it is attributed to the in-plane bond-stretching at all of the sp^2 C sites (Ferrari & Robertson, 2000). With increasing in-plane defects due to heteroatoms or in micro-crystalline graphite (Wang *et al.*, 1990), an A_{1g} breathing mode of sp^2 C within six-fold aromatic rings becomes active and give rise to two D (disordered) bands, respectively the D1 at ~1350 cm^{-1} and D2 at ~1620 cm^{-1}. Additional first-order bands appear with increasing disorder at ~1500 cm^{-1} (D3) and ~1080-1250 cm^{-1} (D4). Further disorder in the carbonaceous structure towards almost completely amorphous CM, such as in extremely low-grade metamorphic rocks, results in the loss of the G peak. In this case, the latter may become replaced completely by the D2 signal and a general broadening of the disordered components will be observed with D1 decreasing in intensity and forming a unique broad band together with D4 and D3 (Ferrari and Robertson, 2000; Kouketsu *et al.*, 2014).In such low-metamorphic CM before the G band in *sensu stricto* (E_{2g}-symmetry) is completely lost, G and D2 both occur combining in a very narrow peak in which the two individual bands greatly overlap resulting in a difficult spectral interpretation. In such poorly ordered CM this narrow peak is named G_L, where "L" stands for Low-temperature or Low-metamorphic (Kouketsu et al., 2014), and correspond to the sum of a prevailing D2 and a decreasing G (*s.s.*) down to a complete loss of G and a D2 band only.

It follows that the Raman spectrum of CM can be deconvoluted by model fitting from two to five curves and using different functions (Gaussian and Lorentzian being the most frequently used) depending on the level of crystallinity of the analyzed CM (Ferrari and Robertson, 2000; Sadezky *et al.*, 2005; Lünsdorf *et al.*, 2014; Kouketsu *et al.*, 2014). The deconvolution process results in peak parameters, such as peak width, intensity and integrated area, or ratios between those, that can then be used to assess the degree of CM disorder and heterogeneity, and to obtain a true Raman geothermometer (Beyssac *et al.*, 2002; Beyssac *et al.*, 2003; Marshall *et al.*, 2012; Sforna *et al.*, 2014; Kouketsu *et al.*, 2014; see legend in S2).

Analytical settings

Confocal Raman spectroscopy on polished petrographic thin sections was carried out at the Assore Raman Lab, housed in the Department of Geology, University of Johannesburg, using a WITec alpha300-R Confocal Laser Raman microscope equipped with an automated sample stage for micro-Raman mapping. Measurements were obtained at room temperature using a 532 nm wavelength of a frequency-doubled solid-state YAG laser source. All spectra were collected in the Stokes Raman shift up to 3800 cm^{-1} using a 600 lines/mm grating and a Peltier-cooled EMCCD sensor for signal detection. Before each experimental session the spectrometer was calibrated with a silicon chip standard. For identification and spatial characterization of minerals punctual and imaging data were collected using 20X, 50X, 100X objectives (N.A. = 0.40; 0.55; 0.90) and a maximum laser power, before the objective, of 3mW, in order to prevent CM thermal alteration. A detailed Raman investigation on different carbonaceous types, identified after optical microscopy, was performed on six petrographic thin sections (D11A, C3A, D1, C9E, C2C, D4A) representative of the main lithofacies described in this work. For each section two different CM microtextures have been selected and each section analysed by means of at least 25 total punctual spectra to produce a statistically significant dataset (Aoya et al., 2010). Measurements on carbonaceous material were collected by focusing the laser beam through a 50X (N.A. = 0.55) objective for 240 s at a power of 3mW. Acquisitions were taken on focal planes selected at more than 3 μm depth into the thin sections excluding possible surface contaminants and eliminating the alteration of the original carbonaceous structure by polishing (Beyssac et al., 2002). Although it has been showed that Raman map-based analyses provide better estimation of the CM average spectra (Sforna et al., 2014), the punctual approach has been preferred during this study for the following reasons: i) a number of 25 spectra is sufficient to explore the within-sample (thin section) CM structural variability (Aoya et al., 2010); ii) the study here focused on the heterogeneity between CM microtextures rather than between facies (Sforna et al., 2014). The punctual analyses in this way are much more accurate to analyze morphological features a few tens of micron in size excluding contamination from adjacent carbonaceous structures and by the diffuse CM particles, furthermore analyzed microstructures were often to small in size when compared to the beam size thus the map-based analyses were pointless; iii) if is true that mapping provide a very large dataset it is also true that this require an extremely long total acquisition time even for very low counts on the single collected spots. On the other hand, the punctual approach allowed to increase the acquisition time and thus the counts providing much better resolved spectra allowing a much more confident fitting and thus increasing the accuracy of extracted parameters and ratio for a much lower total acquisition time, the saved time can be instead used to increase the number of the analyzed structures.

Each recorded spectra was processed using the graphing and data analyses software Origin Lab 8.5 for baseline subtraction, peak identification and curve fitting in the Raman first-order region. For spectral decomposition we applied two different fitting models, a two Voigt curves fitting protocol (D1 and G bands) and a Sadezky (Sadezky *et al.*, 2005) protocol using a combination of four Lorentzian (G, D1, D2, D4 bands) and a Gaussian curve (D3). Parameters and ratios were thus calculated and analyzed to evaluate CM structural order, estimate its syngenicity and assess heterogeneity within and between-samples.

2.2.3 Electron microscopy

In electron microscopy a high-energy, low-wavelength, accelerated electrons beam interacts with matter. Some of those interactions results into scattered or transmitted electrons which can be collected to form an image of the analysed material. As the electrons beam wavelength is many orders of magnitude shorter than that of visible light it is possible to produce images with a resolution power several order greater than what can be obtained in standard optical microscopy, allowing the characterization of details down to the atomic scale. Furthermore, depending on the emission investigated, electron microscopy can be used to provide insights into the elemental composition, the internal structure and crystallinity of the analyzed sample(Watt, 1997).

In this work three electrons beam based microscopic analyses, electron microprobe, scanning and transmitted electron microscopy, have been applied to the BARB3 chert material. Such techniques have been commonly used on the ancient geological record mainly with the purpose to characterize thin section mineralogy and their microfossils and carbonaceous content (Wacey, 2009; Wacey *et al.*, 2017). However, compared to vibrational spectroscopy, electron microscopic methods are more demanding as they work with solids only and, in most of the cases, require a more invasive sample preparation. Moreover, as mentioned above, they make use of an electron beam which is a high energy, destructive, radiation, especially problematic with concern to amorphous CM, whom structure can be easily altered (Gautam *et al.*, 2005). For this reasons electron beam based analyses should be performed only after the less-destructive *in-situ* vibrational spectroscopic techniques and applied being aware that primary signatures, especially carbonaceous structures, could be altered permanently.

2.2.3.1 SEM

In scanning electron microscopy a finely focused electron beam is scanned across the surface of an investigated bulk material, the resulting backscattered and secondary electrons are thus collected to produce an image of the analyzed specimen. Specific further equipments can be used to detect X-radiations, cathodoluminescence and other phenomena in order to gain a chemical and elemental distribution information from the investigated sample (Watt, 1997). It results that *in-situ* topographic and elemental images of the sample surface can be provided having a resolution down to a few microns or even a few nanometres depending on the instrumental capabilities. In ancient life studies SEM associated to energy dispersive X-ray spectrometry (or EDS, which allow a qualitative and semi-quantitative elemental detection within the analyzed volume) has been commonly used as a minero-petrographic tool to investigate the mineralogical context in which possible microbial traces are buried. SEM has been also on HF acid etched silica-rich samples to investigate topographic details of microfossils relieves (Javaux et al., 2004; Wacey, 2009; Agić et al., 2015), however this preparation can easily introduce contamination or alter primary textures and structures. Other thanlimited to the sample surface, with CM and microfossils normally occurring embedded by minerals within the thin sections, another disadvantage of SEM is that, working in a vacuum chamber, the analyzed sample needs to be conductive and thus usually require, especially in the case of highly silicified materials, carbon or gold coating before measurements can be performed. This type of preparation, which in case of carbon coating can contaminate the original CM composition, can be avoided using an environmental SEM (ESEM). In this instrument the sample chamber is kept at a low vacuum allowing the sample surface charging to be suppressed with no need of coating (Reed, 2005).

In this work SEM has been used largely for mineral-petrographic characterization of carbon-rich facies. Further ESEM has been used to map thin sections selected for TEM analyses.

Analytical settings

A selected suite of polished thin section were carbon coated prior to analyses under electrons beam excitation. To preserve them in case of further spectroscopic investigation each section has been only half coated. SEM and EMPA analyses on such prepared material were carried out at Spectrum facilities. Half-coated thin sections were analyzed with a Tescan Vega 3 scanning electron microscope (SEM) coupled with an electron back-scattering detector and an energy dispersive spectrometer (EDS) for elemental mapping and semi-quantitative elemental analyses. The operating conditions were 10 to 14 keV accelerating voltage for imaging and 15 to 17 keV for elemental mapping.

2.2.3.2 TEM and HRTEM coupled to focused ion beam milling

In transmitted electron microscopy the image is produced after transmitted electrons once the beam has passed through an ultra-thin sample. Objects can be magnified up to 10^6 times and resolved down to about 0.1 nm, moreover, as for SEM, other induced phenomena can be exploited to perform elemental and crystallographic microanalyses (Watt, 1997; Egerton, 2005). X-rays can be detected to provide qualitative compositional information in the TEM scanning mode (STEM), furthermore in high resolution transmission electron microscopy (HRTEM), by means of phase contrast imaging, it is possible to produce images of materials at the Ångstrom scale to characterise their crystallinity at the atomic level using magnifications up to 50 million times (Wacey et al., 2017). However, to obtain *in-situ* data with such a high definition and resolution, an invasive and destructive preparation is required to produce samples having thicknesses in the range between 10 nm to 1 µm which can be traversed by an electrons beam. To realize ultra-thin samples, or at least to thin down some sample areas, preparation include some steps of mechanical thinning followed by less-destructive more precise chemical, electrochemical or ion-beam thinning (Egerton, 2005). Of those latter methods focused ion beam (FIB) milling can be used directly on standard petrographic thin sections to extract ultra-thin foils for TEM and HRTEM analyses(Heaney et al., 2015). In FIB milling a focused beam of gallium ions is used to bombard the sample and remove material at the atomic scale through a sputtering process (Egerton, 2005; Heaney *et al.*, 2015). Such technique is normally combined to SEM facilities allowing nano-scale cutting precision which can be planned and controlled *in-situ* at specific locations of the thin section through the electrons beam SEM imaging.

Although FIB sample preparation is an invasive and time consuming technique, FIB-TEM and HRTEM analyses represent important means of characterization of ancient geological materials as they provide *in-situ* chemical and structural insights at the atomic scale. FIB-TEM (but also FIB-SEM; Westall et al., 2006), have been frequently used to investigate chemically and structurally ancient microfossils previously detected in standard petrographic thin sections(Kempe *et al.*, 2005; Moczydłowska and Willman, 2009; Wacey *et al.*, 2012; Foucher and Westall, 2012). Furthermore the application of HRTEM analyses bears a great value in CM investigation supplying unique *in-situ* structural information which are complementary to vibrational spectroscopic results. Particularly HRTEM analyses allow the investigation of the CM nanotexture (or nanostructure) which represent the mutual organization in space of its constitutive nanometric polyaromatic C-rich sheets forming the carbonaceous lattice. In HRTEM imaging the profiles of individual polyaromatic planes are visualized as dark fringes and various parameters can be measured including their length, curvature, tortuosity and the inter-layer distance in the basic structural units (BSU) (Olcott Marshall *et al.*, 2014; Apicella *et al.*, 2015; Deldicque *et al.*, 2016). As the carbonaceous nanotexture and lattice characteristics are dependent on the maturational process of the original carbonaceous precursor and its nature, HRTEM represent an important tool in ancient CM studies. A further advantage of CM high resolution studies is the possibility to discriminate minerals in the form of nanoparticles associated to the carbonaceous lattice as those could give insights concerning the original rock protolith and depositional conditions(Rasmussen *et al.*, 2017) or into possible metabolic pathways exploited by microbial communities now represented in the form of carbonaceous remains (Westall *et al.*, 2011).

In this work FIB-TEM and HRTEM microscopy has been used to characterize carbonaceous rich structures for which an hypothetical biological origin has been hypothesised after previous observations through core, optical and vibrational spectroscopic techniques. The process of FIB-TEM sample preparation is illustrated in Fig. 2.3.

FIB preparation of TEM lamellae

Two standard petrographic thin sections, obtained from the BARB3 shallow-platformal ferruginous laminated chert and granular chert (see chapter 4), have been selected for FIB foils extraction. Thin sections have been accurately mapped through optical and ESEM imaging to allow the location of the exact area of interest at the FIB. Optical mapping was performed using the Zeiss Axioplan Microscope equipped with a Nikon HS DS-Vi1 colour camera at BiGeA, while ESEM imaging was carried out at the Centro Interdipardimentale Grandi Strumenti (CIGS) of the University of Modena and Reggio Emilia, Modena, using a Quanta-200 ESEM microscope operating at low-vacuum (≤ 20 Torr) with no need of conductive sample coating.The extraction of six ultra-thin (less than 100 nm to allow also HR analyses)foils bearing carbonaceous structures of interest was performed at the FIB facilities of the Istituto Nazionale di Ricerca Metrologica (INRiM) of Turin, in collaboration with Dr. Enrico Emanuele. Thin sections were first coated with about 10 nm of gold, than ion cutting was achieved using a Quanta 3D DualBeam microscope equipped with a SEM Field Emission Gun (SEM-FEG), operating between 200V and 30kV with a resolution up to 1.5nm, and a Gallium FIB with a resolution up to 7 nm at 30kV.After trenches milling and foils ion thinning the lamellae where lifted-up from the thin sections and placed on a copper made TEM grid through nanomanipulation. For a review of the FIB foils extraction from thin sections for TEM analyses refer to Wirth (2009).

Analytical settings for TEM and HRTEM analyses

TEM and HRTEM analyses on the six ultra-thin foils were carried out at the Institute for Microelectronics and Microsystems (IMM) of the CNR of Italy in Bologna, in collaboration with Dr. Andrea Parisini. TEM data were obtained using a FEI Tecnai F20 ST transmission electron microscope operating at 200 kV equipped with a Gatan MSC794 CCD camera an EDAX EDS PV9761 SUTW for X-rays EDS spectrometry and a Fischione HAADF detector for STEM. For HRTEM analyses a lower voltage (180 kV) was used to avoid the induction of CM organization by the electron beam energy (Gautam *et al.*, 2005). Measurements where acquired in STEM mode and HR and lamellae were observed before and after short cycles (up to 30 sec) of cleaning with a Fischione 1020 Plasma Cleaner to remove contamination.

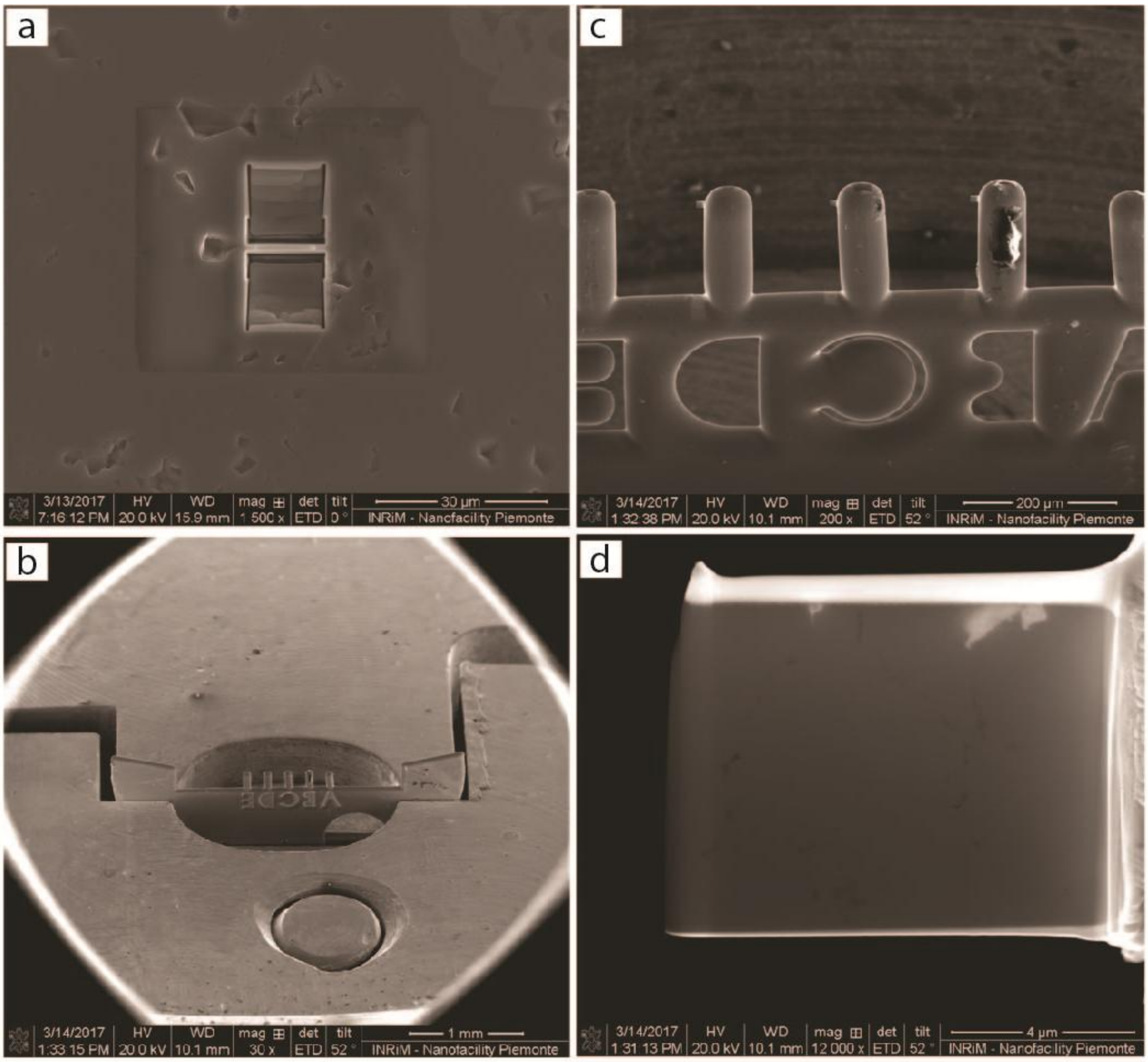

Figure 2.3 – a)SEM imaging at the FIB facility on a gold coated thin section after the first step of ion milling has been completed. Tranches have been cut around a strip which represent the top of the FIB foil which is going to be later thinned, extracted and positioned on the copper grid. (b) for TEM observation. c) A magnification on the copper grid where it's possible to observe tiny lamellae which has been extracted from thin sections and positioned on the comb-like structure of the grid for TEM analyses. TEM-FIB foils have a bigger dimension in th eorder of a few micrometer and a thickness of ≤ 100 nm (d).

Chapter 3

Characterization of the BARB3 carbonaceous-rich shallow-platformal lithofacies

3.1 Overview of the BARB3 core lithofacies

With the exclusion of two minor intrusions, 618 m of the BARB3 core consists of sedimentary banded cherts representative of the platformal-basinal-platformal succession observed along the western limb of the Onverwacht anticline in the BGB (Fig. 1.1, Fig. 2.1; Tice and Lowe, 2004). Although this work focuses on the shallow-platformal facies and their carbonaceous content (results summarized at the end of the chapter in Tab. 3.1), a brief description of the overall BARB3 cherts is here provided. The shallow-platformal BRC lithofacies makes up the majority of the BARB-3 core stratigraphy (Fig. 3.1a,b,d). It consists mainly of intercalated mesobands of greenish-grey crinkly laminated ferruginous chert, with common carbonaceous grains and mat-like laminations, and white bedded chert. Along the greenish-grey and white banded layers, that represent the core equivalent of the black-and-white banded chert observed in outcrop, sparse black carbonaceous facies occur in the form of black massive and black laminated bands. Both the upper and lower units of the platformal facies are characterized by frequent, centimetre-thick, stratiform veins and cavities filled by a lower granular carbonaceous chert and an upper colloform (botryoidal) quartz precipitate. Such structures, which can be used as geopetal indicators, are often associated with adjacent white chert bands being locally fractured. Chert breccia intervals occur especially in the lower facies. In the upper section between 300 and 340 m of the core depth, banded chert deposits have been fractured and veined after lithification, most probably as a consequence of a younger intruding sill (Fig. 3.1). The lower shallow-platformal lithofacies is further characterized by a general higher porosity filled with chert or quartz and heterogeneity at the base of the core that decreases going upwards in the section.

The intermediate BARB3 deep-water division is characterized by a banded iron formation composed by alternating homogenous and more compacted mesobands of ferruginous (concentration of siderite > quartz) and white banded chert (Fig. 3.1c). In the deep water deposits, the ferruginous chert is microbanded and although CM is present, it doesn’t occur in the abundance observed for the platformal lithofacies and neither in microtextures clearly suggesting a microbial origin. Compared to the shallow facies, the BIF lacks evidence of botryoidal quartz filled cavities associated with granular carbonaceous chert and also black carbonaceous bands. A distinctive feature of the BIF is the presence of sparse bright-red jasper mesobands (Fig. 3.1c) characterized by a hematite rich and carbonate poor chert composition, and paucity in CM. Jasper bands along the core consistently occur and grade into the siderite rich deposits.

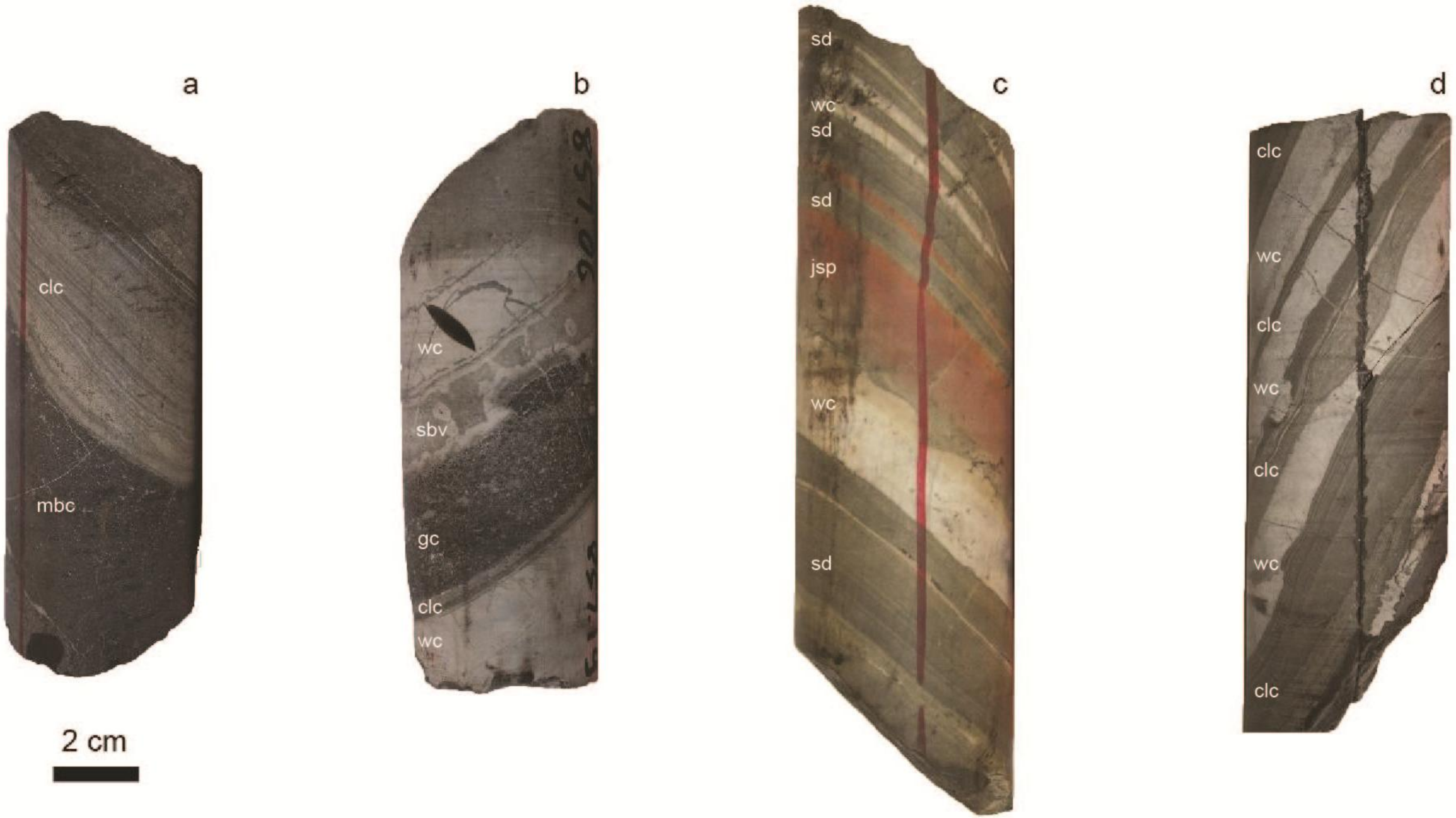

Figure 3.1 – BARB3 core samples from the BRC lower shallow-platformal facies (a,b), deep-basin facies (c) and shallow-water upper unit (d). a) Sample C8 (depth along the core, 865.76-865.63 m) includes a lower massive black chert (mbc) and an overlying greenish-grey crinkly laminated chert (clc). b) Sample C7 (857.19-865.06 m) is representative of a stratiform botryoidal vein (sbv) filled by a a 4 cm thick layer of black granular chert (gc) which is overlying a very thin band of crinkly laminated chert. The top and the bottom of the core sample is composed of white bedded chert (wc) bands. c) Sample F5 (538.30-538.08 m) is part of the deep-water BIF formed by white banded chert (wc) and siderite bands (sd) with sparse jasper mesobands (in red, jsp). d) Sample F2 (256.29-256.10 m) belongs to the upper shallow-platformal section and include again bands of greenish-grey crinkly laminated ferruginous chert and white bedded chert mesobands.

3.2 CM-rich BARB3 shallow-platformal lithofacies

3.2.1 Crinkly laminated chert

Crinkly laminated chert (clc) facies consist of mesobands that range from a few centimetres up to decimetres in thickness[5]. They are characterized by a finely planar laminated texture resulting from the alternation of the following two structural components (Fig. 3.2): (I) discrete, typically greenish-grey, siderite-rich microbands (~1 mm-thick); and (II) interlayered dark black thin (below the mm scale) CM-rich crinkly laminations. Although the facies is usually characterized by a greenish-grey hue it also occurs in darker shades of grey or in a dull yellow colour, reflecting a lower siderite abundance and more frequent CM grains in the first case, and a higher siderite and lower CM content in the second, as observed in thin sections. Pale to white bands, where the crinkly laminated texture is barely recognizable, also occur usually in association with cavities filled with a botryoidal quartz precipitate. In the latter case, the crinkly laminated cherts are characterized by such a low siderite and CM content that they resemble the white bedded cherts facies (Fig. 3.3b).

Fenestrae-like cavities exist together with larger quartz-filled stratiform veins, generally a few mm thick, that can pinch out laterally or extend evenly throughout the whole core diameter appearing to continue as true sedimentary layers (Fig. 3.3a,b). In larger fenestrae-like cavities and stratiform veins the infill turns from white at the margins to a dusky- or greyish-blue in the centre reflecting a symmetrical transition from microcrystalline quartz along the edges, to megaquartz in the cavity core (see also granular carbonaceous chert, Fig. 3.15 and Fig. 3.17a). Such transition is characterized by a botryoidal or colloform banding observable directly at the core hand-samples extending from the margin of the cavities towards their interior. Fenestrae-like cavities usually occur at the interface between individual microbands that appear to be plastically banded or may show a local reduction in thickness however, in each case maintaining their lateral continuity (Fig. 3.3a). Microbands in the immediate surroundings of botryoidal quartz filled cavities show local patterns of higher degrees of silicification as observed directly at the core (Fig. 3.3a,b) or in thin section (Fig. 3.8a,b). Individual or groups of microbands characterized by higher porosity and by the occurrence of numerous quartz-filled cavities have been also observed bearing a granular texture consisting of dark grey sandy material (Fig. 3.3a and Fig. 3.8a,b,c). In this case the

[5] The thickest crinkly laminated chert band observed during this study, not being interrupted substantially by other intercalated facies, is about 35 cm thick. More usually this facies is observed having a thickness averaging around 5 cm.

banding is frequently disrupted and fragmented so that the lateral continuity of individual microbands is difficult to trace. Microbanded deposits have also been affected by the loss of the original depositional continuity as revealed by pressure-dissolution structures. Furthermore, the crinkly laminated facies can be locally faulted or crosscut by carbonate, quartz or botryoidal-quartz filled thin veinlets at various angles with respect to the sedimentary plane (Fig. 3.3a).

3.2.1.1 Microfacies description

In the greenish-grey crinkly laminated chert, microbands (I, Fig. 3.2) consist of translucent, predominantly finely grained (~10-50 μm), rhombic siderite crystals (Fig. 3.4a,b,c,d). These crystals can be found scattered or forming more or less compacted aggregates, up to 1 mm in size, but more commonly about 250 μm, within a microcrystalline quartz matrix. Siderite crystals are typically subhedral to euhedral showing irregular etched margins and frequent chert inclusions, indicating that siderite precipitated probably syn-depositionally with the silicification process (Fig. 3.5a). Zonations are common and reflect different relative abundances of Mg, Mn and Ca in the siderite content, with magnesium being the principal iron-substituting element, as indicated by SEM-EDS studies. They may provide information about element mobilization and redox conditions during the growth of the crystal. Individual siderite rhombs larger than 50 μm are usually shattered or composed of smaller euhedral or subhedral crystals. Finely disseminated siderite is scattered within the chert matrix and often concentrated in large ghost rhombs (Fig. 3.5b) now replaced by silica, suggesting that $FeCO_3$ (or maybe other carbonates) was initially more abundant in this facies. In some cases the iron carbonates bear inclusions of anhedral pyrite suggesting a very early origin for some sulphides (Fig. 3.5c).

Optically opaque material, identified as disordered carbonaceous matter from the typical first- and second-order Raman bands (Fig. 2.2), is found in the form of sub-micron sized particles which occur as diffuse dark domains or concentrated into discrete micron-sized structures including laminae and grains. Laminae (Fig. 3.4a,b,d) are CM enrichments with a thickness of a few microns (usually less than 10 μm), which, although often disrupted at the micron scale, generally continue laterally across the samples. They are characterized by a wavy-crinkly habit, which gives rise to a slight relief of a few microns in amplitude. Individual laminae occur in the ferruginous microbands gently draping carbonaceous grains, siderite grains and also composite grains made of both CM and siderite (Fig. 3.4b). They are also arranged into vertical multi-layered lamina-sets, which in core samples appear as the black laminations (II, Fig. 3.2b, 3.4e) defining the crinkly microbanded texture[6]. As indicated by Raman imaging (Fig. 3.4e, inset), these structures consist of laterally continuous CM-rich laminae divided by chert layers that are usually a few microns thick, equating to a total thickness between ~50 and 100 μm. In the lamina-set, contrary to the ferruginous microbands, siderite and CM-grains are scarce or absent (Fig. 3.4e, inset). Lamina-sets bend plastically into wavy morphologies. Here, ductility and cohesiveness of the original carbonaceous material is evident, as laminae produce loosely attached folded-over structures and show anastomosing behaviour (Fig. 3.4e). Discrete carbonaceous material occurs also in the form of equant, irregular simple fluffy carbonaceous grains, up to about 250 μm in size, scattered within the siderite-bearing microbands (Fig. 3.4c). Other than being scattered in the chert matrix or forming rhomb-shaped aggregates, siderite is in general closely associated with both the individual laminae and CM grains as mineral growth and as a partial replacement of the CM-rich structures. This is evident in the form of siderite crystals being locally aligned along individual laminae (Fig. 3.4d) or forming spherical aggregates or ring structures around CM grains (Fig. 3.5d). Microbands rich in CM-siderite grains have a less homogeneous, more granular texture (Fig. 3.3a).

Another, distinct CM microtexture occurs within the post-depositional cross-cutting quartz veinlets and exist through all the chert facies including the crinkly laminated chert. Such CM is very dense and highly reflective under optical microscopy, while SEM analysis can clearly distinguish the CM as forming dense black blobs in backscattered electron images (Fig. 3.6a,b). At the base of the BARB3 core in a sample of very dark carbonaceous rich, poorly preserved, crinkly laminated ferruginous chert (sample D1), a similar dense CM is observed out of the cross-cutting veins, scattered within the ferruginous microbands in the form of smooth spheroids and blobs of various sizes (up to 50 μm) and shapes (Fig. 3.5c,d) and are characterized by an external rim of compact quartz grains coarser with respect to the immediately surrounding microcrystalline matrix. This material that occurs both in veinlets and within sample D1 displays a microtexture that suggests derivation from a carbonaceous fluid phase.

Other than quartz, siderite and CM, mineral phases in the crinkly laminated chert include frequently scattered Fe-, Co-, Ni-, Cu-, Zn and As-sulphides in the form of euhedral

[6] Although crinkly laminated chert is always composed of discrete ferruginous microbands and interlayered CM-rich laminations, it has to be noted that the CM lamination does not always consist of well preserved mat-like lamina-sets but occurs also as unstructured laminar CM enrichments or even in some cases as CM-rich stylolites.

and subhedral crystals. Pyrite, often bearing different proportions of other transitional metals (Co, Ni, Cu, Zn) and arsenic, is the main sulphide and has been recognized also in pseudomorphs after rhomb-shaped crystals (Fig. 3.7a), probably former carbonates. Small pyrite particles, commonly less than ~50 micron and often enriched in Ni, occur in different ferruginous samples scattered or organized in clusters (Fig. 3.7b) typically not larger than a few hundreds of microns. Other accessory minerals include sparse chamosite (Fig. 3.7c), a common occurrence in iron rich deposits that have been metamorphosed to a greenschist-grade and represent a secondary intergrowth and replacement phase after siderite grains or occur finely dispersed in the chert matrix. Calcite is rarely observed forming cross-cutting veinlets and as a later cement (Fig. 3.7d).

As observed along the core (Fig. 3.8a), crinkly laminated bands showing a more granular texture are characterized by intra-granular spaces filled by white chert rather than siderite, they are closely associated with quartz filled cavities and show a partially disrupted microbanded structure. In thin section, the granular material is composed of a mixture of dark CM-siderite grains (Fig. 3.8b), reminiscent of a peloidal texture, and more rarely rip-up, rolled-over fragments of carbonaceous laminae are also overgrown by iron carbonates (Fig. 3.8c). Microbands having such granular texture are also characterized by silica spherulitic precipitation around the CM-siderite grains enriched in a rim of carbonaceous particles (Fig. 3.8d,e). Poorly sorted granular material of similar composition has been observed in lenses that occur as plastic intrusions within the crinkly laminated chert (Fig. 3.3c, 3.8f,g). Finally, microbands bands of ferruginous chert have also been found disrupted after abundant secondary large rhombs, probably originally diagenetic carbonates, that have now been replaced by silica.

3.2.1.2 Interpretation

Abundant carbonaceous laminations occur within the crinkly laminated ferruginous chert and consist of individual or multilayered laminae that in the sediments retain morphologies indicative of an originally plastic and cohesive behaviour. Features including roll-up, folded structures and anastomosing laminae opening around chert lenses are consistent with fossil and modern benthic microbial mats interacting with pervasive fluids or very gentle eroding currents in low energy aquatic environments (Eriksson, 2007; Walsh, 2010; Tice et al., 2011). The preservation of the features described above and the close association of equant carbonaceous grains, advocate for an original carbonaceous laminar structure rather than representing compression during burial and sediment compaction. The overall morphological features and the characteristic draping of carbonaceous grains strongly support the identification of the BARB3 carbonaceous laminations as microbial mats previously proposed by Tice (2009) and Tice and Lowe (2004, 2006) to represent photosynthetic microbial communities dominating the lower part of the BRC shallow-platformal facies. This suggests that CM simple grains may as well represent microbial remains. In fact, fluffy, irregular, more or less compacted CM-rich grains found in the crinkly laminated chert, as well as in the laminated black BARB3 facies described below, in the BRC outcrop material, closely resemble clotted amorphous CM-rich organic debris documented from many Palaeoarchaean sedimentary cherts and chert veins and from younger sediments where microbial activity is inferred (Ueno et al., 2004; Kiyokawa et al., 2006; Hofmann et al., 2013b; Sugitani et al., 2015). For instance the carbonaceous clotted textures observed in the celebrated fossiliferous Early Devonian cherts of Rhynie and Windyfield in Scotland that represent mainly microbial remains (Fayers and Trewin, 2003; Trewin et al., 2003) bear a close resemblance to the grains of CM documented herein.

A biological origin for diagenetic siderite in Precambrian iron formations has been proposed (Köhler et al., 2013). Carbonaceous grains in the crinkly facies are overgrowth by diagenetic siderite. Siderite beds are known to occur in lacustrine and marine deposits where the mineral is a common diagenetic phase after carbonaceous remnants and iron carbonate can be triggered by exhalative systems or dissolution of less stable carbonates (Bahrig, 1994; Choi et al., 2003; Ohmoto et al., 2004). In Palaeoarchaean deposits the diagenetic growth of siderite on CM cannot imply its microbial origin as CM can, especially in hydrothermal conditions, be generated abiotically (Brasier et al., 2005b; Maurette et al., 2006; Hofmann, 2011). The occurrence of finely disseminated and etched euhedral siderite grains, now partially replaced by chert and the abundance of large quartz pseudomorphs after rhombs, suggest that carbonates were originally more abundant in the core. This provides support for siderite to have represented an early diagenetic phase that possibly occurred soon after CM rich protolith deposition and earlier or syngenetically with respect to the silicification of sediments. Insights about the origin and significance of siderite in the crinkly laminated facies and the reconstruction of the original carbonaceous rich protolith however, requires further investigations.

Despite the nature of the crinkly laminated facies, the protolith is still unclear. The excellent preservational state of the BARB3 carbonaceous mats and their cyclic development into thick anastomosing multilayered structures, detailed by Raman imaging techniques, suggest that the original sedimentary microfabric is still preserved within the BARB3 laminated ferruginous chert and that CM simple grains and laminae are primary. Particularly the alternation of (I) siderite-rich microbands, where frequent CM equant grains occur together with individual carbonaceous laminae, to thin carbonaceous layers (II) composed almost exclusively of multilayered carbonaceous mats appear to reflect an original Palaeoarchaean intermittent low-rate sedimentation. In such a depositional context well developed multilayered epibenthic carbonaceous mats would have been able to grow during a depositional hiatus, while a higher depositional rate would have prevented such microbial proliferation. Individual laminae within the microbands thus could have represented microbial "survival" modes during high sedimentation rates or a later development of endobenthic microbial mats (Noffke, 2010). This cyclic sequence represented by sedimentary bedding development and the successive re-establishment of microbial mats is consistent with planar stromatolite growth found in various aquatic depositional settings including, deep water microbially active methane seepage (Mazzini et al., 2004), carbonate platforms populated by photosynthetic microbial mats (Hips and Haas, 2006), shallow-water deposits affected by seasonal over-riding between different microbial communities (Gerdes, 2007), inter-supratidal mat-rich hypersaline environments (Mastandrea Adelaide *et al.*, 2006) and intratidal sandy deposits (Noffke, 2009). Thus the crinkly laminated chert facies are affine to planar stromatolite growth that can be found in a range of palaeoenvironments and palaeodepth associated with phototrophic and/or chemotrophic microbial communities.

Botryoidal or colloform silica precipitates in cavities and veins are a common feature of Palaeoarchaean greenstone belts and they have been reported from a range of lithologies and environmental settings. Although the origin of such structures in the Palaeoarchaean have not yet been the target of a focused investigation, interpretations for their occurrence have been proposed, or implied, relating them to dissolution, non-hydrothermal, evaporitic processes (Tice and Lowe, 2006b; Sugitani et al., 2013) or to hydrothermal fluid circulation (Paris et al., 1985a; Van Kranendonk, 2006; Hofmann and Bolhar, 2007c; Ledevin et al., 2015). Thus, similar to the above described mat-constructing community, a range of water depths and depositional conditions could have been responsible for the presence of the fenestrae-like structures and thin stratiform cavities characterized by a colloform silica precipitate observed in the crinkly laminated chert. This may have formed very early in the history of the deposit when the sediments were still soft. As suggested by the nomenclature used so far, the fenestrae-like cavities are affine in their morphology to irregular or laminoid fenestrae that typically occur in shallow-water intertidal carbonate deposits as the result of gas entrapment, organic decay or sediments shrinkage (Tucker, 2009). Laminoid fenestrae, particularly, are characteristic of planar stromatolites where they occur after organic matter decay, desiccation and parting of laminae (Tucker, 2009). The interpretation of the crinkly laminated facies as a planar biosedimentary deposit, the laminoid shape of the quartz-filled cavities and the associated parting of microbands may thus support a peritidal depositional environment for the mat-facies. However, sedimentary structures unequivocally supporting such a shallow peritidal environment have not been observed during this study and furthermore the scarce granular material is composed of irregular CM-rich grains that lack a true detrital component and may have been generated locally by means of processes other than current activity and erosion at the seafloor (see 3.2.4 Granular carbonaceous chert). The similar paucity in hydraulically reworked material has been observed in previous studies on the BRC shallow-platformal lithofacies for which the depositional depth has been inferred from about 15 m deep down to the storm wave base (Tice and Lowe, 2006b). Furthermore, fenestrae or other similar irregular cavities are known to form below the peritidal zone even in deep-water deposits (Shinn, 1983; Pratt, 1995; Elrick and Snider, 2002; Tucker, 2009), as a consequence of degassing vesicles in deep-water methane seepages (Mazzini et al., 2004) or resulting from hydrothermal karst after soluble minerals such as limestones, dolomite or gypsum (Tucker, 2009). The latter case seems to closely resemble the crinkly laminated ferruginous facies as both fenestrae-like cavities and stratiform veins are characterized by a botryoidal quartz infilling which is commonly precipitated into vugs and veins after silica-rich hydrothermal fluids in low-sulfidation epithermal systems (Marchev et al., 2004; Marinova et al., 2014), marine seepage (Mazzini et al., 2004), or also sinters at subaerial and sublacustrine hot-springs (Fournier et al., 1991; Guido and Campbell, 2012), with those environments representing viable settings for mat-forming microbial life (Fayers and Trewin, 2003; Trewin et al., 2003; Mazzini et al 2004; Guido and Campbell, 2012). The possible interaction of unconsolidated crinkly laminated sediments with pervasive silica-rich fluids could explain the occurrence of locally disrupted and plastically intruded microbands rich in granular reworked material. Such CM-rich grains are, in fact, characterized by rims of spherulitic precipitate, typical precipitate after hydrothermal silica colloidal fluids (Fayers and Trewin, 2003), which is instead not observed in planar undisturbed microbands. A silica-rich fluid is also consistent with the occurrence of highly silicified pale crinkly laminated microbands in the immediate surroundings of botryoidal stratiform veins as those could have represented subsurface silicification fronts. The ductile nature of the crinkly laminated facies, finally, could be the result of sediment fluidization after a pervasive silica-rich fluid that would have not percolated in the already lithified impermeable white banded cherts.

Black, dense, smooth spheres and blobs occurring in cross-cutting veinlets, but also scattered within the ferruginous bands of sample D1, display a peculiar morphology. They reflect optically and their carbon rich composition most probably indicates an originally viscous hydrocarbon phase that has now solidified into bitumen blobs, a common feature in oil reservoirs and organic rich sediments that have gone through the oil formation window (Buick, 1990; He et al., 2015; Suárez-Ruiz et al., 2016). The presence of bitumen droplets within sedimentary ferruginous microbands suggest the mobilization, at least locally, of a hydrocarbon-rich fluid phase through the crinkly laminated sediments possibly after an hydrocarbon-rich pervading hydrothermal fluid. Similar bitumen globules have been previously reported from an Australian Palaeoarchaean chert-barite unit at the North Pole locality near the base of the Warrawona Group in proximity to a chert dyke (Buick, 1990). Despite these observations constraints about the original water depth of the crinkly laminated facies deposition cannot be provided with certainty, however, early interaction between cherts and hydrothermal silica-rich fluids is strongly suggested and further discussed in the following paragraphs and chapters together with its implications for possible chemotropic life.

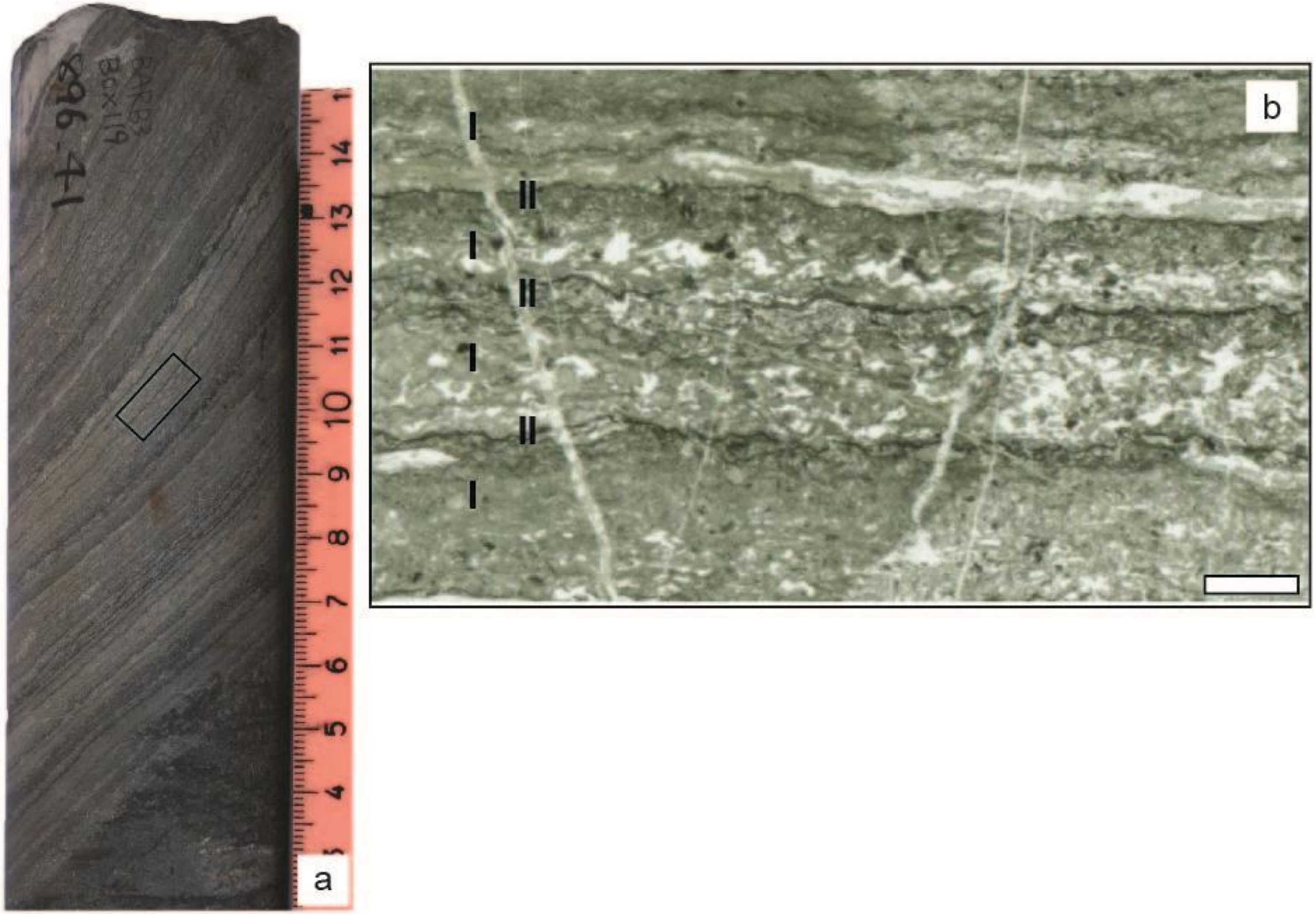

Figure 3.2 – Crinkly laminated chert. a) Sample F13 (896.59-896.41 m) is an extremely well preserved greenish-grey crinkly laminated section. b) A thin section photo from a similar site as the inset in (a). The crinkly laminated chert has a microfabric composed of alternated siderite-rich microbands (I) and interlayered thin mat-like laminations (II). Scale bar 2 mm.

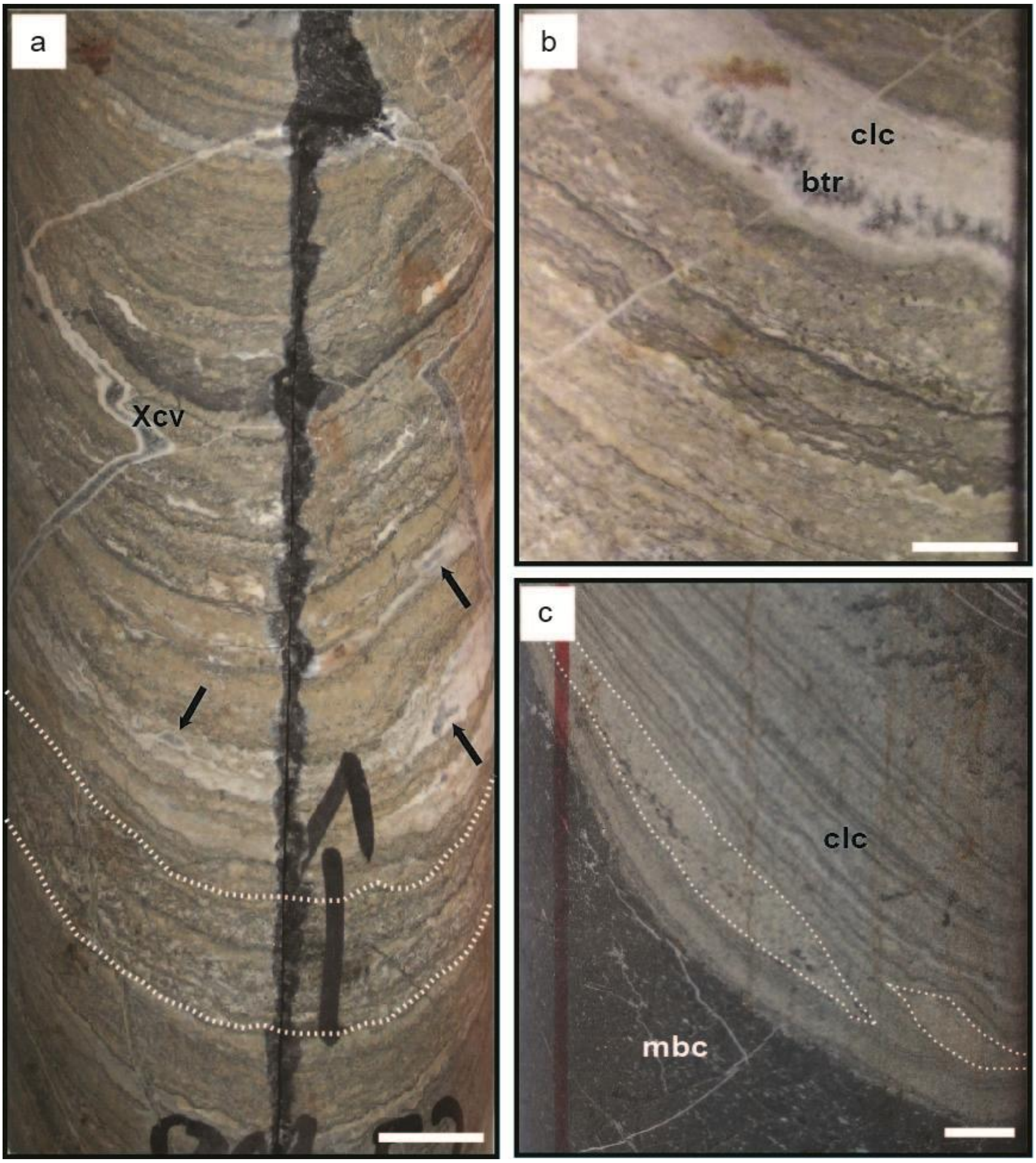

Figure 3.3 – Crinkly laminated chert (clc). a) Sample F11 (894.52-894.35 m). From the bottom to the top it is possible to observe: a group of microbands characterized by a granular texture consisting of dark grey sandy material (between the white dashed lines); a group of microbands associated to multiple botryoidal quartz-filled small cavities and fenestrae-like structures (black arrows), such microbands are softly deformed and highly silicified. Along the sample fenestrae-like structures filled by white quartz are common. The planar microfabric is often disrupted in association to both granular material and fenestrae-like structures. Upper in the core a younger cross cutting vein (XcV) occur. Scale bar: 1 cm. b) A stratiform cavity filled by botryoidal (btr) quartz precipitate occur within this crinckly laminated chert. Note the colloform bending protruding towards the cavity interior which is dusky- or grey-blue consisting of megaquartz crystals. Immediately overlying crinckly laminated microbands (clc) are almost completely silicified, nevertheless the crinkly texture is still recognizable. Scale bar: 2.5 mm c) Sample C8 (865.76-865.63 m). Lenses of granular material representing possible plastic intrusions resulting from sediments fluidization and causing soft- deformation (white dashed lines). The underlying facies is a massive black chert (mbc). The contact between the facies is a thick stylolite seam. Scale bar: 5 mm

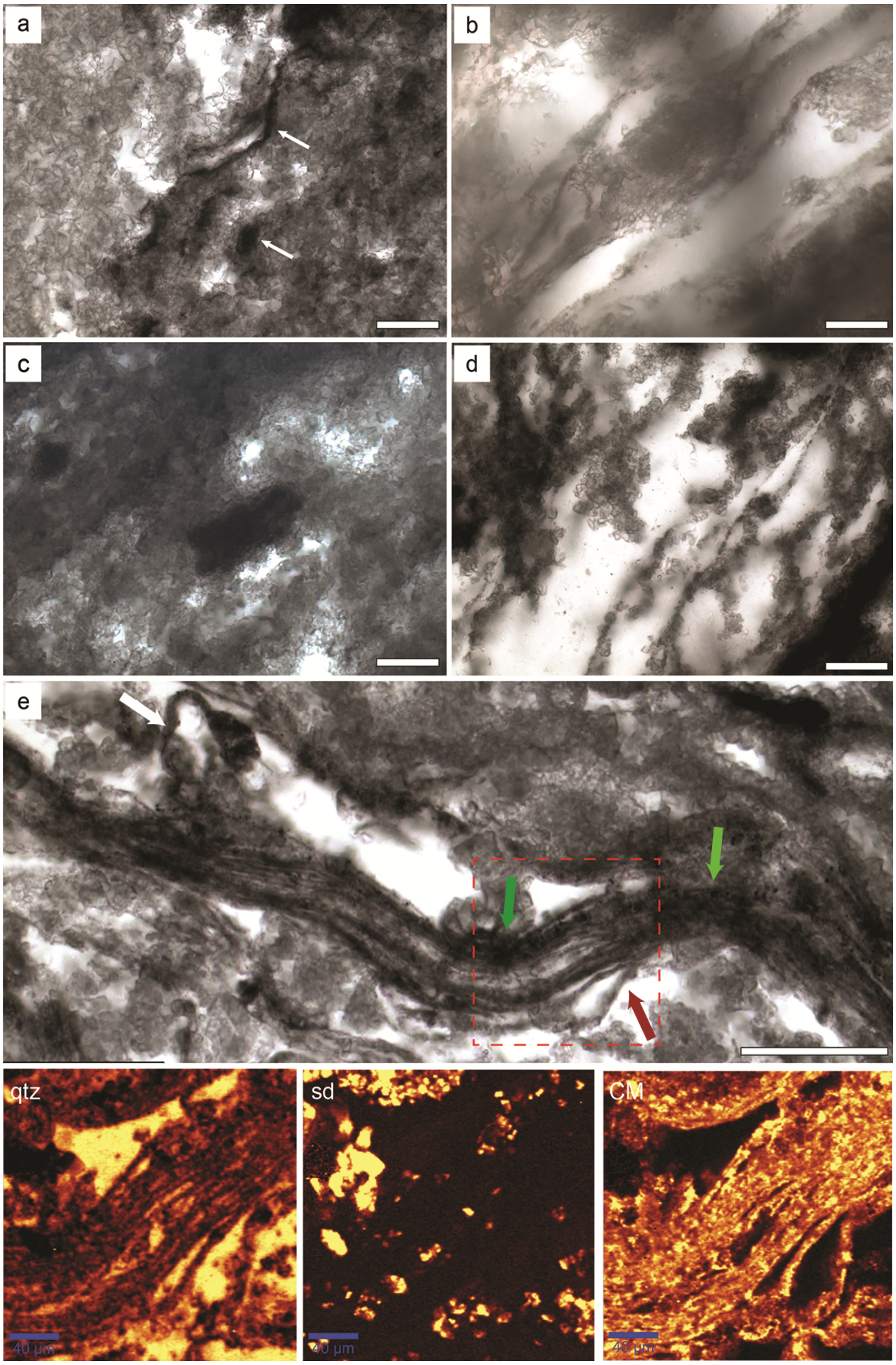

Figure 3.4 – Microphotographs of crinckly laminated chert. a) Discrete siderite-bearing microbands of siderite-rich chert and CM locally forming grains and laminae (arrows). Scale bar: 100 µm. b) CM-rich laminae gently draping siderite and composite grains. Scale bar: 50 µm. c) Discrete grain of CM. Scale bar: 200 µm. d) Siderite crystals associated with CM-rich laminations. Scale bar: 100 µm. e) Carbonaceous lamina-set. Top: photomicrograph of a lamina-set. Scale bar: 200 µm. Note the multilayered structure showing plastic and choesive behaviour including features typical of microbial mats such as folded-over or roll-up structures (white arrow) which can remain partially attached to the main structure, plastic bending (green arrows) and anastomosing layering (red arrow) around lenticular chert domains. Bottom: high-resolution Raman maps showing the quartz (qtz), siderite (sd) and carbonaceous matter (CM) distribution of the above boxed area. Note the lamina-sets composed mainly of CM in a chert cement, with siderite being scarce. Scale bars of the raman maps 40 µm.

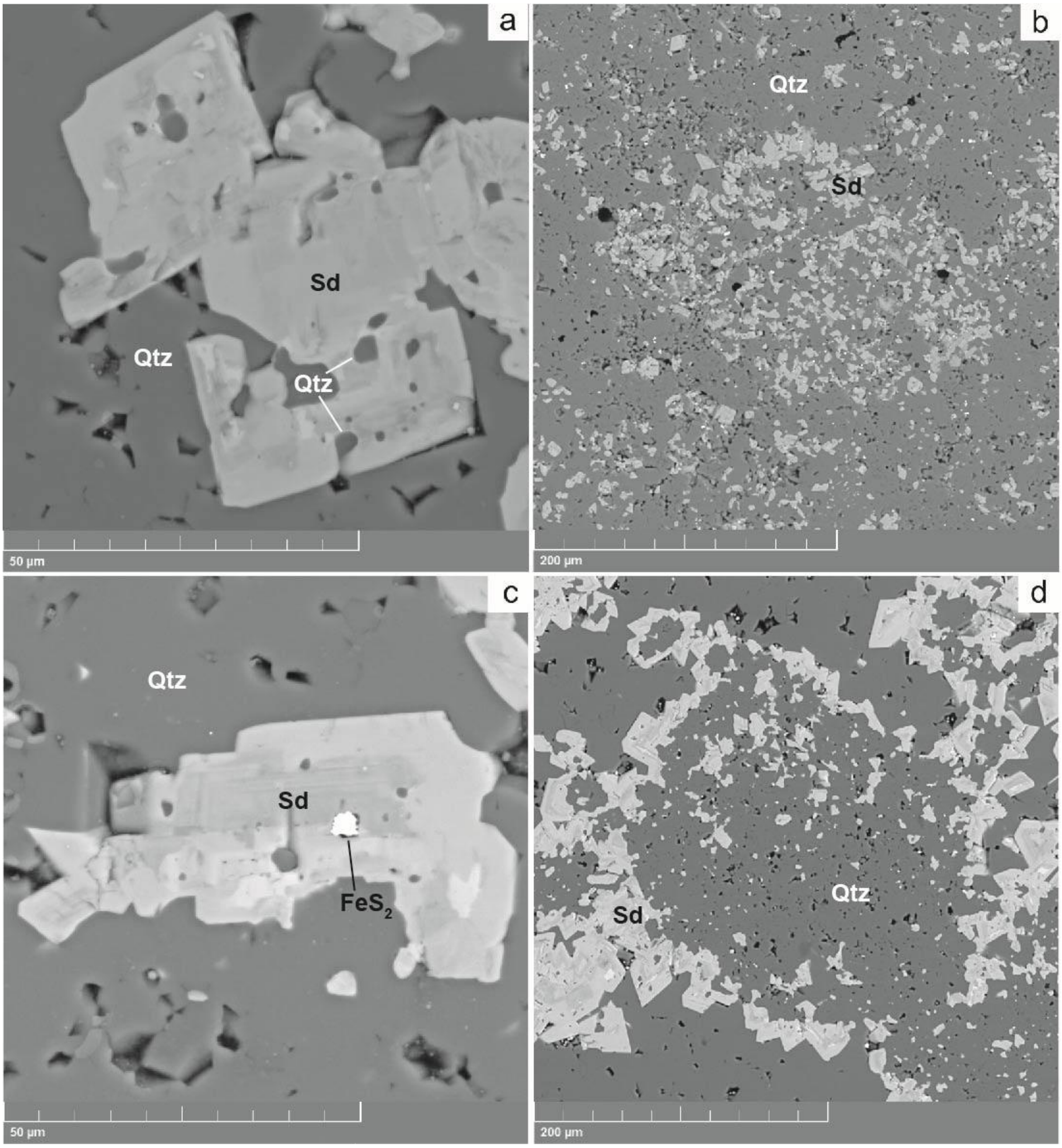

Figure 3.5 – Crinkly laminated chert. a) Rhomboidal euhedral siderite crystals (Sd) in a chert matrix (Qtz). Crystals show zonation reflecting the relative abundance of Mg, Mn and Ca. Margins of the grains are etched and the crystals are partly silica replaced. b) Disseminated siderite grains defining a large rhomboidal crystal now abundantly replaced by silica. c) A subhedral siderite crystal bear a pyrite inclusion (highly reflective mineral, FeS2). d) Siderite crystals form an ellipsoidal structure in association to a carbonaceous grain in the quartz matrix. Note that the CM forming grains and clots can't be clearly distinguished in SEM imaging.

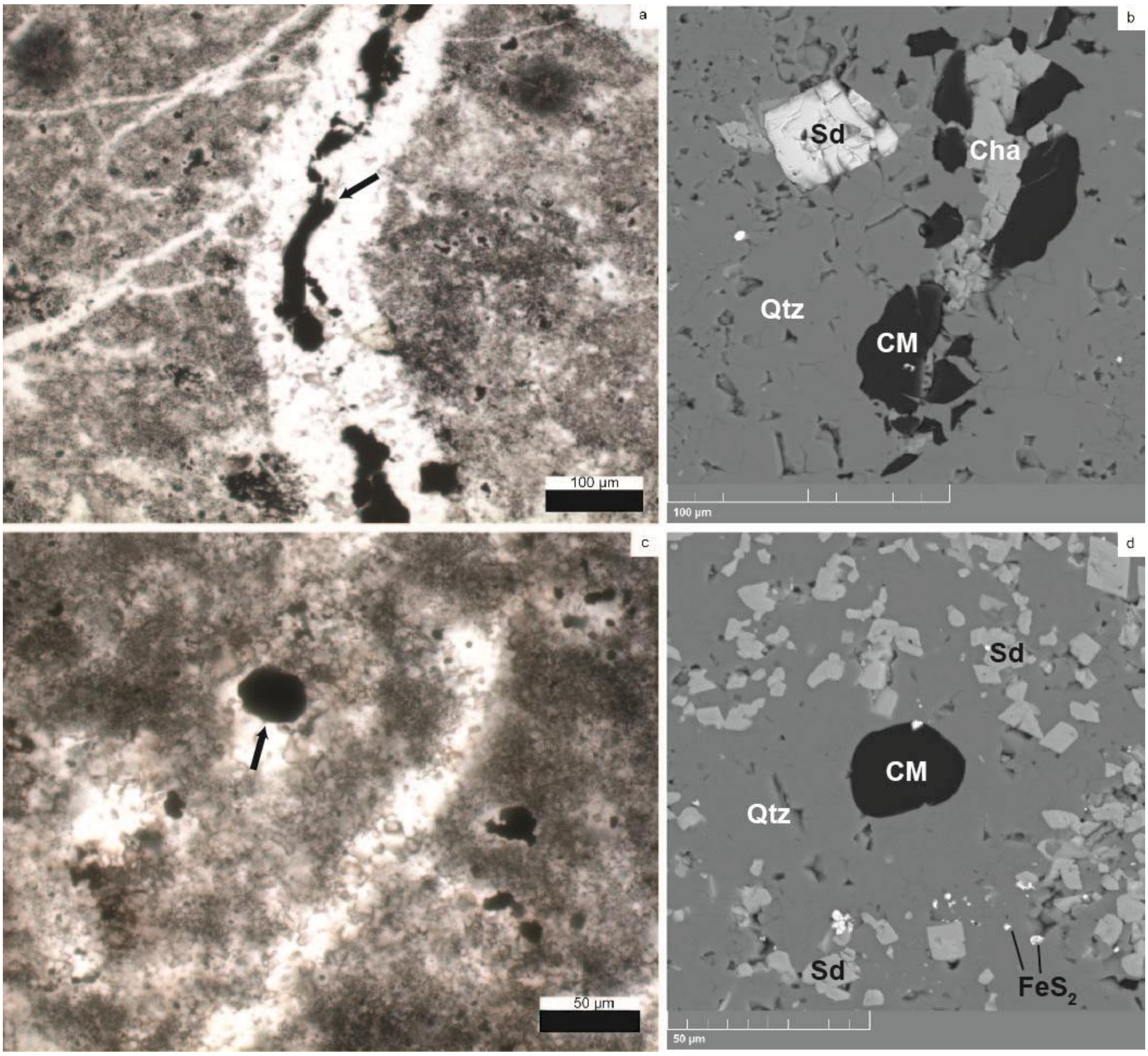

Figure 3.6 – Bituminous CM in the crinkly laminated chert, Sample D1 (896-895.9 m). a) Dense bituminous CM (black arrow) occurring as a cross cutting vein filling. b) At the SEM such carbonaceous microtexture is extremely dense (CM). Interleaved with the dense CM secondary chamosite (Cha) also occur. The rhombohedral crystal is siderite (Sd). c) Other than as a veinlet filling, dense carbonaceous smooth spheres (black arrow) and blobs are also observed scattered within the crinkly ferruginous chert. d) Bituminous blobs (CM) can be easily observed at SEM imaging, differently from the carbonaceous grains and clots. Here the smooth CM-rich blob occur in a chert matrix (Qtz) together with scattered siderite and finely grained pyrite.

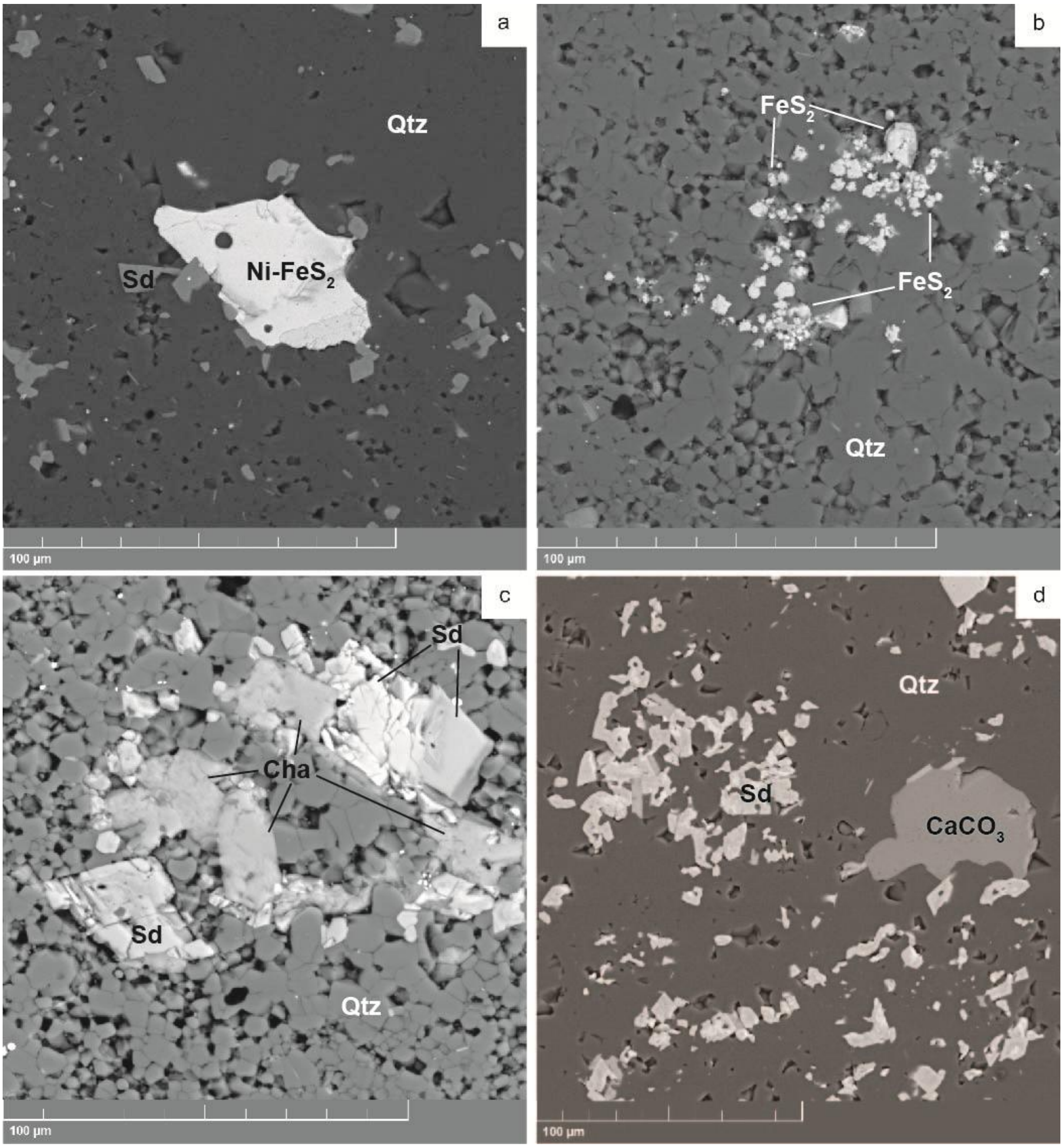

Figure 3.7 – Accessory minerals in the crinkly laminated chert. a) Two Ni-rich pyrite pseudomorphs after rhomboidal crystals in a chert matrix enriched in dispersed siderite. b) A pyrite cluster. c) Euhedral rhomboidal siderite crystals and secondary intergrowing chamosite $(Fe^{2+},Mg,Al,Fe^{3+})_6(Si,Al)_4O_{10}(OH,O)_8$. d) Calcite cement ($CaCO_3$) on the right, occurring in a ferruginous chert.

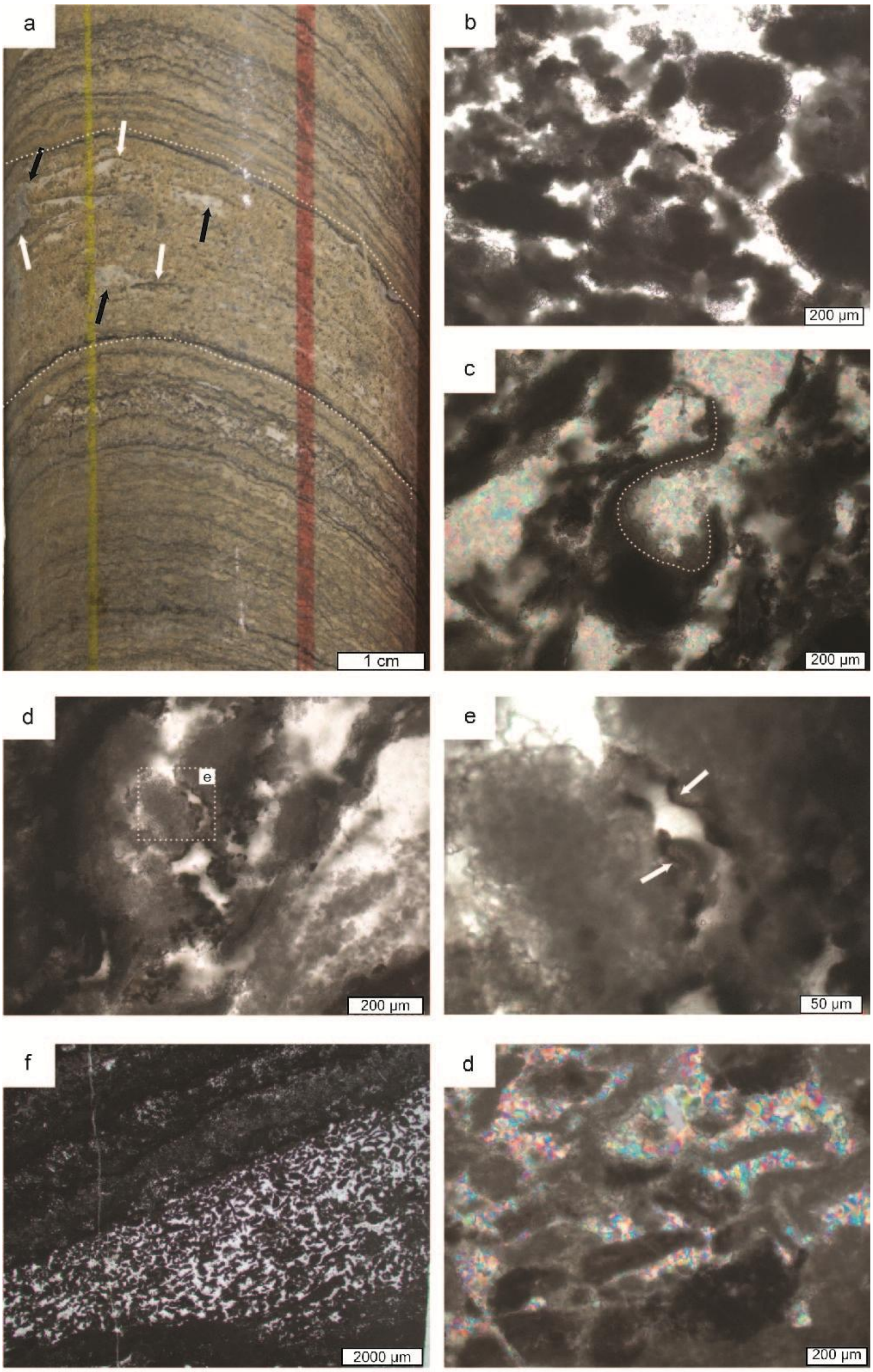

Figure 3.8 – Clc with a granular texture. a) A section of ferruginous chert, from the lower shallow facies, where the microbanded structure is disrupted (between white dashed lines) in association to botryoidal quartz-filled cavities (black arrows). CM mat-like lamina-sets fragments are observed (white arrows). In thin section such bands are characterized by CM-siderite composite grains forming a peloidal-like texture (b) and rip-up mats fragments (white dashed line) now overgrown by siderite (c). d) and (e) Silica spherulitic precipitation around CM-siderite grains is marked by CM particles precipitating within the botryoids (white arrows). f) The plastic intrusion observed in Fig. 3.3c. g) The material in the plastic intrusion is composed of rip-up fragments of CM grains and laminae derived from the ferruginous chert itself probably after sediments fluidization.

3.2.2 Massive black chert

Massive black chert (mbc) consist of homogeneous, unstructured layers, sometimes exceeding 50 cm in thickness but most commonly forming bands about 5 cm thick (Fig. 3.9). It appears particularly rich in well compacted CM, nevertheless white to grey silica filled pores and small irregular cavities up to some millimetre in size, can be observed scattered through the bands especially at the base of the BARB3 (Fig. 3.9). Black massive layers in the studied samples are characterized by unconformable contacts with the adjacent chert facies consisting of well developed wave-like sub-planar stylolites having thick seams enriched in dark CM and sulphides (Fig. 3.9c). Numerous quartz and chlorite-filled veinlets also crosscut the facies at different angles, the latter not extending to the adjacent facies.

3.2.2.1 Microfacies description

In thin section the massive black chert is structureless and appears as a carbonaceous continuum, in a chert matrix, interrupted by disseminated chert-filled pores and elongated cavities (Fig. 3.9b,c and Fig. 3.10a). The cavities are generally a few hundred microns long, some consist of silica-replaced rhomboidal and tabular pseudomorphs possibly after carbonates and anhydrite respectively (Fig. 3.9b,c and Fig. 3.10a). Numerous cross-cutting veinlets occur and other than quartz they are characterized by abundant chlorite infillings (Fig. 3.10b). Tentative grains consist of CM cloudy aggregates having a size typically around 200-250 μm, those can be rounded or irregular (Fig. 3.10a), however with such a poor preservation it is not clear if their morphology is primary, or results from processes such as CM mobilization and displacement during chert crystallization (Pflug, 1967). Diverse CM microtextures also occur (Fig. 3.10), so that massive black chert has a various carbonaceous assortment. Other than cloudy diffuse particles and aggregates a more dense amorphous carbonaceous phase can be observed interspersed between the chert grains within the chert-filled pores an cavities (Fig. 3.10c). However such microtexture may be more diffused, although masked by the carbonaceous cloudy dark haze. Dark, thick and unstructured, interstitial between chert grains it differentiate from morphologically defined mats and grains but also from the cloudy diffuse CM particles. From optical observations it is suggested that this CM microtexture represents originally a suspended fluid sealed within a crystallizing silica-rich mass. Such CM is often closely associated with fine euhedral pyrite crystals and pyrite clusters. Bituminous CM, of the type already reported for the crinkly laminated ferruginous sample D1 (Fig. 3.5c,d), is frequent in the massive black chert, mainly found in stylolite seams (Fig. 3.10f), as a veinlet infilling and in the form of disseminated smooth spheres and blobs a few microns in size (Fig. 3.10d), usually associated with scattered authigenic cubes or particles of pyrite (Fig. 3.10e).

In thin section, the massive black chert in the BARB3 CM-rich facies is also characterized by a greater abundance of sulphides and chlorite. Pyrite, often Ni-bearing, is the most common sulphide and it can be observed as a secondary replacing mineral after rhomboidal pseudomorphs (Fig. 3.11a), frequently with co-occurring chamosite, as scattered fine-grained cubic authigenic crystals (Fig. 3.10e), or finely-grained clusters (Fig. 3.11a). Arsenic Co, Ni-rich subhedral sulphides occur more rarely (Fig. 3.11b). Acicular, or columnar finely dispersed chamosite is particularly rich in the massive black chert (Fig. 3.11c,d,e). Although often obscured by the diffuse CM, it can be observed distributed through the whole volume of the thin section (Fig. 3.11c,d,e). Finally, rare replacement Ti-oxides associated with secondary chamosite have been also detected using SEM-EDS (Fig. 3.11b).

As seen directly along the core, wave-like stylolites are a peculiar feature of the massive black chert. Sub-planar wavy dissolution seams occur at the contact with the adjacent facies, however minor stylolites occur also at an angle to the sedimentary bedding within and limited to the massive black facies. SEM-EDS analysis shows that the stylolites are composed of a complex and dense thick mixture of bituminous CM, copious Ni-pyrite clusters and euhedral crystals, similarly occurring various arsenic Co, Ni-rich sulphides, chamosite and more rarely titanium oxides (Fig. 3.12).

3.2.2.2 Interpretation

Like the bedded and finely laminated microcrystalline quartz deposits, massive black chert is a recurring facies in Palaeoarchaean volcano-sedimentary successions. Depending on the internal texture, composition, and depositional settings, massive black chert have been associated with bedded black carbonaceous sedimentary layers (Walsh and Lowe, 1999; Sugitani et al., 2015) or carbonaceous-rich veins and dikes of hydrothermal origin (Kiyokawa et al., 2006; Hofmann et al., 2013b).

The BARB3 massive black chert lacks sedimentary structures both along the core and internally. A continuous carbonaceous haze including diffused and diverse CM microtextures, scattered sulphides and finely dispersed acicular chamosite, characterizes the facies. Individual carbonaceous grains are barely recognizable and by morphology they cannot be directly compared to grains in the other BARB3 CM-rich facies or to younger CM clotted microbial textures (Fayers and Trewin, 2003; Trewin et al., 2003). Carbonaceous laminae are absent, indicating that no mat-construction was involved in the deposition of this facies. Although occurring in stratiform bands, massive black chert can't be conformably related to the adjacent layers as pressure-dissolution processes have obliterated the original contacts and the material lacks evidence of detrital components or any traces of sedimentary laminations. Thus textural evidence does not support a bedded sedimentary origin for this facies.

On the other hand the lack of detrital grains and sedimentary structures bears a greater similarity with the texturally similar massive black chert previously reported from Palaeoarchaean carbonaceous dikes and hydrothermal veins (Ueno et al., 2004; Kiyokawa et al., 2006; Hofmann et al., 2013b). The massive black chert facies of the BARB3 in thin section is characterized by a greater abundance in authigenic pyrite, sulphide clusters and chamosite, whereas sulphides are a common and conspicuous precipitate in hydrothermal veins (MacLean and Kranidiotis, 1987; Hannington et al., 2001) and chamosite is a typical product of rocks hydrothermal alteration (Kranidiotis and MacLean, 1987; Kamenetsky et al., 2002). Such enrichment is reflected by the characteristic occurrence of thick and sealed stylolites seams that formed due to the abundance of these slowly dissolving phases. Quartz filled cavities which in sedimentary massive black cherts have been interpreted as fenestrae (Sugitani et al., 2015), here are often geometric, reflecting quartz substitution after a former mineral phase, rather than a void formed due to sediment shrinkage or decomposition of possible organic debris. The observed irregular, non-geometric, cavities however, are consistent with a porous original facies. Similar evidence has been presented regarding the lack of compaction for black chert veins in the BGB (Hofmann et al., 2013b). The interpretation of the BARB3 massive black chert as a vein facies may explain the presence of possible quartz pseudomorphs after anhydrite. This is a common precipitate in high-temperature vents (Zhang, 1986; Hannington et al., 2001; Chambefort et al., 2008) but also in mixing low-temperature hydrothermal fluids with seawaters (Bischoff and Seyfried, 1978; James and Elderfield, 1996), and may have provided a sulphur source for the abundant authigenic pyrite. If the massive black chert was deposited as a vein, some of the more regular quartz-filled cavities may also represent silicified fragments ripped-off from the host rock walls due to hydraulic fracturing.

Massive black chert includes a peculiar and diverse CM microtextural assemblage. Morphologies clearly suggesting a possible microbial origin are absent, however disrupted and irregular cloudy carbonaceous aggregates, about 200 μm in size, indicate the CM may have been individual clots originally, now altered almost beyond recognition. Most of the diffuse amorphous cloudy material could represent the relicts of such original clots.

Further CM microtextures occur as dense infillings between microcrystalline quartz grains and in the form of bituminous optically reflective blobs, spheres and veins infilling. As already documented for the crinkly ferruginous chert sample D1, the black bituminous material probably represents an original viscous hydrocarbon phase (Buick, 1990; He et al., 2015; Suárez-Ruiz et al., 2016) and similarly, the dense infilling within the chert matrix appears to be derived from a fluid phase. The co-occurrence of dense carbonaceous infillings and bituminous material often in association with authigenic sulphides suggest an hydrothermal fluid phase mobilizing metals and viscous hydrocarbon materials, whereas the production of hydrocarbon and its mobilization in a fluid phase is consistent with hydrothermal activity (Mazzini et al., 2004). The lack of detrital components, sedimentary structures, the mineralogical composition and the carbonaceous microtextures suggest that the BARB3 massive black chert may be better interpreted as a massive carbonaceous hydrothermal vein or at least it’s deposition was heavily influenced by hydrothermal activity.

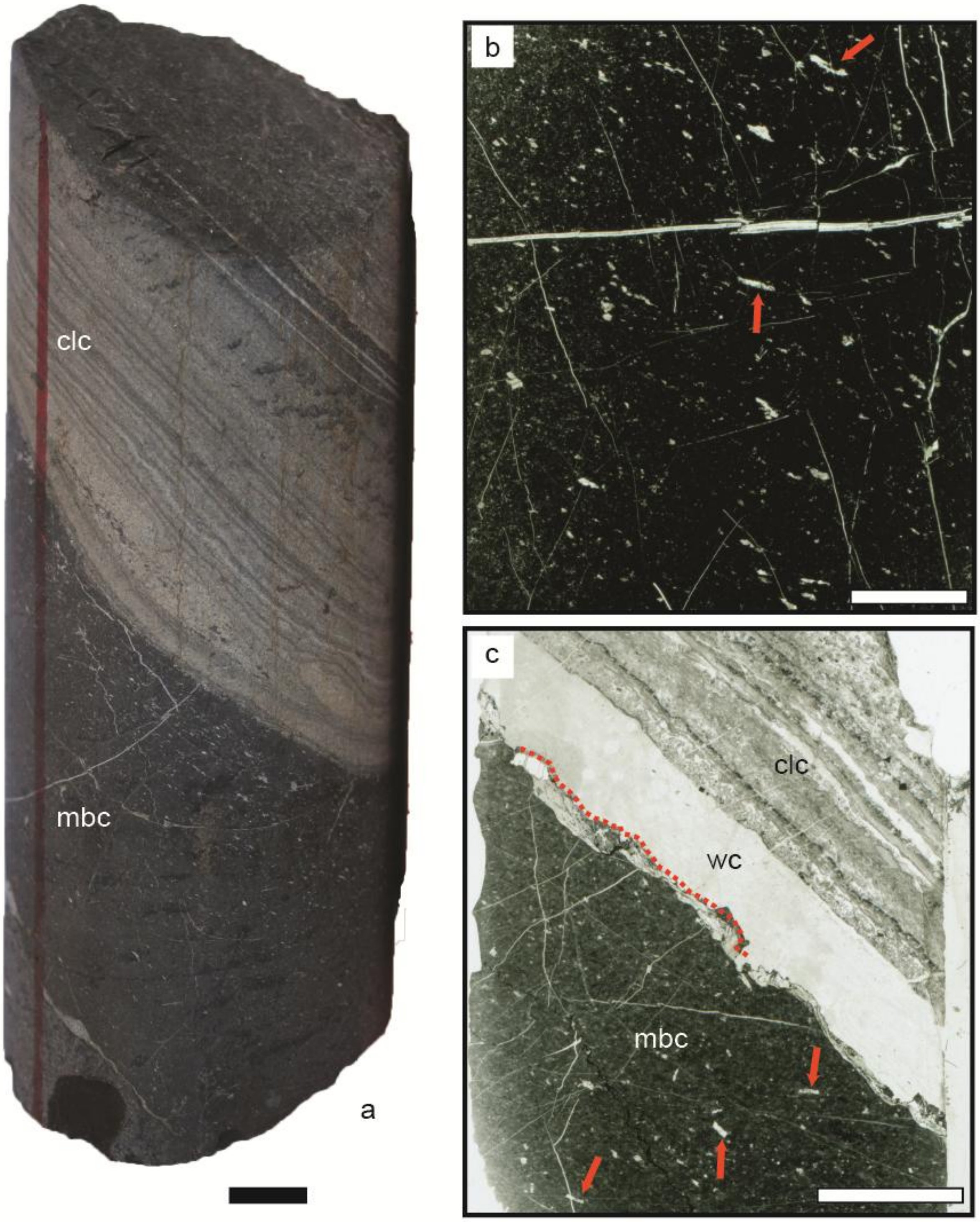

Figure 3.9 – Massive black chert. a) Sample C8 (depth along the core, 865.76-865.63 m) include a lower massive black chert (mbc). This facies is unstructured consisting of dense massive carbonaceous chert, however some porosity is preserved in the form of quartz-filled cavities, although many of those are actually chert pseudomorphs after other large crystals (see also b,c). The upper contact with the overlying crinkly laminated chert (clc) consist of a wave-like stylolite similar to the one observed in thin section on the right (c). b) In thin section the massive black chert is also unstructured. Quartz filled pores occur as well as many quartz pseudomorphs after tabular crystals or clasts (red arrows). Porosity and clasts appear parallel to the bedding. c) A thin section of the contact between a massive black chert and an overlying white chert band show pressure-dissolution manifested in the form of a thick wave-like stylolitic seams (red dashed line). Upper in the section a white chert (wc) and crinkly ferruginous chert (clc). Scale bar for all the figures: 1 cm.

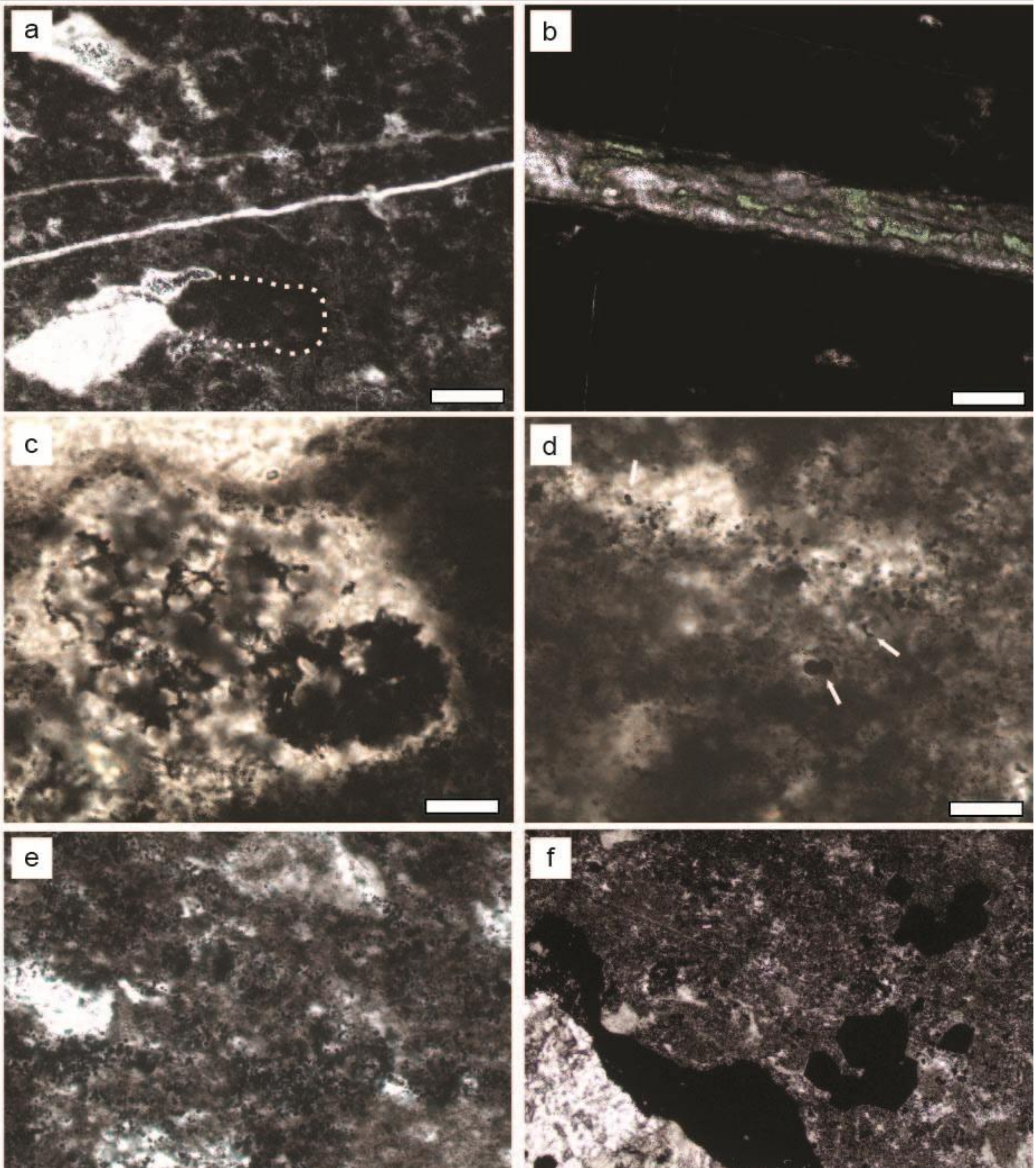

Figure 3.10 – Massive black chert. a) The facies consist of cloudy diffuse CM interrupted by chert-filled pores, cavities and cross-cutting veins. Cavities are often regular and represent quartz pseudomorphs after rhomboidal or tabular geometries. In this figure the upper cavity represent a long tabular pseudomorph partially replaced by CM and superimposed by a quartz pseudomorph after a rhomboidal crystal. The lower cavity has a regular rhomboidal shape. A tentative carbonaceous grain is marked by the dashed white line. Scale bar: 200 µm. b) A cross cutting vein filled by quartz and green chlorite (chamosite). Scale bar: 200 µm. c) Dark, thick interstitial CM is typically observed interfingering between chert grains in quartz-filled pores and cavities. Scale bar: 20 µm. d) Spheres of bituminous CM are found scattered within the CM. Note that due to the richness in cloudy CM those carbonaceous microtexture can be recognized only in some area. Scale bar: 20 µm. e) Scattered black dense tiny particles consist of copious finely dispersed pyrite grains and bituminous CM. Scale bar: 50 µm. f) At the contact between massive black chert and an underlying white chert a thick wave-like stylolite is found enriched in dark material consisting mainly of bituminous CM, sulphides and chlorite. In the massive black chert euhedral hexagonal and cubic authigenic pyrite occur. Scale bar: 200 µm.

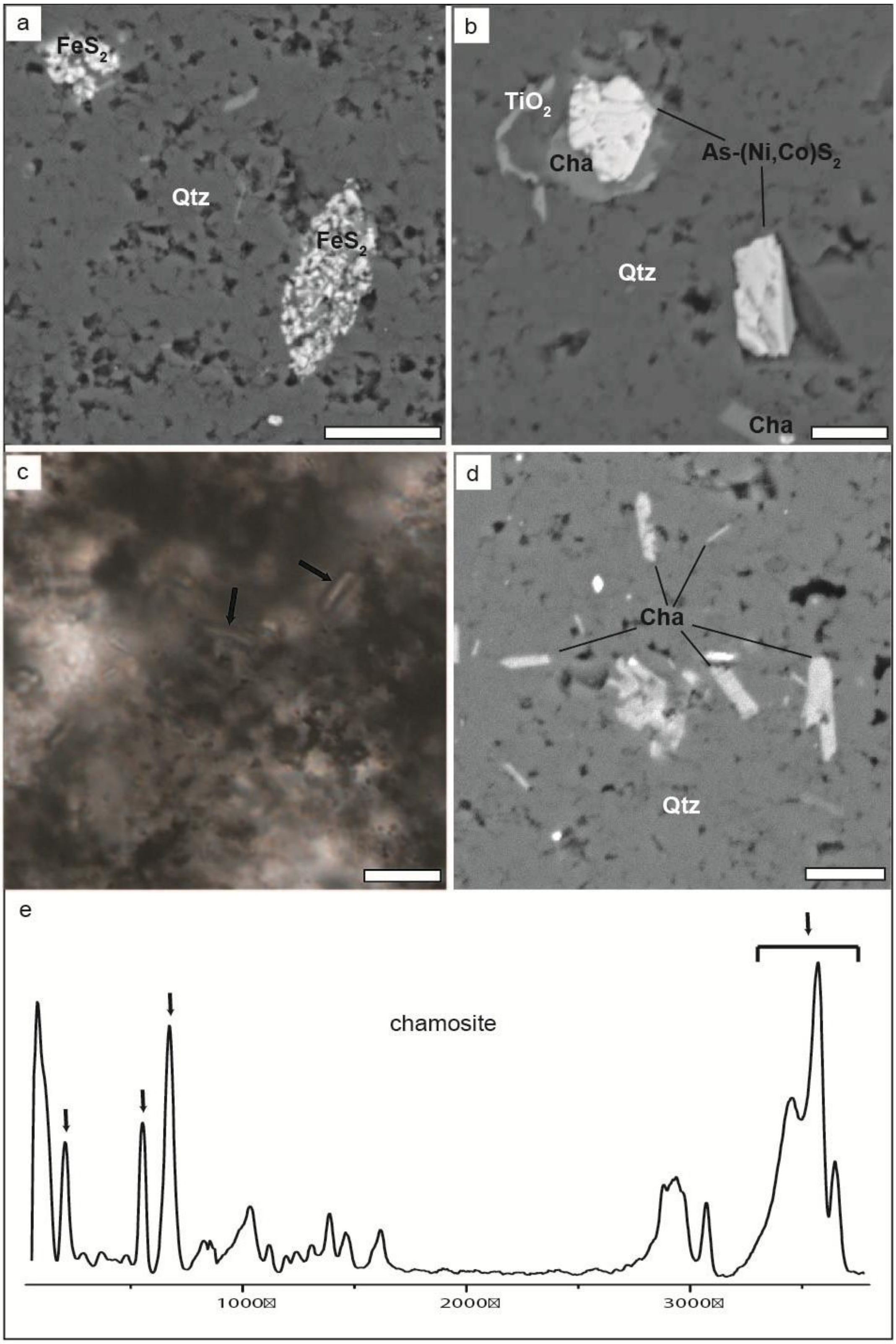

Figure 3.11 – Massive black chert. a) A cluster of finely grained pyrite in a rhomboidal pseudomorph. Scale bar: 20 µm. b) Two arsenic Co, Ni-rich subhedral sulphides in a chert matrix. The sulphide on top is intergrown by secondary chamosite (Cha), and on the left a lamina rich in TiO_2 occur. Scale bar: 10 µm. c) Optical and SEM (d) imaging on finely dispersed acicular or columnar chamosite(black arrows and Cha) which is particularly abundant in the massive black chert. Both scales are 10 µm. e)The peculiar Raman peaks used to identify the columnar chamosite are pointed by the black arrows. The other peaks represent the pattern for the contaminant epoxy resin

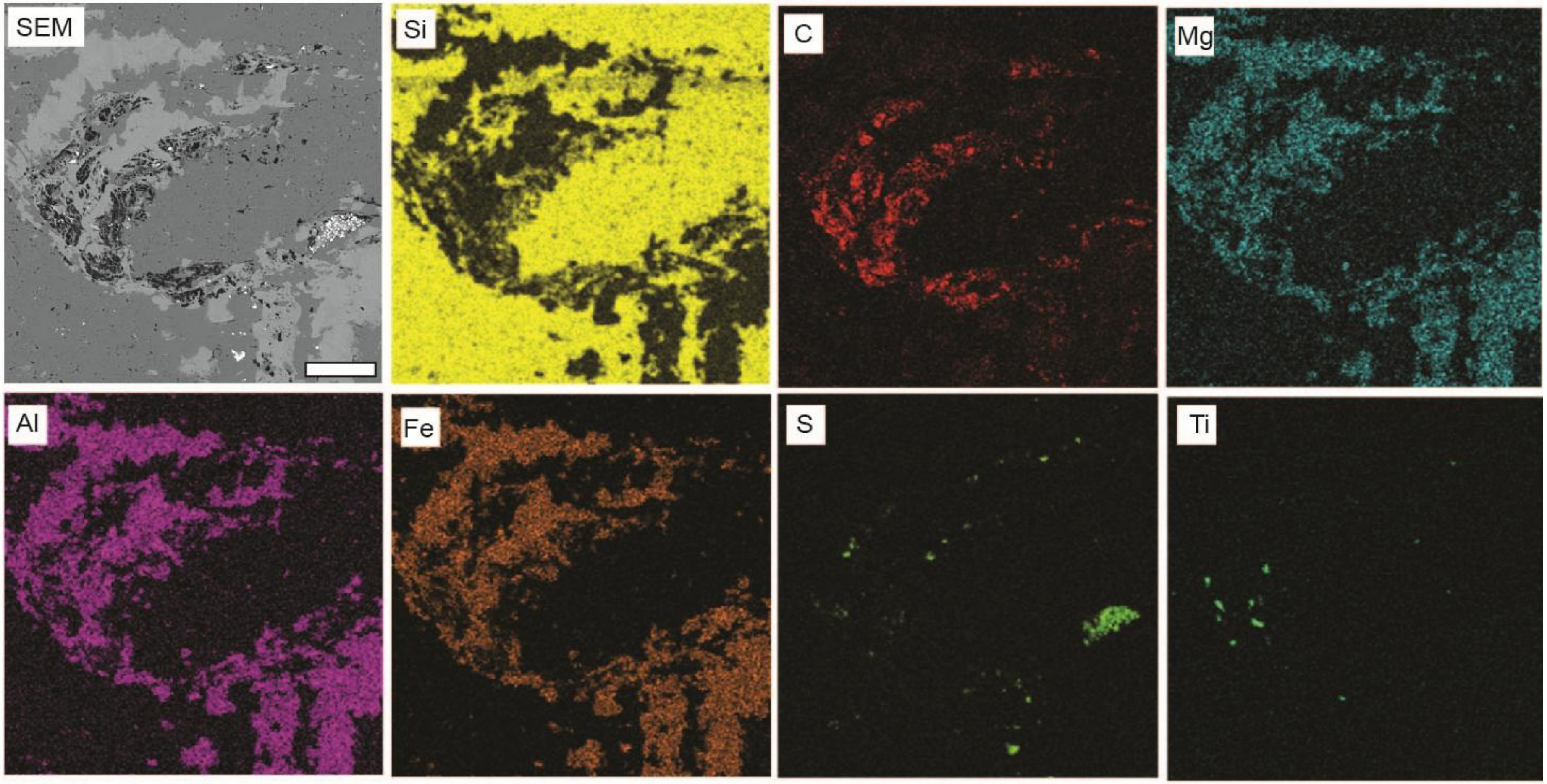

Figure 3.12 – Elemental distribution in a wave-like thick stylolite occurring at the interface between a massive black chert and a different chert facies. Scale bar: 60 μm.

3.2.3 Laminated black chert

At a first glance laminated black chert (lbc) strongly resemble massive black chert both in its aspect and distribution along the core. As for the massive carbonaceous facies, laminated black chert is an extremely homogeneous dark facies characterized by white-grey silica filled pores and small irregular cavities (Fig. 3.13a,c). However it differentiate, as suggested by its name, being composed of superimposed individual carbonaceous rich laminations, commonly a few millimetre thick (Fig. 3.13a,b). Those are separated by extremely thin (less than 1 mm) white-grey quartz layers which are very difficult to distinguish at the naked eye but even in thin section. Nevertheless another feature may help the distinction as along the core laminated black chert layers are found conformably interlayered with the ferruginous-and-white banded facies while as seen before massive black chert is characterized by thick pyrite-rich stylolitic seams indicative of sediment dissolution. Furthermore laminated facies appear also slightly more granular and porous in their texture (Fig. 3.13a).

3.2.3.1 Microfacies description

In thin section laminations are also difficult to distinguish (Fig. 3.13c). However modes of CM deposition and mineralogy are slightly distinct from what observed in the massive black chert. Laminated black chert observed during this study consist of a mixture of randomly oriented carbonaceous grains and diffuse CM within a microcrystalline quartz cement (Fig. 3.14a), with scarce scattered authigenic cubic pyrite crystals and finely dispersed chamosite. As described above for the other carbonaceous rich facies, discrete carbonaceous structures, when observed at high-magnification, consist of sub-micron sized CM particles in a pervasive microcrystalline quartz matrix. Simple grains ranging from a few microns up to ~500 μm predominate in laminated black chert (Fig. 3.14a,b). They consist of fluffy dense concentrations of CM characterized by irregular shapes and margins and showing no evidence of compaction (aspect ratio < 10). Discrete wisps and composite grains also occur with less frequency. The first consist of dense elongated carbonaceous flakes (aspect ratio > 10) up to a few hundred microns long and often less than 10 μm thick resembling carbonaceous laminae (Fig. 3.14c) but differentiating from the latter by their uneven lateral thickness, the lack of continuity and absence of anastomosing behaviour. Composite grains (Fig. 3.14b) represent simple carbonaceous grains aggregated into discrete clumps which reach up to ~1000 μm in size. Dense CM is also observed forming botryoidal rims around discrete grains or as dense, opaque, cavity-filling, interstitial material between grains or between the domains of composite grains (Fig. 3.14b). As for the ferruginous crinkly laminated chert, cross-cutting mainly sub-vertical quartz veinlets often infilled by a dense bituminous CM phase occur in the laminated black chert (Fig. 3.14c). This CM was deposited from a fluid phase and the cross-cutting nature of veinlets is indicative of later fracturing events.

3.2.3.2 Interpretation

Similarly to the black massive facies, the laminated black chert provide scarce textural features that can be used to infer a model for its origin. It is roughly massive and bears a mineralogical composition consisting mainly of CM, scattered sulphides and dispersed chlorite. However the laminated black chert is conformably interlayered with the ferruginous and white banded sediments suggesting its sedimentary origin. The planar laminated texture, the lack of other sedimentary structures, the absence of rounded grains, clastic material or other clear evidence of transportation, suggest a deposition in a low-energy environment. As no carbonaceous laminae have been observed, growing by mat-construction is discredited, and the black laminated chert facies fit better with a cyclic gentle precipitation of fluffy carbonaceous grains out of the water column. Such interpretation is consistent with precipitation of organic debris after microbial activity in the water column or deposition out of carbonaceous rich exhalative fluids during intervals of volcanic quiescence like previously suggested for other Palaeoarchaean laminated black chert (Walsh and Lowe, 1999; Kiyokawa et al., 2006; Hofmann and Bolhar, 2007c). The irregular fluffy carbonaceous grains and wisps are similar to younger microbial clotted textures (Fayers and Trewin, 2003; Trewin et al., 2003) suggesting a possible biological origin.

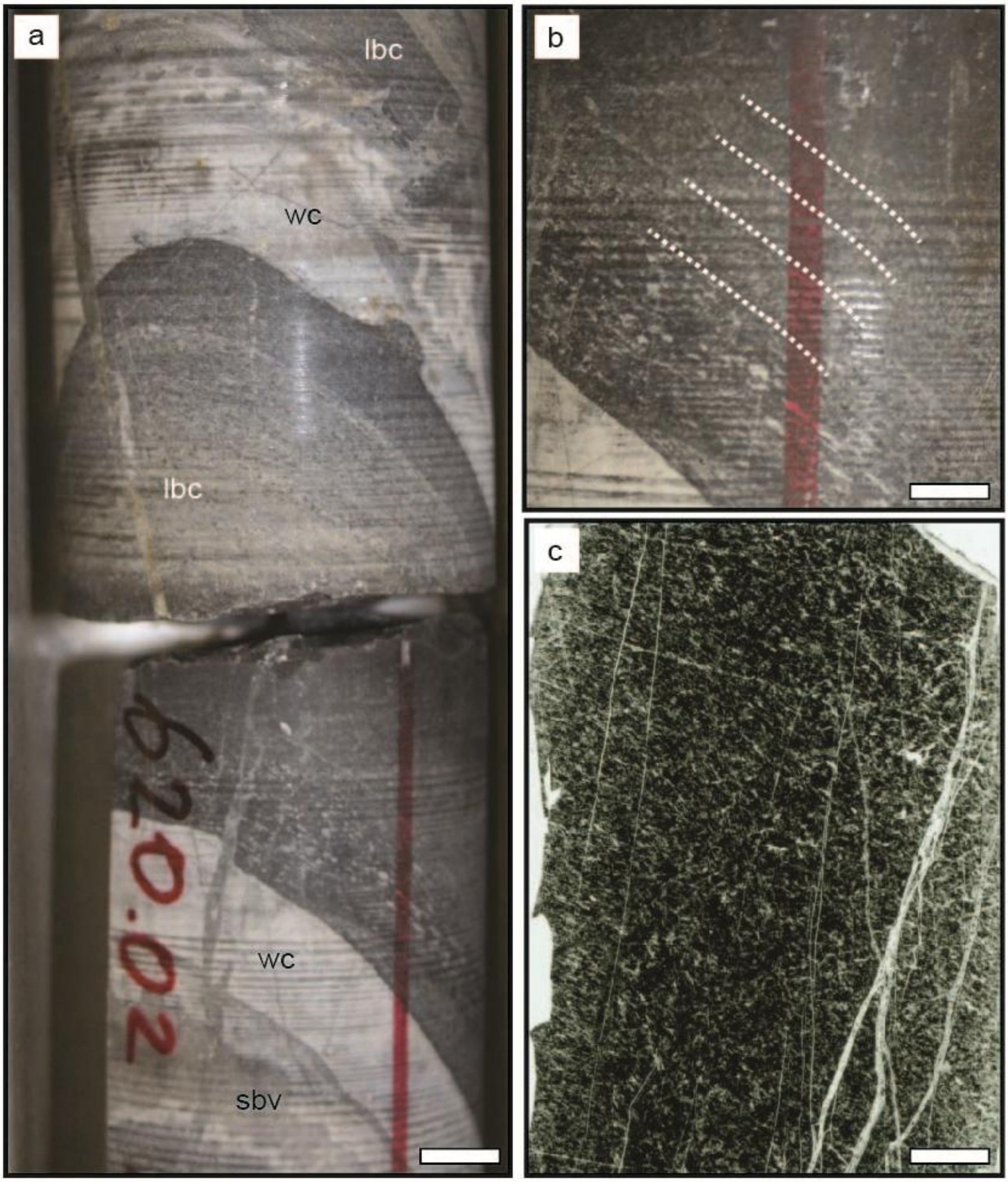

Figure 3.13 – Laminated black chert. a) Sample C2 (620.17-620.02 m) include a thick laminated black chert mesobands (lbc). It is a very homogeneous dark facies characterized by white-grey silica filled pores. The top of the carbonaceous rich band show clear evidence of sedimentary lamination. At the bottom of the sample a botryoidal quartz-filled stratiform vein (sbv) is capped by a white bedded chert band (wc). The laminated black chert is overlaid by a white chert band (wc) and possibly more black laminated chert (lbc). Scale bar: 1 cm. b) An enlarged section of the sample C2 where a white dashed line is used to highlight the individual sedimentary laminations which are not always of easy identification. Scale bar: 5 mm. c) A thin section from the sample C2 show the very homogenous carbonaceous rich character of the laminated black chert. Scale bar: 3 mm.

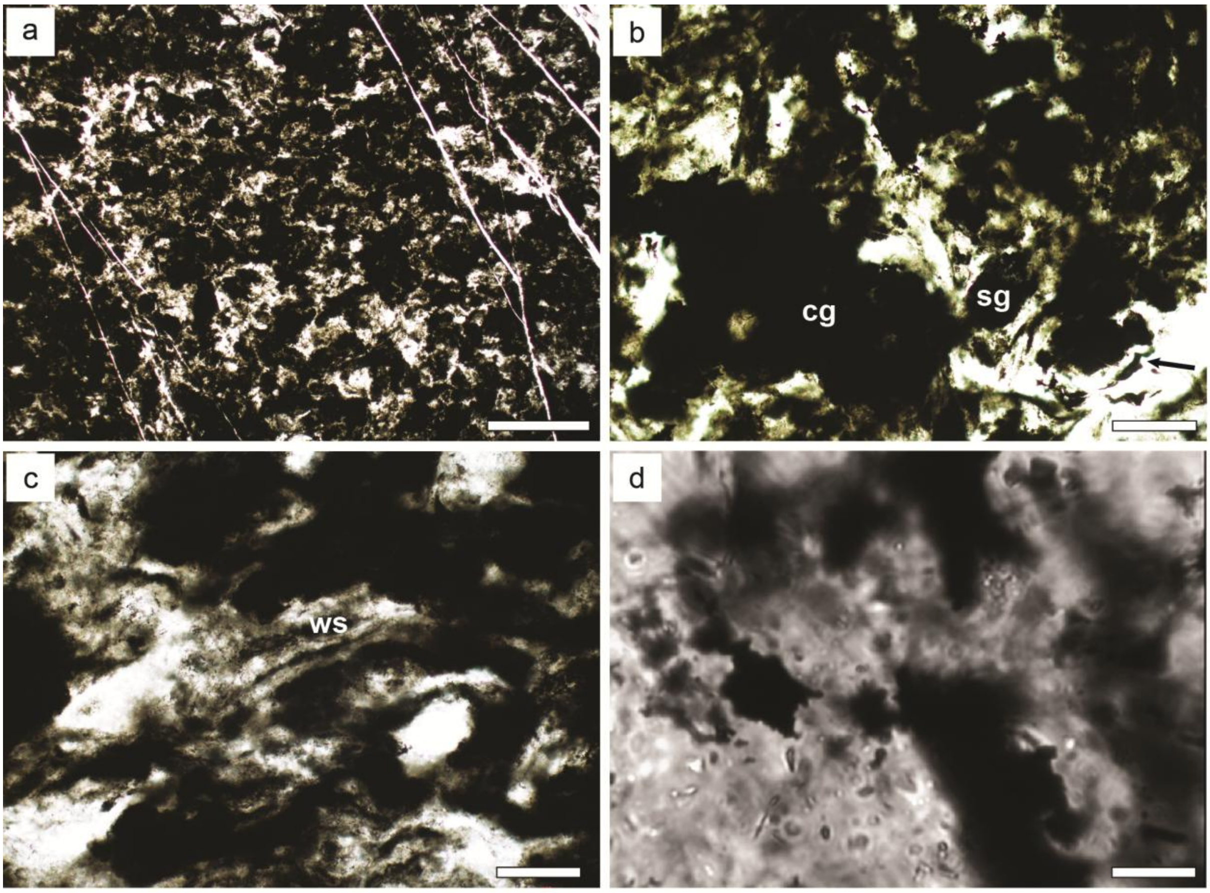

Figure 3.14 – Photomicrographs of laminated black chert. a) Laminated black chert is composed mainly of randomly oriented, equant simple carbonaceous fluffy grains, but also composite carbonaceous grains and wisps. The fabric is cross-cut by later quartz veinlets. Scale bar: 1000 µm. b) A large composite carbonaceous grain (cg) and several simple carbonaceous grains (sg) are present in chert precipitate. The black arrow at the bottom right corner points at a botryoidal CM-rich rim that can often be found around simple or composite grains. Scale bar: 200 µm. c) Elongated wisps (ws) of CM which can be so thin that they may resemble mat-like carbonaceous laminae. Scale bar: 100 µm. d) Dense CM present from cross-cutting quartz veinlets similar to those seen in (a). Scale bar: 20 µm.

3.2.4 Granular carbonaceous chert

The granular carbonaceous chert (gc) is a poorly sorted mixture of abundant sandy carbonaceous grains and rare scattered white, black and greenish-grey pebbles and clasts that can reach dimensions up to a few centimetres (Fig. 3.15a,b). It is a detrital facies and it always occurs as a filling within botryoidal quartz stratiform veins, resulting in a geopetal structure (Fig. 3.16). Such association along the core is consistently found interbedded between an underlying crinkly laminated ferruginous chert (sometimes even just a single microband) and an overlying white bedded chert, so that the way-up succession of crinkly laminated chert-granular carbonaceous chert-botryoidal quartz vein-white bedded chert represents a recurring pattern through the BARB3 core (Fig. 3.15a,b and Fig. 3.16).

The contact between the granular chert and the underlying crinkly laminated facies is erosional and associated with the disruption and soft-deformation of the ferruginous microbands (Fig. 3.15b and Fig. 3.16). The crinkly microbands can be found plastically deformed (Fig. 3.16c) and partially uplifted so that fringes of the clc bands float in the overlying granular carbonaceous material. Crinkly laminated rip-up fragments occur within the granular chert (Fig. 3.15b, Fig.3.16). They are typically large at the base of the granular thickness. Here they sit at the erosional contact, usually parallel to the bedding, close to their site of origin and sometimes form possible imbrication structures (Fig. 3.16b). At the top of the granular chert, the size of such clasts generally decrease. The smaller fragments float in the sandy material usually parallel to bedding and their provenance can’t be faithfully reconstructed also due to the limited size of the core. Crinkly laminated microbands that have been lifted-up or disrupted and now float in the granular chert have typically lost their greenish hue and appear to be entirely silicified. The granular chert also includes white or grey coarse chert sandy grains and pebbles that are usually rounded. Less frequently black carbonaceous rich clasts and pebbles can be observed dispersed in the sandy carbonaceous chert (Fig. 3.15a).

Representing the bulk of the facies, the coarse and poorly sorted sandy carbonaceous grains fill all the spaces available around the lifted-up microbands and the rip-up clasts. Close to the lower contact, the sandy material shows greenish-grey patches similar to the underlying ferruginous bands suggesting that here some siderite may be present. The granular carbonaceous chert forms stratiform thicknesses that range from less than 1 mm, composed of fine sandy material only, to a few centimetres, often including large rip-up clasts. Well compacted centimetre thick layers along the core may show evidence of internal bedding forming individual laminations a few mm thick indicating that the facies was piled up during several phases of detrital input (Fig. 3.15a).

The upper contact of the granular facies is irregular and it is coated by the lower colloform banding of the overlying botryoidal quartz-filled vein. The botryoidal quartz filled vein is characterized by the colloform silica precipitate protruding towards the cavity centre and by a transition from marginal white quartz towards a dusky-blue mega quartz (Fig. 3.15, 3.16, 3.17a), similar to stratiform cavities in the crinkly laminated chert. The roof of the vein always consist of a white chert band, occasionally greenish chert fragments hang down from the white chert band; such fragments appear to be affine by texture and composition to the crinkly laminated bands observed, in the same veins, at the base of the granular chert (Fig. 3.16a,b).

The occurrence of botryoidal quartz-filled chert veins and granular carbonaceous chert is often associated to the local brecciation or tensile failure of white chert bands in the immediately underlying core bands (Fig. 3.16c). In these cases the granular material tends to move downwards, filling fractures and open spaces demonstrating the plastic and intruding attitude of such cavity filling facies. Fragments of the fractured white chert bands may be displaced and incorporated into the granular facies. Brecciated fragments of white chert, even still in place, show evidence of roundness (Fig. 3.16c).

3.2.4.1 Microfacies description

Apart from some siderite at the base of the facies (Fig. 3.17f), rare secondary chamosite and quartz rhomboidal pseudomorphs possibly after carbonates, the granular carbonaceous chert is almost entirely composed of carbonaceous grains in a chert matrix (Fig. 3.17b). As observed along the core, disrupted, softly-deformed and typically highly silicified layers of crinkly laminated facies occur at the base of the granular chert (Fig. 3.17d). Immediately above, the bulk of the granular facies is composed of sandy carbonaceous material consisting mainly of fluffy equant carbonaceous grains and clot aggregates (Fig. 3.17b,c); wispy grains are less frequently observed. The sandy carbonaceous material varies in dimension, encompassing grain size from silt to very fine gravel. Large carbonaceous-rich or white quartz rounded pebbles up to a few centimetres occurs. Rip-up fragments mainly of crinkly laminated chert (Fig. 3.17d and Fig. 3.18a) facies but also of more carbonaceous rich beds, possibly black laminated chert, are found scattered within the sandy material. At the base of the granular chert, rip-up fragments of mat-like laminations (Fig. 3.18 a,b,c,d) float in the quartz matrix maintaining their original cohesiveness and plastic behaviour, forming rolled-up and folded over structures. Always at the base of the facies close to the underlying ferruginous chert, CM clots and laminae are associated to finely grained siderite (Fig. 3.17f). Siliceous rounded grains, ranging between 100 and 200 μm, appear in this facies (Fig. 3.17e). Both carbonaceous and siliceous grains are characterized by rims of botryoidal silica precipitate enriched in dense CM (Fig. 3.17c), like previously observed in the black laminated chert (Fig. 3.14b).

In thin section the laminated texture of the granular carbonaceous material can be observed (Fig. 3.18a). The top of the granular chert is coated by a characteristic silica colloform precipitate forming a botryoidal isopachous lamination (Fig. 3.15b and Fig. 3.17a) which can be a few mm thick and it is composed by an alternation of thin dark carbonaceous rich and poor white chert laminae. The lamination is thus capped by a thin layer of coarser quartz crystals which after a few hundred microns turn into the megaquartz crystals which make up the main part of the veins filling.

At the bottom of the quartz-filled veins is a very peculiar CM microtexture, that has been observed in several samples existing on top of the microcrystalline isopachuous botryoidal lamination. It clearly differs from the CM observed in the granular chert, as well as from the botryoidal laminations and consists of a carbonaceous network up to 100 μm thick which gently coat the fine colloform precipitate immediately overlying the sandy detritus (Fig. 3.18 a,f,g,h,i). Although often disrupted and fragmented the carbonaceous network can extend for several mm or even throughout the thin section width, draping the bedded colloform thickness. At high magnification (Fig. 3.18 g,h,i) it consists of a continuous interconnected web of CM that appears to be trapping rounded, typically elongated silty or very fine sandy quartz grains. Such grains are packed together and preferentially oriented along the bedding plane (Fig. 3.18 g,h,i). The carbonaceous network shows an overall plastic and trapping behaviour which suggest it was originally a cohesive substance.

3.2.4.2 Interpretation

It is clear from the sedimentological textures described above that the granular carbonaceous chert represents a detrital component consisting of a mixture of carbonaceous grains and clasts derived from the erosion and reworking of material originally deposited in other primary sedimentary settings. The majority of the detritus appears to have originated from the ripping-up and reworking of crinkly laminated ferruginous chert facies. This is evident as the granular chert consistently occurs on top of an eroded and softly deformed ferruginous laminated band and includes mainly individual irregular carbonaceous clots and clot aggregates, crinkly laminated rip-up fragments, rip-up and rolled-over lamina-sets and CM-siderite composed grains thus reflecting the textural and mineralogical composition of the underlying facies. Additional grains and clasts may have come possibly from black laminated chert facies, and from the white chert bands, probably derived from the reworking and rounding of the white chert brecciated fragments usually associated to this facies. However is not always possible to unequivocally retrace the origin of the granular material.

The granular carbonaceous chert is puzzling with respect to its origin and many questions raised during its investigation. What would have been the stress or the source of energy responsible for the ripping up, reworking and mixing of such coarse and poorly sorted material? Where did the such process took place, at the seafloor or in the subsurface, and at which stage in the depositional history? Why are the granular facies virtually always associated with the botryoidal quartz-filled vein and frequently with the underlying white bands that are found fractured? What is the significance of this, cyclic recurring pattern where the granular material consistently sits on a crinkly laminated facies and the colloform cavity is capped by a band of white chert?

As observed along the BARB3, the shallow-platformal lithofacies bears no evidence for strong current activity at the seafloor, as the core is lacking detrital material and current induced sedimentary structures. This is consistent with facies deposition in a very low-energy shallow-water environment. The occurrence of granular chert exclusively as a cavity filling material in such an environment suggests that this facies formed in the subsurface rather than at the seafloor during storm events, as in the latter case one would expect similar material conformably interbedded between the ferruginous and white chert and not only filling colloform cavities. The origin of the botryoidal stratiform veins in the subsurface is supported by the occurrence of greenish laminated chert fragments hanging from the roof of the veins (Fig. 3.16a,b), conformably overlaid by the banded white chert. Such ferruginous fragments are also texturally conformable with the greenish-grey bands found at the base of the granular component, indicating that originally crinkly ferruginous bands were directly overlaid by the white chert that now represents the cavity roof. Thus the botryoidal cavity with its granular chert represents a later introduced offset in the original stratigraphy that consistently occurs between the crinkly laminated chert and the overlying banded white chert.

Although the granular chert includes regular, tabular clasts ripped-up from the crinkly laminated chert, non-rigid, plastically deformed disrupted microbands have also been observed together with folded over mat chunks. This indicates that the ripping-up and reworking occurred early in the history of the deposit or at least when the crinkly laminated chert was not yet completely lithified. This is also supported by the occurrence of copious carbonaceous clots in their original irregular form and not as rigid fragments possibly rounded by mechanical friction, unlike the white pebbles which may have been derived from the brecciation of the already lithified white banded chert.

It has been proposed that the botryoidal quartz-filled cavities of the BRC shallow-platformal facies originated in non-hydrothermal settings, from the dissolution of evaporites in the phreatic zone, or as fluid escape structures resulting from soft-sediment disruption after storm events in the deeper platformal facies (Tice and Lowe 2004, 2006). Both processes are consistent with a subsurface origin for the botryoidal cavities but both processes cannot justify the occurrence of the copious amount of granular material exclusively filling cavities as observed in the BARB3 during this study. Whether the cavity originated due to shrinkage of sediments, or evaporite dissolution, an eroding and reworking force would have been necessary to produce the sandy material. In non-hydrothermal conditions the force would have come from current or wave activity at the sea-floor, but in this case, as for the storm events, one would expect copious detrital material deposited at the seafloor and not only in the subsurface cavities. Although sediment dehydration and shrinkage, evaporite dissolution and storm events are all possible causes for the formation of the cavities, such processes alone fail in justifying the exclusive presence of granular chert as a cavity filling facies.

Hofmann and Bolhar (2007) provided an extensive description of the processes and dynamics that could have led to the formation of hydrothermal dykes and stratiform veins in the BGB, including the origin of the filling detrital material. In their model, upwelling hydrothermal fluids encountering non-permeable silicified horizons would have generated an overpressure resulting in the opening of lateral stratiform veins through more porous and permeable paths. This model appears to fit the observations reported here on the BARB3 botryoidal veins and granular chert. Firstly, other than producing an offset in the stratigraphy, a hydrothermal fluid that laterally pervades buried sediments could also justify the absence of detrital material on the seafloor and their localization instead within stratiform veins. As observed along the core the sandy carbonaceous material occurs in a recurring pattern represented by the succession of crinkly laminated chert-granular carbonaceous chert-botryoidal quartz-filled vein-white chert band. Such a pattern is consistent with the white chert cavity roof representing a non permeable early silicified cap that would have forbidden vertical fluid escape forcing it laterally through the more permeable non-completely lithified crinkly laminated chert. Thus the fluid would have been forced by a non-permeable silicified cap through lateral preferential paths represented by more permeable lithologies as suggested by Hofmann and Bolhar (2007). The granular chert would have then been derived from the brecciation, erosion and ripping-up of material from the ferruginous facies due to the pervading silica-rich fluid. The same fluid would have also been responsible for the increased silicification of ferruginous clasts and layers interested by the process, as observed at the core facies and microfacies. The laminated texture observed in the granular material is consistent with pulses of pervasive fluid, as previously reported in dykes and veins of the BGB (Hofmann and Bolhar, 2007).

The co-occurrence of stratiform botryoidal veins and granular chert fit better with the convection of hydrothermal silica-rich fluid in a sediment column characterized by heterogeneous permeability. Although this doesn't exclude the possibility that cavities may have formed by different processes in different circumstances, it is strongly suggested that an up-welling of low-temperature silica-rich fluid had a pivotal role, considering that the colloform silica precipitate, as already discussed earlier in this chapter, is a common feature in hydrothermal systems (Marchev et al., 2004; Marinova et al., 2014). Interesting in such optic is the presence of an 2-3 m large extensive quartz dyke in the Hooggenoeg Formation just below the Buck Reef Chert outcrop (Fig. 3.19a,b) which unfortunately cannot be traced completely, disappearing before the contact with the basal BRC facies.

The only autochthonous CM microtexture observed in the granular carbonaceous chert, or better, in the associated botryoidal quartz-filled cavity, is the carbonaceous network draping the colloform precipitate on top of the sandy carbonaceous material. Such structures retain morphologies indicative of an originally plastic and cohesive behaviour. They consist of an anastomosing network of carbonaceous material that differs in texture from carbonaceous infillings found interleaved between chert grains in the black massive chert for which also an hydrothermal influence has been proposed. Furthermore the carbonaceous network in the botryoidal vein is bearing oriented quartz rounded grains suggesting a binding and trapping behaviour similar to that observed in modern microbial mats in siliciclastic environments (Eriksonn et al., 2007; Noffke, 2010). All those features are consistent with an interpretation of the carbonaceous network as the remains of an original microbial community rather than remobilized CM along crystals boundaries. Similar structures have been previously observed, in different context, in the BRC and identified as possible microbial mats (Tice and Lowe, 2006). Although bizarre a trapping and binding behaviour would be functional in such sub-surface environment, securing the mats against fluids circulating within the veins. The presence of a possible microbial mat community in a subsurface hydrothermal environment is consistent with the theory of subsurface chemotrophic niches that has been proposed for the early evolution of life and will be further discussed in the next chapters.

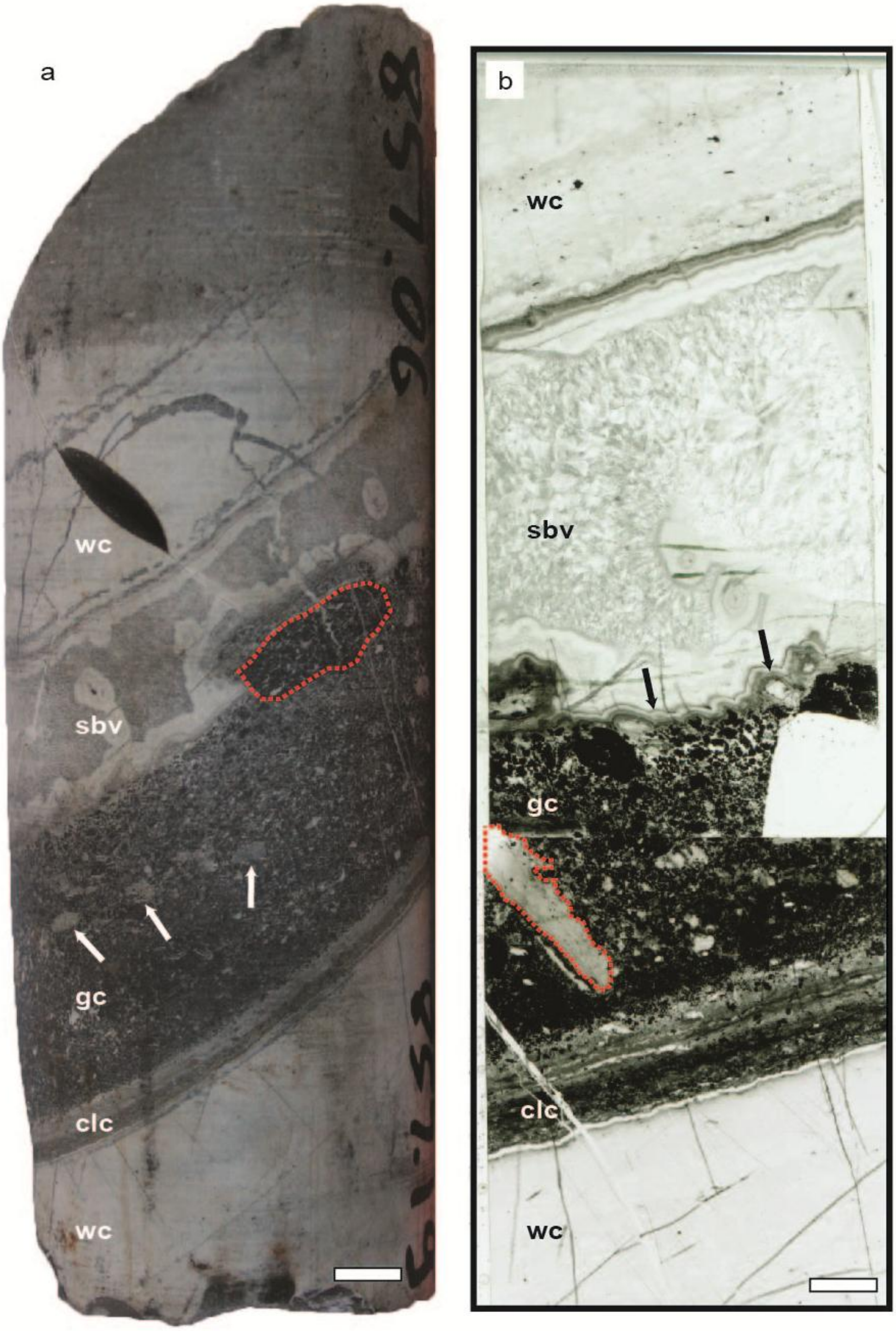

Figure 3.15 – Granular carbonaceous chert and stratiform botryoidal veins. a) Sample C7 (857.19-857.06 m) is a thick granular carbonaceous chert layer (gc) associated to an overlying botryoidal quartz-filled stratiform vein (sbv). It consist of a poorly sorted mixture of abundant sandy carbonaceous grains, but it is possible to observe as well white-grey quartz rounded sandy grains (arrows) and even a large carbonaceous clast or pebble on top of the granular material (dashed red line). The colloform precipitate extend towards the cavity interior. Here the recurrent way-up succession of crinkly laminated chert (clc)-granular carbonaceous chert (gc)-botryoidal vein (sbv)-white bedded chert (wc) can be observed, although the ferruginous chert (clc) at the base of the pattern is composed of just a few microbands. Scale bar: 1 cm. b) Two thin section obtained from sample C7 are used to retrace the relations between the different facies. The ferruginous microbands (clc) are evident and a rip-up clast of crinkly laminated chert sits with an angle to the bedding (dashed red line) supported by the copious sandy carbonaceous grains. The granular chert (gc) is poorly sorted. At the top of the granular material a chert colloform banding (black arrows) grade towards coarse megaquartz crystals. Scale bar: 600 μm.

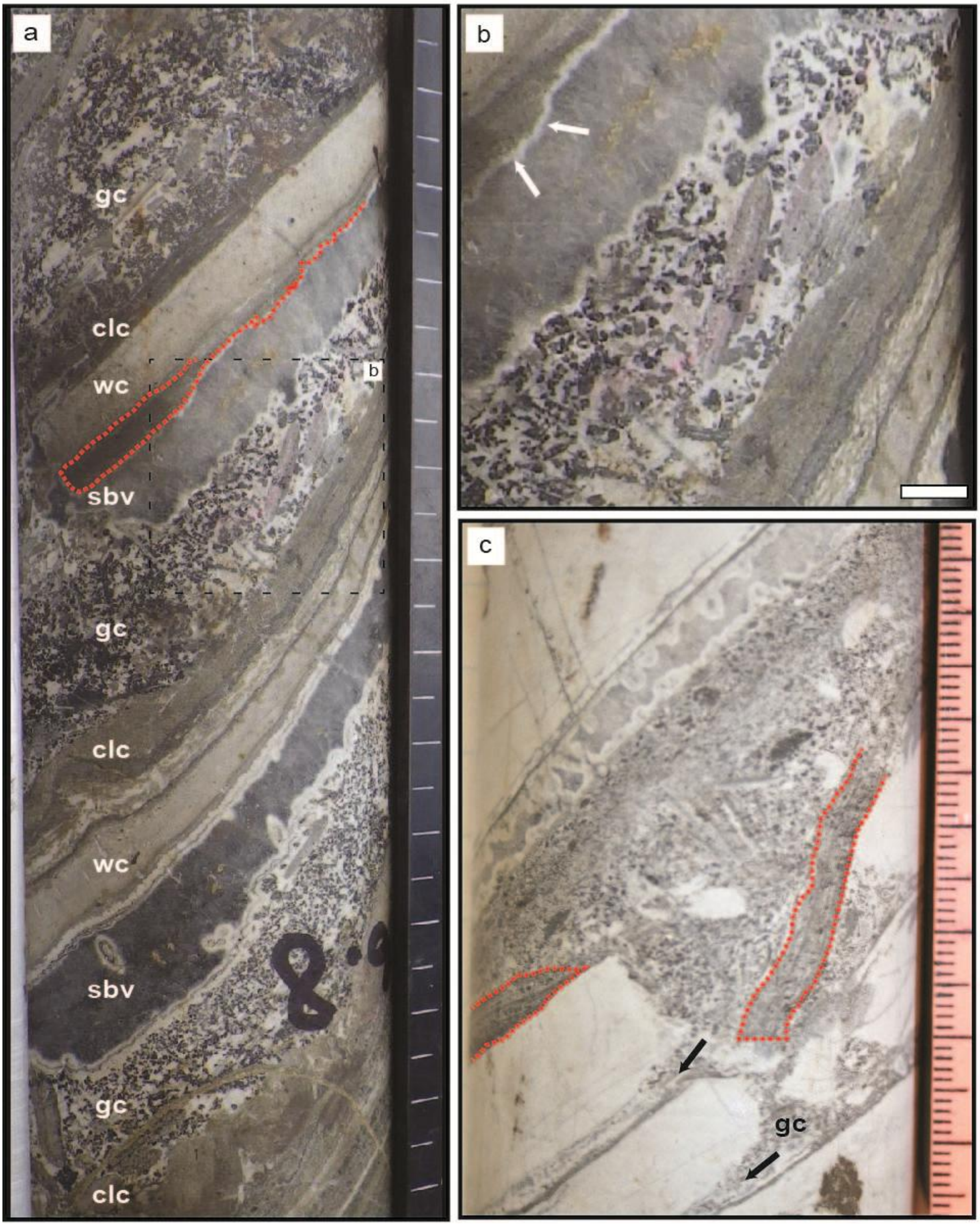

Figure 3.16 – Granular carbonaceous chert and stratiform botryoidal veins. a) In this sample from the lower part of the BARB3 core the recurrent way-up pattern composed by the superimposition of crinkly laminated chert (clc)-granular carbonaceous chert (gc)- stratiform botryoidal vein (sbv)-white bedded chert (wc), is beautifully preserved as two veins occur (and a third is just capping the granular chert seen at the top of the sample). Note that the upper botryoidal stratiform vein is characterized by an irregular contact with the capping white chert bands whereas the latter present hanging fragments of crinkly laminated ferruginous chert (red dashed line). Such fragments are related to the ferruginous bands seen below the underlying granular carbonaceous chert, suggesting the ferruginous chert and the white chert band once were in a conformable, direct, contact. This suggest a brecciation occurred and the granular chert originated afterwards as a cavity filling phase. Ruler for scale, unit: 5 mm. b) The nset in (a) is enlarged. Two very interesting features here are the imbricate structure showed by some rip-up ferruginous clasts and again the crinkly laminated chert hanging from the vein (continue)

roof (white arrows). c) Sample C6 (800-799.82 m) show a tensile failure of the early lithified white chert bands while at the same time the disrupted crinkly ferruginous chert (red dashed lines) bend down plastically into the formed void, while the granular material (gc) fills it. Such fracturing associated with the granular chert and botryoidal vein is here interpreted as caused by overpressure due to hydrothermal fluid, however tectonic processes could as well be involved. Note how the granular material makes is way also at the interface between different white chert bands (black arrows). Brittle fragments detached from the white chert bands take part to the granular material and they can be possibly mobilized within the flux becoming rounded. The granular chert appear to have been deposited in consecutive pulses, as it is suggested by its laminated texture. Ruler on the right, unit is 1 mm.

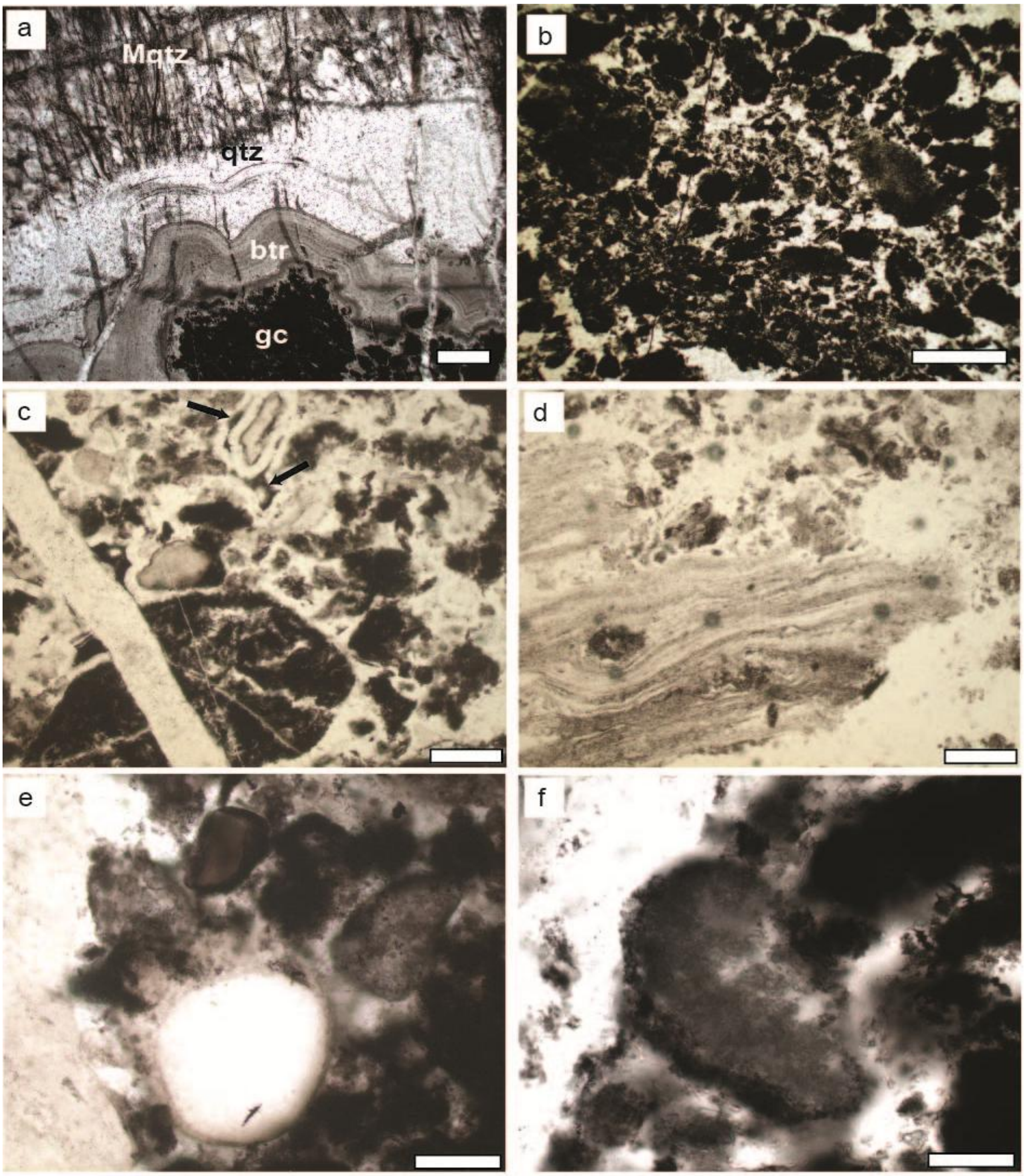

Figure 3.17 – Granular carbonaceous chert include grains of different morphologies, size and origin, mainly sandy carbonaceous grains. a) Botryoidal bending (btr) at the interface between the granular carbonaceous chert (gc) and the quartz filled cavity. Note the transition between the chert colloform precipitate to quartz (qtz) and megaquartz (Mqtz) up in the figure. Scale bar: 1 mm b) Sandy carbonaceous material is composed of simple fluffy CM grains but also composite grains and larger aggregates or clasts. Scale bar: 1 mm c) Spherulitic precipitation associated to rims of dense CM (black arrows) occur around the granular material. Scale bar: 200 μm d) A rip-up fragment of crinkly laminated chert bears evidence for CM mat-like laminae draping around a carbonaceous grain. Scale bar: 200 μm e) Other than CM-rich fluffy grains, clots and aggregates, silica grains occur. Those may be extremely rounded like the one in this picture. Many rounded grains derive probably from the reworking and mechanical frictioning on white chert bands brecciated fragments. Scale bar: 600 μm f) In the lower part of the granular chert layers, close to the underlying ferruginous chert, CM-siderite composite grains occur. Scale bar: 100 μm.

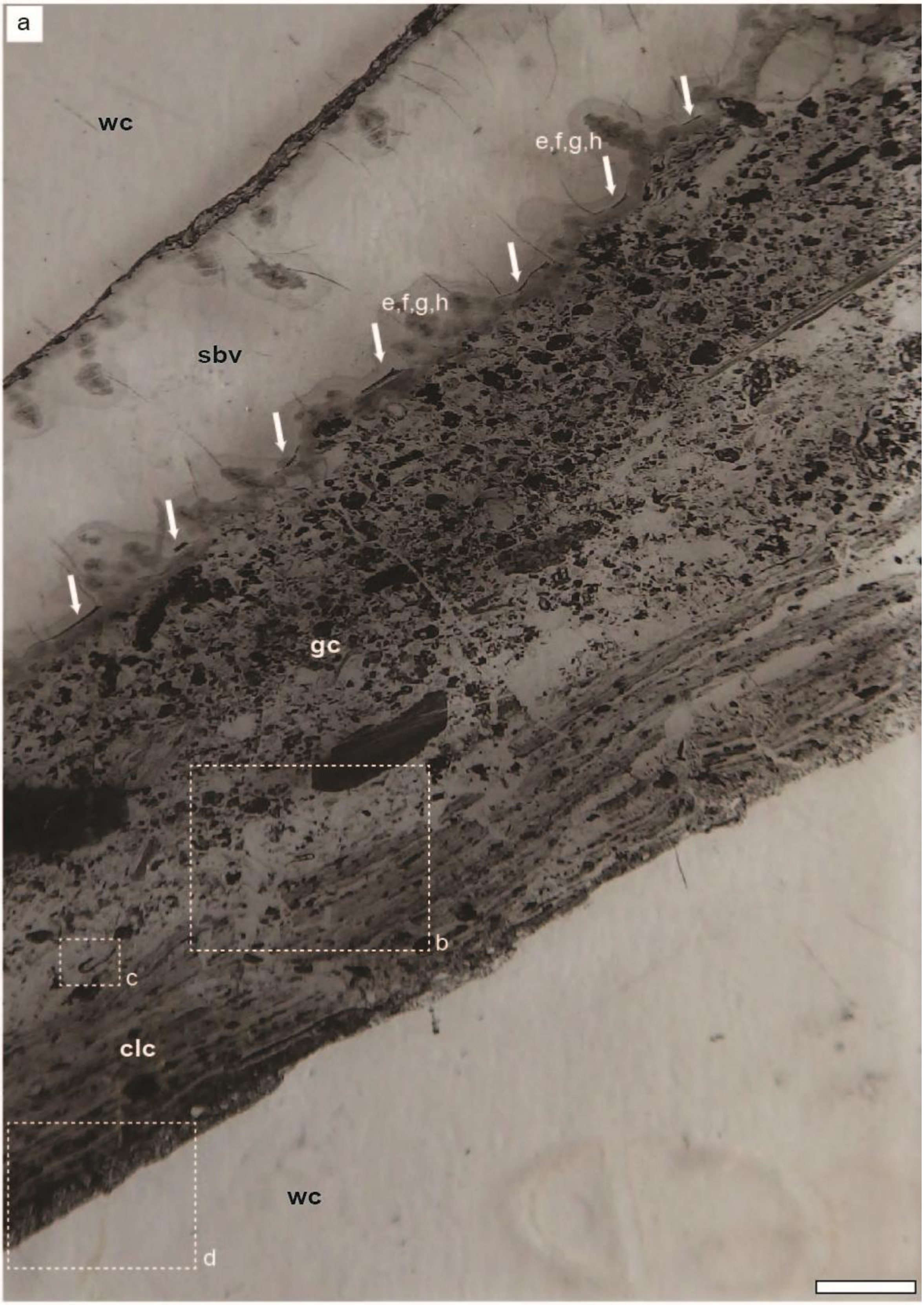

Figure 3.18 – a**)** Thin section C6D bears evidence for two CM-rich possible microbial structures in the form of mat-like laminae and networks. Note how the lower part of the granular chert is composed of crinkly laminated deformed ferruginous microbands which have been uplifted and disrupted. The more sandy granular component up in the detrital facies has been probably deposited following multiple events as suggest by a laminated texture of the granular facies. Insets are shown in the second part of the figure (b,c,d). Arrows show the site at which, within the stratiform vein the carbonaceous network is commonly observed. Scale bar: 2 mm (...continue).

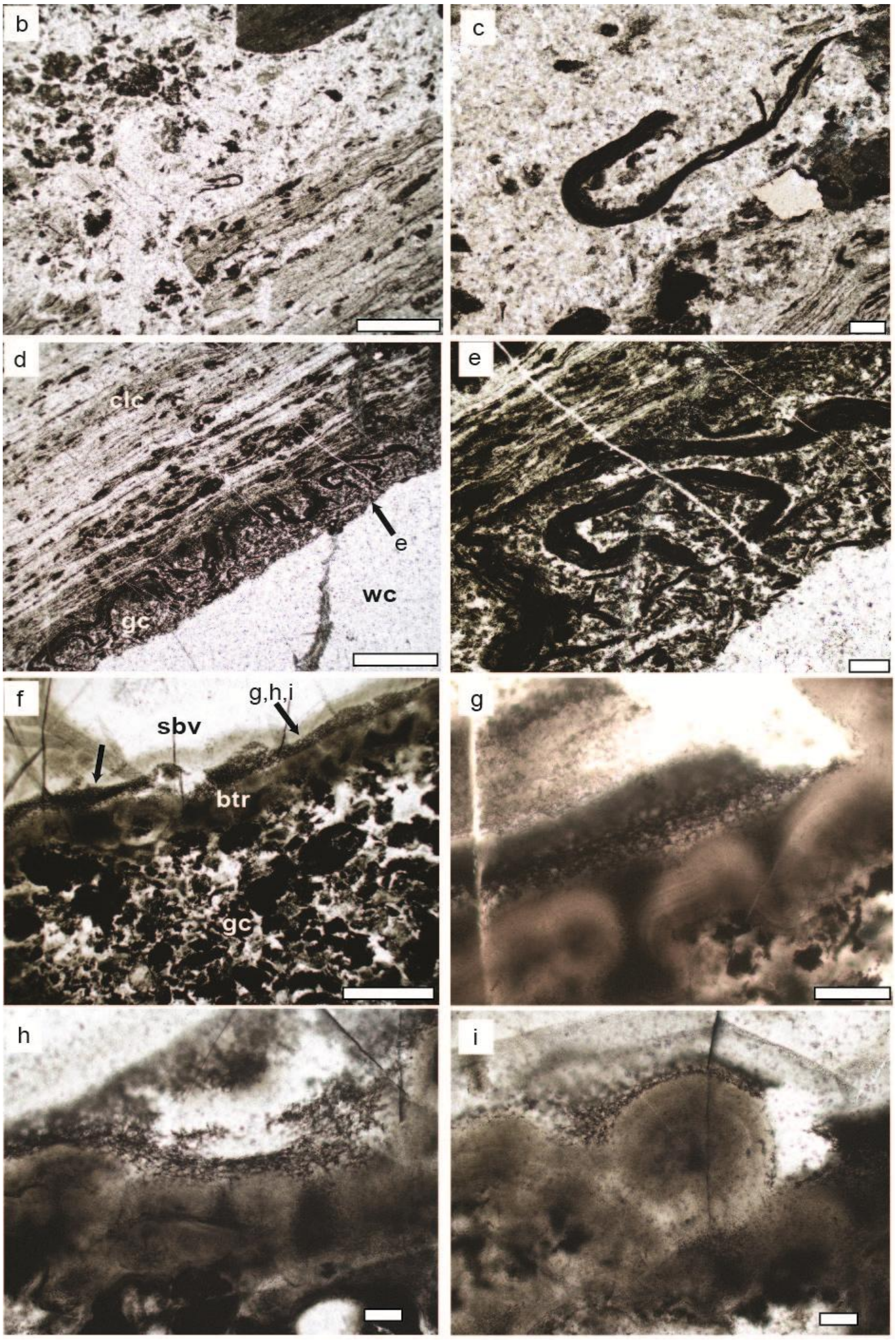

Figure 3.18 (continue) – b) A rip-up mat—like lamination at the base of the granular chert has been folded over. Scale bar: 1 mm c) An other rip-up mat show clearly a plastic cohesive behaviour and it represent a laminae-set, thus the remains of mats consturctor preserved in the crinkly laminated ferruginous chert. Scale bar: μm. d) Fluidization of the sediments togheter with co-occuring microbands up-lifting have resulted into plastic intrusion between the deformed crinkly ferruginous microbands ant the underlying white chert. Intruded material is rich in mats-like structures consisting of plastic, folded carbonaceous laminae-sets. Scale bar: 1000 μm. e) Carbonaceous laminae-sets observed in (d). Scale bar: 100 μm , f) The carbonaceous rich network sits on top of the colloform precipitation and form thicknesses of a few hundred microns. Scale bar: 1 mm. g) CM-rich networks appear to actively trap quartz rounded grains as those are also preferentially oriented planarly to the bedding plane. Scale bar: 1 mm, h) Detail on the CM network, it drapes gently the underlying botryoidal lamination and appear to have a plastic cohesive behaviour draping around protruding colloform precipitates (i). Scale bar: 100 μm for both pics.

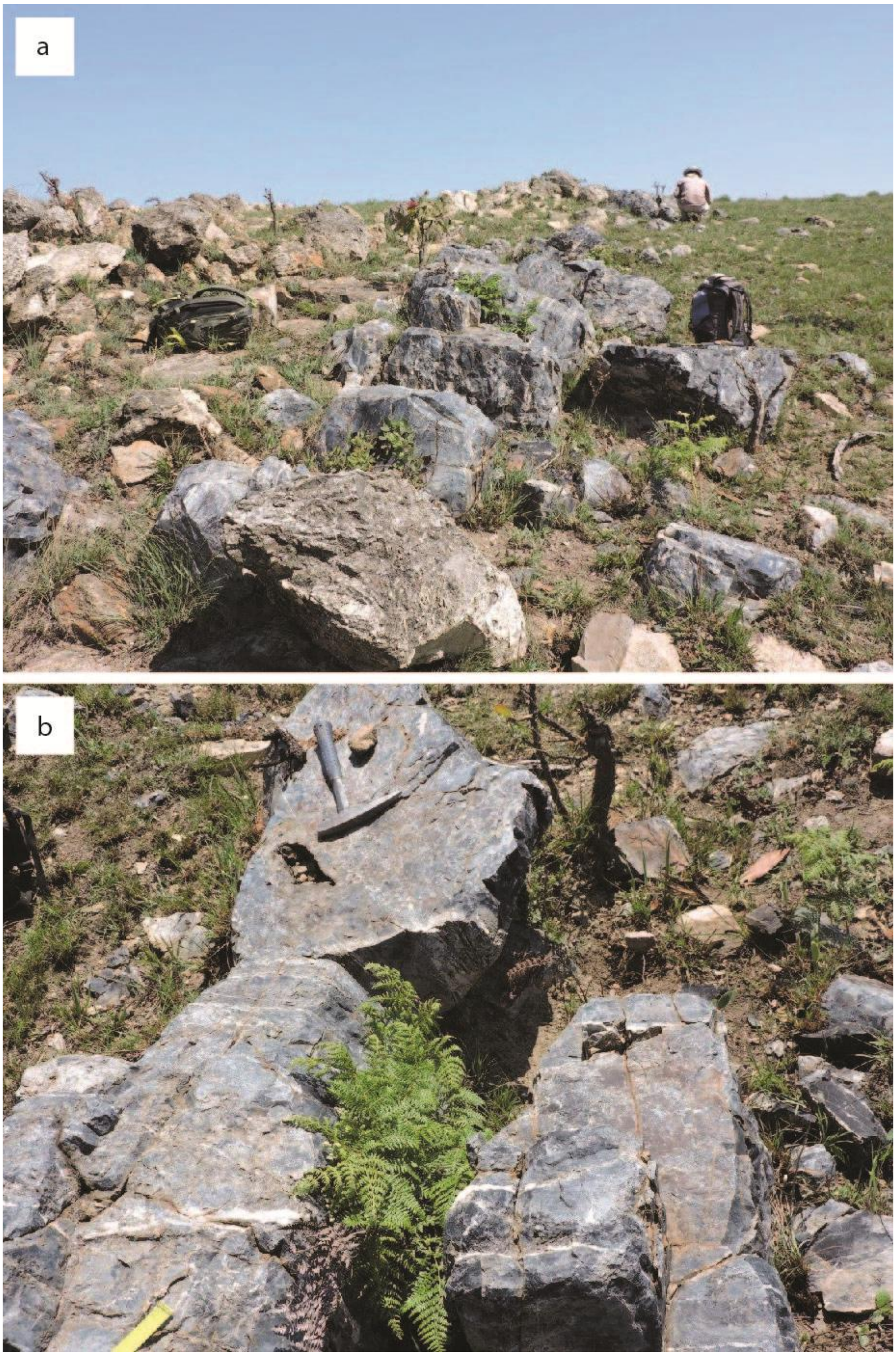

Figure 3.19 – a) An about 2-3 m wide extensive quartz dyke (dusky-grey boulders on the right) in the Hooggenoeg Formation occur just below the Buck Reef Chert outcrop. The dyke can be traced for about 300 m cutting through the Hooggenoeg dacite (grey-brown boulders on the left). Unfortunately the outcrop disappear just before the contact with the basal section of the BRC so that the path and fate of the dike can't be further traced. The picture is taken standing in the Hooggenoeg dacite and it is directed towards the stratigraphic-down so the BRC starts virtually some tens of meters behind the observer. Scale: 20 liters backpacks and Axel Hofmann in the background dressed like a dacite boulder. b) A closer look at the dyke boulders. Scale: hammer

Table. 3.1 – Summary of the BARB3 shallow-platformal core investigation and minero-petrographic results

facies	texture	mineralogy	botryoidal quartz	detrital grains	CM microtextures	CM microtexture proposed origin	proposed depositional setting
clc	planar crinkly laminated texture, superposed microbands (~1 mm-thick)	abundant siderite, scattered pyrite, scarce Co, Ni, Cu, Zn, As-sulphides, sparse chamosite and rare calcite	in fenestrae and stratiform cavities (a few mm thick), around rip-up CM-grains in fluid-intruded bands	detrital CM-grains and rip-up CM-laminae in fluid-intruded bands	laminae	*in situ* microbial mats remains	low-energy benthic aquatic environment dominated by mat-constructing microbial communities, possible diffuse silica-rich hydrothermalism
					simple grains	microbial debris	
					bitumen-like	hydrocarbon rich fluid after abiotic hydrothermal CM or biotic OM diagenesis	
					cloudy diffuse	microbial debris or abiotic hydrothermal	
mbc	structureless stratiform mesobands (~5 cm-thick), thick stylolites seams	frequent pyrite and acicular chamosite and As,Co,Ni-sulphides, rare TiO_2	no botryoidal quartz recognized during this investigation	sparse tabular and angular fragments filled with chert	cloudy grains	microbial debris or abiotic hydrothermal	CM-rich stratiform hydrothermal vein; seafloor deposit heavily influenced by hydrothermal activity
					dense interstitial	hydrocarbon rich fluid after abiotic hydrothermal CM or biotic OM diagenesis	
					bitumen-like	hydrocarbon rich fluid after abiotic hydrothermal CM or biotic OM diagenesis	
					cloudy diffuse	microbial debris or abiotic hydrothermal	
lbc	planar laminated texture, superposed microbands (a few mm thick)	scarce pyrite and finely grained chamosite	rims of botryoidal precipitate around CM-grains	no clear derital grain recognized	simple grains	microbial debris or abiotic hydrothermal	low-energy benthic acquatic environment dominated by precipitation of CM out of the water column after planctonic communities and/or CM-rich exhalative fluids
					wisps	microbial debris or abiotic hydrothermal	
					composite grains	microbial debris or abiotic hydrothermal	
					dense interstitial	hydrocarbon rich fluid after abiotic hydrothermal CM or biotic OM diagenesis	
Gc	sandy, planar laminations, associated to sbv	rare siderite and chamosite	within ubiquitous large sbv, rims around the sandy grains	detrital CM-rich grains, rip-up fragments from the clc	network	*in situ* microbial mats remains	subsurface environment resulting from the interaction between pervading silca-rich hydrothermal fluids and soft sediments, possible subsurface mat-forming communities
					laminae	microbial mats (detrital material derived from the clc facies)	
					CM-rich grains	microbial debris (detrital material derived from the clc facies)	
					dense interstitial	hydrocarbon rich fluid after abiotic hydrothermal CM or biotic OM diagenesis	

Chapter 4

BARB3 carbonaceous matter structure and nanotexture

4.1 Structural characterization of the BARB3 carbonaceous matter

As observed in the previous chapter, although representing a minor component in the Archaean cherts, CM is widely distributed within the BARB3 shallow-platformal deposits in the form of various microtextures (Tab. 3.1). These can be facies specific or may occur in a similar form across the different facies. For instance, while mat-like carbonaceous laminae preserved *in situ* are specific to the crinkly laminated chert, CM clotted textures occur analogously in the ferruginous microbands, in the laminated black chert and possibly, although poorly preserved, in the massive black chert. In other cases, like for the massive black chert, the overall CM assemblage is so peculiar that it represents a discriminating factor by which the facies can be distinguished. Finally the granular carbonaceous chert consists of a mixture of allochthonous microtextures derived from other primary deposits, mainly the crinkly laminated chert. However the granular carbonaceous chert also bears a peculiar carbonaceous network that caps the colloform quartz precipitate immediately overlying the sandy carbonaceous material and that is not observed in the other BARB3 facies.

The between-facies divergences and affinities in the CM microtextural assemblage advocate for exclusive and shared pathways in the CM cycle, implying segregated and overlapping depositional conditions or interactions, apparently mediated by circulating fluids, between the different lithofacies CM. To further explore the BARB3 CM possible sources and evolution and to support or reject proposed environmental settings, the chemical structure of such carbonaceous microtextures is here investigated by means of Raman microspectroscopy. The CM microtextures analyzed are summarized in Tab. 4.1 and Fig. 4.1. As reported already in the method section (Chapter 2) for each thin section a number of at least 25 collected spectra has been used in the calculations to take into account the within-sample CM structural variability (Aoya et a., 2010). The so obtained dataset is thus truly reflective of the average CM structural characteristic for each sample so that a between-sample heterogeneity can be investigated. Spectra have been collected so to cover most of the thin section volume homogeneously like showed in Fig.4.2.

Table. 4.1 –CM microtextures analyzed through Raman microspectroscopy during this study. The depositional set is again reported. Each microtexture is visualized in the following Fig. 4.1

facies	proposed depositional setting	CM analyzed microtextures	CM microtexture proposed origin	analyzed sample
clc	low-energy benthic aquatic environment dominated by mat-constructing microbial communities, possible diffuse silica-rich hydrothermalism	mat-like laminae (Fig.4.1a)	microbial mats remains preserved *in situ*	D11A, C3A
		simple grains (Fig. 4.1b)	microbial debris	D11A, C3A
		bitumen-like (Fig. 4.1c)	hydrocarbon rich fluid after abiotic hydrothermal CM or biotic OM diagenesis	D1
mbc	CM-rich stratiform hydrothermal vein; seafloor deposit heavily influenced by hydrothermal activity	cloudy grains (Fig. 4.1e)	microbial debris or abiotic hydrothermal CM	C9E
		dense interstitial (Fig. 4.1d)	hydrocarbon rich fluid after abiotic hydrothermal CM or biotic OM diagenesis	C9E
		bitumen-like (Fig. 4.1c)	hydrocarbon rich fluid after abiotic hydrothermal CM or biotic OM diagenesis	C9E
		cloudy diffuse (Fig. 4.1e)	microbial debris or abiotic hydrothermal CM	C9E
lbc	low-energy benthic acquatic environment dominated by precipitation of CM out of the water column after planctonic communities and/or CM-rich exhalative fluids	simple grains (Fig. 4.1f)	microbial debris or abiotic hydrothermal CM	C2C
		bitumen-like XcV (Fig. 4.1g)	hydrocarbon rich fluid after abiotic hydrothermal CM or biotic OM diagenesis	C2C
gc	subsurface environment resulting from the interaction between pervading silca-rich hydrothermal fluids and soft sediments, possible subsurface mat-forming communities	mat-like network (Fig. 4.1h)	microbial mats remains preserved *in situ*	D4A
		CM-rich grains (Fig. 4.1h)	microbial debris (detrital material derived from the clc facies)	D4A

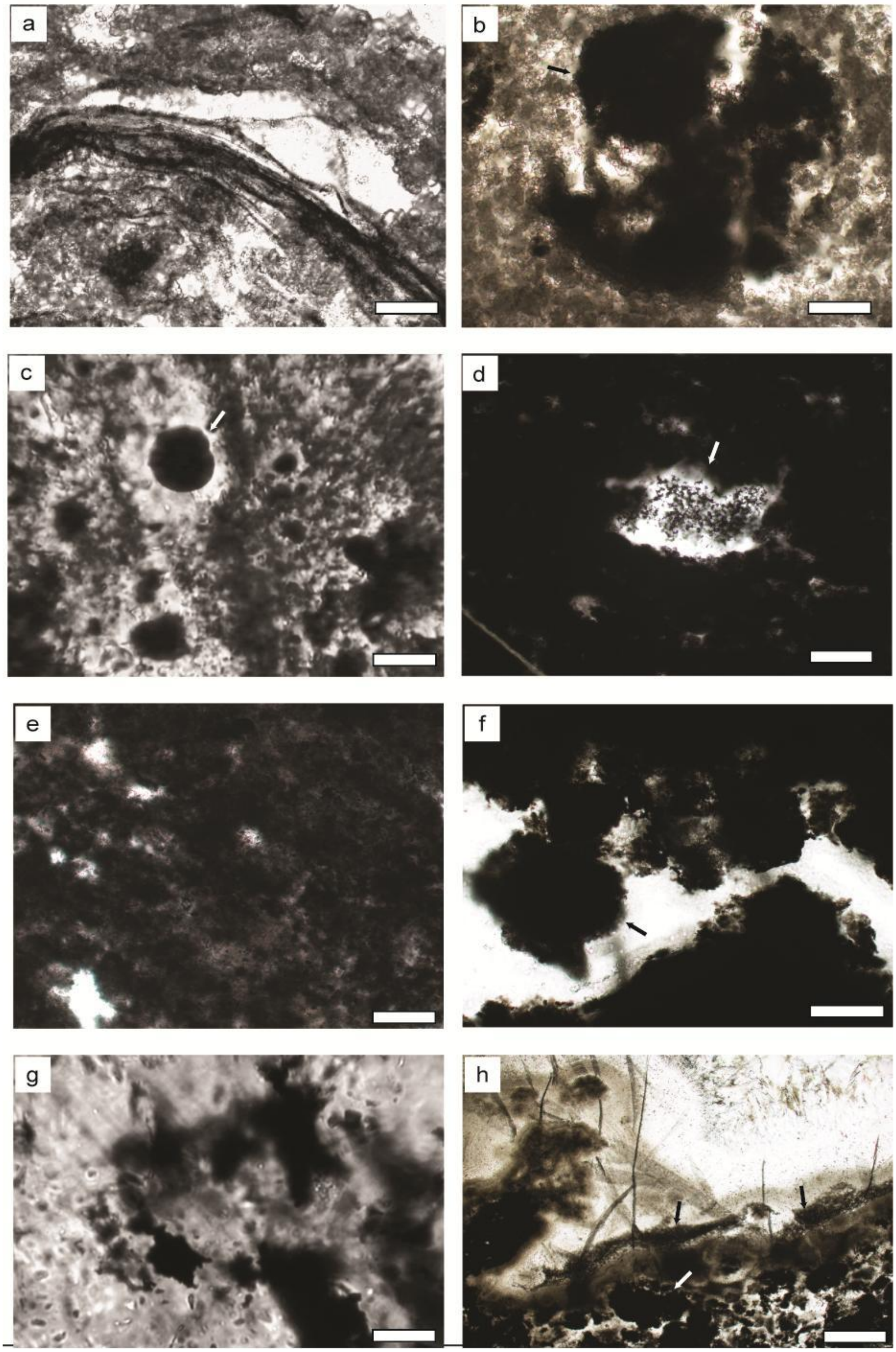

Figure 4.1 – CM microtextures characterized by Raman spectroscopy. a)Mat-like carbonaceous laminae and lamina-sets occurring in the crinkly laminated ferruginous chert. Scale bar: 100 µm. b) Simple carbonaceous grains occurring in the crinkly laminated chert. Scale bar: 50 µm. c) Bitumen-like spheres and blobs occurring mainly within the massive black chert, but also in the crinkly laminated chert sample D1. Scale bar: 50 µm. d) Interstitial carbonaceous material occurring in the massive black chert. Scale bar: 100 µm. e) Diffuse cloudy CM of the massive black chet. Scale bar: 200 µm. f) Simple carbonaceous grains within laminated black chert. Scale bar: 100 µm. g) Bituminous CM within cross-cutting veins analyzed within the laminated black facies. Scale bar: 20 µm. h) Simple carbonaceous grains (white arrow) and mat-like carbonaceous network (black arrows) within the granular carbonaceous chert. Scale bar: 200 µm.

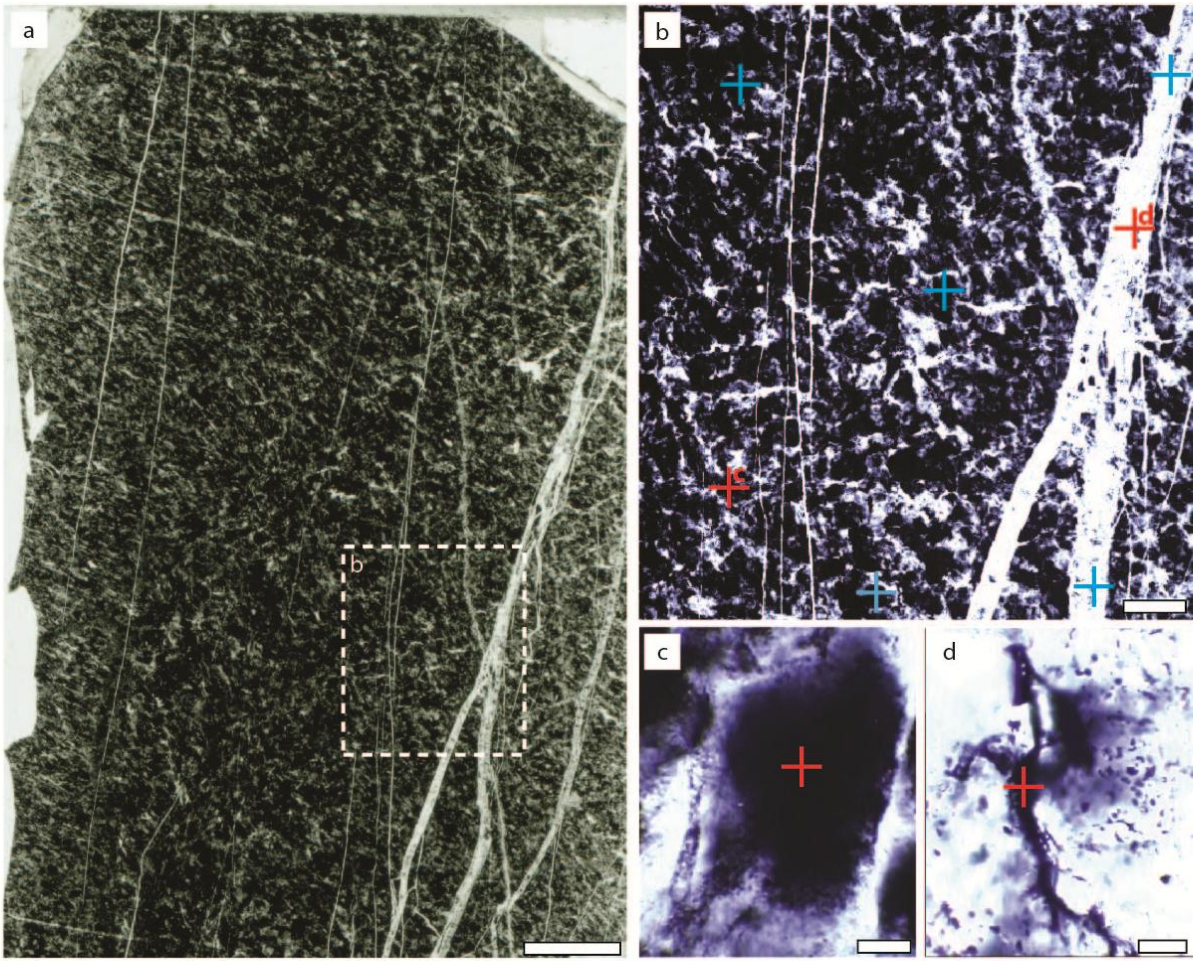

Figure 4.2 – This figure exemplify how Raman spectra have been collected on the thin sections for this specific CM microtextures structural characterization. a) Thin section C2C is representative of the laminated black chert. As reported in Tab. 4.1 for this carbonaceous rich chert the analyzed microtextures are: CM simple grains (c) and bitumen-like CM (d) observed within the cross-cutting veinlets (XcV). Spectra have been collected throughout the whole thin section. Several areas of the section have been characterized like for inset (b). Here each collected spectra (red and blue crosses) is representative of a discrete CM microtexture, like visualized by the red crosses (c) and (d) and respective microtextures (figures c and d), meaning that to each spectra correspond an individual grain or a discrete bitumen-like microtexture. Out of all the spectra collected the ones having the best resolution and thus resulting in the more accurate fit have been used in the calculation starting from a minimal number of 25 spectra per section. The approach has been the same for all the thin sections microtextures except for the crinkly laminated chert whereas each individual CM lamina-set has been analyzed by multiple regularly spaced spectra. Scales are: a) 3 mm; b) 500 µm; c and d) 20 µm.

4.1.1 General characteristics of the BARB3 CM

Spectral characteristics of the analyzed CM are consistent throughout the whole data-set so that Raman results, at first glance, appear very homogeneous (Fig. 4.3). All spectral profiles are characterized in the first-order by a well-developed D peak having a weak down-shifted shoulder (D4 band) and a less intense G band including an up-shifted shoulder (D2 band). A further Raman shift arises in between D and G (D3 band) that occurs closer to the graphitic band base producing a slightly asymmetric aspect. In the second-order range, three weak broad signals appear at about 2690 cm^{-1}, 2950 cm^{-1} and 3220 cm^{-1}, respectively. This overall spectral pattern is similar to that from disordered CM in meta-sediments subjected to a greenschist facies metamorphic grade (chlorite zone; e.g., Yui et al., 1996). The spectra similarities are especially evident when comparing CM belonging to the crinkly laminated chert, laminated black chert and granular carbonaceous chert. Between the facies there is a minor difference is observed in the CM from the massive black chert (Fig. 4.3), as this is characterized by a more intense G, D4 and D3 bands together with a slightly wider D1.

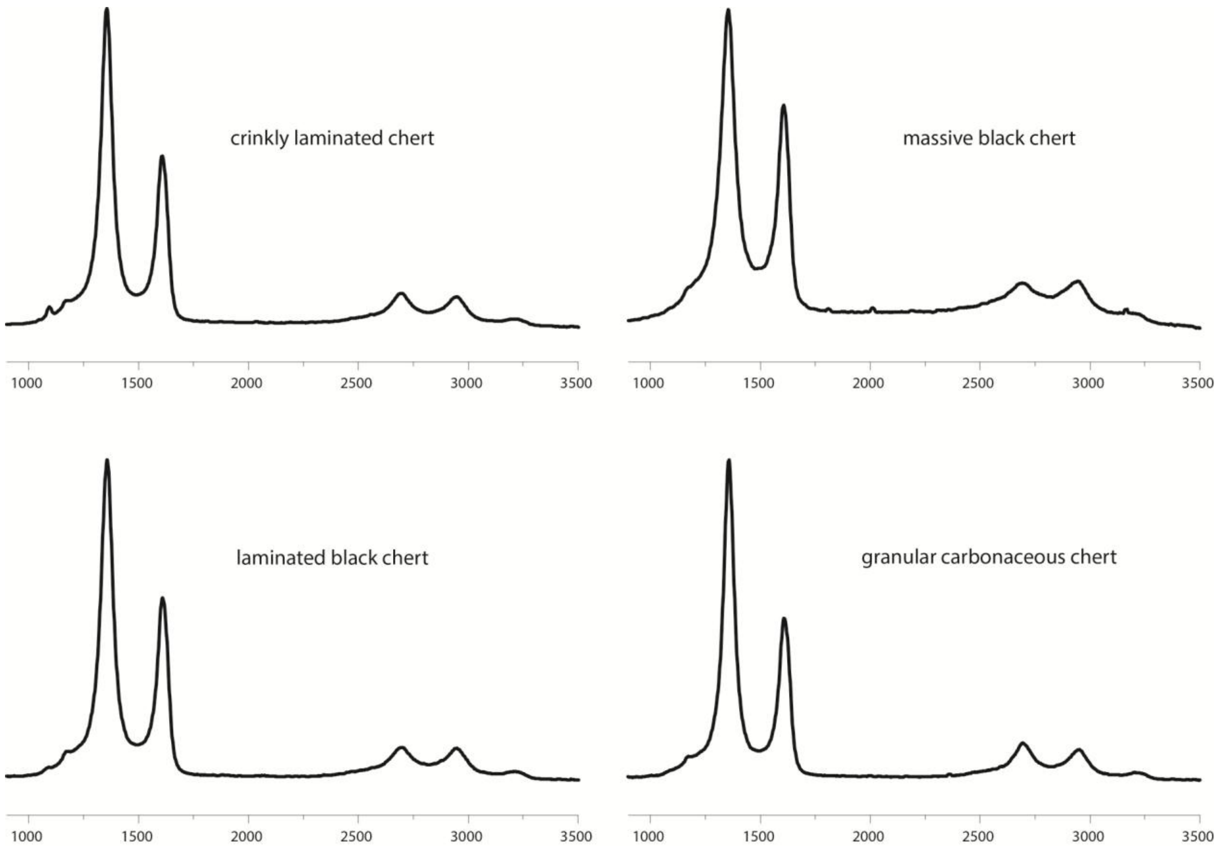

Figure 4.3 – Comparison of the average Raman signal obtained by the sum of all spectra reported in S2 for each BARB3 facies (at least 25 spectra par facies). All the spectra show a striking similarity in their profile, nevertheless the massive black chert has a higher G intensity as well as more developed D3 and D4 bands.

Out of several possible fitting models a five-curves deconvolution protocol, such as that proposed by Sadezky et al. (2005), best fits the analyzed BARB3 CM resulting in the highest adjusted-R^2 values (which in Origin represent the parameter estimating the fitting accuracy whereas the perfect fitting result in adjusted-R^2= 10). The first-order carbonaceous spectra are thus decomposed into four Lorentzian at about 1199 cm^{-1} (D4), 1355 cm^{-1} (D1), 1604 cm^{-1} (G), 1626 cm^{-1} (D2) and a Gaussian at ~1544 cm^{-1} (D3). The most significant bands parameters and calculated ratios obtained after spectra deconvolution are here reported as average values by sample (Tab. 4.2), by facies (Tab. 4.3) and by carbonaceous microtexture

(Tab. 4.4). Parameters and ratios for each decomposed spectra can be found in the supplementary material (Supplementary material S2).

Kouketsu et al. (2014) proposed a five-curves fitting (called Fitting E), similar to the one used here, as the most appropriate for sedimentary CM that experienced peak metamorphic temperatures ranging between 300 and 340°C. In agreement with such evidence and with the overall spectral similarity to CM subjected to greenschist facies metamorphism (Yui et al., 1996) we used two CM Raman geothermometers calibrated for low-metamorphic rocks. The first, proposed by Beyssac et al. (2002), works best at temperatures ranging between 330 and 650 °C and relies on the ratio R_2 (1) and its relation with temperature expressed in (2).

$$R_2 = A_{D1}/(A_{D1} + A_{D2} + A_G) \qquad (1)$$

with

$$T = -445 * R_2 + 641 \ (\pm 50°C) \qquad (2)$$

The second, proposed by Kouketsu et al. (2014), works for temperatures ranging between 150 and 400 °C and consists of two possible equations (3), (4) in which the metamorphic temperature is correlated to the full-width at half maximum intensity (FWHM) of D1 and D2.

$$T\ (°C) = -2.15\ (FWHM\text{-}D1) + 478\ (\pm 30°C) \qquad (3)$$

and

$$T\ (°C) = -6.78\ (FWHM\text{-}D2) + 535\ (\pm 50°C) \qquad (4)$$

Average temperatures calculated for the whole dataset correspond to 326 ± 50 °C (2), 337 ± 50°C (3) and 361± 50 °C (4) respectively. The three Raman geothermometers (Beyssac et al., 2002, Kouketsu et al., 2014) show a metamorphic imprint that falls within the lower greenschist metamorphic temperature range (Tab. 4.2, 4.3, 4.4 and S2), coherently with the thermal history of the Onverwacht Group (Tice et al., 2004).

Several characteristics of all the fitted spectra including (i) the regular presence of well developed D3 and D4 bands, (ii) the prevailing D1 intensity on G, (iii) the D1 width range $FWHM_{D1}$= ~53-93 cm^{-1} (~65 cm^{-1} on average) and (iv) the I_D/I_G range R_1= 1.36-2.62 (2.07 in average) are consistent with poorly ordered CM typical of low-greenschist Archaean metasediments (Delarue et al., 2016; Sforna et al., 2014). All the analyzed material fits well with the Archaean carbonization continuum proposed by Delarue et al., (2016), as the BARB3 material situates at high R1 values (Fig. 4.4), almost at the limits of the carbonization/graphitization continuum, consistent with previously analyzed CM from the Kromberg and Hooggenoeg formations (Delarue et al., 2016; Hofmann et al., 2013). The BARB3 CM thus appears to consists of very poorly organized (developed D4) stacks of nanometric, polyaromatic, graphene-like layers characterized by out of plane defects (D3) (Beyssac et al., 2003), corresponding to a carbonaceous structural grade which reached the end phases of the carbonization process (Charon et al., 2014; Delarue et al., 2016).

All investigated CM has a geothermal imprint and a crystallinity level that is consistent with the degree of organization usually found in CM from Archaean terrains of comparable metamorphic grade (Delarue et al., 2016; Marshall et al., 2007; Sforna et al., 2014) confirming the BARB3 CM Archaean authenticity.

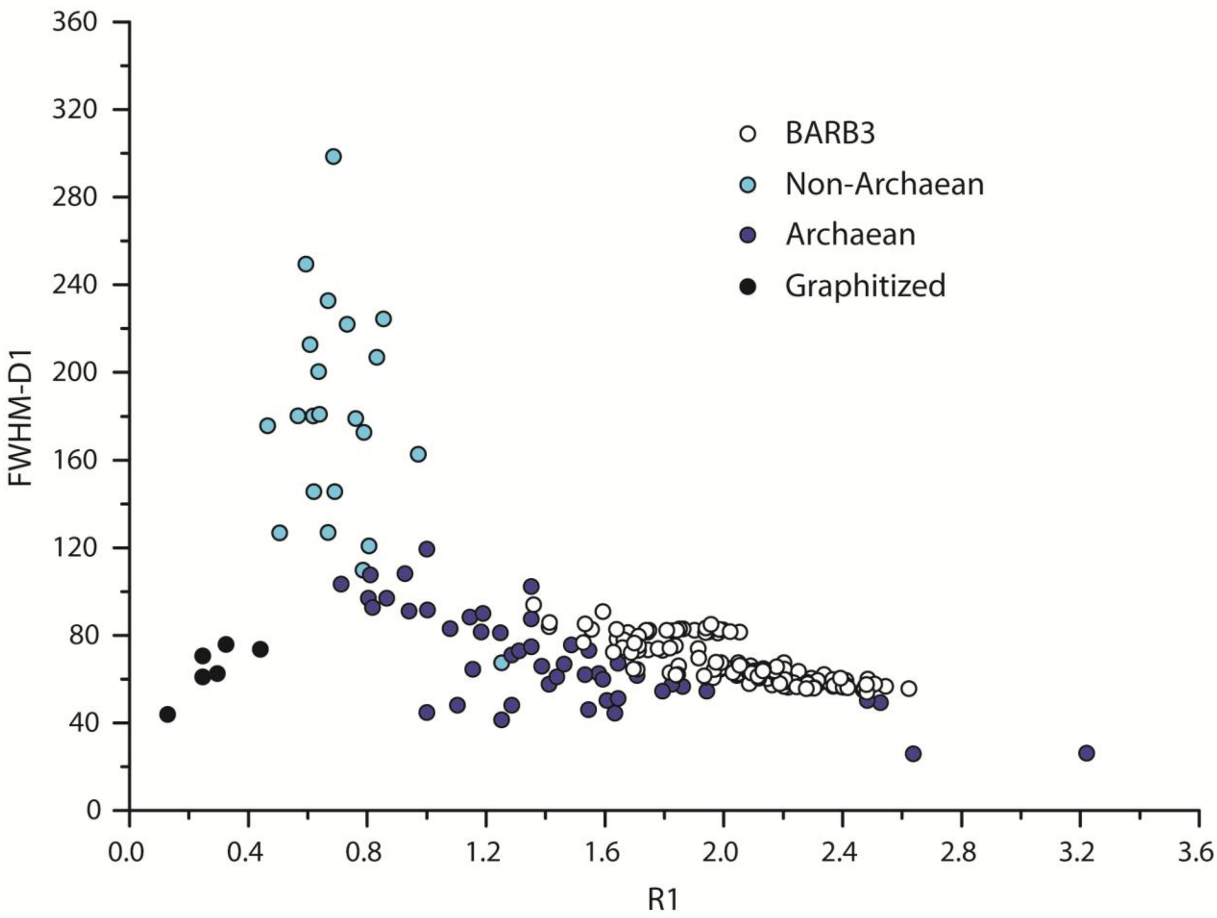

Figure 4.4 – Compilation of R1 ratio and FWHM-D1 representing the Raman-derived carbonization continuum showing evolution of Archaean and Non-Archaean CM with structural disorder. Modified from Delarue et al., 2016.

Table 4.2 – Raman parameters and ratios calculated by sample

Sample	Facies	ω_{D1}	Γ_{D1}	ω_G	Γ_G	R_1	$\Gamma_{D1/G}$	$I_{D1}/(I_{D1}+I_G)$	A_{D1}/A_G	R_2 (1)	ΔT C° (3)	R_{D3} (5)	R_{D4} (6)
D11A	**Crinkly laminated chert**	1355,48	60,04	1603,57	43,89	2,19	1,37	0,69	3,01	0,70	349,92	0,05	0,05
	σ	0,24	3,05	1,16	2,03	0,16	0,10	0,02	0,28	0,01	6,55	0,01	0,00
C3A	**Crinkly laminated chert**	1356,66	60,52	1604,23	44,20	2,23	1,37	0,69	3,05	0,71	348,89	0,06	0,05
	σ	0,70	4,31	1,04	1,41	0,20	0,10	0,02	0,21	0,01	9,27	0,01	0,01
D1	**Crinkly laminated chert**	1354,05	80,59	1603,98	42,26	1,85	1,91	0,65	3,50	0,72	305,73	0,10	0,07
	σ	0,55	4,12	0,99	2,46	0,15	0,16	0,02	0,46	0,02	8,85	0,01	0,01
C9E	**Massive black chert**	1354,01	74,55	1603,83	46,02	1,72	1,63	0,63	2,79	0,69	318,72	0,08	0,07
	σ	1,55	8,96	1,72	4,18	0,14	0,20	0,02	0,39	0,02	19,26	0,02	0,01
C2C	**Laminated black chert**	1356,52	62,73	1605,37	42,00	2,14	1,49	0,68	3,16	0,71	344,13	0,06	0,06
	σ	0,57	7,11	0,84	1,79	0,26	0,13	0,03	0,26	0,01	15,28	0,01	0,01
D4A	**Granular carbonaceous chert**	1356,61	60,08	1604,64	42,74	2,23	1,41	0,69	3,13	0,71	349,83	0,05	0,05
	σ	0,46	4,82	0,61	1,33	0,18	0,11	0,02	0,19	0,01	10,35	0,01	0,01

Table 4.3 – Raman parameters and ratios calculated by facies. Crinkly laminated chert is further calculated excluding the bitumen-like sphere. Laminated black chert is calculated excluding the bitumen-like CM from cross-cutting veins.

Facies	ω_{D1}	Γ_{D1}	ω_G	Γ_G	R_1	$\Gamma_{D1/G}$	$I_{D1}/(I_{D1}+I_G)$	A_{D1}/A_G	R_2 (1)	ΔT C° (3)	R_{D3} (5)	R_{D4} (6)
Crinkly laminated chert (all)	**1355,40**	**66,85**	**1603,92**	**43,46**	**2,09**	**1,55**	**0,6747**	**3,18**	**0,7112**	**335,27**	**0,0662**	**0,0640**
σ	1,18	10,30	1,09	2,16	0,24	0,28	0,0261	0,40	0,0145	22,15	0,0227	0,0285
Mats-Grains	1356,05	60,27	1603,89	44,04	2,21	1,37	0,6874	3,03	0,7051	349,43	0,0521	0,0590
σ	0,79	3,67	1,14	1,75	0,18	0,10	0,0180	0,25	0,0071	7,90	0,0082	0,0335
Bitumen-like	1354,05	80,59	1603,98	42,26	1,85	1,91	0,6482	3,50	0,7239	305,73	0,0956	0,0744
σ	0,55	4,12	0,99	2,46	0,15	0,16	0,0196	0,46	0,0176	8,85	0,0126	0,0053
Massive black chert	**1354,01**	**74,55**	**1603,83**	**46,02**	**1,72**	**1,63**	**0,6320**	**2,79**	**0,6930**	**318,72**	**0,0801**	**0,0716**
σ	1,55	8,96	1,72	4,18	0,14	0,20	0,0200	0,39	0,0205	19,26	0,0173	0,0080
Laminated black chert (all)	**1356,52**	**62,73**	**1605,37**	**42,00**	**2,14**	**1,49**	**0,6788**	**3,16**	**0,7108**	**344,13**	**0,0601**	**0,0572**
σ	0,57	7,11	0,84	1,79	0,26	0,13	0,0303	0,26	0,0093	15,28	0,0146	0,0099
Grains	1356,69	60,46	1605,24	41,62	2,22	1,45	0,6886	3,22	0,7132	349,02	0,0553	0,0541
σ	0,33	3,15	0,74	1,40	0,13	0,08	0,0127	0,20	0,0061	6,76	0,0065	0,0045
Bitumen-like XcV	1355,25	79,41	1606,31	44,84	1,55	1,77	0,6067	2,71	0,6937	308,28	0,0953	0,0799
σ	0,16	5,32	1,15	2,02	0,14	0,08	0,0220	0,26	0,0116	11,43	0,0008	0,0090
Granular carbonaceous chert	**1356,61**	**60,08**	**1604,64**	**42,74**	**2,23**	**1,41**	**0,6896**	**3,13**	**0,7084**	**349,83**	**0,0539**	**0,0532**
σ	0,46	4,82	0,61	1,33	0,18	0,11	0,0172	0,19	0,0071	10,35	0,0085	0,0058

Table 4.4 – Raman parameters and ratios calculated by microtexture. Crinkly laminated chert (clc), massive black chert (mbc), laminated black chert (lbc), granular carbonaceous chert (gcc).

CM microtexture	Facies	Sample	ω_{D1}	Γ_{D1}	ω_G	Γ_G	R_1	$\Gamma_{D1/G}$	$I_{D1}/(I_{D1}+I_G)$	A_{D1}/A_G	R_2 (1)	ΔT C° (3)	R_{D3} (5)	R_{D4} (6)
Mat-like laminae	Clc	D11A	1355,57	57,81	1603,12	44,42	2,28	1,30	0,6944	2,98	0,7023	354,70	0,0456	0,0522
		σ	0,26	1,71	0,77	1,96	0,12	0,06	0,0107	0,25	0,0070	3,68	0,0063	0,0045
Grain	Clc	D11A	1355,37	62,45	1604,06	43,31	2,09	1,44	0,6760	3,03	0,7061	344,74	0,0533	0,0570
		σ	0,16	2,20	1,34	2,02	0,15	0,07	0,0160	0,32	0,0078	4,73	0,0056	0,0043
Mat-like laminae	Clc	C3A	1356,75	58,09	1603,77	44,25	2,33	1,31	0,6996	3,08	0,7066	354,10	0,0515	0,0504
		σ	0,78	1,61	0,85	1,66	0,13	0,05	0,0116	0,24	0,0078	3,47	0,0057	0,0043
Grain	Clc	C3A	1356,47	66,06	1605,30	44,07	2,00	1,50	0,6664	2,99	0,7054	336,97	0,0634	0,0622
		σ	0,48	3,19	0,51	0,60	0,12	0,06	0,0144	0,09	0,0026	6,87	0,0081	0,0047
Bitumen-like	Clc	D1	1354,05	80,59	1603,98	42,26	1,85	1,91	0,6482	3,50	0,7239	305,73	0,0956	0,0744
		σ	0,55	4,12	0,99	2,46	0,15	0,16	0,0196	0,46	0,0176	8,85	0,0126	0,0053
Bitumen-like	Mbc	C9E	1353,47	79,75	1603,59	46,07	1,67	1,74	0,6250	2,89	0,6990	307,55	0,0889	0,0722
		σ	1,65	6,96	2,06	4,89	0,15	0,13	0,0208	0,41	0,0202	14,96	0,0153	0,0087
Interstitial	Mbc	C9E	1354,48	72,06	1604,21	43,21	1,77	1,67	0,6390	2,94	0,6970	324,08	0,0776	0,0679
		σ	1,18	2,82	1,41	1,41	0,12	0,06	0,0158	0,22	0,0010	6,06	0,0064	0,0020
Cloudy	Mbc	C9E	1355,02	63,66	1604,20	47,29	1,82	1,35	0,6448	2,47	0,6769	342,13	0,0606	0,0719
		σ	0,86	1,60	0,87	2,70	0,10	0,08	0,0128	0,26	0,0191	3,44	0,0046	0,0087
Grain	Lbc	C2C	1356,69	60,46	1605,24	41,62	2,22	1,45	0,6886	3,22	0,7132	349,02	0,0553	0,0541
		σ	0,33	3,15	0,74	1,40	0,13	0,08	0,0127	0,20	0,0061	6,76	0,0065	0,0045
Bituminous-XcV	Lbc	C2C	1355,25	79,41	1606,31	44,84	1,55	1,77	0,6067	2,71	0,6937	308,28	0,0953	0,0799
		σ	0,16	5,32	1,15	2,02	0,14	0,08	0,0220	0,26	0,0116	11,43	0,0008	0,0090
Mat-like network	Gcc	D4A	1356,88	56,24	1604,74	42,61	2,34	1,32	0,7003	3,11	0,7079	358,08	0,0485	0,0489
		σ	0,24	1,05	0,59	1,06	0,11	0,04	0,0104	0,18	0,0078	2,26	0,0045	0,0019
Grain	Gcc	D4A	1356,34	63,92	1604,53	42,87	2,12	1,49	0,6789	3,15	0,7089	341,58	0,0592	0,0575
		σ	0,47	3,92	0,63	1,58	0,16	0,10	0,0160	0,21	0,0067	8,42	0,0083	0,0051
Mat-like			**1356,45**	**57,38**	**1603,91**	**43,74**	**2,32**	**1,31**	**0,6983**	**3,06**	**0,7058**	**355,64**	**0,0488**	**0,0504**
		σ	0,76	1,67	0,98	1,76	0,12	0,05	0,0110	0,23	0,0078	3,59	0,0059	0,0039
Grains - Cloudy			**1356,16**	**62,62**	**1604,75**	**43,08**	**2,11**	**1,46**	**0,6770**	**3,07**	**0,7064**	**344,36**	**0,0573**	**0,0606**
		σ	0,74	3,55	0,97	2,29	0,18	0,09	0,0189	0,31	0,0130	7,63	0,0074	0,0070
Bituminous - Interstitial			**1353,98**	**79,64**	**1604,03**	**43,75**	**1,77**	**1,83**	**0,6371**	**3,21**	**0,7118**	**307,78**	**0,0921**	**0,0736**
		σ	1,14	5,49	1,56	3,74	0,17	0,17	0,0235	0,52	0,0217	11,81	0,0135	0,0070

4.1.2 BARB3 CM structural heterogeneity

Although all the Raman spectra collected during this study show a striking similarity in their profiles, some structural differences in the CM do occur and is apparent by slight changes in the relative intensity and width of select peaks (Fig. 4.3). Such changes can be better resolved by a comparison between parameters and ratios calculated after deconvolution. Particularly, it has been shown that for the low-greenschist range of metamorphic conditions a combination of $FWHM_G$, R_1 (I_{D1}/I_G) and $I_{D1}/I_{D1}+I_G$, rather than just $R_{1,}$ which alone becomes unreliable for this grade of CM maturation (Ferrari and Robertson, 2000). This combination of ratios is a good proxy for variations in CM maturity, with $FWHM_G$ decreasing and R_1 and $I_{D1}/I_{D1}+I_G$ increasing with increasing order (Jehlička et al., 2003; Allwood et al., 2006). Ratios including A_{D1}/A_G, R_{D3} (I_{D4}/I_{D1}) and R_{D4} (I_{D3}/I_{D1}), together with R_1 and R_2 allows the heterogeneity in the BARB3 CM type of maturation to be estimated (Yui et al., 1996; Beyssac et al., 2003; Sforna et al., 2014; Delarue et al., 2016). Similar results can be observed also for $FWHM_D$ and $FWHM_D/FWHM_G$ against R_1, whereas the variation of peak widths as a function of the R_1 ratio is sensitive to variations in the structure of poorly organized CM of the type found in Archean rocks (Sforna et al., 2014; Delarue et al., 2016). Combinations of such parameters and ratios can be used to fully appreciate CM heterogeneities.

Here, possible structural differences in the BARB3 CM are tested through three consecutive steps in order to explore the carbonaceous heterogeneity between samples, between facies and finally between microtextures. To do so, ratios and parameters described above have been used together with $FWHM_{D1}/_G$-vs-R_1 and $FWHM_{D1}$-vs-R_1 plots for sample (Tab. 4.2, Fig. 4.5), facies (Tab. 4.3, Fig. 4.6) and microtexture (Tab. 4.4, Fig. 4.7) levels.

At the sample scale the $FWHM_{D1}/_G$-vs-R_1 plot (Fig. 5.4) is very chaotic and the measurements obtained for each thin section greatly overlap with the only partial exception of D1 and C9E. Those two samples show lower R_1 and higher $FWHM_{D1}/_G$ ($\Gamma_{D1/G}$) values together with the highest R_{D3} and R_{D4} (Tab. 4.2). This suggests that D1 and C9E host CM with a lower structural order. However, the CM signal in D1 derives from the bituminous-like blobs that only occur in this crinkly laminated chert sample. C9E instead is representative of the massive black chert with its unique bituminous and interstitial dense textures. Thus the two samples strongly differentiate from the other investigated thin sections in term of microstructure and facies respectively. At the same time other samples belonging to the same facies or including similar microtextures, such as D11A and C3A, greatly overlap, suggesting the absence of a merely between-sample heterogeneity.

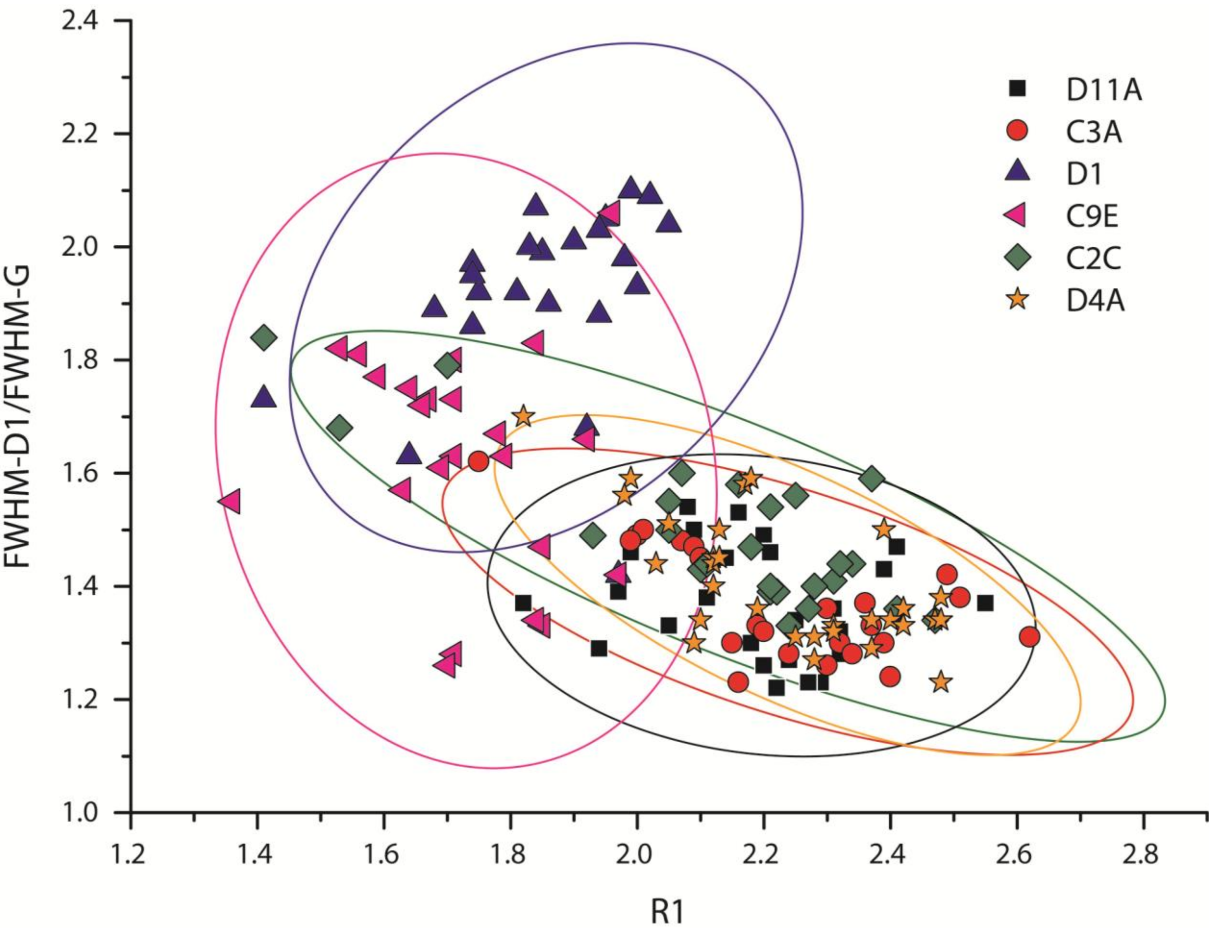

Figure 4.5 – $FWHM_{D1/G}$-vs-R_1 plot showing between-sample variability. 95% confidence ellipses are marked for each sample.

A better understanding of the BARB3 carbonaceous heterogeneity can be obtained when comparing CM from the different depositional facies (Fig. 4.6). Although the crinkly laminated chert shows a very wide scatter of values, it can be observed that this actually consists of two distinct groups. One group showing higher $\Gamma_{D1/G}$ and lower R_1 values is defined entirely by the bituminous-like CM of the D1 sample which is atypical in the crinkly laminated facies and shows no evidence of primary deposition. A similar reasoning can be presented for the highest $\Gamma_{D1/G}$ and lowest R_1 values observed for the laminated black chert whereas those derived from the measurements taken on the bitumen-like CM found in crosscutting veinlets, which are ubiquitous in the BARB3 and not confined to this depositional facies. In both the crinkly laminated and laminated black chert, when excluding the bituminous CM from parameters and ratios calculations, the facies resulted in values of $\Gamma_{D1/G}$ and R_1 displaying a dramatically reduced standard deviation (Tab. 4.3). Thus, although this suggests a role of the microtexture analyzed, it also highlights that a between-facies heterogeneity may exist. When the bituminous material is excluded, the crinkly laminated

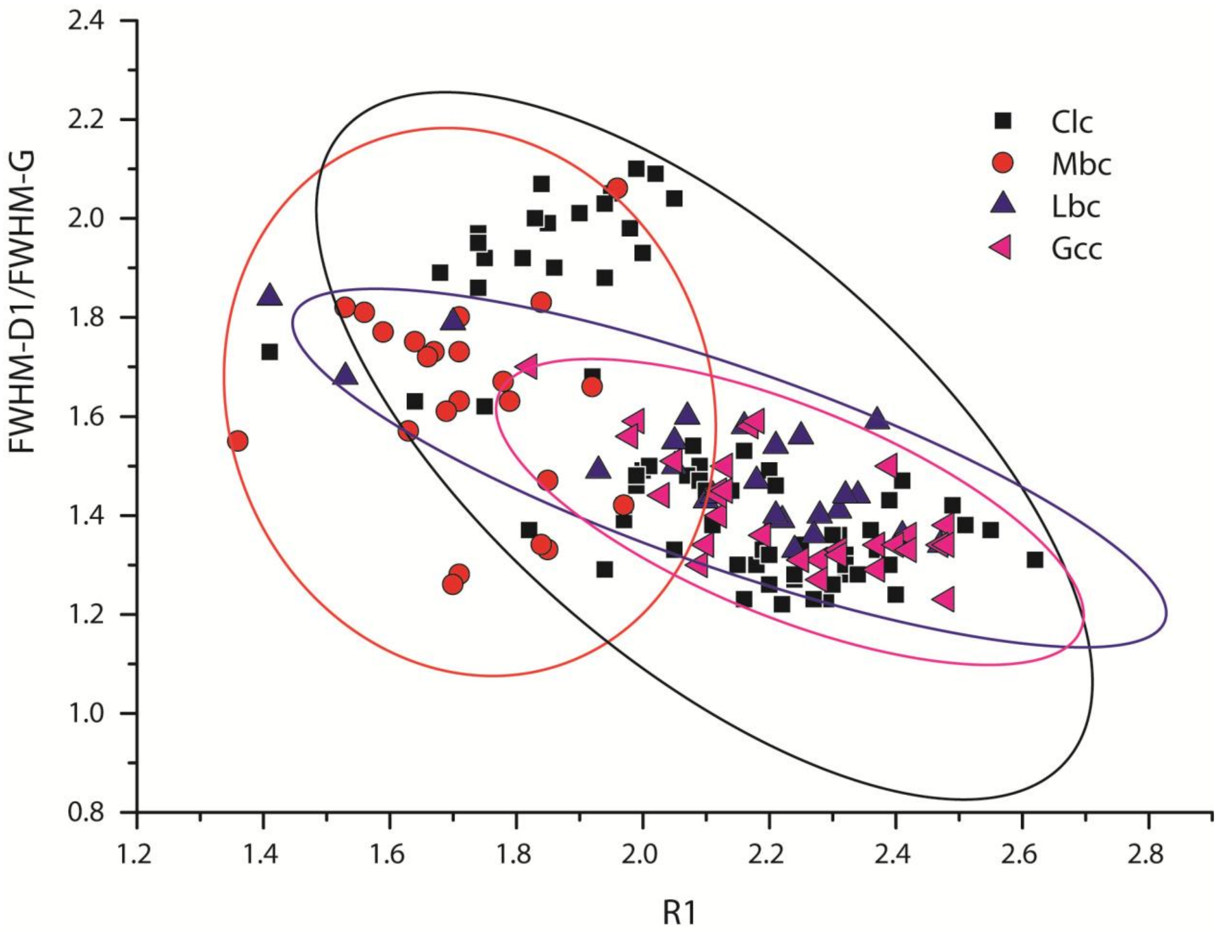

Figure 4.6 – $FWHM_{D1}/_{G}$-vs-R_1 plot showing between-facies variability. 95% confidence ellipses are marked for each facies. Crinkly laminated chert (Clc), Massive black chert (Mbc), Laminated black chert (Lbc); Granular carbonaceous chert (Gcc).

chert, laminated black chert and granular carbonaceous chert group together and with the exception of the black massive chert, most likely reflect depositional differences described in the previous chapter. The peculiarity of the black massive facies suggests a comparison with hydrothermal veins rather than primary sedimentary deposits.

By exploring the possible between-sample and between-facies heterogeneity it has already been suggested that CM microtextures may also have a role in the distribution of parameter and ratio values. As illustrated at the beginning of the chapter the CM microtextures observed in the BARB3 shallow-platformal deposits can be defined as three major entities: bituminous-like or interstitial CM, carbonaceous grains and mat-like structures (laminae and network). It is this categorization, proposed after the core facies interpretation and sample minero-petrographic characterization, that show the best correlation with the range of structural disorder expressed by the analyzed CM. As observed in the $FWHM_{D1}/_{G}$-vs-R_1 plot (Fig. 4.7), such microtexture outlines three well-defined clusters in the data

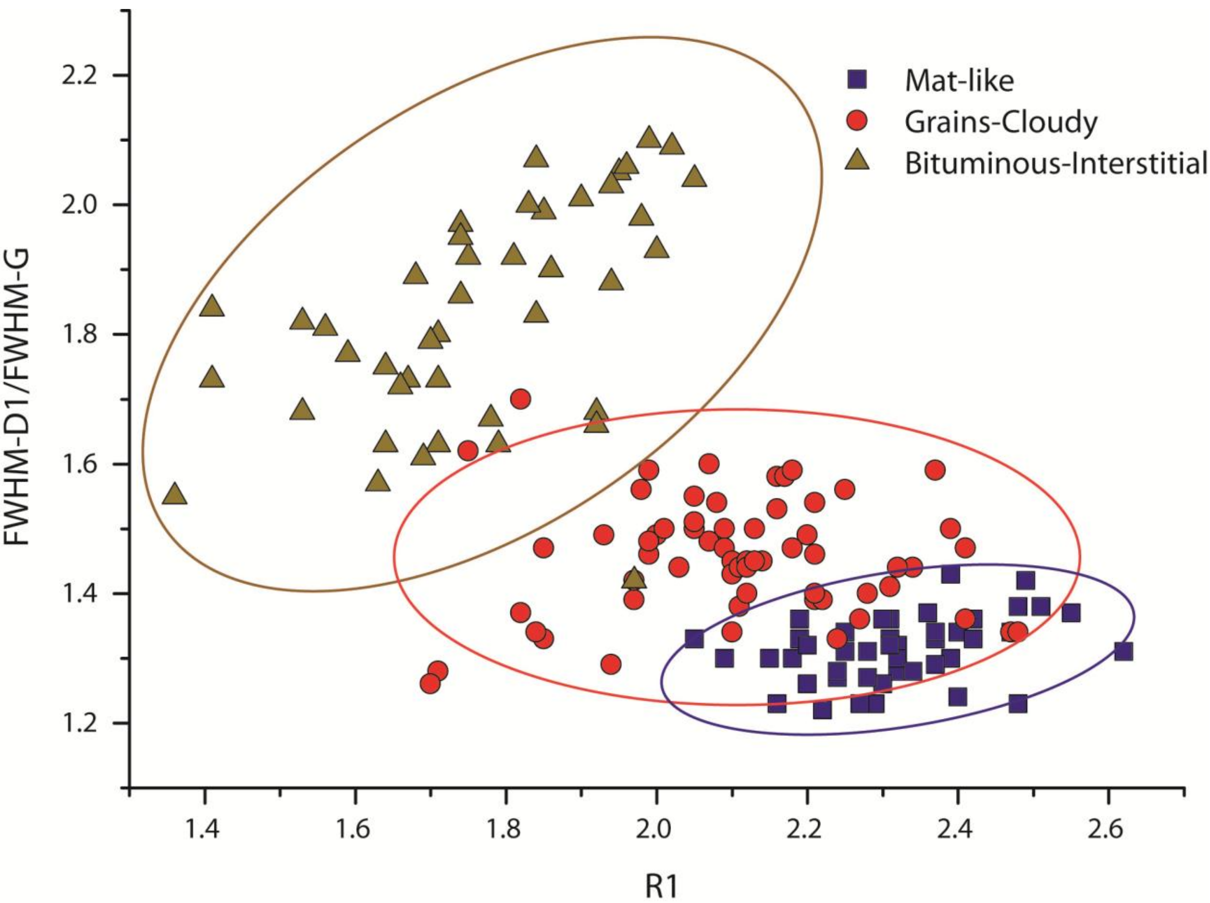

Figure 4.7 – $FWHM_{D1/G}$-vs-R_1 plot showing between-microtexture variability. 95% confidence ellipses are marked for each CM microtexture.

scattering. Similar results are obtained for the $I_{D1}/I_{D1}+I_G$, A_{D1}/A_G, R_2, R_{D3} and R_{D4} ratios (Tab. 4.4) and results have low standard deviations indicating a reliable grouping of the microtextures. The three defined clusters consist of: (I) microbial mat-like laminae and carbonaceous network from the crinkly laminated chert and the granular carbonaceous chert (botryoidal vein), respectively; (II) CM-rich individual grains from the crinkly laminated facies, the laminated black chert, the sandy carbonaceous material occurring within the granular chert but also the diffuse cloudy CM forming putative grains within the black massive facies; and (III) CM which is observed as structureless material in the form of smooth spheres, blobs, or as an interstitial, vein filling substance suggesting it was originally part of a fluid carbonaceous rich phase. Such between-microtexture heterogeneity indicates that different carbonaceous morphologies correspond to a different chemical structure and has implications concerning the origin of the BARB CM and the depositional relations between the carbonaceous rich facies.

4.1.3 Possible sources for the BARB3 CM heterogeneity

The degree of order reached by natural CM during its irreversible maturation within meta-sedimentary rocks is reflected by the characteristics of its Raman spectrum and depends mainly on the metamorphic P-T conditions and on the nature of the original carbonaceous precursor (Yui et al., 1996; Beyssac et al., 2002). In light of such correlations Raman spectroscopy has been used to reconstruct the metamorphic history of CM-hosting rocks and to investigate the degree of its structural disorder and heterogeneity (Beyssac et al., 2003; Lahfid et al., 2010; Marshall et al., 2012; Kouketsu et al., 2014). However caution must be taken when investigating the structure of CM through Raman spectroscopy as some steps in the analytical procedures can potentially introduce extrinsic variability. Thus before exploring possible causes for the BARB3 CM heterogeneity some preliminary consideration must be given with regards to the experimental approach.

During this study a low laser power (3 mW) was used focusing only on CM structures embedded in quartz below the thin section surface to avoid sample heating (Everall et al., 1991) and excluding a contribution to CM defect by surface polishing (Beyssac *et al.*, 2003). Due to the anisotropic character of graphite-like materials, in Raman spectroscopy a preferential orientation of the analyzed CM with respect to the incoming laser radiation can result in a structural sampling bias. All discrete CM analyzed during this study consists of concentrations of sub-micron sized particles interweaved between the chert grains showing no preferential orientation in space, as will be illustrated also in the following CM nanotexture section. The overall similarity of all collected spectra allowed the application of a consistent linear baseline correction and the fitting through the same deconvolution model applied with no fixed parameters, leading to highly comparable results (Beyssac et al., 2003; Lünsdorf et al., 2014). The quality of fitting has been evaluated visually and based on the adjusted-R^2 values, which in the Origin software reflects the goodness of the deconvolution; poorly fitted spectra have been excluded from any calculation or discussion. Thus, minimizing and excluding extrinsic inputs, allowing for a reliable reading of CM intrinsic structural heterogeneity.

4.1.3.1 Structural divergence of the massive black chert

When scrutinizing possible sources for the facies and microtextural-related structural heterogeneity observed in the BARB3 CM, it is important to consider, perhaps counter

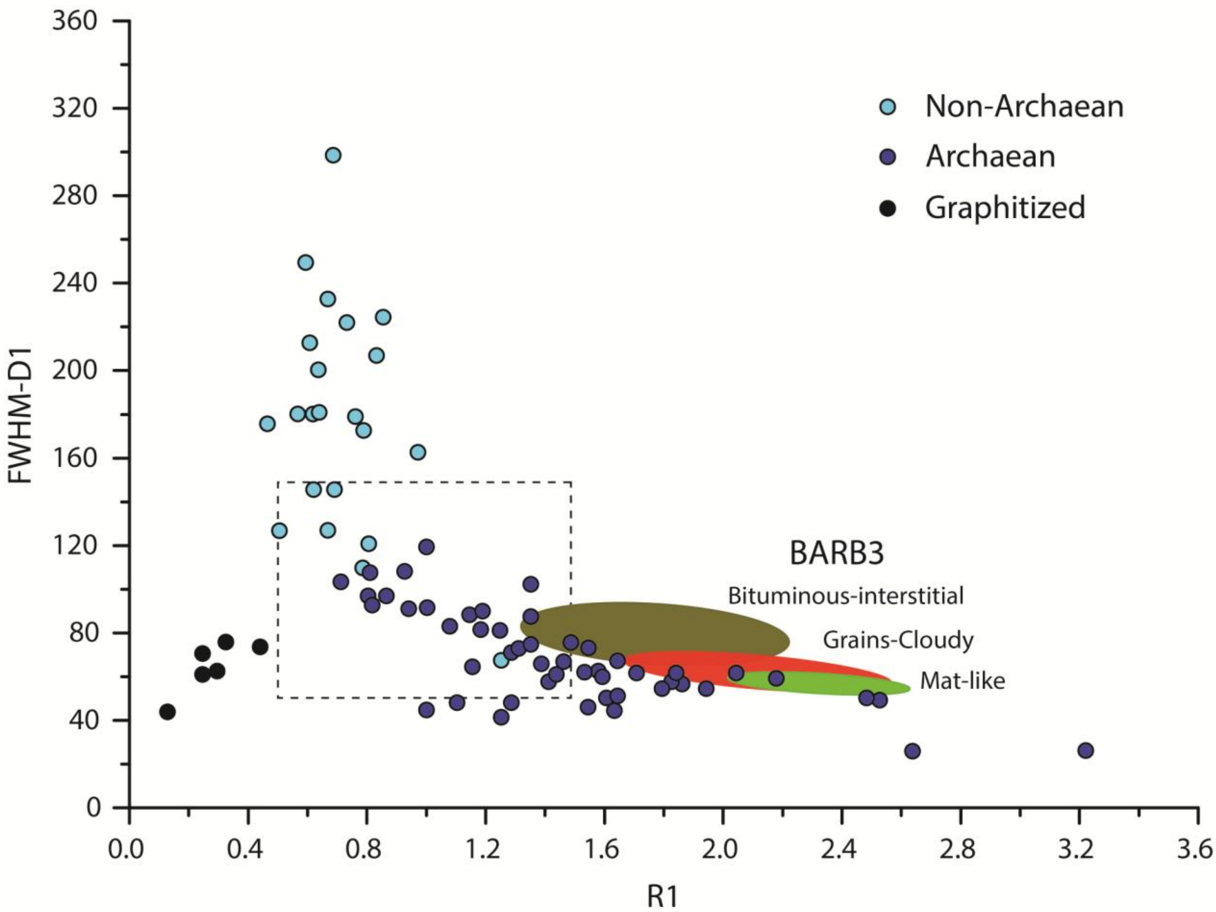

Figure 4.8 – Compilation of R1 ratio and FWHM-D1 representing the Raman-derived carbonization continuum showing evolution of Archaean and Non-Archaean CM with structural disorde. The cluster related to the main three microtexture groups observed in the BARB3 are marked with their respectively 95% confidence ellipses. Modified from Delarue et al., 2016

intuitively, that the exquisitely preserved mat-like laminae, and the carbonaceous network, show the higher grade of structural order when compared to the grains and the structureless bituminous and interstitial CM. This can be observed by superimposing the three clusters (defined by their 95% confidence ellipses, Fig. 4.8) onto the Archaean carbonization continuum developed by Delarue et al. (2016). Furthermore, the carbonaceous grains and mat-like structures greatly overlap so that the structural distinction is greater between those primary microtextures and the structureless CM.

Probably deriving from an originally viscous hydrocarbon phase (Buick, 1990; He et al., 2015; Suárez-Ruiz et al., 2016), bituminous and dense interstitial CM occur mainly in the BARB3 massive black facies. This facies has been here interpreted as either a massive carbonaceous hydrothermal vein or as an hydrothermally influenced deposit. Using equation (3), which is the more accurate in the 200-400 °C range (Kouketsu et al., 2014), it can be seen that, although still falling within the range of error of ± 50°C, the massive black chert is the facies that dissociates most from the average values, resulting in a temperature of 318 ± 50°C

(3) (Tab. 4.3). Similar values were obtained from the analysis on the bitumen-like material from sample D1 and from the cross-cutting veinlets (Tab. 4.3). However the massive black facies also includes diffuse cloudy CM that instead has a structural order and geothermal imprint comparable to that of the grains and mat-like structures observed in the other chert facies (Tab. 4.4). Thus the massive black chert, includes at least two categories of carbonaceous microtextures bearing a very diverse structural order.

4.1.3.2 Carbonaceous grains vs carbonaceous mats

CM-rich laminae observed in the crinkly laminated ferruginous chert shows features consistent with fossil and modern benthic microbial mats. Most notably their plastic behaviour, cohesiveness and morphologies produced by the interaction of mats with pervading fluids and gentle currents in low energy aquatic environments (Eriksson et al., 2007; Walsh, 2010; Tice et al., 2011). Morphological evidence suggesting an original plastic and cohesive carbonaceous nature have also been observed in the carbonaceous networks that drapes the colloform precipitate on top of the granular carbonaceous material. Furthermore such CM-rich networks show evidence for possible trapping and binding behaviour, usually observed in modern mats in siliciclastic environments (Eriksonn et al., 2007; Noffke, 2010). The interpretation of those carbonaceous microtextures as possible microbial mats is strengthened by the extremely similar structural order of their constitutive CM as shown by Raman analyses (Tab. 4.4). The analyzed structures, other than bearing exquisitely preserved mat-like morphologies, come from different depth along the core, yet show an almost perfect overlapping in their structural features forming a very well defined cluster in the $FWHM_{D1}/_{G}$-vs-R_1 and $FWHM_{D1}$-vs-R_1 plots (Fig. 4.7 and 4.8). In this case the CM structural homogeneity can be more readily correlated to a common microbial molecular precursor.

Carbonaceous fluffy grains resemble clotted amorphous microbial remains observed in younger sediments (Fayers and Trewin, 2003; Trewin et al., 2003) and occur in association with mat-like laminae within the crinkly laminated chert. However, they are particularly abundant in the laminated black chert, where no evidence of mat-constructors has been observed. They are also possibly within the massive black chert, which is now disrupted by diffuse carbonaceous material, as suggested by the structural similarities between the grains and the cloudy material occurring in sample C9E (Tab. 4.4). Although there is a lack of evidence to provide better constrains on the origin of the carbonaceous grains, the occurrence of such clots within all the characterized facies and their clustering observed after Raman investigation suggest that all the CM-rich grains may share a common origin, and that their precursor differ at least to a small extent, and it is wider than the molecular pool of the mat-like structures.

4.2 Carbonaceous nanotexture of potential microbial mats

Simple and high-resolution (HR-) transmitted electron microscopy (TEM) allow *in-situ* high-resolution microscopy and microanalyses on the BARB3 CM, providing complementary results to the minero-petrography and Raman investigation. Particularly TEM is used to explore the CM features and distribution within the different microtextures at the nano-scale, while HR-TEM analyses allow the characterization of the CM nanotexture (or nanostructure) which is the mutual organization in space of the constitutive nanometric polyaromatic C-rich sheets forming the carbonaceous matter lattice. During HRTEM imaging, the profiles of individual polyaromatic planes are visualized as dark fringes and various parameters can be measured including their length, curvature, tortuosity and the inter-layer distance in the basic structural units (BSU) (Olcott Marshall et al., 2014; Apicella et al., 2015; Deldicque et al., 2016). As the carbonaceous nanotexture and lattice characteristics are dependent on the maturational process of the original carbonaceous precursor and its nature, HRTEM represent an important tool in ancient CM studies. A further advantage of CM high resolution studies is the possibility to discriminate minerals in the form of nanoparticles associated with the carbonaceous lattice, as the results could give insights concerning the original rock protholite and depositional conditions (Rasmussen et al., 2017) or into possible metabolic pathways exploited by microbial communities that are now represented in the form of carbonaceous remains (Westall et al., 2011). TEM and HRTEM analyses have been conducted on mat-like CM-rich laminae-sets from the crinkly laminated chert (sample F13B) and on the CM-rich network (sample C6D), found on top of the black granular chert, which has been interpreted as a possible microbial mat as supported by Raman analyses. Consequently, both potential microbial structures are explored here with the aim of investigating their nanotexture and to potentially discriminate minerals in the form of nanoparticles that could strengthen the microbial interpretation and suggest possible exploited metabolic pathways.

4.2.1 Carbonaceous lamina-sets vs carbonaceous networks

At TEM dark-field imaging FIB-lamellae from both microtextures (Fig. 4.9a and 4.10a) are characterized by the association between sparse CM nanometre-sized elongated clots (lower ass, dark grey) and quartz grains (higher mass, light grey) ranging in size from less than 1 μm up to about 10 μm wide. The CM appear interweaved between the chert crystals in a distribution which following the boundaries between the grains is consistent with the carbonaceous discontinuity already observed at the optical microscope scale (at 40X) and suggest that even for such well preserved microtextures a certain level of CM redistribution probably occurred. However both the network and lamina-sets-forming CM is characterized by a contact with the adjacent quartz grains which is non-linear but rather cuspate (Fig. 4.9b,c and 4.10b,c). At this contact the CM show patches of lighter grey due to the presence of low levels of silica or pervasive quartz nano-grains. Such non-linear partially silicified carbonaceous margins at the contact with the quartz crystals suggest that quartz nucleation started from the CM. This indicate that both the network and lamina-set where present prior to the silicification supporting their origin *in-situ* and thus their biogenicity rather than a remobilized CM trapping after chert crystallization (Brasier et al., 2002, 2005). On the other hand in the CM network nanotexture is possible to observe the presence of CM clots internal to the chert grains having a sub-spherical shape and characterized by regular margins at the contact with the surrounding quartz (Fig. 4.10a, Fig.4.11a,b). Such features suggest the presence of a CM remobilized phase which was trapped forming CM-rich inclusions during crystal growth after a silica-rich hydrothermal fluid (Wacey *et al.*, 2012). This evidence is consistent with the interpretation of the stratiform botryoidal cavities as related to hydrothermal fluid circulation.

High resolution analyses have showed that both the investigated CM types have nanotextures that are largely homogeneous and consist mainly of turbostratic CM and isolated basic structural units (BSUs) a few nanometres long. In the BSU the aromatic layers interplanar distance of 3.6 Å correspond to a defective crystalline structure (Fig. 4.9d, Fig. 4.10d). In some cases in both the mat-like structures the fringes organized in 3.6 Å spaced stacks can reach about 20 nm in length. The nanotexture observed for both the carbonaceous mat-like structures is consistent with the structural organization of CM found at the end of the carbonization process as previously observed by Raman spectroscopic analyses (Delarue et al., 2016). TEM analyses have showed that the CM of the carbonaceous network is often associated with Fe, Cu, Ni-sulphides in the form of subhedral nanometre-sized crystal. The significance of this occurrence require further investigation and the interpretation is still on-going. Further HRTEM analyses on the microtextures defining the structural heterogeneity observed after Raman analyses are required.

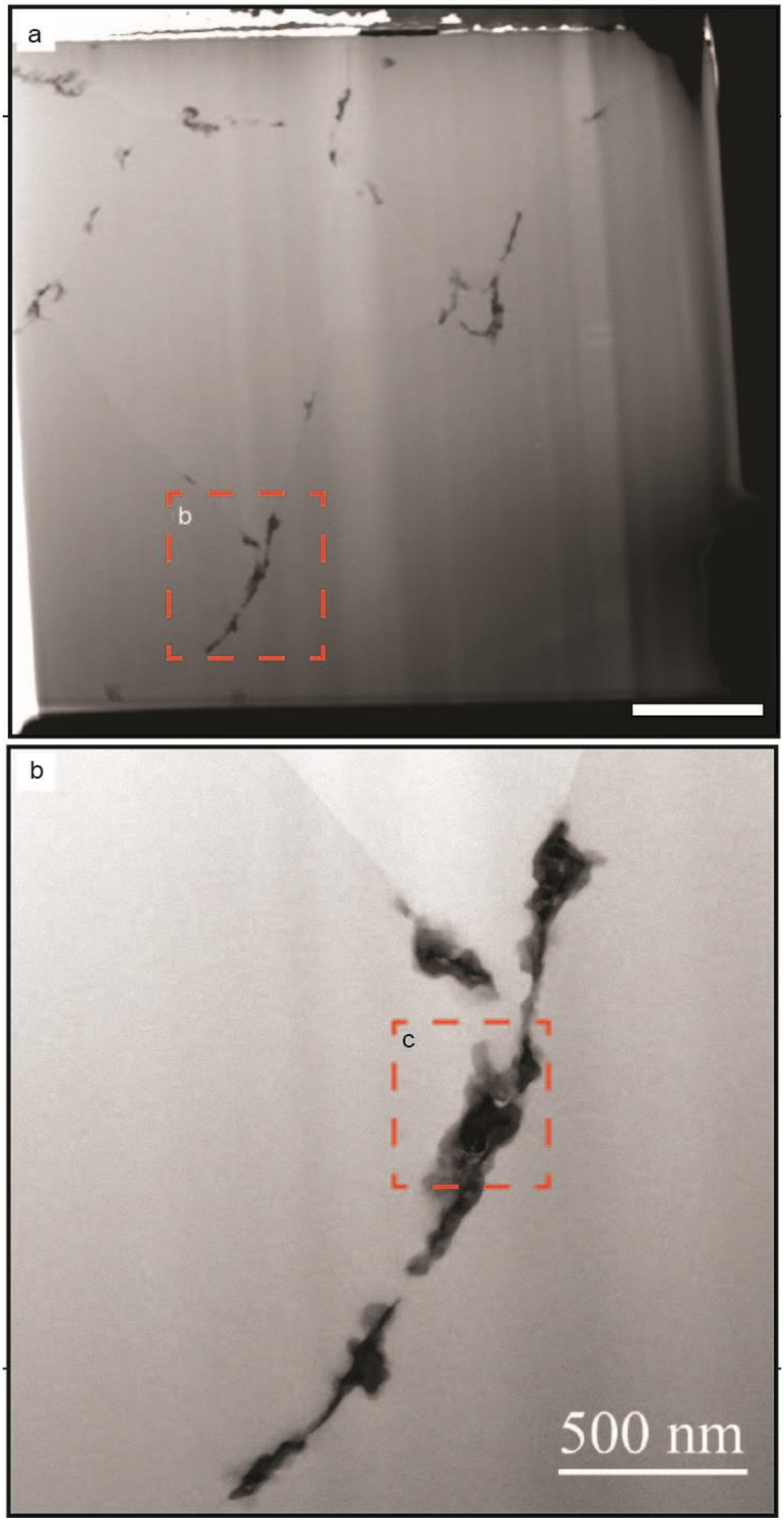

Figure 4.9a,b (continue) – CM forming the mat-like laminae occur in the form of nanometre-sized clots interleaved between chert crystals. a) CM from the lamina-sets occurring within the crinkly laminated chert sample F13. Scale bar: 2000 nm b) enlargement of the area in (a).

Figure 4.9c,d (continue) – c) The inset in (b) is enlarged. C) HRTEM image took on the red dot in (c).

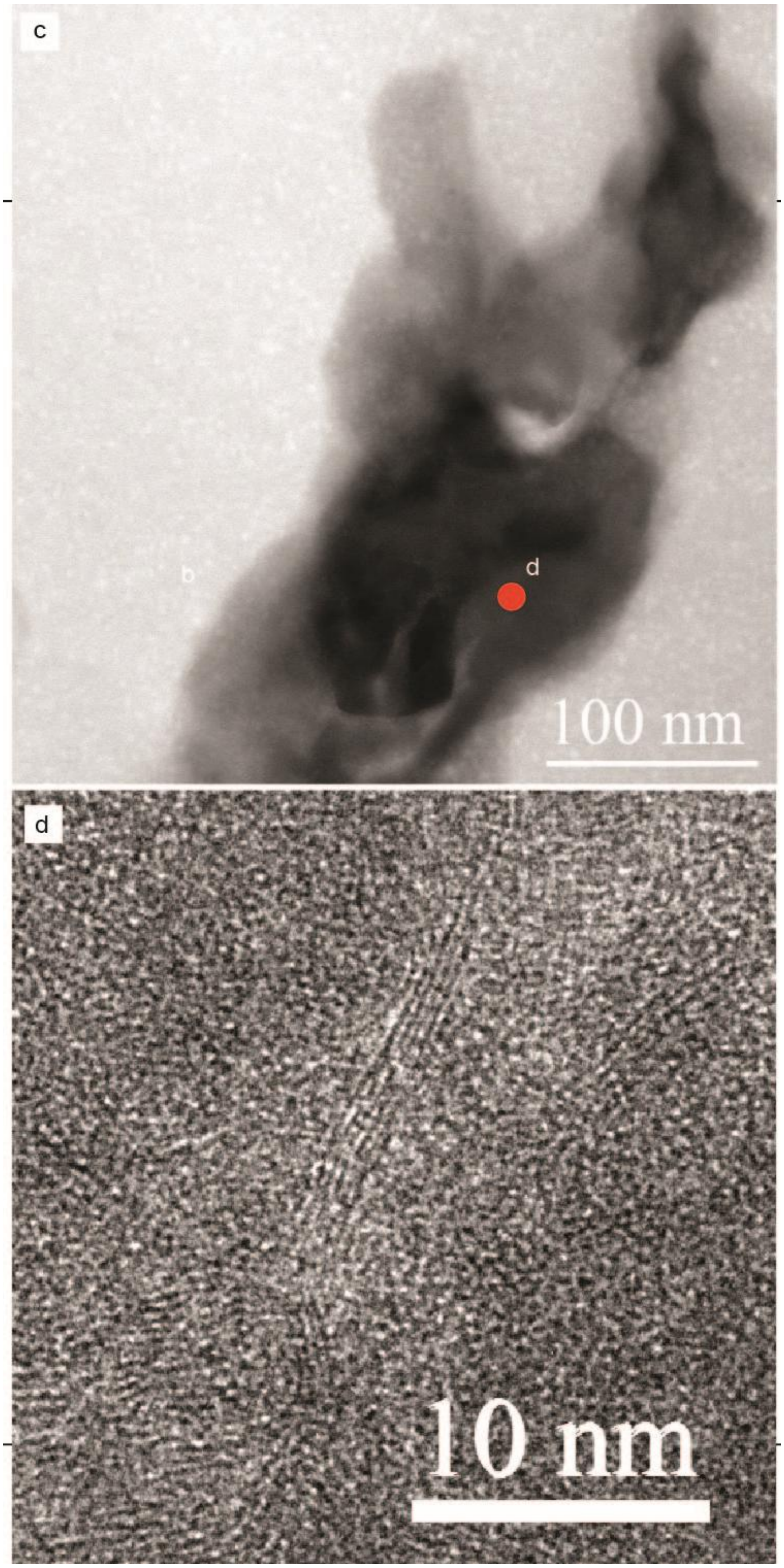

Figure 4.9c,d (continue) – c) The inset in (b) is enlarged. C) HRTEM image took on the red dot in (c).

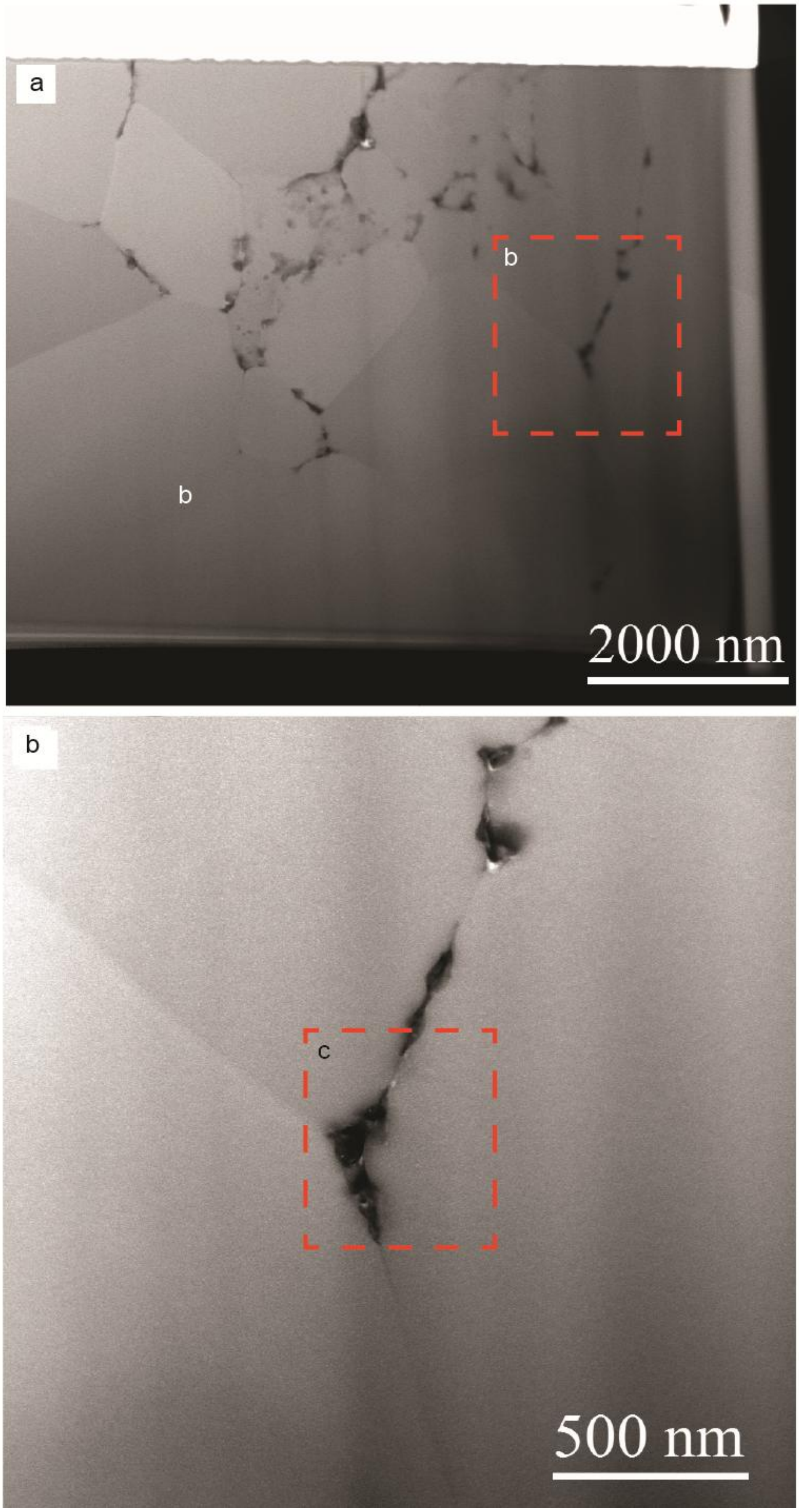

Figure 4.10a,b (continue) – CM forming the mat-like carbonaceous network occur in the form of nanometre-sized clots interleaved between chert crystals. a) CM from the lamina-sets occurring within the botryoidal quartz-filled vein at capping the granular carbonaceous chert of Sample C6D. b) enlargement of the area in (a).

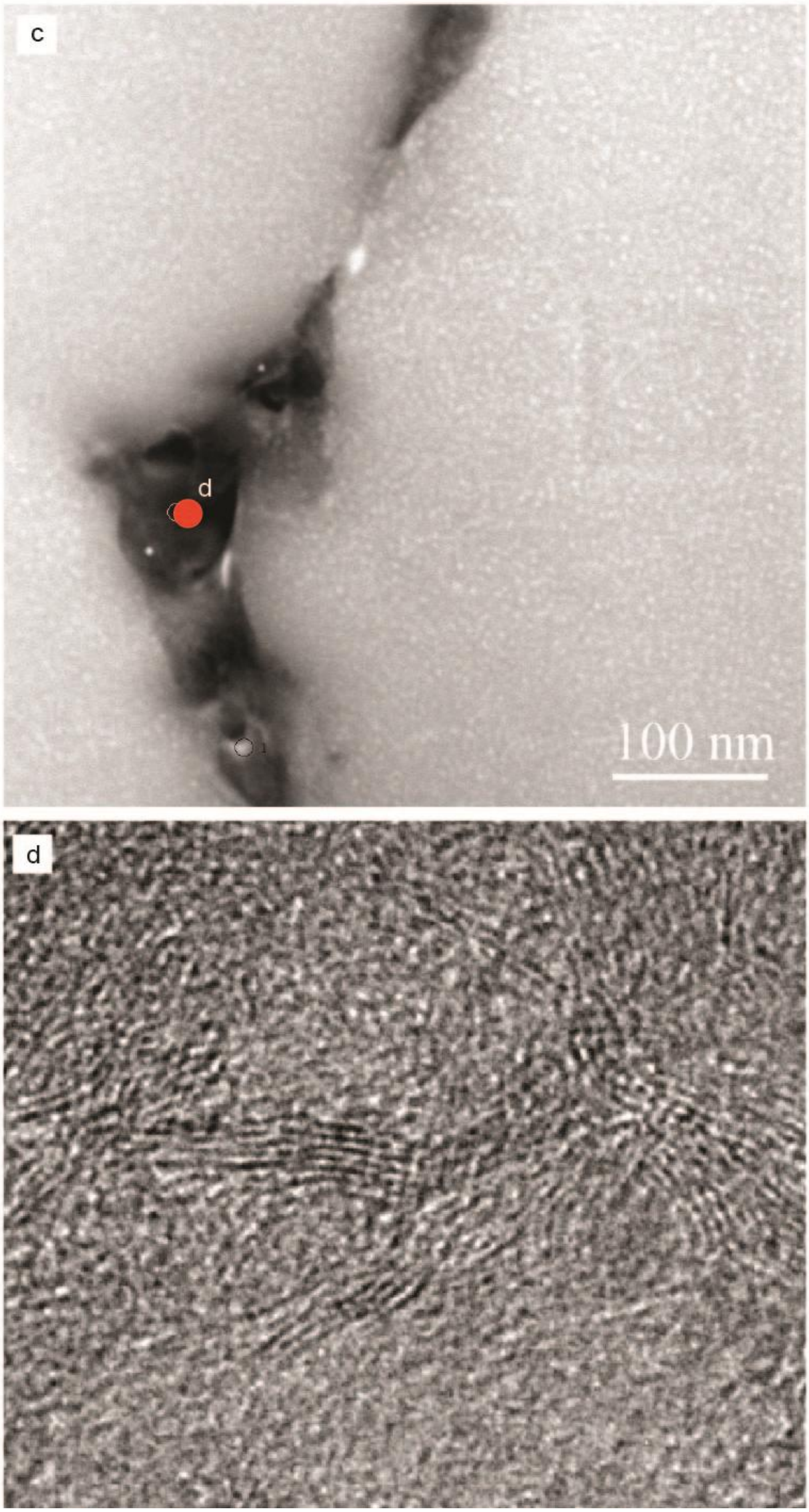

Figure 4.10c,d (continue) – c) The inset in (b) is enlarged. C) HRTEM image took on the red dot in (c).

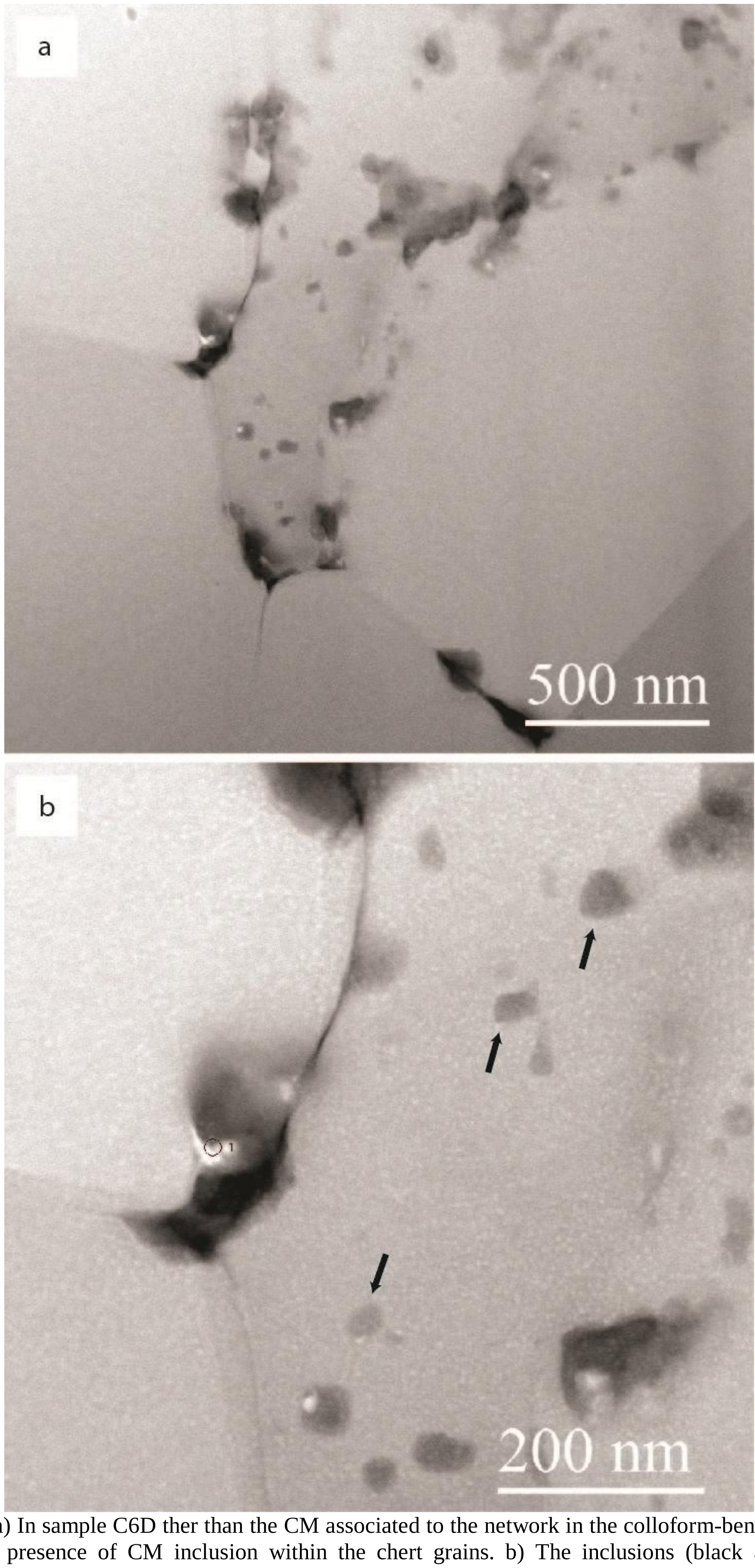

Figure 4.11 – a) In sample C6D ther than the CM associated to the network in the colloform-bending is possible to observe the presence of CM inclusion within the chert grains. b) The inclusions (black arrows) have a spheroidal shape characterized by regular margins at the contact with the surrounding quartz grain.

Chapter 5

Early microbial communities flourishing in a shallow-water hydrothermal field: a revisited Palaeoarchaean tale from the Buck Reef Chert

5.1 Discussion on the BAB3 core results

Understanding the significance of carbonaceous matter preserved in the ancient geological record represents a fundamental step to retrace the history of early microbial life on Earth. The task is challenging as ancient sedimentary deposits are scarce, often highly metamorphosed and formed under non-actualistic conditions, leading to problematic environmental reconstructions. Moreover widespread hydrothermalism on the Archaean Earth may affect our ability to discriminate biogenic CM. This is due to the potential input of abiotic carbon and the alteration of primary carbonaceous microtextures after chert crystallization out of the pervasive silica-rich fluids (Brasier et al., 2006, 2006; García-Ruiz et al., 2003; Wacey, 2009). Despite this, there are regions such as the 3.6 to 3.2 Ga years old Pilbara and Kaapvaal cratons, that offer well-preserved meta-sedimentary rocks where multiple reports of life, in the form of carbonaceous microbial remains have been documented (Altermann, 2001; Altermann and Kazmierczak, 2003; Schopf et al., 2007). It has also been shown how Palaeoarchaean CM may be better compared to the younger Precambrian biogenic carbonaceous record, rather than tested against an infinite set of null abiotic hypothesis (Walsh and Lowe, 1999; Tice and Lowe, 2006). Although, recognizing biotic CM in the fossil record is difficult, multiple lines of evidence indicate the existence of an early microbial biosphere from approximately 3.5 Ga years ago.

A classic location for studying ancient CM and the early evolution of microbial life is the 3.4 Ga old Buck Reef Chert of South Africa (Walsh, 1992; Walsh and Lowe, 1999; Tice and Lowe, 2006b). However, the environmental context in which the unit was deposited is still disputed (Hofmann, 2011). The observations resulting from this investigation on the BARB3 core and its carbonaceous content are herein discussed, including the palaeoenvironment of the Buck Reef Chert and its implications for the trophic identity of the BRC microbial communities. The outcome is a revisited picture from a corner of the early Earth.

5.1.1 Shallow-water diffuse hydrothermalism at the Buck Reef Chert

Previous outcrop investigations have discredited hydrothermalism at the BRC pointing at the absence of hot-springs or fluid conduits throughout the unit (Walsh and Lowe, 1999; Tice and Lowe 2006a,b). The BARB3 core however, provides this evidence in the form of stratiform botryoidal-quartz filled veins. Multiple observations support the origin of these structures as the result of sub-surface interactions between hydrothermal silica-rich fluids and a sediment column characterized by heterogeneous permeability. (I) Discrepancy in the timing of lithification of interbedded chert mesobands has been commonly observed in the BGB, whereas during early deposition white chert bands were already lithified occurring in alternation with carbonaceous-rich sediments that were not completely lithified (Lowe and Knauth, 1977; Lowe, 1999). In the BARB3 core, stratiform botryoidal veins developed as fractures within a crinkly laminated chert. This occurred immediately below a band of white chert with the two chert facies originally conformably superimposed (Fig. 3.16b). This is consistent with upwelling hydrothermal fluids, that get trapped by the non-permeable early-silicified white chert bands, building overpressure, resulting in lateral veining through non-completely lithified crinkly laminated layers. Analogous models have been already proposed for the generation of hydrothermal veining at the BGB (Paris et al., 1985; Hofmann and Bolhar, 2007; Hofmann and Harris, 2008). (II) The granular carbonaceous chert is a cavity filling facies found at the bottom of the stratiform veins. It is composed of CM-rich detritus mainly generated by the ripping-off, subsequent fluid-mediated transport and re-sedimentation of material previously deposited as a crinkly laminated layer. Non-hydrothermal models for the genesis of veins filled by granular carbonaceous material have been proposed. However, all models rely on the activity of currents that are responsible for the downward injection of detritus previously deposited at the sediment-water interface (Lowe, 1999; Tice and Lowe 2004, 2006). The BARB3 core bears no such evidence for current activity nor for granular carbonaceous layers that are formed directly at the sea-floor. The exclusive localization of granular-chert within stratiform veins is here regarded as proof of its genesis in the sub-surface due to lateral circulation of upwelling fluids within the sediment column. (III) The presence of botryoidal-quartz precipitate in the BARB3 core is the most definitive indicator for a hydrothermal nature of the circulating fluids. Colloform-banded quartz typically precipitates out of cooling-down colloidal silicothermal fluids in low-temperature hydrothermal environments (Marinova et al., 2014; Prokofiev et al., 2017). In fact, the overall structure, texture and mineralogy of the BARB3 stratiform botryoidal veins are strikingly similar and find their best analogous to hydrothermal veins occurring in low-sulfidation epithermal systems (Marchev et al., 2004; Marinova et al., 2014; Papavassiliou et al., 2017) and sinters at subaerial and sublacustrine environments (Fournier et al., 1991; Guido and Campbell, 2012). Spheroidal CM inclusions within chert crystals at the colloform-bending observed by TEM analyses (Fig. 4.10 and Fig. 4.11) and botryoidal carbonaceous rims around individual grains (Fig. 3.17c) in the granular chert indicate the trapping of a mobile CM-rich fluid phase by quartz precipitation and processes of spherulitic chert crystallization, both consistent with quartz precipitation out of a silica-rich hydrothermal gel (Brasier *et al.*, 2006; Wacey, 2009).

The presence of diffusively circulating silica-rich hydrothermal fluids in more permeable sediments is also supported by a combination of less explicit evidence; such as spherulitic precipitation around CM-siderite composite grains in fluid-intruded crinkly laminated chert (Fig. 3.8d,e), the presence in the same facies of fenestrae-like and lens-shaped cavities characterized by a colloform quartz precipitate and the role of such structures as internal silicification fronts in the ferruginous chert (Fig. 3.3a,b). More sporadic hydrothermal events of higher magnitude appear to be represented by the massive black chert mesobands. The mesobands are structureless and characterized by a greater abundance of pyrite, As,Ni,Co-sulphides and bituminous-interstitial CM. The massive black chert is better interpreted as a massive carbonaceous-rich hydrothermal vein mobilizing metals and viscous CM derived from the local thermal pyrolysis of carbonaceous debris recycled from the host rock (Buick, 1990; He et al., 2015; Suárez-Ruiz et al., 2016) or possibly from a different source of hydrothermal hydrocarbon input (Mazzini et al., 2004).

Multiple lines of evidence reveal that venting at the Buck Reef Chert is present, at least in the shallow-platformal lithofacies. The interaction between circulating fluids and non-completely lithified sediments is also suggested by the presence of plastically deformed ripped-up mat-like laminae in the granular chert, indicating that hydrothermalism occurred early during the deposition of the unit. The absence of focused discharge zones, such as black smokers or massive sulphide deposits, is not a sufficient argument to exclude syn-depositional hydrothermalism at the BRC. The BARB3 core instead provides indications for a more diffuse hydrothermal discharge in a system characterized by low-temperature hydrothermal fluids pervading the unit veining and interfingering laterally within permeable layers. Similar features develop in low-sulfidation epithermal environments characterized by low-temperature, low-pressure hydrothermal fluids migrating along the sediment bedding planes (Glasby et al., 2005). Diffuse hydrothermalism at the BRC shallow-platformal facies could have thus resulted from either a widespread heat flow that characterizes the hot hydrothermal Palaeoarchaean Earth (Hofmann 2011), or the unit being distally deposited from a focused discharge zone (Alt 1995; German and von Damm 2003). The observation in outcrop of an extensive CM-rich quartz dike (Fig. 3.19) cutting the Hooggenoeg Formation immediately below the BRC may advocate for the latter hypothesis representing a fluid conduit branching from a major distal discharge source.

The interpretation that several BARB3 sedimentary features are a result of syn-depositional hydrothermalism, generates doubts concerning the BRC depositional palaeodepth reconstructions. The “shallow-platformal” facies, for which deposition was previously envisaged to be between 15 and 200 m (Tice and Lowe, 2004; 2006b), in the BARB3 core show no evidence of wave activity, nor of episodic storm events as both the granular chert and botryoidal cavities are better explained by hydrothermal fluid circulation. The restriction of mat-like laminations to this facies has been interpreted as a microbial community confined to the photic zone (Tice and Lowe 2004). Considering the absence of botryoidal stratiform veins, granular chert and black chert mesobands in the BIF section along the BARB3 core, it is here suggested that the differences between the shallow-platformal and deep-basinal lithofacies may instead reflect periods of quiescence in hydrothermalism rather than variation in the depositional depth or plausibly a combination of both. For instance, the subsidence of the volcanic platform may have increased pressure in the sedimentary column contrasting with the diffuse hydrothermal veining by low-temperature, low-pressure upwelling fluids in the “deep-basinal” facies. The most convincing evidence for shallow-water current activity at the BRC remains the observation of ripple-marks at the evaporitic facies (Lowe and Worrell, 1999; Tice and Lowe, 2004, 2006b). However, an unconformity has been reported between this basal section and the upper banded chert facies (Tice and Lowe, 2006b) preventing clear palaeodepth reconstructions.

In general the BARB3 facies has been deposited in a very low-energy environment. An extremely shallow depth, lower than previously reported, is suggested for the BRC shallow facies deposition. The porosity and band heterogeneity decreases upwards along the core and this advocates for an increasing depth in deposition for the BIF. Although this may additionally reflect a gradual closure in the venting system. Finally, any higher-energy current activity was confined to the evaporitic facies. The overall picture is consistent with a well-protected coastal-lagunal environment but either with a saline pond or lake.

5.1.2 Multiple carbonaceous generations

This study represent one of the few works which have found systematic variation in the structure of CM from Palaeoarchaean cherts constrained by field mapping and microfabric analysis. In particular it is showed how the BARB3 CM molecular structure varies depending on the analyzed facies and more specifically on the carbonaceous microtexture. Three major groups have been defined based on microtexture-related CM structural heterogeneity groups:

(I) microbial mat-like structures from the crinkly laminated chert and the granular carbonaceous chert (botryoidal vein); (II) CM-rich individual grains and (III) bitumen-interstitial dense CM. Such between-microtexture heterogeneity is indicative of multiple carbonaceous generations and suggests that divergence in the carbonaceous precursors and in the CM post-depositional histories are still preserved in the BRC and not completely masked by the metamorphic overprint.

A major structural divergence has been observed in the black massive chert CM assemblage characterized by a great abundance of bituminous-interstitial CM. A range of different explanations are consistent with such an observation. The massive black carbonaceous chert could have formed during hydrothermal events post-dating the BGB metamorphic peak reached at about 3.2 Ga years ago (Tice et al., 2004). In this way, the poorly ordered bituminous CM would be millions of years younger than the BRC deposits, and at the same time the co-occurring more mature cloudy CM could have been derived from the reworking of the ancient carbonaceous material originally deposited in the host-rock. However there are is no evidence for a younger hydrothermal event and the stratiform occurrence of the black massive chert, in the absence of clear hydraulic fracturing or hydrothermal breccia and dikes, fits better with an hydrothermally influenced deposit or an early carbonaceous stratiform hydrothermal veining through non-completely lithified rocks during the early stage of burial. At the same time the bitumen-like CM order doesn’t differ much from that of the grains and the mat-like structures, fitting with the carbonization continuum of the Hooggenoeg and Kromberg formations (Fig. 4.8, Delarue et al., 2016), so causes other then the thermal imprint could be responsible for the structural heterogeneity.

It has been observed in younger organic rich sediments, that have gone through the oil window, that the thermal maturation of kerogen can result in the formation of a porous and cavity-filling aliphatic-rich asphaltite bitumen (Bernard et al., 2012). Similar occurrences have been reported from hydrothermally influenced deposits and methane seepage where organic debris can undergo thermal pyrolysis (Simoneit and Lonsdale, 1982; Savard et al., 1996; Kelly et al., 1995). The BARB3 bitumen-like CM, as indicated by the microtexture name, shows textural similarities to the interstitial bitumen that has been documented from coeval carbonaceous-rich and younger organic-rich deposits (Buick, 1990; He et al., 2015; Suárez-Ruiz et al., 2016). In fact, if such Palaeoarchaean bituminous CM originated from the concentration of aliphatic-rich carbonaceous molecules, then, at equal low P-T conditions, its thermal maturation would have proceeded much slower than other carbonaceous precursors that include more abundant aromatic compounds (Buseck and Huang, 1985; Jehlička et al., 2003; Quirico et al., 2009; Marshall et al., 2010) , as the aromatic C-rich compounds are more easily reorganized into polyaromatic graphite-like planes. It is well-known that the original CM composition affect its evolution within low-metamorphic sediments, with the most explicative case of a “precursor effect” represented by the so called non-graphitizing carbonaceous materials which even at extremely high temperature do not transform into graphite (Franklin, 1951). Thus the lower structural order of the BARB3 bituminous CM is consistent with a “precursor effect” whereas the original carbonaceous material was selectively enriched in aliphatic molecules. The interpretation of the massive black facies as a hydrothermal vein is consistent with bitumen formation and transportation as a viscous substance through veins or within adjacent deposits. This could explain the occurrence of such material in veinlets cross-cutting the other chert facies, or the localized evidence of bitumen-like spheres in the massive black chert and exceptionally, remobilized, in the crinkly laminated sample D1.

The structural homogeneity of CM in the carbonaceous networks and mat-like laminations could be correlated to a common microbial molecular precursor, , possibly Extracellular Polymeric Substances (EPS). These substances are the building blocks of the cohesive and plastic extracellular organic matrix used by microbes to secure themselves to the substrate and develop a complex colonial organization (Madigan et al., 1997). Such an interpretation is suitable for several reasons. First, all EPS are within the most resistant and most easily preserved microbial remains in ancient sedimentary deposits (Wacey, 2009; Kremer and Kaźmierczak, 2017). Including a limited amount of molecules when compared to the entire microbial molecular pool, it is reasonable to expect such an EPS precursor to result in a mature CM species characterized by a low standard deviation, or scattering, in their structural parameters. Last, the highest degree of carbonaceous structural order shown by the mat-like structures when compared to the other non-bituminous carbonaceous microtextures is consistent with the EPS being mostly composed by polysaccharides. Polysaccharides are characterized by the repeated hexagonal unit bearing 5 carbon atoms, and this could be potentially more prone to the carbonization/graphitization evolution than other molecular diverse biogenic products. Such a hypothesis is consistent with the use of natural polysaccharides as a suitable precursor to efficiently synthesise graphitic material (Chaldun et al., 2013; El Kadib, 2016) or in experiments where cellulose has been graphitized, yet still retains its original morphology (Kim et al., 2001).

5.1.3 Complex microbial communities at the BRC

During this investigation on the BARB3 drill core, no evidence for body microfossils was observed. Despite the exceptional state of preservation, the primary CM microtextures and the sedimentary microfabrics that are readily ascribable to microbial activity (the crinkly laminated chert) have not supplied any individual microfossils. This however, is not surprising but rather consistent with previous findings. Putative microfossils in the Palaeoarchaean are in fact extremely rare and their biogenicity is strongly debated (Schopf, 1993; Brasier *et al.*, 2005; Brasier *et al.*, 2006; Schopf *et al.*, 2007). Investigating the Barberton Greenstone Belt, Walsh and Lowe (1999) reported the presence of "possible fossils" in just 9 carbonaceous chert specimens out of more than 400 scrutinized samples. Tice and Lowe (2004, 2006) during their extensive work on the Buck Reef Chert CM provided only a single piece of morphological evidence that may be interpreted as possible filaments.

As documented here, not only does the diffuse CM, but also the primary carbonaceous structures, consist of an aggregation of individual sub-micron sized CM particles. This is confirmed by HRTEM analyses conducted on the carbonaceous mat-like laminae and network. Although such structures show morphological signatures supporting an originally cohesive precursor, at the nano-scale they lack carbonaceous continuity, consisting of nanometre-sized clots interweaved between chert crystals. Such observations are consistent with a certain degree of chert recrystallization (Knauth and Epstein, 1976; Knoll *et al.*, 1988) and with CM volume reduction during carbonization/graphitization, after the loss of the heteroatoms mass (Brooks and Taylor, 1965; Buseck and Huang, 1985). As both processes occur at low-metamorphic grade they are expected for such ancient meta-sedimentary deposits. Furthermore, chert spherulitic recrystallization, a process typical of Archaean hydrothermal cherts, is also capable of CM disaggregation (Brasier *et al.*, 2005; Brasier *et al.*, 2006). Evidence of spherulitic chert and botryoidal rims around grains within the BARB3 crinkly laminated and laminated black chert has been reported here.

If the carbonaceous mat-like structures, which are microtexturally and structurally consistent with a resistant EPS-rich precursor, have undergone disaggregation and CM displacement, then it is highly plausible that weak individual microfossils would now consist of sparse CM particles in the chert matrix. At the same time, CM redistribution at the cell-scale, could have generated carbonaceous pseudo-fossils. Another potential explanation for the difficulty in the detection of individual microfossils concerns the possibility of nanobacteria communities (Southam and Donald, 1999; Walsh, 2004). Although this represents a fascinating avenue for future research it remains untested in the BRC.

Despite having not detected any individual microfossils, the BARB3 core represents a fantastic window to the Archaean world. In the facies corresponding to the so-called BRC shallow-platformal deposits (Tice and Lowe, 2006), there are several hundreds of meters of mat-like carbonaceous laminae that provides strong evidence for an original interaction between microbial communities and the surrounding environment. The crinkly laminated chert represents a bio-sedimentary microfabric and the thick lamina-sets developed periodically in response to cyclic environmental factors. Although carbonaceous mats from the BRC have been previously suggested to represent anoxygenic photosynthetic microbial communities living in a photic marine environment (Tice and Lowe, 2004, 2006), the planar stromatolite growth preserved in the crinkly laminated chert is consistent with a wide range of environmental settings, possibly supporting phototrophic and/or chemotrophic microbial communities (Mazzini et al., 2004; Hips and Haas, 2006; Mastrandrea et al., 2006; Gerdes, 2007; Noffke, 2009).

In the BARB3 core, carbonaceous networks about 100 μm thick gently coat the chert colloform precipitate, immediately overlying the granular carbonaceous chert facies. Such structures consist of a carbonaceous web that develops around fine quartz grains. These grains are well compacted and preferentially lay parallel to the bedding plane suggesting an original active trapping behaviour of the carbonaceous network (Eriksonn et al., 2007; Noffke, 2010). Similar cohesive carbonaceous networks have been previously reported from the BRC (Tice and Lowe, 2006) and have been regarded as the remains of microbial mats. The morphology and behaviour of the BARB3 carbonaceous networks are consistent with such a interpretation. This is further supported by Raman analyses, as the structural order of the networks overlap almost perfectly with that of carbonaceous mats preserved in the crinkly laminated chert. It is thus suggested that these structures may also derive from an EPS-rich precursor. However, while mat-like laminae preserved in the crinkly laminated chert probably represented epibenthic communities, the carbonaceous networks occur consistently within the botryoidal quartz-filled cavities, which are independent from the mechanism of formation and represent sub-surface environments.

The restriction of the carbonaceous network microtexture to the botryoidal veins suggests that a non-phototrophic microbial community adapted to sub-surface niches was present during the deposition of the BRC. This may discredit previous interpretations of the BRC mats, as exclusively photosynthetic (Tice and Lowe, 2004), an interpretation based entirely on their confinement to a shallow photic zone (Tice and Lowe, 2006). Instead, independently to water depth, trophic sources other than solar light must have been present to sustain such cavity-colonizing microbial communities and may as well have supported sea-floor communities.

5.2 Synopsis

5.2.1 A revisited Palaeoarchaean tale from the Buck Reef Chert

The integration of observations obtained from a multiple analytical approach from the outcrop to the atomic scale provide a revisited picture for the Buck Reef Chert shallow facies and the hosted microbial communities. About 3.4 Ga years ago this corner of Earth was characterized by extremely calm shallow waters. Under the water column, soft-sediments were gently bubbling due to diffuse low-temperature, silica-rich hydrothermalism. Epibenthic mat-constructing communities flourished in such conditions resulting in the cyclic development of laterally extensive microbial carpets. Periods of intense microbial activity alternated to intervals of quick silicification at the sediment-water interface caused by silica-rich hydrothermal fluids. The burial of early-lithified layers created non-permeable caps trapping the upwelling fluids and forcing them laterally through permeable organic-rich still soft sediments. The stratiform veining resulted in the remobilization of not yet lithified carbonaceous mats and microbial debris but represented as well the opportunity for a new ecological niche. Sub-surface chemotrophic dwelling microbial communities possibly colonized the stratiform veins resisting fluid circulation through a trapping-and-binding behaviour most commonly recognized in epibenthic communities. Eventually the veins sealed through precipitation of botryoidal silica out of the cooling silicothermal fluid.

Deeper in the sediment column higher temperature-pressure fluids resulted into the episodic opening of larger stratiform veins where insoluble CM was collected and recycled from the host-rocks. Here pyrolysis of microbial debris possibly occurred liberating an aliphatic rich viscous CM phase. Such CM was thus remobilized locally within sediments at the vein contact or distally through the conduits system up to the botryoidal stratiform veins. The viscous CM was eventually trapped by precipitating quartz or cooled down solidifying into asphaltite-like spheres and blobs.

5.2.2 Future perspectives

The original aim of this study was to: (I) recognize evidence of biological activity within the BARB3 core through the morpho-chemical characterization of potential microbial fossils; (II) investigate the provenance and relationships between CM in the different lithofacies to test theories for CM origin and evolution; (III) develop biosignatures, if any, and techniques for early life detection; (IV) contribute to the Paleoarchean environmental reconstruction. While points I, II and IV have been explicitly discussed in Chapter 3 and 4 to be further integrated in this section 5.1, point III has been so far only implicitly engaged. However it is clear from this investigation that, like for all the previous early Life studies, the search for a definitive biosignature ultimately rely on the integration of multiple analytical approaches from the outcrop to the atom scale.

Resulting in a revised picture of the Buck Reef Chert this research provide a starting point for future works finalized to better understand and constrain the structure of the hydrothermal system and its possible heat sources. The trophic identity and potential interaction between complex microbial communities should be also deeply investigated, especially focusing on the carbonaceous network biogenicity. A wise direction would be to extend the CM nanotexture characterization to all the microtextures that in this study showed a systematic structural variation and the integration of microtexture-based structural and textural results with in-situ C isotopic data. A confrontation of so-collected data with analogous information obtained from CM within the quartz-dike observed in outcrop and more generally from veins and deposits at the BRC basal-evaporitic facies and underlying horizons from the Hooggenoeg Formation would greatly improve our understanding of the C-cycle on the Palaeoarchaean Earth with major implication for the reconstruction of early Life evolution.

Acknowledgments

This work is a contribution to the Barberton drilling project. This research was supported by the Marie-Curie Action grant to Barbara Cavalazzi in the frame of the project Inorganic Nanoparticles in Archaean Carbonaceous Matter (INACMa) – a key to early life and palaeoenviromental reconstructions, projet FP7-PEOPLE-2013-CIG-618657, PI. Barbara Cavalazzi.

I'm grateful to my supervisor Barbara Cavalazzi for the opportunity she gave me introducing me to the fascinating and enigmatic early Earth. I would like to thank her especially for the lack of prejudice she showed accepting a PhD student with a biological background to investigate life in such complicated and ancient rocks; an open-mindedness which is reflected by the intriguing and challenging topics at the centre of her scientific work. Much gratitude goes also to my co-supervisor Axel Hofmann for all the knowledge he transmitted to me, his invaluable lead in the field and for his ability in always stimulating criticism. Our field-trips are some of my best memories from this last three years. I thank sincerely the reviewers Frédérich Foucher and Nicola McLoughlin for their very constructive comments on this thesis. Facing their reviews represented one of the most valuable and stimulating moment of my PhD. I'd like to thank similarly Kenichiro Sugitani for his comments during our e-mail discussions on the nature of the botryoidal-quartz filled cavities. I thank as well Giovanni Hearne from the Physics Department of the University of Johannesburg for his help in understanding the process of Raman spectra deconvolution.

Gratitude goes to my good friend Tim Topper for all the support he always gave me, for all the times he had to face my emails and my requests to double-check my writing. I thank as well my friends Guido Gnecchi, Jaganmoy Jodder and Silvia Cattò for their great help during all these years. Immense gratitude finally goes to Shannon Webb for having introduced me to South Africa, for the unique support she gave to me and the beautiful time spent together. This work is dedicated to her to my friends and to my amazing parents and sisters.

References

Agić, H., Moczydłowska, M., and Yin, L.-M. (2015). Affinity, life cycle, and intracellular complexity of organic-walled microfossils from the Mesoproterozoic of Shanxi, China. J. Paleontol. *89*, 28–50.

Allwood, A.C., Walter, M.R., Kamber, B.S., Marshall, C.P., and Burch, I.W. (2006a). Stromatolite reef from the Early Archaean era of Australia. Nature *441*, 714–718.

Allwood, A.C., Walter, M.R., and Marshall, C.P. (2006b). Raman spectroscopy reveals thermal palaeoenvironments of c.3.5 billion-year-old organic matter. Vib. Spectrosc. *41*, 190–197.

Altermann, W. (2001). The oldest fossils of Africa – a brief reappraisal of reports from the Archean. J. Afr. Earth Sci. *33*, 427–436.

Altermann, W., and Kazmierczak, J. (2003). Archean microfossils: a reappraisal of early life on Earth. Res. Microbiol. *154*, 611–617.

Andò, S., and Garzanti, E. (2014). Raman spectroscopy in heavy-mineral studies. Geol. Soc. Lond. Spec. Publ. *386*, 395–412.

Apicella, B., Pré, P., Alfè, M., Ciajolo, A., Gargiulo, V., Russo, C., Tregrossi, A., Deldique, D., and Rouzaud, J.N. (2015). Soot nanostructure evolution in premixed flames by High Resolution Electron Transmission Microscopy (HRTEM). Proc. Combust. Inst. *35*, 1895–1902.

Arndt, N.T., and Nisbet, E.G. (2012). Processes on the Young Earth and the Habitats of Early Life. Annu. Rev. Earth Planet. Sci. *40*, 521–549.

Arndt, N.T., Wilson, A., Mason, P., Hofmann, A., and Lowe, D. (2013). Overview of the Barberton Drilling Project. pp. EGU2013-3909.

Awramik, S.M., Schopf, J.W. and Walter, M.R., 1983. Filamentous Fossil Bacteria from the Archean of Western Australia. In: *Developments in Precambrian Geology, Developments and Interactions of the Precambrian Atmosphere, Lithosphere and Biosphere* (Nagy, B.,, Weber, R.,, Guerrero, J.C., and Schidlowski, M., eds.) Elsevier, p. 249–266.

Ayres, D.E. (1972). Genesis of iron-bearing minerals in banded iron formation mesobands in the Dales Gorge Member, Hamersley Group, Western Australia. Econ. Geol. *67*, 1214–1233.

Bahrig, B. (1994). Chapter 6 The Formation of Alternating Chalk/Siderite Units During the Neogene in The Black Sea—An Example of Climatic Control of Early Diagenetic Processes. In Developments in Sedimentology, K.H. Wolf, and G.V. Chilingarian, eds. (Elsevier), pp. 133–153.

Beran, A., and Libowitzky, E. (2004). Spectroscopic methods in mineralogy (The Mineralogical Society of Great Britain and Ireland).

Bernard, S., Wirth, R., Schreiber, A., Schulz, H.-M., and Horsfield, B. (2012). Formation of nanoporous pyrobitumen residues during maturation of the Barnett Shale (Fort Worth Basin). Int. J. Coal Geol. *103*, 3–11.

Beyssac, O., Goffé, B., Chopin, C., and Rouzaud, J.N. (2002). Raman spectra of carbonaceous material in metasediments: a new geothermometer. J. Metamorph. Geol. *20*, 859–871.

Beyssac, O., Goffé, B., Petitet, J.-P., Froigneux, E., Moreau, M., and Rouzaud, J.-N. (2003). On the characterization of disordered and heterogeneous carbonaceous materials by Raman spectroscopy. Spectrochim. Acta. A. Mol. Biomol. Spectrosc. *59*, 2267–2276.

Bischoff, J.L., and Seyfried, W.E. (1978). Hydrothermal chemistry of seawater from 25 degrees to 350 degrees C. Am. J. Sci. *278*, 838–860.

Bolhar, R., Van Kranendonk, M.J., and Kamber, B.S. (2005). A trace element study of siderite–jasper banded iron formation in the 3.45Ga Warrawoona Group, Pilbara Craton—Formation from hydrothermal fluids and shallow seawater. Precambrian Res. *137*, 93–114.

Bontognali, T.R.R., Sessions, A.L., Allwood, A.C., Fischer, W.W., Grotzinger, J.P., Summons, R.E., and Eiler, J.M. (2012). Sulfur isotopes of organic matter preserved in 3.45-billion-year-old stromatolites reveal microbial metabolism. Proc. Natl. Acad. Sci. *109*, 15146–15151.

Boorn, S.H.J.M. van den, Bergen, M.J. van, Nijman, W., and Vroon, P.Z. (2007). Dual role of seawater and hydrothermal fluids in Early Archean chert formation: Evidence from silicon isotopes. Geology *35*, 939–942.

Brasier, M.D., and Wacey, D. (2012). Fossils and astrobiology: new protocols for cell evolution in deep time. Int. J. Astrobiol. *11*, 217–228.

Brasier, M., McLoughlin, N., Green, O., and Wacey, D. (2006). A fresh look at the fossil evidence for early Archaean cellular life. Philos. Trans. R. Soc. B Biol. Sci. *361*, 887–902.

Brasier, M.D., Green, O.R., Lindsay, J.F., McLoughlin, N., Steele, A., and Stoakes, C. (2005a). Critical testing of Earth’s oldest putative fossil assemblage from the 3.5 Ga Apex chert, Chinaman Creek, Western Australia. Precambrian Res. *140*, 55–102.

Brasier, M.D., Matthewman, R., McMahon, S., and Wacey, D. (2011). Pumice as a Remarkable Substrate for the Origin of Life. Astrobiology *11*, 725–735.

Brasier, M.D., Antcliffe, J., Saunders, M., and Wacey, D. (2015). Changing the picture of Earth’s earliest fossils (3.5–1.9 Ga) with new approaches and new discoveries. Proc. Natl. Acad. Sci. *112*, 4859–4864.

Brooks, J.D., and Taylor, G.H. (1965). The formation of graphitizing carbons from the liquid phase. Carbon *3*, 185–193.

Buick, R., 1984. Carbonaceous filaments from North Pole, Western Australia: Are they fossil bacteria in Archaean stromatolites? *Precambrian Research*, **24**, p. 157–172, doi: 10.1016/0301-9268(84)90056-1.

Buick, R. (1990). Microfossil Recognition in Archean Rocks: An Appraisal of Spheroids and Filaments from a 3500 M.Y. Old Chert-Barite Unit at North Pole, Western Australia. PALAIOS *5*, 441–459.

Buseck, P.R., and Huang, B.-J. (1985). Conversion of carbonaceous material to graphite during metamorphism. Geochim. Cosmochim. Acta *49*, 2003–2016.

Byerly, G.R., Lower, D.R., and Walsh, M.M. (1986). Stromatolites from the 3,300–3,500-Myr Swaziland Supergroup, Barberton Mountain Land, South Africa. Nature *319*, 489–491.

Byerly, G.R., Kröner, A., Lowe, D.R., and Walsh, M.M. (1993). Sequential magmatic evolution of the early Archean Onverwacht Group: evidence from the upper formations. Eos Trans. Am. Geophys. Union *74*, 660.

Byerly, G.R., Kröner, A., Lowe, D.R., Todt, W., and Walsh, M.M. (1996). Prolonged magmatism and time constraints for sediment deposition in the early Archean Barberton greenstone belt: evidence from the Upper Onverwacht and Fig Tree groups. Precambrian Res. *78*, 125–138.

Chaldun, E.R., Karina, M., and Purwasasmita, B.S. (2013). Synthesis and Characterization of Bacterial Cellulose-Based Carbon Nanotube by Catalytic Graphitization. Adv. Mater. Res. *789*, 232–236.

Chambefort, I., Dilles, J.H., and Kent, A.J.R. (2008). Anhydrite-bearing andesite and dacite as a source for sulfur in magmatic-hydrothermal mineral deposits. Geology *36*, 719–722.

Charon, E., Aléon, J., and Rouzaud, J.-N. (2014). Impact delivery of organic matter on the acapulcoite–lodranite parent-body deduced from C, N isotopes and nanostructures of carbon phases in Acapulco and Lodran. Geochim. Cosmochim. Acta *142*, 224–239.

Choi, K.S., Khim, B.K., and Woo, K.S. (2003). Spherulitic siderites in the Holocene coastal deposits of Korea (eastern Yellow Sea): elemental and isotopic composition and depositional environment. Mar. Geol. *202*, 17–31.

Delarue, F., Rouzaud, J.-N., Derenne, S., Bourbin, M., Westall, F., Kremer, B., Sugitani, K., Deldicque, D., and Robert, F. (2016). The Raman-Derived Carbonization Continuum: A Tool to Select the Best Preserved Molecular Structures in Archean Kerogens. Astrobiology *16*, 407–417.

Deldicque, D., Rouzaud, J.-N., and Velde, B. (2016). A Raman – HRTEM study of the carbonization of wood: A new Raman-based paleothermometer dedicated to archaeometry. Carbon *102*, 319–329.

Dieing, T., Hollricher, O., and Toporski, J. (2011). Confocal raman microscopy (Springer Science & Business Media).

Dodd, M.S., Papineau, D., Grenne, T., Slack, J.F., Rittner, M., Pirajno, F., O'Neil, J., and Little, C.T.S. (2017). Evidence for early life in Earth's oldest hydrothermal vent precipitates. Nature *543*, 60.

Duda, J.-P., Kranendonk, M.J.V., Thiel, V., Ionescu, D., Strauss, H., Schäfer, N., and Reitner, J. (2016). A Rare Glimpse of Paleoarchean Life: Geobiology of an Exceptionally Preserved Microbial Mat Facies from the 3.4 Ga Strelley Pool Formation, Western Australia. PLOS ONE *11*, e0147629.

Egerton, R.F. (2005). Physical principles of electron microscopy (Springer).

El Kadib, A. (2016). Metal–Polysaccharide Interplay: Beyond Metal Immobilization, Graphenization-Induced-Anisotropic Growth. ChemSusChem *9*, 238–240.

Ellis-Evans, J.C. (2011). Carbon Cycle (Biological). In Encyclopedia of Astrobiology, M. Gargaud, P.R. Amils, J.C. Quintanilla, H.J. (Jim) C. II, W.M. Irvine, P.D.L. Pinti, and M. Viso, eds. (Springer Berlin Heidelberg), pp. 238–239.

Elrick, M., and Snider, A.C. (2002). Deep-water stratigraphic cyclicity and carbonate mud mound development in the Middle Cambrian Marjum Formation, House Range, Utah, USA. Sedimentology *49*, 1021–1047.

Eriksson, P.G. (2007). Classification of structures left by microbial mats in their host sediments. 39.

Eriksson, K.A., and Simpson, E.L. (2000). Quantifying the oldest tidal record: The 3.2 Ga Moodies Group, Barberton Greenstone Belt, South Africa. Geology *28*, 831–834.

Everall, N.J., Lumsdon, J., and Christopher, D.J. (1991). The effect of laser-induced heating upon the vibrational raman spectra of graphites and carbon fibres. Carbon *29*, 133–137.

Fayers, S.R., and Trewin, N.H. (2003). A review of the palaeoenvironments and biota of the Windyfield chert. Earth Environ. Sci. Trans. R. Soc. Edinb. *94*, 325–339.

Ferrari, A.C., and Robertson, J. (2000). Interpretation of Raman spectra of disordered and amorphous carbon. Phys. Rev. B *61*, 14095–14107.

Foucher, F., and Westall, F. (2012). Raman Imaging of Metastable Opal in Carbonaceous Microfossils of the 700–800 Ma Old Draken Formation. Astrobiology *13*, 57–67.

Fournier, R.O., Thompson, J.M., Cunningham, C.G., and Hutchinson, R.A. (1991). Conditions leading to a recent small hydrothermal explosion at Yellowstone National Park. GSA Bull. *103*, 1114–1120.

Franklin, R.E. (1951). Crystallite growth in graphitizing and non-graphitizing carbons. Proc R Soc Lond A *209*, 196–218.

Frezzotti, M.L., Tecce, F., and Casagli, A. (2012). Raman spectroscopy for fluid inclusion analysis. J. Geochem. Explor. *112*, 1–20.

García-Ruiz, J.M., Hyde, S.T., Carnerup, A.M., Christy, A.G., Kranendonk, M.J.V., and Welham, N.J. (2003). Self-Assembled Silica-Carbonate Structures and Detection of Ancient Microfossils. Science *302*, 1194–1197.

Gargaud, M., Martin, H., López-García, P., Montmerle, T., and Pascal, R. (2013). Young Sun, Early Earth and the Origins of Life: Lessons for Astrobiology (Springer Science & Business Media).

Gautam, U.K., Vivekchand, S.R.C., Govindaraj, A., Kulkarni, G.U., Selvi, N.R., and Rao, C.N.R. (2005). Generation of Onions and Nanotubes of GaS and GaSe through Laser and Thermally Induced Exfoliation. J. Am. Chem. Soc. *127*, 3658–3659.

Guido, D.M., and Campbell, K.A. (2012). Diverse subaerial and sublacustrine hot spring settings of the Cerro Negro epithermal system (Jurassic, Deseado Massif), Patagonia, Argentina. J. Volcanol. Geotherm. Res. *229–230*, 1–12.

Hannington, M., Herzig, P., Stoffers, P., Scholten, J., Botz, R., Garbe-Schönberg, D., Jonasson, I.R., and Roest, W. (2001). First observations of high-temperature submarine hydrothermal vents and massive anhydrite deposits off the north coast of Iceland. Mar. Geol. *177*, 199–220.

Harley, S.L., and Kelly, N.M. (2007). Chapter 3.2 Ancient Antarctica: The Archaean of the East Antarctic Shield. In Developments in Precambrian Geology, M.J. van Kranendonk, R.H. Smithies, and V.C. Bennett, eds. (Elsevier), pp. 149–186.

He, L., Zhang, Y., Lin, F., Xu, Z., Li, X., and Sui, H. (2015). Image analysis of heavy oil liberation from host rocks/sands. Can. J. Chem. Eng. *93*, 1126–1137.

Heaney, P.J., Vicenzi, E.P., Giannuzzi, L.A., and Livi, K.J.T. (2015). Focused ion beam milling: A method of site-specific sample extraction for microanalysis of Earth and planetary materials. Am. Mineral. *86*, 1094–1099.

Hessler, A.M., and Lowe, D.R. (2006). Weathering and sediment generation in the Archean: An integrated study of the evolution of siliciclastic sedimentary rocks of the 3.2Ga Moodies Group, Barberton Greenstone Belt, South Africa. Precambrian Res. *151*, 185–210.

Hickman, A.H. (2012). Review of the Pilbara Craton and Fortescue Basin, Western Australia: Crustal evolution providing environments for early life. Isl. Arc *21*, 1–31.

Hofmann, A. (2005). The geochemistry of sedimentary rocks from the Fig Tree Group, Barberton greenstone belt: Implications for tectonic, hydrothermal and surface processes during mid-Archaean times. Precambrian Res. *143*, 23–49.

Hofmann, A. (2011). Archaean Hydrothermal Systems in the Barberton Greenstone Belt and Their Significance as a Habitat for Early Life. In Earliest Life on Earth: Habitats, Environments and Methods of Detection, (Springer, Dordrecht), pp. 51–78.

Hofmann, A., and Bolhar, R. (2007). Carbonaceous Cherts in the Barberton Greenstone Belt and Their Significance for the Study of Early Life in the Archean Record. Astrobiology *7*, 355–388.

Hofmann, A., and Harris, C. (2008). Silica alteration zones in the Barberton greenstone belt: A window into subseafloor processes 3.5–3.3 Ga ago. Chem. Geol. *257*, 221–239.

Hofmann, A., Uwe Reimold, W., and Koeberl, C. (2006). Archean spherule layers in the Barberton greenstone belt, South Africa: A discussion of problems related to the impact interpretation. In Special Paper 405: Processes on the Early Earth, (Geological Society of America), pp. 33–56.

Hofmann, A., Karykowski, B., Mason, P., Chunnet, G., and Arndt, N. (2013a). Barberton drilling project - Buck Reef Chert core BARB3. p. EGU2013.

Hofmann, A., Bolhar, R., Orberger, B., and Foucher, F. (2013b). Cherts of the Barberton Greenstone Belt, South Africa: Petrology and Trace-Element Geochemistry of 3.5 to 3.3 Ga Old Silicified Volcaniclastic Sediments. South Afr. J. Geol. *116*, 297–322.

Homann, M., Heubeck, C., Airo, A., and Tice, M.M. (2015). Morphological adaptations of 3.22 Ga-old tufted microbial mats to Archean coastal habitats (Moodies Group, Barberton Greenstone Belt, South Africa). Precambrian Res. *266*, 47–64.

Homann, M., Heubeck, C., Bontognali, T.R.R., Bouvier, A.-S., Baumgartner, L.P., and Airo, A. (2016). Evidence for cavity-dwelling microbial life in 3.22 Ga tidal deposits. Geology *44*, 51–54.

Igisu, M., Nakashima, S., Ueno, Y., Awramik, S.M., and Maruyama, S. (2006). In situ Infrared Microspectroscopy of ∼850 Million-Year-Old Prokaryotic Fossils. Appl. Spectrosc. *60*, 1111–1120.

Igisu, M., Ueno, Y., Shimojima, M., Nakashima, S., Awramik, S.M., Ohta, H., and Maruyama, S. (2009). Micro-FTIR spectroscopic signatures of Bacterial lipids in Proterozoic microfossils. Precambrian Res. *173*, 19–26.

Igisu, M., Ueno, Y., Nakashima, S., Awramik, S.M., and Maruyama, S. (2011). Micro-FTIR Spectroscopic Imaging of ~1,900 Ma Stromatolitic Chert. In STROMATOLITES: Interaction of Microbes with Sediments, (Springer, Dordrecht), pp. 445–461.

Igisu, M., Komiya, T., Kawashima, M., Nakashima, S., Ueno, Y., Han, J., Shu, D., Li, Y., Guo, J., Maruyama, S., et al. (2014). FTIR microspectroscopy of Ediacaran phosphatized microfossils from the Doushantuo Formation, Weng'an, South China. Gondwana Res. *25*, 1120–1138.

Iizuka, T., Komiya, T., and Maruyama, S. (2007). Chapter 3.1 The Early Archean Acasta Gneiss Complex: Geological, Geochronological and Isotopic Studies and Implications for Early Crustal Evolution. In Developments in Precambrian Geology, M.J. van Kranendonk, R.H. Smithies, and V.C. Bennett, eds. (Elsevier), pp. 127–147.

James, R.H., and Elderfield, H. (1996). Chemistry of ore-forming fluids and mineral formation rates in an active hydrothermal sulfide deposit on the Mid-Atlantic Ridge. Geology *24*, 1147–1150.

Javaux, E.J., Knoll, A.H., and Walter, M.R. (2004). TEM evidence for eukaryotic diversity in mid-Proterozoic oceans. Geobiology *2*, 121–132.

Javaux, E.J., Marshall, C.P., and Bekker, A. (2010). Organic-walled microfossils in 3.2-billion-year-old shallow-marine siliciclastic deposits. Nature *463*, 934–938.

Jehlička, J., Urban, O., and Pokorný, J. (2003). Raman spectroscopy of carbon and solid bitumens in sedimentary and metamorphic rocks. Spectrochim. Acta. A. Mol. Biomol. Spectrosc. *59*, 2341–2352.

Kamenetsky, V.S., Achterbergh, E. van, Ryan, C.G., Naumov, V.B., Mernagh, T.P., and Davidson, P. (2002). Extreme chemical heterogeneity of granite-derived hydrothermal fluids: An example from inclusions in a single crystal of miarolitic quartz. Geology *30*, 459–462.

Kelly, S.R., Ditchfield, P.W., Doubleday, P.A., and Marshall, J.D. (1995). An Upper Jurassic methane-seep limestone from the fossil Bluff Group forearc basin of Alexander Island, Antarctica. J. Sediment. Res. *65*.

Kempe, A., Wirth, R., Altermann, W., Stark, R.W., Schopf, J.W., and Heckl, W.M. (2005). Focussed ion beam preparation and in situ nanoscopic study of Precambrian acritarchs. Precambrian Res. *140*, 36–54.

Kim, D.-Y., Nishiyama, Y., Wada, M., and Kuga, S. (2001). Graphitization of highly crystalline cellulose. Carbon *39*, 1051–1056.

Kiyokawa, S., Ito, T., Ikehara, M., and Kitajima, F. (2006). Middle Archean volcano-hydrothermal sequence: Bacterial microfossil-bearing 3.2 Ga Dixon Island Formation, coastal Pilbara terrane, Australia. Geol. Soc. Am. Bull. *118*, 3–22.

Knauth, L.P., and Epstein, S. (1976). Hydrogen and oxygen isotope ratios in nodular and bedded cherts. Geochim. Cosmochim. Acta *40*, 1095–1108.

Knoll, A.H., and Barghoorn, E.S. (1977). Archean Microfossils Showing Cell Division from the Swaziland System of South Africa. Science *198*, 396–398.

Knoll, A.H., Strother, P.K., and Rossi, S. (1988). Distribution and diagenesis of microfossils from the lower proterozoic duck creek dolomite, Western Australia. Precambrian Res. *38*, 257–279.

Köhler, I., Konhauser, K.O., Papineau, D., Bekker, A., and Kappler, A. (2013). Biological carbon precursor to diagenetic siderite with spherical structures in iron formations. Nat. Commun. *4*, 1741.

Komiya, T., Yamamoto, S., Aoki, S., Sawaki, Y., Ishikawa, A., Tashiro, T., Koshida, K., Shimojo, M., Aoki, K., and Collerson, K.D. (2015). Geology of the Eoarchean, >3.95Ga, Nulliak supracrustal rocks in the Saglek Block, northern Labrador, Canada: The oldest geological evidence for plate tectonics. Tectonophysics *662*, 40–66.

Konhauser, K.O., Hamade, T., Raiswell, R., Morris, R.C., Ferris, F.G., Southam, G., and Canfield, D.E. (2002). Could bacteria have formed the Precambrian banded iron formations? Geology *30*, 1079–1082.

Kouketsu, Y., Mizukami, T., Mori, H., Endo, S., Aoya, M., Hara, H., Nakamura, D., and Wallis, S. (2014). A new approach to develop the Raman carbonaceous material geothermometer for low-grade metamorphism using peak width. Isl. Arc *23*, 33–50.

Kranendonk, M.J.V. (2011). Morphology as an Indictor of Biogenicity for 3.5–3.2 Ga Fossil Stromatolites from the Pilbara Craton, Western Australia. In Advances in Stromatolite Geobiology, (Springer, Berlin, Heidelberg), pp. 537–554.

Kranendonk, M.J. van, Bennett, V., and Smithies, H.R.H. (2007). Earth's Oldest Rocks (Elsevier).

Kranidiotis, P., and MacLean, W.H. (1987). Systematics of chlorite alteration at the Phelps Dodge massive sulfide deposit, Matagami, Quebec. Econ. Geol. *82*, 1898–1911.

Kremer, B., and Kaźmierczak, J. (2017). Cellularly preserved microbial fossils from ∼3.4Ga deposits of South Africa: A testimony of early appearance of oxygenic life? Precambrian Res. *295*, 117–129.

Krüner, A., Byerly, G.R., and Lowe, D.R. (1991). Chronology of early Archaean granite-greenstone evolution in the Barberton Mountain Land, South Africa, based on precise dating by single zircon evaporation. Earth Planet. Sci. Lett. *103*, 41–54.

Kudryavtsev, A.B., Schopf, J.W., Agresti, D.G., and Wdowiak, T.J. (2001). In situ laser-Raman imagery of Precambrian microscopic fossils. Proc. Natl. Acad. Sci. *98*, 823–826.

Lahfid, A., Beyssac, O., Deville, E., Negro, F., Chopin, C., and Goffé, B. (2010). Evolution of the Raman spectrum of carbonaceous material in low-grade metasediments of the Glarus Alps (Switzerland). Terra Nova *22*, 354–360.

Ledevin, M., Arndt, N., Simionovici, A., Jaillard, E., and Ulrich, M. (2014). Silica precipitation triggered by clastic sedimentation in the Archean: New petrographic evidence from cherts of the Kromberg type section, South Africa. Precambrian Res. *255*, 316–334.

Ledevin, M., Arndt, N., Davaille, A., Ledevin, R., and Simionovici, A. (2015). The rheological behaviour of fracture-filling cherts: example of Barite Valley dikes, Barberton Greenstone Belt, South Africa. Solid Earth *6*, 253.

Lowe, D.R. (1999). Petrology and sedimentology of cherts and related silicified sedimentary rocks in the Swaziland Supergroup. Geol. Evol. Barberton Greenstone Belt South Afr. Geol. Soc. Am. Spec. Pap. *329*, 83–114.

Lowe, D.R., and Byerly, G.R. (1999). Geologic Evolution of the Barberton Greenstone Belt, South Africa (Geological Society of America).

Lowe, D.R., and Byerly, G.R. (2003). Ironstone pods in the Archean Barberton greenstone belt, South Africa: Earth's oldest seafloor hydrothermal vents reinterpreted as Quaternary subaerial springs. Geology *31*, 909–912.

Lowe, D.R., and Knauth, L.P. (1977). Sedimentology of the Onverwacht Group (3.4 Billion Years), Transvaal, South Africa, and Its Bearing on the Characteristics and Evolution of the Early Earth. J. Geol. *85*, 699–723.

Lowe, D.R., and Tice, M.M. (2007). Tectonic controls on atmospheric, climatic, and biological evolution 3.5–2.4Ga. Precambrian Res. *158*, 177–197.

Lowe, D.R., and Worrell, G.F. (1999). Sedimentology, mineralogy, and implications of silicified evaporites in the Kromberg Formation, Barberton Greenstone Belt, South Africa. In Special Paper 329: Geologic Evolution of the Barberton Greenstone Belt, South Africa, (Geological Society of America), pp. 167–188.

Lowe, D.R., Byerly, G.R., Kyte, F.T., Shukolyukov, A., Asaro, F., and Krull, A. (2003). Spherule Beds 3.47–3.24 Billion Years Old in the Barberton Greenstone Belt, South Africa: A Record of Large Meteorite Impacts and Their Influence on Early Crustal and Biological Evolution. Astrobiology *3*, 7–48.

Lünsdorf, N.K., Dunkl, I., Schmidt, B.C., Rantitsch, G., and von Eynatten, H. (2014). Towards a Higher Comparability of Geothermometric Data obtained by Raman Spectroscopy of Carbonaceous Material. Part I: Evaluation of Biasing Factors. Geostand. Geoanalytical Res. *38*, 73–94.

MacLean, W.H., and Kranidiotis, P. (1987). Immobile elements as monitors of mass transfer in hydrothermal alteration; Phelps Dodge massive sulfide deposit, Matagami, Quebec. Econ. Geol. *82*, 951–962.

Madigan, M.T., Martinko, J.M., Parker, J., and Brock, T.D. (1997). Biology of microorganisms (prentice hall Upper Saddle River, NJ).

Maliva, R.G., Knoll, A.H., and Simonson, B.M. (2005). Secular change in the Precambrian silica cycle: Insights from chert petrology. GSA Bull. *117*, 835–845.

Marchev, P., Singer, B.S., Jelev, D., Hasson, S., Moritz, R., and Bonev, N. (2004). The Ada Tepe deposit: a sediment-hosted, detachment fault-controlled, low-sulfidation gold deposit in the Eastern Rhodopes, SE Bulgaria. Swiss Bull. Mineral. Petrol. *84*, 59–78.

Marinova, I., Ganev, V., and Titorenkova, R. (2014). Colloidal origin of colloform-banded textures in the Paleogene low-sulfidation Khan Krum gold deposit, SE Bulgaria. Miner. Deposita *49*, 49–74.

Marshall, A.O., Emry, J.R., and Marshall, C.P. (2012). Multiple Generations of Carbon in the Apex Chert and Implications for Preservation of Microfossils. Astrobiology *12*, 160–166.

Marshall, C.P., Love, G.D., Snape, C.E., Hill, A.C., Allwood, A.C., Walter, M.R., Van Kranendonk, M.J., Bowden, S.A., Sylva, S.P., and Summons, R.E. (2007). Structural characterization of kerogen in 3.4 Ga Archaean cherts from the Pilbara Craton, Western Australia. Precambrian Res. *155*, 1–23.

Marshall, C.P., Edwards, H.G.M., and Jehlicka, J. (2010). Understanding the Application of Raman Spectroscopy to the Detection of Traces of Life. Astrobiology *10*, 229–243.

Maurette, M., Brack, A., Duprat, J., and Engrand, C. (2006). Kerogen-rich Micrometeorites and Crude Petroleum in Hadean Time. p.

Mazzini, A., Ivanov, M.K., Parnell, J., Stadnitskaia, A., Cronin, B.T., Poludetkina, E., Mazurenko, L., and van Weering, T.C.E. (2004). Methane-related authigenic carbonates from the Black Sea: geochemical characterisation and relation to seeping fluids. Mar. Geol. *212*, 153–181.

Moczydłowska, M., and Willman, S. (2009). Ultrastructure of cell walls in ancient microfossils as a proxy to their biological affinities. Precambrian Res. *173*, 27–38.

Mojzsis, S.J., and Harrison, T.M. (2002). Establishment of a 3.83-Ga magmatic age for the Akilia tonalite (southern West Greenland). Earth Planet. Sci. Lett. *202*, 563–576.

Nakamura, K., Zolensky, M.E., Tomita, S., Nakashima, S., and Tomeoka, K. (2002). Hollow organic globules in the Tagish Lake meteorite as possible products of primitive organic reactions. Int. J. Astrobiol. *1*, 179–189.

Nakashima, S. (1992a). Complexation and reduction of uranium by lignite. Sci. Total Environ. *117–118*, 425–437.

Nakashima, S. (1992b). Kinetics and thermodynamics of U reduction by natural and simple organic matter. Org. Geochem. *19*, 421–430.

Noffke, N. (2010). Geobiology: Microbial Mats in Sandy Deposits from the Archean Era to Today (Springer Science & Business Media).

Noffke, N., Eriksson, K.A., Hazen, R.M., and Simpson, E.L. (2006). A new window into Early Archean life: Microbial mats in Earth's oldest siliciclastic tidal deposits (3.2 Ga Moodies Group, South Africa). Geology *34*, 253–256.

Noffke, N., Christian, D., Wacey, D., and Hazen, R.M. (2013). Microbially Induced Sedimentary Structures Recording an Ancient Ecosystem in the ca. 3.48 Billion-Year-Old Dresser Formation, Pilbara, Western Australia. Astrobiology *13*, 1103–1124.

Nutman, A., Friend, C., and Bennett, V.C. (2001). Review of the oldest (4400-3600 Ma) geological and mineralogical record: Glimpses of the beginning.

Nutman, A.P., Friend, C.R.L., Kinny, P.D., and McGregor, V.R. (1993). Anatomy of an Early Archean gneiss complex: 3900 to 3600 Ma crustal evolution in southern West Greenland. Geology *21*, 415–418.

Nutman, A.P., Friend, C.R.L., Horie, K., and Hidaka, H. (2007). Chapter 3.3 The Itsaq Gneiss Complex of Southern West Greenland and the Construction of Eoarchaean Crust at Convergent Plate Boundaries. In Developments in Precambrian Geology, M.J. van Kranendonk, R.H. Smithies, and V.C. Bennett, eds. (Elsevier), pp. 187–218.

Nutman, A.P., Bennett, V.C., Friend, C.R.L., Kranendonk, M.J.V., and Chivas, A.R. (2016). Rapid emergence of life shown by discovery of 3,700-million-year-old microbial structures. Nature *537*, 535.

Oehler, D.Z., and Cady, S.L. (2014). Biogenicity and Syngeneity of Organic Matter in Ancient Sedimentary Rocks: Recent Advances in the Search for Evidence of Past Life. Challenges *5*, 260–283.

Ogg, J.G., Ogg, G., and Gradstein, F.M. (2016). A Concise Geologic Time Scale: 2016 (Elsevier).

Ohmoto, H., Watanabe, Y., and Kumazawa, K. (2004). Evidence from massive siderite beds for a CO_2-rich atmosphere before ~ 1.8 billion years ago. Nature *429*, 395.

Olcott Marshall, A., and Marshall, C.P. (2015). Vibrational spectroscopy of fossils. Palaeontology *58*, 201–211.

Olcott Marshall, A., Jehlička, J., Rouzaud, J.-N., and Marshall, C.P. (2014). Multiple generations of carbonaceous material deposited in Apex chert by basin-scale pervasive hydrothermal fluid flow. Gondwana Res. *25*, 284–289.

O'Neil, J., Carlson, R.W., Paquette, J.-L., and Francis, D. (2012). Formation age and metamorphic history of the Nuvvuagittuq Greenstone Belt. Precambrian Res. *220–221*, 23–44.

Paris, I., Stanistreet, I.G., and Hughes, M.J. (1985). Cherts of the Barberton Greenstone Belt Interpreted as Products of Submarine Exhalative Activity. J. Geol. *93*, 111–129.

Pasteris, J.D., and Wopenka, B. (1991). Raman spectra of graphite as indicators of degree of metamorphism. Can. Mineral. *29*, 1–9.

Pflug, H.D. (1967). Structured organic remains from the Fig Tree Series (Precambrian) of the Barberton mountain land (South Africa). Rev. Palaeobot. Palynol. *5*, 9–29.

Pratt, B.R. (1995). The origin, biota and evolution of deep-water mud-mounds. Carbonate Mud-Mounds Their Orig. Evol. Spec Publ Int Assoc Sedimentol. *23*, 49–123.

Preston, L. j., Izawa, M. r. m., and Banerjee, N. r. (2011). Infrared Spectroscopic Characterization of Organic Matter Associated with Microbial Bioalteration Textures in Basaltic Glass. Astrobiology *11*, 585–599.

Qu, Y., Engdahl, A., Zhu, S., Vajda, V., and McLoughlin, N. (2015). Ultrastructural Heterogeneity of Carbonaceous Material in Ancient Cherts: Investigating Biosignature Origin and Preservation. Astrobiology *15*, 825–842.

Qu, Y., Wang, J., Xiao, S., Whitehouse, M., Engdahl, A., Wang, G., and McLoughlin, N. (2017). Carbonaceous biosignatures of diverse chemotrophic microbial communities from chert nodules of the Ediacaran Doushantuo Formation. Precambrian Res. *290*, 184–196.

Quirico, E., Montagnac, G., Rouzaud, J.-N., Bonal, L., Bourot-Denise, M., Duber, S., and Reynard, B. (2009). Precursor and metamorphic condition effects on Raman spectra of poorly ordered carbonaceous matter in chondrites and coals. Earth Planet. Sci. Lett. *287*, 185–193.

Raman, C.V. (1928). A new radiation.

Raman, C.V. (1930). Nobel lecture. In Proc Phys Soc, pp. 309–320.

Rasmussen, B., Meier, D.B., Krapež, B., and Muhling, J.R. (2013). Iron silicate microgranules as precursor sediments to 2.5-billion-year-old banded iron formations. Geology *41*, 435–438.

Rasmussen, B., 2000. Filamentous microfossils in a 3,235-million-year-old volcanogenic massive sulphide deposit: *Nature*, **405**, p. 676–679, doi: 10.1038/35015063.

Rasmussen, B., Muhling, J.R., Suvorova, A., and Krapež, B. (2017). Greenalite precipitation linked to the deposition of banded iron formations downslope from a late Archean carbonate platform. Precambrian Res. *290*, 49–62.

Reed, S.J.B. (2005). Electron microprobe analysis and scanning electron microscopy in geology (Cambridge University Press).

Rochdi, A., and Landais, P. (1991). Transmission micro-infrared spectroscopy: An efficient tool for microscale characterization of coal. Fuel *70*, 367–371.

Ronde, C.E.J.D., Wit, M.J.D., and Spooner, E.T.C. (1994). Early Archean (>3.2 Ga) Fe-oxide-rich, hydrothermal discharge vents in the Barberton greenstone belt, South Africa. GSA Bull. *106*, 86–104.

Sadezky, A., Muckenhuber, H., Grothe, H., Niessner, R., and Pöschl, U. (2005). Raman microspectroscopy of soot and related carbonaceous materials: Spectral analysis and structural information. Carbon *43*, 1731–1742.

Salzer, R., and Siesler, H.W. (2009). Infrared and Raman spectroscopic imaging (John Wiley & Sons).

Savard, M.M., Beauchamp, B., and Veizer, J. (1996). Significance of aragonite cements around Cretaceous marine methane seeps. J. Sediment. Res. *66*.

Schopf, J.W. (1993). Microfossils of the Early Archean Apex Chert: New Evidence of the Antiquity of Life. Science *260*, 640–646.

Schopf, J.W. (2006). Fossil evidence of Archaean life. Philos. Trans. R. Soc. B Biol. Sci. *361*, 869–885.

Schopf, J.W., and Kudryavtsev, A.B. (2009). Confocal laser scanning microscopy and Raman imagery of ancient microscopic fossils. Precambrian Res. *173*, 39–49.

Schopf, J.W., Kudryavtsev, A.B., Czaja, A.D., and Tripathi, A.B. (2007). Evidence of Archean life: Stromatolites and microfossils. Precambrian Res. *158*, 141–155.

Schrader, B., Dippel, B., Erb, I., Keller, S., Löchte, T., Schulz, H., Tatsch, E., and Wessel, S. (1999). NIR Raman spectroscopy in medicine and biology: results and aspects. J. Mol. Struct. *480–481*, 21–32.

Sforna, M.C., van Zuilen, M.A., and Philippot, P. (2014). Structural characterization by Raman hyperspectral mapping of organic carbon in the 3.46 billion-year-old Apex chert, Western Australia. Geochim. Cosmochim. Acta *124*, 18–33.

Shinn, E.A. (1983). Birdseyes, Fenestrae, Shrinkage Pores, and Loferites: A Reevaluation. J. Sediment. Res. *53*.

Simoneit, B.R.T., and Lonsdale, P.F. (1982). Hydrothermal petroleum in mineralized mounds at the seabed of Guaymas Basin. Nature *295*, 198.

Southam, G., and Donald, R. (1999). A structural comparison of bacterial microfossils vs. `nanobacteria' and nanofossils. Earth-Sci. Rev. *48*, 251–264.

Suárez-Ruiz, I., Juliao, T., Suárez-García, F., Marquez, R., and Ruiz, B. (2016). Porosity development and the influence of pore size on the CH4 adsorption capacity of a shale oil reservoir (Upper Cretaceous) from Colombia. Role of solid bitumen. Int. J. Coal Geol. *159*, 1–17.

Sugitani, K., Mimura, K., Nagaoka, T., Lepot, K., and Takeuchi, M. (2013). Microfossil assemblage from the 3400Ma Strelley Pool Formation in the Pilbara Craton, Western Australia: Results form a new locality. Precambrian Res. *226*, 59–74.

Sugitani, K., Mimura, K., Takeuchi, M., Yamaguchi, T., Suzuki, K., Senda, R., Asahara, Y., Wallis, S., and Van Kranendonk, M.J. (2015). A Paleoarchean coastal hydrothermal field inhabited by diverse microbial communities: the Strelley Pool Formation, Pilbara Craton, Western Australia. Geobiology *13*, 522–545.

Tashiro, T., Ishida, A., Hori, M., Igisu, M., Koike, M., Méjean, P., Takahata, N., Sano, Y., and Komiya, T. (2017). Early trace of life from 3.95 Ga sedimentary rocks in Labrador, Canada. Nature *549*, 516.

Tice, M.M. (2009). Environmental Controls on Photosynthetic Microbial Mat Distribution and Morphogenesis on a 3.42 Ga Clastic-Starved Platform. Astrobiology *9*, 989–1000.

Tice, M.M., and Lowe, D.R. (2004). Photosynthetic microbial mats in the 3,416-Myr-old ocean. Nature *431*, 549–552.

Tice, M.M., and Lowe, D.R. (2006a). Hydrogen-based carbon fixation in the earliest known photosynthetic organisms. Geology *34*, 37–40.

Tice, M.M., and Lowe, D.R. (2006b). The origin of carbonaceous matter in pre-3.0 Ga greenstone terrains: A review and new evidence from the 3.42 Ga Buck Reef Chert. Earth-Sci. Rev. *76*, 259–300.

Tice, M.M., Bostick, B.C., and Lowe, D.R. (2004). Thermal history of the 3.5–3.2 Ga Onverwacht and Fig Tree Groups, Barberton greenstone belt, South Africa, inferred by Raman microspectroscopy of carbonaceous material. Geology *32*, 37–40.

Tice, M.M., Thornton, D.C.O., Pope, M.C., Olszewski, T.D., and Gong, J. (2011). Archean Microbial Mat Communities. Annu. Rev. Earth Planet. Sci. *39*, 297–319.

Trewin, N.H., Fayers, S.R., and Kelman, R. (2003). Subaqueous silicification of the contents of small ponds in an Early Devonian hot-spring complex, Rhynie, Scotland. Can. J. Earth Sci. *40*, 1697–1712.

Tucker, M.E. (2009). Sedimentary petrology: an introduction to the origin of sedimentary rocks (John Wiley & Sons).

Ueno, Y., Yoshioka, H., Maruyama, S., and Isozaki, Y. (2004). Carbon isotopes and petrography of kerogens in ~3.5-Ga hydrothermal silica dikes in the North Pole area, Western Australia1 1Associate editor: G. Cody. Geochim. Cosmochim. Acta *68*, 573–589.

Van Kranendonk, M.J. (2006). Volcanic degassing, hydrothermal circulation and the flourishing of early life on Earth: A review of the evidence from c. 3490-3240 Ma rocks of the Pilbara Supergroup, Pilbara Craton, Western Australia. Earth-Sci. Rev. *74*, 197–240.

Van Kranendonk, M.J. (2007). Chapter 7.2 A Review of the Evidence for Putative Paleoarchean Life in the Pilbara Craton, Western Australia. In Developments in Precambrian Geology, M.J. van Kranendonk, R.H. Smithies, and V.C. Bennett, eds. (Elsevier), pp. 855–877.

Van Kranendonk, M.J., Webb, G.E., and Kamber, B.S. (2003). Geological and trace element evidence for a marine sedimentary environment of deposition and biogenicity of 3.45 Ga stromatolitic carbonates in the Pilbara Craton, and support for a reducing Archaean ocean. Geobiology *1*, 91–108.

Viljoen, M.J., and Viljoen, R. (1969). An introduction to the geology of the Barberton granite-greenstone terrain. Geol. Soc. South Afr. Spec. Publ. *2*, 9–28.

de Vries, S.T., and Touret, J.L.R. (2007). Early Archaean hydrothermal fluids; a study of inclusions from the ~3.4 Ga Buck Ridge Chert, Barberton Greenstone Belt, South Africa. Chem. Geol. *237*, 289–302.

de Vries, S.T., Nijman, W., and Armstrong, R.A. (2006). Growth-fault structure and stratigraphic architecture of the Buck Ridge volcano-sedimentary complex, upper Hooggenoeg Formation, Barberton Greenstone Belt, South Africa. Precambrian Res. *149*, 77–98.

de Vries, S.T., Nijman, W., and de Boer, P.L. (2010). Sedimentary geology of the Palaeoarchaean Buck Ridge (South Africa) and Kittys Gap (Western Australia) volcano-sedimentary complexes. Precambrian Res. *183*, 749–769.

Vries, Sjoukje Tsjitske de, and University Utrecht (2004). Early Archaean sedimentary basins: depositional environment and hydrothermal systems : Utrecht University.

Wacey, D. (2009). Early life on earth: a practical guide (Springer Science & Business Media).

Wacey, D. (2010). Stromatolites in the ~3400 Ma Strelley Pool Formation, Western Australia: Examining Biogenicity from the Macro- to the Nano-Scale. Astrobiology *10*, 381–395.

Wacey, D. (2012). Earliest evidence for life on Earth: an Australian perspective. Aust. J. Earth Sci. *59*, 153–166.

Wacey, D., Mcloughlin, N., and Brasier, M.D. (2009). Looking Through Windows onto the Earliest History of Life on Earth and Mars. In From Fossils to Astrobiology, (Springer, Dordrecht), pp. 39–68.

Wacey, D., Menon, S., Green, L., Gerstmann, D., Kong, C., Mcloughlin, N., Saunders, M., and Brasier, M. (2012). Taphonomy of very ancient microfossils from the ∼3400Ma Strelley Pool Formation and ∼1900Ma Gunflint Formation: New insights using a focused ion beam. Precambrian Res. *220–221*, 234–250.

Wacey, D., Menon, S., Green, L., Gerstmann, D., Kong, C., Mcloughlin, N., Saunders, M. and Brasier, M., 2012. Taphonomy of very ancient microfossils from the ∼3400Ma Strelley Pool Formation and ∼1900Ma Gunflint Formation: New insights using a focused ion beam: *Precambrian Research*, **220**–**221**, p. 234–250, doi: 10.1016/j.precamres.2012.08.005.

Wacey, D., Battison, L., Garwood, R.J., Hickman-Lewis, K., and Brasier, M.D. (2017). Advanced analytical techniques for studying the morphology and chemistry of Proterozoic microfossils. Geol. Soc. Lond. Spec. Publ. *448*, 81–104.

Walsh, M.M. (2004). Evaluation of Early Archean Volcaniclastic and Volcanic Flow Rocks as Possible Sites for Carbonaceous Fossil Microbes. Astrobiology *4*, 429–437.

Walsh, M.M. (2010). Microbial Mats on the Early Earth: The Archean Rock Record. In Microbial Mats, (Springer, Dordrecht), pp. 41–51.

Walsh, M.W. (1992). Microfossils and possible microfossils from the early archean onverwacht group, Barberton mountain land, South Africa. Precambrian Res. *54*, 271–293.

Walsh, M.M., and Lowe, D.R. (1985). Filamentous microfossils from the 3,500-Myr-old Onverwacht Group, Barberton Mountain Land, South Africa. Nature *314*, 530–532.

Walsh, M.M., and Lowe, D.R. (1999). Modes of accumulation of carbonaceous matter in the early Archean: A petrographic and geochemical study of the carbonaceous cherts of the Swaziland Supergroup. Spec. Pap.-Geol. Soc. Am. 115–132.

Walsh, M.M., and Westall, F. (2003). Archean Biofilms Preserved in the Swaziland Supergroup, South Africa. In Fossil and Recent Biofilms, W.E. Krumbein, D.M. Paterson, and G.A. Zavarzin, eds. (Springer Netherlands), pp. 307–316.

Wang, Y., Alsmeyer, D.C., and McCreery, R.L. (1990). Raman spectroscopy of carbon materials: structural basis of observed spectra. Chem. Mater. *2*, 557–563.

Watt, I.M. (1997). The principles and practice of electron microscopy (Cambridge University Press).

Westall, F., Ronde, C.E.J. de, Southam, G., Grassineau, N., Colas, M., Cockell, C., and Lammer, H. (2006). Implications of a 3.472–3.333 Gyr-old subaerial microbial mat from the Barberton greenstone belt, South Africa for the UV environmental conditions on the early Earth. Philos. Trans. R. Soc. Lond. B Biol. Sci. *361*, 1857–1876.

Westall, F., Cavalazzi, B., Lemelle, L., Marrocchi, Y., Rouzaud, J.-N., Simionovici, A., Salomé, M., Mostefaoui, S., Andreazza, C., Foucher, F., et al. (2011). Implications of in situ calcification for photosynthesis in a ~3.3Ga-old microbial biofilm from the Barberton greenstone belt, South Africa. Earth Planet. Sci. Lett. *310*, 468–479.

Westall, F., de Wit, M.J., Dann, J., van der Gaast, S., de Ronde, C.E.J. and Gerneke, D., 2001. Early Archean fossil bacteria and biofilms in hydrothermally-influenced sediments from the Barberton greenstone belt, South Africa: *Precambrian Research*, **106**, p. 93–116, doi: 10.1016/S0301-9268(00)00127-3.

Westall, F., Campbell, K.A., Bréhéret, J.G., Foucher, F., Gautret, P., Hubert, A., Sorieul, S., Grassineau, N., and Guido, D.M. (2015). Archean (3.33 Ga) microbe-sediment systems were diverse and flourished in a hydrothermal context. Geology *43*, 615–618.

Wirth, R. (2009). Focused Ion Beam (FIB) combined with SEM and TEM: Advanced analytical tools for studies of chemical composition, microstructure and crystal structure in geomaterials on a nanometre scale. Chem. Geol. *261*, 217–229.

Wit, M.J. de, Hart, R., Martin, A., and Abbott, P. (1982). Archean abiogenic and probable biogenic structures associated with mineralized hydrothermal vent systems and regional metasomatism, with implications for greenstone belt studies. Econ. Geol. *77*, 1783–1802.

Wopenka, B., and Pasteris, J.D. (1993). Structural characterization of kerogens to granulite-facies graphite : applicability of Raman microprobe spectroscopy. Am. Mineral. *78*, 533–557.

Yui, T.-F., Huang, E., and Xu, J. (1996). Raman spectrum of carbonaceous material: a possible metamorphic grade indicator for low-grade metamorphic rocks. J. Metamorph. Geol. *14*, 115–124.

Zegers, De Wit, Dann, and White (1998). Vaalbara, Earth's oldest assembled continent? A combined structural, geochronological, and palaeomagnetic test. Terra Nova *10*, 250–259.

Zhang, R. (1986). Sulfur isotopes and pyrite-anhydrite equilibria in a volcanic basin hydrothermal system of the middle to lower Yangtze River valley. Econ. Geol. *81*, 32–45.

Supplementary material

S1 – BARB3 samples

Crinkly laminated chert (clc), White chert (Wc), Stratiform botryoidal vein (Sbv), Granular carbonaceous chert (Gcc), Massive black chert (Mbc), Laminated black chert (Lbc), Siderite bands (Sb), Jasperlite bands (Jsp), Fractured chert (Fc).

	Core sample	Depth		Box	Section	Facies	Core survey	Optical	IR		Raman	SEM	TEM
		From	To						in situ	bulk			
v	F13	896.59	896.41	119	F13A	Clc	✔	✔	-	-	✔	✔	-
		896.59	896.41	119	F13B	Clc	✔	✔	✔	-	✔	✔	✔
	D1	896	895.9	119	D1	Clc	✔	✔	✔	-	✔	✔	-
	F12	895.9	895.67	119	F12	Clc -Wc-Sbv	✔	✔	-	-	✔	✔	-
	F11	894.52	894.35	119	F11A	Clc	✔	✔	-	-	✔	-	-
		894.52	894.35	119	F11B	Clc	✔	✔	-	-	✔	✔	-
	C9	889.10	888.86	118	C9A	Gcc-Wc	✔	✔	-	-	✔	✔	-
		889.10	888.86	118	C9B	Clc	✔	✔	-	-	✔	-	-
		889.10	888.86	118	C9C	Clc-Wc	✔	✔	-	-	✔	✔	-
		889.10	888.86	118	C9D	Clc-Mbc	✔	✔	-	✔	✔	✔	-
		889.10	888.86	118	C9E	Mbc	✔	✔	-	-	✔	✔	-
	F10	887.54	887.30	118	F10A	Clc	✔	✔	-	-	✔	-	-
		887.54	887.30	118	F10B	Clc	✔	✔	-	-	✔	✔	-
		887.54	887.30	118	F10C	Clc	✔	✔	-	-	✔	-	-
Shallow	D4	869.8	869.67	116	D4A	Wc-Gcc	✔	✔	-	-	✔	-	-
		869.8	869.67	116	D4B	Clc	✔	✔	-	-	✔	✔	-
	C8	865.76	865.63	115	C8A	Mbc	✔	✔	-	-	✔	-	-
		865.76	865.63	115	C8B	Mbc-Clc	✔	✔	-	-	✔	-	-
		865.76	865.63	115	C8C	Clc	✔	✔	-	-	✔	-	-
	C7	857.19	857.06	114	C7A	Wc-Clc-Gcc	✔	✔	-	-	✔	-	-
		857.19	857.06	114	C7B	Gcc-Sbv-Wc	✔	✔	✔	-	✔	-	-
	D5	845.06	844.91	113	D5	Clc	✔	✔	-	-	✔	-	-
	D6	824.9	824.78	110	D6	Mbc-Clcc	✔	✔	-	-	✔	-	-
	D7	801.28	801.12	108	D7	Gcc	✔	✔	-	-	-	-	-
	C6	800	799.82	107	C6Z	Wc	✔	✔	-	-	-	-	-
		800	799.82	107	C6A	Wc-Clc-Gcc-Sbv	✔	✔	-	-	-	-	-
		800	799.82	107	C6B	Gcc-Sbv-Wc-Clc	✔	✔	✔	-	✔	-	-
		799	799.81	106	C6C	Gcc-Sbv-Wc-Clc	✔	✔	✔	-	✔	-	-
^		800	799.82	107	C6D	Gcc-Sbv-Wc-Clc	✔	✔	-	-	✔	✔	✔

	Core sample	Depth		Box	Section	Facies	Core survey	Optical	IR		Raman	SEM	TEM
Shallow	C5	794.39	794.12	107	C5A	Wc-Gcc	✔	✔	-	-	-	-	-
		794.39	794.12	107	C5B	Wc-Gcc	✔	✔	-	-	-	-	-
		794.39	794.12	107	C5C	Wc-Mbc	✔	✔	-	-	-	-	-
		794.39	794.12	107	C5D	Wc-Mbc-Sbv	✔	✔	-	-	-	-	-
	D11	762.38	761.91	103	D11A	Clc	✔	✔	✔	-	✔	✔	-
		762.38	761.91	103	D11B	Clc	✔	✔	-	-	✔	-	-
	F9	762.38	761.91	103	F9	Clc	✔	✔	✔	-	✔	-	-
	C4	754.80	754.57	102	C4A	Wc-Clc-Gcc	✔	✔	-	-	✔	-	-
		754.80	754.57	102	C4B	Wc-Clc-Gcc	✔	✔	-	-	✔	-	-
		754.80	754.57	102	C4C	Wc	✔	✔	-	-	✔	-	-
	D12	712.06	711.85	96	D12	Wc-Clc	✔	✔	-	-	✔	-	-
	C3	708.18	707.97	95	C3A	Clc-Wc-Gc	✔	✔	✔	✔	✔	-	-
		708.18	707.97	95	C3B	Clc-Wc-Gc-Sbv	✔	✔	✔	-	✔	-	-
		708.18	707.97	95	C3C	Clc-Wc-Gc-Sbv	✔	✔	✔	-	✔	-	-
	D13	699.28	699.1	93	D13	Wc-Lbc	✔	✔	-	-	-	-	-
	D15	664.04	663.79	88	D15A	Wc-Clc-Gcc	✔	✔	-	-	-	-	-
		664.04	663.79	88	D15B	Wc-Gcc	✔	✔	-	-	-	-	-
	F8	632.06	631.90	83	F8A	Wc-Clc	✔	✔	-	-	✔	-	-
		632.06	631.90	83	F8B	Wc-Clc	✔	✔	-	-	✔	-	-
	C2	620.17	620.02	83	C2A	Gcc	✔	✔	-	-	✔	-	-
		620.17	620.02	83	C2B	Gcc-Sbv	✔	✔	✔	-	✔	-	-
		620.17	620.02	83	C2C	Lbc	✔	✔	-	-	✔	-	-
Deep	F7	583.03	582.79	79	F7	Sb-Wc	✔	✔	-	-	-	-	-
	F6	554.54	554.42	74	F6	Sb-Wc	✔	✔	-	-	-	-	-
	F5	538.30	538.08	72	F5	Sb-Wc-Jsp	✔	✔	-	-	✔	✔	-
	F4	471.48	471.26	62	F4	Sb-Wc-Jsp	✔	✔	-	-	✔	✔	-
	F3	419.13	418.88	55	F3A	Sb-Wc	✔	✔	-	-	-	-	-
		419.13	418.88	55	F3B	Sb-Wc	✔	✔	-	-	-	-	-

< Shallow >	C1	331.17	331.02	44	C1A	Fc	✔	✔	-	-	✔	-	-
		331.17	331.02	44	C1B	Fc	✔	✔	✔	-	✔	-	-
		331.17	331.02	44	C1C	Fc	✔	✔	-	-	-	-	-
	F2	256.29	256.10	33	F2	Wc-Clc	✔	✔	-	-	-	-	-
	F1	250.77	250.61	32	F1	Wc-Clc	✔	✔	-	-	✔	-	-

S1 – Raman dataset

				Lorentzian (D4)				Lorentzian (D1)			
Facies	Sample	CM microtexture	N	A	ω	I	Γ	A	ω	I	Γ
Crinkly laminated chert	D11A	Mat-like laminae	1	101632.30	1193.91	393.50	193.78	675314.23	1355.32	7749.18	57.84
Crinkly laminated chert	D11A	Mat-like laminae	2	116163.98	1196.65	483.03	177.80	862288.09	1355.12	9781.46	58.54
Crinkly laminated chert	D11A	Mat-like laminae	3	100533.48	1214.33	361.65	210.45	527102.91	1355.72	6292.92	55.49
Crinkly laminated chert	D11A	Mat-like laminae	4	158132.49	1193.73	524.11	234.65	875371.35	1355.48	10353.43	56.04
Crinkly laminated chert	D11A	Mat-like laminae	5	152262.75	1205.59	549.05	210.41	937777.39	1355.69	10822.23	57.49
Crinkly laminated chert	D11A	Mat-like laminae	6	90384.45	1193.89	394.99	167.84	726538.30	1355.25	8159.77	59.15
Crinkly laminated chert	D11A	Mat-like laminae	7	118530.21	1197.02	456.78	194.67	790278.30	1355.60	9025.31	58.12
Crinkly laminated chert	D11A	Mat-like laminae	8	108182.27	1196.36	432.62	186.26	749033.31	1355.86	8678.93	57.25
Crinkly laminated chert	D11A	Mat-like laminae	9	134481.73	1204.67	469.50	219.00	688974.39	1355.90	7365.91	62.28
Crinkly laminated chert	D11A	Mat-like laminae	10	120927.08	1210.29	417.86	221.37	719539.46	1355.74	8453.27	56.43
Crinkly laminated chert	D11A	Mat-like laminae	11	93477.13	1197.92	404.47	169.61	714358.97	1355.23	8139.83	58.26
Crinkly laminated chert	D11A	Mat-like laminae	12	144337.04	1206.56	449.62	252.51	759141.88	1355.82	8909.00	56.50
Crinkly laminated chert	D11A	Mat-like laminae	13	142689.55	1213.27	443.31	252.71	676898.78	1355.72	7726.69	58.15
Crinkly laminated chert	D11A	Grain	14	124624.79	1105.81	2291.55	35.91	815753.86	1355.13	8115.82	67.17
Crinkly laminated chert	D11A	Grain	15	91669.68	1192.28	345.47	200.32	587373.41	1355.34	6337.35	61.69
Crinkly laminated chert	D11A	Grain	16	104921.67	1189.18	423.29	184.75	673614.97	1355.14	7050.00	63.69
Crinkly laminated chert	D11A	Grain	17	102609.07	1197.42	399.84	192.06	654472.76	1355.53	7183.68	60.59
Crinkly laminated chert	D11A	Grain	18	145525.64	1195.64	527.52	209.79	921799.91	1355.40	9523.33	64.56
Crinkly laminated chert	D11A	Grain	19	102531.04	1194.10	413.84	184.35	676434.98	1355.43	7216.88	62.41
Crinkly laminated chert	D11A	Grain	20	125699.22	1193.81	512.03	182.36	770329.51	1355.49	8198.84	62.57
Crinkly laminated chert	D11A	Grain	21	172339.88	1205.83	582.29	227.98	951121.55	1355.66	10677.57	59.18
Crinkly laminated chert	D11A	Grain	22	137789.09	1176.68	459.91	234.39	678857.91	1355.39	7059.10	64.12
Crinkly laminated chert	D11A	Grain	23	82224.35	1195.14	364.12	165.19	664242.37	1355.41	7314.02	60.39
Crinkly laminated chert	D11A	Grain	24	118115.67	1196.03	433.53	206.59	681796.68	1355.40	7476.03	60.65
Crinkly laminated chert	D11A	Grain	25	90991.15	1189.58	384.21	174.99	659993.46	1355.17	7044.93	62.38

				Lorentzian (D4)				Lorentzian (D1)			
Facies	Sample	CM microtexture		*A*	ω	*I*	*Γ*	*A*	ω	*I*	*Γ*
Crinkly laminated chert	C3A	Mat-like laminae	1	147712.80	1200.12	543.28	205.66	915128.747	1356.379	10188.473	59.691
Crinkly laminated chert	C3A	Mat-like laminae	2	132171.22	1192.01	406.81	257.88	691054.003	1357.014	8159.891	56.135
Crinkly laminated chert	C3A	Mat-like laminae	3	120527.17	1181.01	362.12	267.61	713235.046	1355.822	8245.631	57.387
Crinkly laminated chert	C3A	Mat-like laminae	4	163553.39	1201.56	557.72	225.59	987365.978	1357.369	11822.675	55.324
Crinkly laminated chert	C3A	Mat-like laminae	5	105770.06	1185.65	372.32	218.22	631954.480	1356.664	7371.969	56.851
Crinkly laminated chert	C3A	Mat-like laminae	6	133272.53	1197.28	469.55	216.99	800885.190	1356.839	9094.311	58.472
Crinkly laminated chert	C3A	Mat-like laminae	7	123196.53	1192.17	442.11	212.53	789574.550	1357.208	9280.246	56.406
Crinkly laminated chert	C3A	Mat-like laminae	8	81012.33	1201.56	334.88	178.70	653497.267	1357.498	7570.993	57.260
Crinkly laminated chert	C3A	Mat-like laminae	9	123350.95	1203.20	482.50	190.74	881953.278	1357.378	10104.710	57.929
Crinkly laminated chert	C3A	Mat-like laminae	10	152144.92	1192.39	445.54	275.14	681107.502	1357.427	7452.713	60.784
Crinkly laminated chert	C3A	Mat-like laminae	11	111103.65	1196.83	488.22	166.54	898436.309	1357.373	10002.701	59.691
Crinkly laminated chert	C3A	Mat-like laminae	12	110165.03	1193.30	499.09	160.88	937927.057	1357.312	10352.400	60.233
Crinkly laminated chert	C3A	Mat-like laminae	13	97762.18	1192.22	338.93	221.79	566103.575	1357.241	6493.491	57.859
Crinkly laminated chert	C3A	Mat-like laminae	14	148791.38	1184.83	433.35	278.49	643069.646	1355.512	7485.485	56.979
Crinkly laminated chert	C3A	Mat-like laminae	15	124448.46	1196.28	485.47	191.88	849740.335	1355.155	9630.284	58.592
Crinkly laminated chert	C3A	Mat-like laminae	16	97408.59	1198.03	339.84	219.72	571831.256	1355.784	6345.884	59.894
Crinkly laminated chert	C3A	Grain	17	156809.39	1194.93	486.22	255.18	745175.213	1356.685	6841.899	73.097
Crinkly laminated chert	C3A	Grain	18	124564.88	1197.98	456.07	207.00	748306.767	1356.491	7613.095	65.605
Crinkly laminated chert	C3A	Grain	19	124324.52	1194.82	452.85	208.54	737950.471	1357.187	7613.824	64.646
Crinkly laminated chert	C3A	Grain	20	137558.50	1197.22	518.91	199.67	848020.054	1356.904	8610.362	65.743
Crinkly laminated chert	C3A	Grain	21	130422.09	1194.52	479.19	206.70	768383.830	1356.028	7902.042	64.993
Crinkly laminated chert	C3A	Grain	22	124319.83	1196.98	463.17	200.95	759835.751	1355.982	8004.995	63.437
Crinkly laminated chert	C3A	Grain	23	132012.27	1189.90	524.45	205.44	771202.293	1356.033	7936.287	64.894

				Gaussian (D3)				Lorentzian (G)			
Facies	Sample	CM microtexture	N	A	ω	I	Γ	A	ω	I	Γ
Crinkly laminated chert	D11A	Mat-like laminae	1	47541.72	1544.16	372.89	119.78	223762.10	1603.57	3447.49	43.24
Crinkly laminated chert	D11A	Mat-like laminae	2	74177.17	1548.73	436.86	159.53	301255.82	1604.43	4481.04	44.87
Crinkly laminated chert	D11A	Mat-like laminae	3	29053.58	1531.91	267.06	102.20	186322.87	1603.03	2748.38	45.26
Crinkly laminated chert	D11A	Mat-like laminae	4	53893.28	1535.45	423.37	119.59	322036.45	1603.58	4668.97	46.09
Crinkly laminated chert	D11A	Mat-like laminae	5	68087.91	1539.79	516.17	123.92	306214.81	1602.47	4670.79	43.69
Crinkly laminated chert	D11A	Mat-like laminae	6	43042.21	1536.48	290.55	139.17	230097.05	1602.33	3534.09	43.37
Crinkly laminated chert	D11A	Mat-like laminae	7	44728.56	1530.49	409.19	102.69	279860.97	1603.41	3975.54	47.09
Crinkly laminated chert	D11A	Mat-like laminae	8	45339.58	1532.95	307.17	138.66	261587.39	1602.58	3871.45	45.09
Crinkly laminated chert	D11A	Mat-like laminae	9	38936.12	1533.16	402.19	90.95	251163.47	1603.84	3592.70	46.75
Crinkly laminated chert	D11A	Mat-like laminae	10	50352.77	1543.54	421.64	112.19	205297.51	1601.48	3319.90	41.09
Crinkly laminated chert	D11A	Mat-like laminae	11	49826.66	1542.41	355.83	131.55	238034.72	1603.51	3504.26	45.35
Crinkly laminated chert	D11A	Mat-like laminae	12	47171.11	1533.60	428.36	103.45	272461.29	1603.55	4043.32	44.97
Crinkly laminated chert	D11A	Mat-like laminae	13	54094.44	1546.25	436.64	116.38	197651.72	1602.84	3230.38	40.64
Crinkly laminated chert	D11A	Grain	14	46747.52	1533.24	421.46	104.20	248299.52	1601.60	3682.54	44.99
Crinkly laminated chert	D11A	Grain	15	36595.94	1538.82	314.42	109.34	200815.53	1604.30	3006.31	44.57
Crinkly laminated chert	D11A	Grain	16	61720.15	1554.75	452.95	128.01	204294.75	1603.53	3266.40	41.59
Crinkly laminated chert	D11A	Grain	17	46124.30	1538.78	379.25	114.25	260710.38	1606.22	3701.83	47.14
Crinkly laminated chert	D11A	Grain	18	57557.67	1542.37	553.40	97.71	287564.42	1604.04	4575.64	41.81
Crinkly laminated chert	D11A	Grain	19	59274.84	1550.42	373.75	149.00	216775.45	1604.10	3457.65	41.70
Crinkly laminated chert	D11A	Grain	20	34708.71	1529.75	362.14	90.04	308542.05	1606.39	4505.21	45.77
Crinkly laminated chert	D11A	Grain	21	88770.65	1553.72	567.17	147.04	268684.63	1602.53	4425.86	40.31
Crinkly laminated chert	D11A	Grain	22	49067.68	1541.07	410.68	112.24	233379.13	1604.53	3552.54	43.80
Crinkly laminated chert	D11A	Grain	23	38387.51	1541.14	343.36	105.03	242581.55	1604.42	3719.58	43.46
Crinkly laminated chert	D11A	Grain	24	56813.02	1545.72	435.12	122.66	218952.26	1603.58	3487.45	41.76
Crinkly laminated chert	D11A	Grain	25	43466.47	1541.17	354.70	115.12	205359.42	1603.48	3191.64	42.85

				Gaussian (D3)				Lorentzian (G)			
Facies	Sample	CM microtexture		*A*	ω	*I*	*Γ*	*A*	ω	*I*	*Γ*
Crinkly laminated chert	C3A	Mat-like laminae	1	85087.636	1543.559	581.038	137.573	258071.039	1603.021	4097.261	41.904
Crinkly laminated chert	C3A	Mat-like laminae	2	55014.609	1538.267	358.448	144.186	230228.350	1602.775	3404.911	45.139
Crinkly laminated chert	C3A	Mat-like laminae	3	56079.454	1553.147	436.651	120.653	205123.861	1603.170	3287.392	41.495
Crinkly laminated chert	C3A	Mat-like laminae	4	80540.331	1548.189	596.331	126.880	286263.712	1602.311	4505.056	42.287
Crinkly laminated chert	C3A	Mat-like laminae	5	50879.819	1535.390	356.725	133.992	216773.249	1603.959	3198.825	45.254
Crinkly laminated chert	C3A	Mat-like laminae	6	67837.931	1540.460	416.650	152.962	263071.726	1604.209	3914.629	44.860
Crinkly laminated chert	C3A	Mat-like laminae	7	69522.789	1540.577	522.604	124.975	249276.092	1603.803	3917.473	42.360
Crinkly laminated chert	C3A	Mat-like laminae	8	43076.499	1541.974	329.539	122.801	226069.936	1603.899	3374.590	44.710
Crinkly laminated chert	C3A	Mat-like laminae	9	67647.034	1533.715	509.701	124.681	282516.730	1603.122	4233.564	44.522
Crinkly laminated chert	C3A	Mat-like laminae	10	58986.926	1539.957	391.104	141.689	231812.000	1604.694	3396.064	45.606
Crinkly laminated chert	C3A	Mat-like laminae	11	65437.632	1530.948	476.538	129.003	297809.372	1603.762	4282.182	46.503
Crinkly laminated chert	C3A	Mat-like laminae	12	74881.188	1547.150	561.664	125.246	299884.418	1604.922	4509.511	44.374
Crinkly laminated chert	C3A	Mat-like laminae	13	52431.749	1548.129	359.539	137.000	175127.424	1604.656	2753.337	42.348
Crinkly laminated chert	C3A	Mat-like laminae	14	50798.449	1538.571	361.580	131.982	239580.515	1604.759	3458.671	46.308
Crinkly laminated chert	C3A	Mat-like laminae	15	84974.047	1543.114	639.398	124.848	289778.823	1604.604	4369.860	44.232
Crinkly laminated chert	C3A	Mat-like laminae	16	45178.661	1535.389	325.180	130.520	204098.673	1602.584	2953.955	46.165
Crinkly laminated chert	C3A	Grain	17	75979.129	1543.964	552.877	129.102	264188.534	1606.262	3919.566	45.012
Crinkly laminated chert	C3A	Grain	18	70759.334	1548.030	472.797	140.599	252572.347	1605.566	3814.687	44.171
Crinkly laminated chert	C3A	Grain	19	63033.426	1542.870	491.740	120.421	239921.334	1605.241	3669.570	43.588
Crinkly laminated chert	C3A	Grain	20	59743.682	1535.263	518.544	108.237	275963.758	1605.343	4117.208	44.741
Crinkly laminated chert	C3A	Grain	21	58507.969	1542.098	480.967	113.740	257061.016	1604.913	3934.435	43.467
Crinkly laminated chert	C3A	Grain	22	62423.809	1544.256	454.422	128.604	249186.790	1604.710	3808.481	43.650
Crinkly laminated chert	C3A	Grain	23	55658.992	1540.472	464.526	111.897	261971.443	1605.053	3980.099	43.886

Facies	Sample	CM microtexture	N	Lorentzian (D2) A	ω	I	Γ
Crinkly laminated chert	D11A	Mat-like laminae	1	54605.22	1626.66	1529.16	23.35
Crinkly laminated chert	D11A	Mat-like laminae	2	54319.50	1626.91	1651.87	21.45
Crinkly laminated chert	D11A	Mat-like laminae	3	43005.72	1626.49	1194.27	23.55
Crinkly laminated chert	D11A	Mat-like laminae	4	62371.22	1626.35	1853.92	21.96
Crinkly laminated chert	D11A	Mat-like laminae	5	86259.16	1625.64	2324.75	24.28
Crinkly laminated chert	D11A	Mat-like laminae	6	74042.11	1625.92	1715.04	28.39
Crinkly laminated chert	D11A	Mat-like laminae	7	62763.57	1626.25	1621.32	25.37
Crinkly laminated chert	D11A	Mat-like laminae	8	65549.41	1626.69	1739.00	24.68
Crinkly laminated chert	D11A	Mat-like laminae	9	49901.33	1626.22	1348.69	24.21
Crinkly laminated chert	D11A	Mat-like laminae	10	96275.08	1623.88	2151.96	29.45
Crinkly laminated chert	D11A	Mat-like laminae	11	55243.41	1625.56	1473.34	24.55
Crinkly laminated chert	D11A	Mat-like laminae	12	63791.53	1626.03	1704.73	24.50
Crinkly laminated chert	D11A	Mat-like laminae	13	70868.64	1625.57	1745.03	26.65
Crinkly laminated chert	D11A	Grain	14	93992.49	1623.32	2056.13	30.11
Crinkly laminated chert	D11A	Grain	15	44088.16	1626.22	1193.18	24.18
Crinkly laminated chert	D11A	Grain	16	64011.67	1625.64	1546.55	27.18
Crinkly laminated chert	D11A	Grain	17	24440.74	1629.93	910.69	17.43
Crinkly laminated chert	D11A	Grain	18	89771.40	1626.67	2158.18	27.32
Crinkly laminated chert	D11A	Grain	19	63410.72	1626.93	1562.05	26.64
Crinkly laminated chert	D11A	Grain	20	32007.95	1630.40	1221.95	17.01
Crinkly laminated chert	D11A	Grain	21	106658.46	1624.92	2370.26	29.63
Crinkly laminated chert	D11A	Grain	22	50728.55	1627.32	1348.28	24.64
Crinkly laminated chert	D11A	Grain	23	48970.21	1627.67	1393.83	22.96
Crinkly laminated chert	D11A	Grain	24	57047.59	1626.50	1556.80	23.98
Crinkly laminated chert	D11A	Grain	25	61268.07	1625.65	1445.55	27.85

Facies	Sample	CM microtexture		Lorentzian (D2) *A*	ω	*I*	*Γ*
Crinkly laminated chert	C3A	Mat-like laminae	1	105509.358	1625.270	2416.567	28.724
Crinkly laminated chert	C3A	Mat-like laminae	2	68932.645	1626.285	1671.545	27.082
Crinkly laminated chert	C3A	Mat-like laminae	3	72479.840	1626.420	1779.199	26.743
Crinkly laminated chert	C3A	Mat-like laminae	4	105842.827	1626.149	2557.785	27.178
Crinkly laminated chert	C3A	Mat-like laminae	5	51944.476	1627.519	1468.631	23.125
Crinkly laminated chert	C3A	Mat-like laminae	6	67485.755	1627.504	1799.107	24.566
Crinkly laminated chert	C3A	Mat-like laminae	7	73478.882	1628.347	2011.037	23.913
Crinkly laminated chert	C3A	Mat-like laminae	8	48978.810	1629.220	1424.184	22.472
Crinkly laminated chert	C3A	Mat-like laminae	9	97856.308	1627.371	2264.211	28.432
Crinkly laminated chert	C3A	Mat-like laminae	10	58328.835	1628.013	1517.436	25.194
Crinkly laminated chert	C3A	Mat-like laminae	11	90381.601	1627.215	2176.892	27.276
Crinkly laminated chert	C3A	Mat-like laminae	12	79911.570	1628.036	2080.408	25.176
Crinkly laminated chert	C3A	Mat-like laminae	13	51376.223	1628.032	1341.569	25.097
Crinkly laminated chert	C3A	Mat-like laminae	14	35275.509	1628.722	1205.125	19.048
Crinkly laminated chert	C3A	Mat-like laminae	15	52271.979	1628.221	1685.250	20.210
Crinkly laminated chert	C3A	Mat-like laminae	16	46513.557	1626.488	1285.714	23.662
Crinkly laminated chert	C3A	Grain	17	52644.942	1628.585	1377.004	25.053
Crinkly laminated chert	C3A	Grain	18	53681.363	1628.189	1838.873	18.995
Crinkly laminated chert	C3A	Grain	19	69455.472	1627.241	1721.879	26.472
Crinkly laminated chert	C3A	Grain	20	80631.474	1626.536	1828.041	29.031
Crinkly laminated chert	C3A	Grain	21	63652.929	1627.369	1630.059	25.149
Crinkly laminated chert	C3A	Grain	22	64630.013	1627.132	1662.396	24.849
Crinkly laminated chert	C3A	Grain	23	61628.289	1627.662	1644.057	24.109

Facies	Sample	CM microtexture		R_1	$\Gamma_{D1/G}$	$I_{D1}/(I_{D1}+I_G$	A_D/A_G	R_2 (1)	ΔT C° (2)	ΔT C° (3)	ΔT C° (4	R_{D3}	R_{D4}
Crinkly laminated chert	C3A	Mat-like laminae	1	2.49	1.42	0.7132	3.55	0.7157	322.53	350.66	340.25	0.0570	0.0533
Crinkly laminated chert	C3A	Mat-like laminae	2	2.40	1.24	0.7056	3.00	0.6979	330.44	358.31	351.38	0.0439	0.0499
Crinkly laminated chert	C3A	Mat-like laminae	3	2.51	1.38	0.7150	3.48	0.7198	320.68	355.62	353.68	0.0530	0.0439
Crinkly laminated chert	C3A	Mat-like laminae	4	2.62	1.31	0.7241	3.45	0.7158	322.49	360.05	350.73	0.0504	0.0472
Crinkly laminated chert	C3A	Mat-like laminae	5	2.30	1.26	0.6974	2.92	0.7016	328.77	356.77	378.21	0.0484	0.0505
Crinkly laminated chert	C3A	Mat-like laminae	6	2.32	1.30	0.6991	3.04	0.7078	326.01	353.29	368.44	0.0458	0.0516
Crinkly laminated chert	C3A	Mat-like laminae	7	2.37	1.33	0.7032	3.17	0.7098	325.12	357.73	372.87	0.0563	0.0476
Crinkly laminated chert	C3A	Mat-like laminae	8	2.24	1.28	0.6917	2.89	0.7038	327.82	355.89	382.64	0.0435	0.0442
Crinkly laminated chert	C3A	Mat-like laminae	9	2.39	1.30	0.7047	3.12	0.6987	330.09	354.45	342.23	0.0504	0.0478
Crinkly laminated chert	C3A	Mat-like laminae	10	2.19	1.33	0.6870	2.94	0.7013	328.93	348.32	364.18	0.0525	0.0598
Crinkly laminated chert	C3A	Mat-like laminae	11	2.34	1.28	0.7002	3.02	0.6983	330.26	350.66	350.07	0.0476	0.0488
Crinkly laminated chert	C3A	Mat-like laminae	12	2.30	1.36	0.6966	3.13	0.7118	324.26	349.50	364.31	0.0543	0.0482
Crinkly laminated chert	C3A	Mat-like laminae	13	2.36	1.37	0.7022	3.23	0.7142	323.17	354.60	364.84	0.0554	0.0522
Crinkly laminated chert	C3A	Mat-like laminae	14	2.16	1.23	0.6840	2.68	0.7006	329.25	356.49	405.86	0.0483	0.0579
Crinkly laminated chert	C3A	Mat-like laminae	15	2.20	1.32	0.6879	2.93	0.7130	323.72	353.03	397.98	0.0664	0.0504
Crinkly laminated chert	C3A	Mat-like laminae	16	2.15	1.30	0.6824	2.80	0.6953	331.60	350.23	374.57	0.0512	0.0536
Crinkly laminated chert	C3A	Grain	17	1.75	1.62	0.6358	2.82	0.7017	328.76	321.84	365.14	0.0808	0.0711
Crinkly laminated chert	C3A	Grain	18	2.00	1.49	0.6662	2.96	0.7096	325.23	337.95	406.22	0.0621	0.0599
Crinkly laminated chert	C3A	Grain	19	2.07	1.48	0.6748	3.08	0.7046	327.45	340.01	355.52	0.0646	0.0595
Crinkly laminated chert	C3A	Grain	20	2.09	1.47	0.6765	3.07	0.7040	327.73	337.65	338.17	0.0602	0.0603
Crinkly laminated chert	C3A	Grain	21	2.01	1.50	0.6676	2.99	0.7055	327.04	339.27	364.49	0.0609	0.0606
Crinkly laminated chert	C3A	Grain	22	2.10	1.45	0.6776	3.05	0.7077	326.07	342.61	366.52	0.0568	0.0579
Crinkly laminated chert	C3A	Grain	23	1.99	1.48	0.6660	2.94	0.7044	327.53	339.48	371.54	0.0585	0.0661

Facies	Sample	CM microtexture	N	R_1	$\Gamma_{D1/G}$	$I_{D1}/(I_{D1}+I_G$	A_{D1}/A_G	R_2 (1)	ΔT C° (2)	ΔT C° (3)	ΔT C° (4	R_{D3} (5)	R_{D4} (6)
Crinkly laminated chert	D11A	Mat-like laminae	1	2.25	1.34	0.6921	3.02	0.7081	325.89	354.65	376.70	0.0481	0.0508
Crinkly laminated chert	D11A	Mat-like laminae	2	2.18	1.30	0.6858	2.86	0.7080	325.93	353.15	389.54	0.0447	0.0494
Crinkly laminated chert	D11A	Mat-like laminae	3	2.29	1.23	0.6960	2.83	0.6968	330.91	359.69	375.34	0.0424	0.0575
Crinkly laminated chert	D11A	Mat-like laminae	4	2.22	1.22	0.6892	2.72	0.6949	331.79	358.52	386.11	0.0409	0.0506
Crinkly laminated chert	D11A	Mat-like laminae	5	2.32	1.32	0.6985	3.06	0.7050	327.29	355.39	370.36	0.0477	0.0507
Crinkly laminated chert	D11A	Mat-like laminae	6	2.31	1.36	0.6978	3.16	0.7049	327.31	351.83	342.52	0.0356	0.0484
Crinkly laminated chert	D11A	Mat-like laminae	7	2.27	1.23	0.6942	2.82	0.6976	330.58	354.03	363.00	0.0453	0.0506
Crinkly laminated chert	D11A	Mat-like laminae	8	2.24	1.27	0.6915	2.86	0.6960	331.27	355.91	367.65	0.0354	0.0498
Crinkly laminated chert	D11A	Mat-like laminae	9	2.05	1.33	0.6722	2.74	0.6959	331.32	345.10	370.83	0.0546	0.0637
Crinkly laminated chert	D11A	Mat-like laminae	10	2.55	1.37	0.7180	3.50	0.7047	327.43	357.67	335.35	0.0499	0.0494
Crinkly laminated chert	D11A	Mat-like laminae	11	2.32	1.28	0.6991	3.00	0.7089	325.52	353.74	368.58	0.0437	0.0497
Crinkly laminated chert	D11A	Mat-like laminae	12	2.20	1.26	0.6878	2.79	0.6930	332.60	357.53	368.91	0.0481	0.0505
Crinkly laminated chert	D11A	Mat-like laminae	13	2.39	1.43	0.7052	3.42	0.7160	322.39	353.97	354.31	0.0565	0.0574
Crinkly laminated chert	D11A	Grain	14	2.20	1.49	0.6879	3.29	0.7044	327.53	334.59	330.86	0.0519	0.2824
Crinkly laminated chert	D11A	Grain	15	2.11	1.38	0.6783	2.92	0.7057	326.94	346.38	371.05	0.0496	0.0545
Crinkly laminated chert	D11A	Grain	16	2.16	1.53	0.6834	3.30	0.7151	322.76	342.08	350.73	0.0642	0.0600
Crinkly laminated chert	D11A	Grain	17	1.94	1.29	0.6599	2.51	0.6965	331.05	348.74	416.80	0.0528	0.0557
Crinkly laminated chert	D11A	Grain	18	2.08	1.54	0.6755	3.21	0.7095	325.25	340.20	349.76	0.0581	0.0554
Crinkly laminated chert	D11A	Grain	19	2.09	1.50	0.6761	3.12	0.7071	326.34	344.81	354.35	0.0518	0.0573
Crinkly laminated chert	D11A	Grain	20	1.82	1.37	0.6454	2.50	0.6934	332.42	344.47	419.69	0.0442	0.0625
Crinkly laminated chert	D11A	Grain	21	2.41	1.47	0.7070	3.54	0.7170	321.92	351.77	334.12	0.0531	0.0545
Crinkly laminated chert	D11A	Grain	22	1.99	1.46	0.6652	2.91	0.7050	327.29	341.14	367.95	0.0582	0.0652
Crinkly laminated chert	D11A	Grain	23	1.97	1.39	0.6629	2.74	0.6950	331.74	349.17	379.31	0.0469	0.0498
Crinkly laminated chert	D11A	Grain	24	2.14	1.45	0.6819	3.11	0.7118	324.23	348.60	372.44	0.0582	0.0580
Crinkly laminated chert	D11A	Grain	25	2.21	1.46	0.6882	3.21	0.7123	324.05	344.88	346.16	0.0503	0.0545

				Lorentzian (D4)				Lorentzian (D1)			
Facies	Sample	CM microtexture		*A*	ω	*I*	*Γ*	*A*	ω	*I*	*Γ*
Crinkly laminated chert	D1	Bitumen-like	1	144127.42	1201.35	504.45	218.50	781040.688	1354.020	6509.423	81.001
Crinkly laminated chert	D1	Bitumen-like	2	135532.14	1200.06	496.60	206.66	783847.183	1353.994	6514.104	81.248
Crinkly laminated chert	D1	Bitumen-like	3	249840.79	1208.66	680.20	300.91	1022100.000	1354.021	8412.418	82.088
Crinkly laminated chert	D1	Bitumen-like	4	129534.26	1196.40	512.21	188.72	828064.969	1354.006	6925.444	80.701
Crinkly laminated chert	D1	Bitumen-like	5	148087.60	1195.61	651.36	166.44	1075840.000	1353.437	8830.643	82.327
Crinkly laminated chert	D1	Bitumen-like	6	145429.08	1197.32	560.51	194.56	931972.906	1354.062	7757.765	81.107
Crinkly laminated chert	D1	Bitumen-like	7	130413.23	1190.06	575.02	166.23	906514.984	1353.756	7433.069	82.418
Crinkly laminated chert	D1	Bitumen-like	8	170685.50	1196.71	588.87	222.80	925209.721	1353.831	7624.203	81.982
Crinkly laminated chert	D1	Bitumen-like	9	148047.62	1196.20	588.57	187.53	948567.987	1353.906	7881.077	81.269
Crinkly laminated chert	D1	Bitumen-like	10	134972.35	1196.66	556.95	179.37	910638.057	1354.299	7595.130	80.937
Crinkly laminated chert	D1	Bitumen-like	11	124668.24	1197.66	489.18	190.39	800295.734	1353.714	6645.324	81.319
Crinkly laminated chert	D1	Bitumen-like	12	148578.74	1196.78	615.18	178.64	976519.402	1353.421	7951.105	83.036
Crinkly laminated chert	D1	Bitumen-like	13	117596.22	1195.22	520.40	165.28	855719.664	1353.437	6990.227	82.749
Crinkly laminated chert	D1	Bitumen-like	14	166188.69	1193.42	676.44	182.49	1182080.000	1353.149	9666.371	82.656
Crinkly laminated chert	D1	Bitumen-like	15	168415.93	1197.26	620.24	205.58	999239.470	1354.019	8257.722	81.734
Crinkly laminated chert	D1	Bitumen-like	16	89120.89	1197.24	392.04	166.34	726273.359	1354.404	6271.580	78.004
Crinkly laminated chert	D1	Bitumen-like	17	293098.22	1202.40	1043.79	213.81	1683330.000	1355.560	17523.545	64.042
Crinkly laminated chert	D1	Bitumen-like	18	139182.01	1194.33	696.17	143.53	1023930.000	1353.782	8424.063	82.123
Crinkly laminated chert	D1	Bitumen-like	19	170446.93	1196.44	676.18	187.99	1086200.000	1353.999	8989.516	81.607
Crinkly laminated chert	D1	Bitumen-like	20	174423.91	1202.62	670.55	194.82	1042770.000	1355.007	9495.793	73.736
Crinkly laminated chert	D1	Bitumen-like	21	236358.77	1206.49	853.09	210.04	1268900.000	1355.023	10260.269	83.653
Crinkly laminated chert	D1	Bitumen-like	22	137903.78	1194.25	544.47	189.20	880652.234	1354.329	7258.862	81.960
Crinkly laminated chert	D1	Bitumen-like	23	156634.98	1197.71	623.21	186.24	1010969.79	1353.94	8320.53	81.93

				Lorentzian (D4)				Lorentzian (D1)			
Facies	Sample	CM microtexture		*A*	ω	*I*	*Γ*	*A*	ω	*I*	*Γ*
Massive black chert	C9E	Bitumen-like	1	148802.95	1211.33	451.45	260.26	643787.16	1355.13	5929.04	72.84
Massive black chert	C9E	Bitumen-like	2	26147.32	1199.49	133.58	139.85	239131.16	1351.19	1793.80	90.62
Massive black chert	C9E	Bitumen-like	3	30824.76	1202.91	139.86	160.09	270621.17	1353.29	2488.38	72.97
Massive black chert	C9E	Bitumen-like	4	25587.66	1203.63	139.96	129.37	233500.62	1350.50	1697.23	93.73
Massive black chert	C9E	Bitumen-like	5	34238.01	1206.04	134.25	190.03	216234.26	1355.31	1873.77	77.72
Massive black chert	C9E	Bitumen-like	6	48892.59	1206.08	227.92	155.15	401032.89	1353.62	3290.89	82.35
Massive black chert	C9E	Bitumen-like	7	190025.45	1204.29	710.39	201.36	1186100.000	1352.447	10080.343	79.337
Massive black chert	C9E	Bitumen-like	8	11288.33	1195.22	63.13	126.46	126974.178	1356.144	1137.789	75.005
Massive black chert	C9E	Bitumen-like	9	59184.69	1202.57	238.38	184.11	368973.616	1352.815	2948.212	84.698
Massive black chert	C9E	Bitumen-like	10	82638.26	1207.88	268.18	239.22	396141.581	1352.007	3153.828	85.027
Massive black chert	C9E	Bitumen-like	11	58555.68	1202.00	274.95	154.01	457474.324	1355.379	4168.249	73.694
Massive black chert	C9E	Bitumen-like	12	91470.80	1219.16	355.18	191.58	545579.329	1354.114	4946.864	74.074
Massive black chert	C9E	Bitumen-like	13	72495.17	1206.37	261.21	194.33	410118.80	1352.96	3460.46	82.37
Massive black chert	C9E	Bitumen-like	14	225586.28	1227.58	702.71	250.47	989872.803	1353.750	9219.415	72.003
Massive black chert	C9E	Interstitial	15	97069.56	1221.14	345.46	212.51	562909.810	1353.193	5047.286	74.936
Massive black chert	C9E	Interstitial	16	39548.89	1207.96	151.47	195.36	233631.197	1354.738	2177.860	71.937
Massive black chert	C9E	Interstitial	17	134780.24	1223.47	319.66	361.83	504482.497	1355.511	4872.111	69.301
Massive black chert	C9E	Cloudy	18	39966.01	1209.52	166.97	176.11	266380.603	1356.107	2703.049	65.786
Massive black chert	C9E	Cloudy	19	237929.62	1245.36	617.16	316.00	742911.451	1355.227	7988.333	61.892
Massive black chert	C9E	Cloudy	20	293098.22	1202.40	1043.79	213.81	1683330.000	1355.560	17523.545	64.042
Massive black chert	C9E	Cloudy	21	239808.65	1246.68	626.10	313.09	739770.221	1355.229	7988.321	61.618
Massive black chert	C9E	Cloudy	22	52140.81	1237.04	182.36	216.17	226854.927	1353.988	2355.363	64.206
Massive black chert	C9E	Cloudy	23	50733.42	1235.26	181.68	210.14	227898.705	1353.981	2358.814	64.417

				Gaussian (D3)				Lorentzian (G)			
Facies	Sample	CM microtexture		*A*	ω	*I*	*Γ*	*A*	ω	*I*	*Γ*
Crinkly laminated chert	D1	Bitumen-like	1	81139.014	1551.531	616.518	123.638	249454.102	1606.072	3876.344	42.875
Crinkly laminated chert	D1	Bitumen-like	2	84247.965	1553.306	649.703	121.818	231471.362	1605.348	3733.886	41.224
Crinkly laminated chert	D1	Bitumen-like	3	110234.967	1551.837	832.472	124.399	309154.216	1604.520	4808.418	42.822
Crinkly laminated chert	D1	Bitumen-like	4	81274.197	1551.485	661.178	115.479	214316.034	1603.485	3496.225	40.729
Crinkly laminated chert	D1	Bitumen-like	5	117812.291	1554.320	874.884	126.505	283513.843	1603.635	4421.517	42.695
Crinkly laminated chert	D1	Bitumen-like	6	96482.040	1554.486	791.638	114.495	237663.586	1603.396	3984.699	39.581
Crinkly laminated chert	D1	Bitumen-like	7	99740.363	1554.801	797.880	117.436	221909.302	1602.708	3742.231	39.337
Crinkly laminated chert	D1	Bitumen-like	8	104722.049	1558.045	799.461	123.058	245483.988	1604.009	4005.609	40.723
Crinkly laminated chert	D1	Bitumen-like	9	94621.424	1550.700	766.662	115.945	230445.622	1602.560	3836.014	39.873
Crinkly laminated chert	D1	Bitumen-like	10	76401.849	1544.128	634.839	113.060	252903.046	1603.536	3915.663	43.020
Crinkly laminated chert	D1	Bitumen-like	11	90889.988	1558.370	700.319	121.924	193056.281	1603.173	3285.541	38.967
Crinkly laminated chert	D1	Bitumen-like	12	113871.145	1556.947	820.680	130.350	251880.273	1603.482	4097.431	40.850
Crinkly laminated chert	D1	Bitumen-like	13	76513.960	1547.316	624.013	115.190	245066.786	1603.608	3750.230	43.551
Crinkly laminated chert	D1	Bitumen-like	14	132448.332	1554.747	975.609	127.538	326564.198	1603.165	5220.696	41.598
Crinkly laminated chert	D1	Bitumen-like	15	110470.471	1555.271	866.164	119.816	277536.267	1604.486	4521.064	40.797
Crinkly laminated chert	D1	Bitumen-like	16	72087.414	1538.250	548.111	123.555	272692.790	1602.229	3818.621	47.797
Crinkly laminated chert	D1	Bitumen-like	17	110889.820	1541.386	901.137	115.603	599404.068	1603.953	8898.087	44.965
Crinkly laminated chert	D1	Bitumen-like	18	114886.137	1558.910	904.841	119.279	273586.080	1604.877	4571.685	39.728
Crinkly laminated chert	D1	Bitumen-like	19	100901.822	1551.196	757.029	125.215	340452.029	1605.336	5174.524	43.877
Crinkly laminated chert	D1	Bitumen-like	20	96074.261	1544.465	744.465	121.236	327065.491	1604.363	4958.295	43.988
Crinkly laminated chert	D1	Bitumen-like	21	163183.065	1538.629	1094.847	140.021	524237.465	1604.534	7257.978	48.396
Crinkly laminated chert	D1	Bitumen-like	22	89369.269	1554.932	701.100	119.750	263474.699	1605.488	4171.490	42.039
Crinkly laminated chert	D1	Bitumen-like	23	110334.95	1550.28	823.61	124.09	299098.48	1603.59	4599.60	42.57

				Gaussian (D3)				Lorentzian (G)			
Facies	Sample	CM microtexture		*A*	ω	*I*	*Γ*	*A*	ω	*I*	*Γ*
Massive black chert	C9E	Bitumen-like	1	69612.14	1548.76	469.88	139.18	221388.94	1604.50	3303.76	44.70
Massive black chert	C9E	Bitumen-like	2	31187.12	1535.24	216.22	135.50	85978.57	1599.56	1124.68	51.31
Massive black chert	C9E	Bitumen-like	3	21098.50	1535.36	181.59	109.15	97529.75	1601.57	1451.49	44.81
Massive black chert	C9E	Bitumen-like	4	27608.63	1515.01	201.65	128.62	111436.05	1599.30	1246.28	60.60
Massive black chert	C9E	Bitumen-like	5	20427.94	1545.46	158.68	120.94	75649.01	1605.09	1125.37	44.88
Massive black chert	C9E	Bitumen-like	6	39748.22	1542.12	301.93	123.67	144272.61	1605.45	2114.72	45.59
Massive black chert	C9E	Bitumen-like	7	97204.997	1542.728	852.732	107.089	388676.928	1603.553	5881.250	44.076
Massive black chert	C9E	Bitumen-like	8	10397.979	1555.648	92.951	105.091	38232.394	1605.485	618.826	41.085
Massive black chert	C9E	Bitumen-like	9	41352.992	1553.830	293.811	132.223	93359.438	1603.338	1505.781	41.200
Massive black chert	C9E	Bitumen-like	10	46439.656	1537.138	292.734	149.036	143880.758	1604.217	2055.097	46.808
Massive black chert	C9E	Bitumen-like	11	44166.430	1545.344	323.070	128.429	154691.095	1604.856	2341.484	44.071
Massive black chert	C9E	Bitumen-like	12	56312.058	1545.008	402.571	131.410	192282.549	1604.963	2980.033	42.993
Massive black chert	C9E	Bitumen-like	13	45188.85	1540.45	311.95	135.43	145661.94	1603.38	2108.69	46.94
Massive black chert	C9E	Bitumen-like	14	73168.431	1534.178	638.322	107.684	388753.272	1605.064	5659.766	45.912
Massive black chert	C9E	Interstitial	15	54644.138	1543.151	426.080	120.481	191223.571	1603.361	2943.444	43.266
Massive black chert	C9E	Interstitial	16	22972.160	1545.971	156.175	138.185	86118.975	1605.840	1289.016	44.601
Massive black chert	C9E	Interstitial	17	45086.031	1547.815	374.275	113.167	159631.697	1603.427	2541.982	41.778
Massive black chert	C9E	Cloudy	18	23480.728	1544.831	168.900	130.602	98138.269	1605.696	1461.283	44.844
Massive black chert	C9E	Cloudy	19	67657.471	1536.023	485.767	130.845	301956.262	1603.389	4328.772	46.621
Massive black chert	C9E	Cloudy	20	110889.820	1541.386	901.137	115.603	599404.068	1603.953	8898.087	44.965
Massive black chert	C9E	Cloudy	21	70376.149	1535.115	507.870	130.179	299426.852	1603.341	4341.793	46.064
Massive black chert	C9E	Cloudy	22	21742.166	1510.810	149.671	136.468	102844.712	1604.316	1377.942	50.076
Massive black chert	C9E	Cloudy	23	20173.527	1507.694	146.310	129.532	105933.719	1604.500	1389.979	51.196

				Lorentzian (D2)			
Facies	Sample	CM microtexture		*A*	ω	*I*	*Γ*
Crinkly laminated chert	D1	Bitumen-like	1	46109.808	1627.318	1212.370	24.915
Crinkly laminated chert	D1	Bitumen-like	2	57608.213	1626.641	1484.149	25.441
Crinkly laminated chert	D1	Bitumen-like	3	81163.559	1625.531	2151.683	24.699
Crinkly laminated chert	D1	Bitumen-like	4	93574.661	1623.625	2067.600	29.801
Crinkly laminated chert	D1	Bitumen-like	5	110950.990	1622.727	2313.182	31.646
Crinkly laminated chert	D1	Bitumen-like	6	101730.116	1624.416	2290.850	29.225
Crinkly laminated chert	D1	Bitumen-like	7	98738.463	1624.010	2188.244	29.710
Crinkly laminated chert	D1	Bitumen-like	8	82641.228	1624.282	1953.575	27.794
Crinkly laminated chert	D1	Bitumen-like	9	118407.196	1623.036	2571.134	30.341
Crinkly laminated chert	D1	Bitumen-like	10	102360.795	1623.556	2216.096	30.437
Crinkly laminated chert	D1	Bitumen-like	11	88126.586	1623.699	2007.864	28.870
Crinkly laminated chert	D1	Bitumen-like	12	95363.448	1623.872	2205.517	28.428
Crinkly laminated chert	D1	Bitumen-like	13	83820.462	1624.025	1888.527	29.207
Crinkly laminated chert	D1	Bitumen-like	14	104491.436	1624.157	2559.427	26.792
Crinkly laminated chert	D1	Bitumen-like	15	82490.853	1626.255	2016.079	26.861
Crinkly laminated chert	D1	Bitumen-like	16	63522.875	1624.909	1528.006	27.301
Crinkly laminated chert	D1	Bitumen-like	17	141881.175	1625.635	3690.129	25.190
Crinkly laminated chert	D1	Bitumen-like	18	78972.189	1626.361	2069.010	25.004
Crinkly laminated chert	D1	Bitumen-like	19	71615.932	1626.869	1890.165	24.817
Crinkly laminated chert	D1	Bitumen-like	20	109813.280	1625.800	2583.016	27.943
Crinkly laminated chert	D1	Bitumen-like	21	77826.145	1627.169	2131.118	23.895
Crinkly laminated chert	D1	Bitumen-like	22	57721.293	1627.481	1618.215	23.325
Crinkly laminated chert	D1	Bitumen-like	23	96221.77	1624.16	2215.88	28.57

				Lorentzian (D2)			
Facies	Sample	CM microtexture		*A*	ω	*I*	*Γ*
Massive black chert	C9E	Bitumen-like	1	46017.55	1626.46	1221.05	24.67
Massive black chert	C9E	Bitumen-like	2	22150.03	1620.28	434.98	33.65
Massive black chert	C9E	Bitumen-like	3	27970.44	1623.54	598.16	30.82
Massive black chert	C9E	Bitumen-like	4	15035.78	1617.20	293.62	33.83
Massive black chert	C9E	Bitumen-like	5	15179.21	1626.84	414.40	23.97
Massive black chert	C9E	Bitumen-like	6	27292.66	1626.92	698.27	25.63
Massive black chert	C9E	Bitumen-like	7	99472.825	1624.747	2398.142	27.240
Massive black chert	C9E	Bitumen-like	8	11850.523	1627.903	261.296	29.890
Massive black chert	C9E	Bitumen-like	9	37799.193	1623.515	830.879	29.951
Massive black chert	C9E	Bitumen-like	10	18429.284	1625.407	510.800	23.588
Massive black chert	C9E	Bitumen-like	11	41155.769	1628.075	1024.930	26.355
Massive black chert	C9E	Bitumen-like	12	45012.994	1626.634	1280.696	22.974
Massive black chert	C9E	Bitumen-like	13	28412.12	1624.72	713.94	26.97
Massive black chert	C9E	Bitumen-like	14	70858.421	1626.825	1769.482	26.276
Massive black chert	C9E	Interstitial	15	54157.279	1624.787	1364.438	26.020
Massive black chert	C9E	Interstitial	16	14929.826	1627.033	413.200	23.637
Massive black chert	C9E	Interstitial	17	60264.826	1624.690	1327.657	29.902
Massive black chert	C9E	Cloudy	18	14915.711	1628.996	449.751	21.650
Massive black chert	C9E	Cloudy	19	53089.834	1627.620	1832.329	18.844
Massive black chert	C9E	Cloudy	20	141881.175	1625.635	3690.129	25.190
Massive black chert	C9E	Cloudy	21	53712.184	1627.643	1857.415	18.807
Massive black chert	C9E	Cloudy	22	15703.651	1626.691	532.811	19.175
Massive black chert	C9E	Cloudy	23	14123.983	1626.623	479.619	19.158

Facies	Sample	CM microtexture		R_1	$\Gamma_{D1/G}$	$I_{D1}/(I_{D1}+I_G$	A_D/A_G	R_2 (1)	ΔT C° (2)	ΔT C° (3)	ΔT C° (4	R_{D3}	R_{D4}
Crinkly laminated chert	D1	Bitumen-like	1	1.68	1.89	0.6268	3.13	0.7255	318.17	304.85	366.07	0.0947	0.0775
Crinkly laminated chert	D1	Bitumen-like	2	1.74	1.97	0.6356	3.39	0.7306	315.90	304.32	362.51	0.0997	0.0762
Crinkly laminated chert	D1	Bitumen-like	3	1.75	1.92	0.6363	3.31	0.7237	318.97	302.51	367.54	0.0990	0.0809
Crinkly laminated chert	D1	Bitumen-like	4	1.98	1.98	0.6645	3.86	0.7290	316.61	305.49	332.95	0.0955	0.0740
Crinkly laminated chert	D1	Bitumen-like	5	2.00	1.93	0.6664	3.79	0.7317	315.39	302.00	320.44	0.0991	0.0738
Crinkly laminated chert	D1	Bitumen-like	6	1.95	2.05	0.6607	3.92	0.7330	314.79	304.62	336.86	0.1020	0.0723
Crinkly laminated chert	D1	Bitumen-like	7	1.99	2.10	0.6651	4.09	0.7387	312.27	301.80	333.56	0.1073	0.0774
Crinkly laminated chert	D1	Bitumen-like	8	1.90	2.01	0.6556	3.77	0.7382	312.50	302.74	346.56	0.1049	0.0772
Crinkly laminated chert	D1	Bitumen-like	9	2.05	2.04	0.6726	4.12	0.7311	315.65	304.27	329.29	0.0973	0.0747
Crinkly laminated chert	D1	Bitumen-like	10	1.94	1.88	0.6598	3.60	0.7194	320.89	304.99	328.64	0.0836	0.0733
Crinkly laminated chert	D1	Bitumen-like	11	2.02	2.09	0.6692	4.15	0.7400	311.70	304.16	339.26	0.1054	0.0736
Crinkly laminated chert	D1	Bitumen-like	12	1.94	2.03	0.6599	3.88	0.7377	312.73	300.47	342.26	0.1032	0.0774
Crinkly laminated chert	D1	Bitumen-like	13	1.86	1.90	0.6508	3.49	0.7224	319.55	301.09	336.97	0.0893	0.0744
Crinkly laminated chert	D1	Bitumen-like	14	1.85	1.99	0.6493	3.62	0.7328	314.91	301.29	353.35	0.1009	0.0700
Crinkly laminated chert	D1	Bitumen-like	15	1.83	2.00	0.6462	3.60	0.7351	313.87	303.27	352.88	0.1049	0.0751
Crinkly laminated chert	D1	Bitumen-like	16	1.64	1.63	0.6216	2.66	0.6836	336.82	311.29	349.90	0.0874	0.0625
Crinkly laminated chert	D1	Bitumen-like	17	1.97	1.42	0.6632	2.81	0.6943	332.05	341.31	364.21	0.0514	0.0596
Crinkly laminated chert	D1	Bitumen-like	18	1.84	2.07	0.6482	3.74	0.7439	309.98	302.44	365.47	0.1074	0.0826
Crinkly laminated chert	D1	Bitumen-like	19	1.74	1.86	0.6347	3.19	0.7250	318.39	303.55	366.74	0.0842	0.0752
Crinkly laminated chert	D1	Bitumen-like	20	1.92	1.68	0.6570	3.19	0.7047	327.39	320.47	345.55	0.0784	0.0706
Crinkly laminated chert	D1	Bitumen-like	21	1.41	1.73	0.5857	2.42	0.6782	339.20	299.15	372.99	0.1067	0.0831
Crinkly laminated chert	D1	Bitumen-like	22	1.74	1.95	0.6351	3.34	0.7327	314.93	302.79	376.86	0.0966	0.0750
Crinkly laminated chert	D1	Bitumen-like	23	1.81	1.92	0.6440	3.38	0.7189	321.09	302.85	341.27	0.0990	0.0749

Facies	Sample	CM microtexture		R_1	$\Gamma_{D1/G}$	$I_{D1}/(I_{D1}+I_G$	A_D/A_G	R_2 (1)	ΔT C° (2)	ΔT C° (3)	ΔT C° (4	R_{D3}	R_{D4}
Massive black chert	C9E	Bitumen-like	1	1.79	1.63	0.6422	2.91	0.7065	326.59	322.38	367.72	0.0793	0.0761
Massive black chert	C9E	Bitumen-like	2	1.59	1.77	0.6146	2.78	0.6886	334.56	284.18	306.85	0.1205	0.0745
Massive black chert	C9E	Bitumen-like	3	1.71	1.63	0.6316	2.77	0.6832	336.99	322.12	326.07	0.0730	0.0562
Massive black chert	C9E	Bitumen-like	4	1.36	1.55	0.5766	2.10	0.6487	352.35	277.47	305.63	0.1188	0.0825
Massive black chert	C9E	Bitumen-like	5	1.67	1.73	0.6248	2.86	0.7042	327.63	311.91	372.48	0.0847	0.0716
Massive black chert	C9E	Bitumen-like	6	1.56	1.81	0.6088	2.78	0.7004	329.33	301.95	361.24	0.0917	0.0693
Massive black chert	C9E	Bitumen-like	7	1.71	1.80	0.6315	3.05	0.7084	325.75	308.43	350.31	0.0846	0.0705
Massive black chert	C9E	Bitumen-like	8	1.84	1.83	0.6477	3.32	0.7171	321.87	317.74	332.35	0.0817	0.0555
Massive black chert	C9E	Bitumen-like	9	1.96	2.06	0.6619	3.95	0.7378	312.70	296.90	331.93	0.0997	0.0809
Massive black chert	C9E	Bitumen-like	10	1.53	1.82	0.6055	2.75	0.7094	325.34	296.19	375.07	0.0928	0.0850
Massive black chert	C9E	Bitumen-like	11	1.78	1.67	0.6403	2.96	0.7002	329.40	320.56	356.31	0.0775	0.0660
Massive black chert	C9E	Bitumen-like	12	1.66	1.72	0.6241	2.84	0.6969	330.88	319.74	379.24	0.0814	0.0718
Massive black chert	C9E	Bitumen-like	13	1.64	1.75	0.6214	2.82	0.7020	328.60	301.91	352.12	0.0901	0.0755
Massive black chert	C9E	Bitumen-like	14	1.63	1.57	0.6196	2.55	0.6829	337.10	324.19	356.85	0.0692	0.0762
Massive black chert	C9E	Interstitial	15	1.71	1.73	0.6316	2.94	0.6964	331.09	317.89	358.59	0.0844	0.0684
Massive black chert	C9E	Interstitial	16	1.69	1.61	0.6282	2.71	0.6981	330.36	324.34	374.74	0.0717	0.0695
Massive black chert	C9E	Interstitial	17	1.92	1.66	0.6571	3.16	0.6964	331.09	330.00	332.27	0.0768	0.0656
Massive black chert	C9E	Cloudy	18	1.85	1.47	0.6491	2.71	0.7020	328.59	337.56	388.21	0.0625	0.0618
Massive black chert	C9E	Cloudy	19	1.85	1.33	0.6486	2.46	0.6766	339.90	345.93	407.23	0.0608	0.0773
Massive black chert	C9E	Cloudy	20	1.97	1.42	0.6632	2.81	0.6943	332.05	341.31	364.21	0.0514	0.0596
Massive black chert	C9E	Cloudy	21	1.84	1.34	0.6479	2.47	0.6769	339.79	346.52	407.49	0.0636	0.0784
Massive black chert	C9E	Cloudy	22	1.71	1.28	0.6309	2.21	0.6568	348.73	340.96	405.00	0.0635	0.0774
Massive black chert	C9E	Cloudy	23	1.70	1.26	0.6292	2.15	0.6550	349.54	340.50	405.11	0.0620	0.0770

				Lorentzian (D4)				Lorentzian (D1)			
Facies	Sample	CM microtexture		*A*	ω	*I*	*Γ*	*A*	ω	*I*	*Γ*
Laminated black chert	C2C	Grain	1	110888.27	1195.16	401.73	209.69	714507.90	1356.33	8005.59	59.28
Laminated black chert	C2C	Grain	2	133780.70	1186.85	393.05	274.44	642000.06	1356.33	7138.29	59.76
Laminated black chert	C2C	Grain	3	74280.81	1177.52	266.75	213.45	370808.96	1356.60	4479.16	54.81
Laminated black chert	C2C	Grain	4	84303.25	1187.84	369.96	167.13	692698.96	1356.74	8013.66	57.33
Laminated black chert	C2C	Grain	5	141702.82	1195.54	510.81	210.94	903186.90	1356.43	9369.25	64.27
Laminated black chert	C2C	Grain	6	134078.29	1191.95	561.60	176.33	1025870.00	1356.51	10794.74	63.31
Laminated black chert	C2C	Grain	7	148409.62	1197.91	556.18	201.03	886707.92	1356.13	8806.43	67.27
Laminated black chert	C2C	Grain	8	101128.99	1192.61	409.04	183.75	723511.31	1356.60	7848.08	61.33
Laminated black chert	C2C	Grain	9	94040.30	1196.41	412.04	167.03	736152.37	1356.41	7918.25	61.87
Laminated black chert	C2C	Grain	10	91210.73	1193.33	430.02	153.54	781551.46	1356.56	8016.25	65.03
Laminated black chert	C2C	Grain	11	75658.61	1196.05	303.90	185.08	502913.07	1356.75	5286.02	63.39
Laminated black chert	C2C	Grain	12	113570.42	1188.19	490.63	170.22	875042.19	1356.42	9913.66	58.60
Laminated black chert	C2C	Grain	13	81221.90	1204.90	350.32	169.74	615411.84	1356.68	6693.75	61.15
Laminated black chert	C2C	Grain	14	85691.64	1200.56	327.54	196.12	569783.61	1356.55	6492.96	58.25
Laminated black chert	C2C	Grain	15	107487.74	1203.91	374.85	219.05	619027.89	1357.15	6963.57	59.04
Laminated black chert	C2C	Grain	16	55063.12	1188.30	240.78	167.81	376339.21	1357.09	4361.01	57.24
Laminated black chert	C2C	Grain	17	122290.35	1202.73	408.26	231.33	681324.07	1357.00	7698.50	58.76
Laminated black chert	C2C	Grain	18	63959.04	1198.46	273.82	171.53	462545.55	1357.12	5286.24	58.07
Laminated black chert	C2C	Grain	19	112394.81	1190.23	382.53	226.94	637699.27	1357.48	7399.50	57.16
Laminated black chert	C2C	Grain	20	51992.10	1179.28	257.14	145.86	350733.61	1356.92	3908.49	59.62
Laminated black chert	C2C	Grain	21	157322.40	1197.44	643.15	181.17	1074650.00	1356.49	11028.91	64.99
Laminated black chert	C2C	Grain	22	127200.13	1194.63	430.16	228.35	733657.60	1356.95	8193.53	59.49
Laminated black chert	C2C	Bituminous-XcV	23	93552.93	1203.42	370.23	187.97	520298.20	1355.42	4588.67	76.26
Laminated black chert	C2C	Bituminous-XcV	24	105770.04	1203.83	410.28	192.50	660841.26	1355.10	5817.20	76.41
Laminated black chert	C2C	Bituminous-XcV	25	102173.56	1203.21	414.18	182.68	591957.86	1355.23	4685.97	85.55

				Lorentzian (D4)				Lorentzian (D1)			
Facies	Sample	CM microtexture		*A*	ω	*I*	*Γ*	*A*	ω	*I*	*Γ*
Granular carbonaceous chert	D4A	Mats-like network	1	146783.25	1199.64	530.22	210.31	921251.526	1356.435	10782.531	56.653
Granular carbonaceous chert	D4A	Mats-like network	2	94290.10	1193.20	386.52	180.97	664291.674	1356.706	7643.005	57.675
Granular carbonaceous chert	D4A	Mats-like network	3	156880.63	1197.04	571.90	208.17	997801.984	1356.511	11691.717	56.587
Granular carbonaceous chert	D4A	Mats-like network	4	108416.82	1213.15	408.14	199.18	688799.584	1356.628	8041.664	56.802
Granular carbonaceous chert	D4A	Mats-like network	5	83519.13	1198.88	358.46	171.13	621021.756	1356.852	7140.186	57.717
Granular carbonaceous chert	D4A	Mats-like network	6	111076.88	1200.32	412.69	203.18	721823.561	1356.973	8637.836	55.358
Granular carbonaceous chert	D4A	Mats-like network	7	106863.06	1196.18	377.93	216.13	631045.161	1357.015	7448.779	56.155
Granular carbonaceous chert	D4A	Mats-like network	8	144162.04	1195.22	531.29	205.55	914167.588	1357.079	10851.579	55.826
Granular carbonaceous chert	D4A	Mats-like network	9	126868.79	1195.55	474.91	201.66	809623.385	1356.897	9322.197	57.629
Granular carbonaceous chert	D4A	Mats-like network	10	187812.78	1207.98	621.71	233.61	1038100.000	1356.740	12140.436	56.701
Granular carbonaceous chert	D4A	Mats-like network	11	123236.22	1204.10	401.39	238.75	743436.031	1356.852	8872.571	55.514
Granular carbonaceous chert	D4A	Mats-like network	12	90632.40	1202.02	333.03	205.81	592336.070	1357.180	7081.274	55.416
Granular carbonaceous chert	D4A	Mats-like network	13	109637.56	1199.33	378.78	222.20	672528.875	1357.083	7956.220	56.024
Granular carbonaceous chert	D4A	Mats-like network	14	148483.17	1207.82	456.68	256.43	773798.586	1357.150	9522.561	53.768
Granular carbonaceous chert	D4A	Mats-like network	15	135801.09	1201.65	462.04	226.27	848006.545	1357.141	10074.487	55.779
Granular carbonaceous chert	D4A	Grain	16	99741.27	1193.91	357.76	212.58	591926.820	1356.211	6186.134	63.780
Granular carbonaceous chert	D4A	Grain	17	132189.94	1202.52	452.93	224.23	727238.593	1356.294	7760.763	62.398
Granular carbonaceous chert	D4A	Grain	18	109305.09	1199.09	442.35	183.42	728837.847	1355.930	7655.861	63.440
Granular carbonaceous chert	D4A	Grain	19	113713.90	1191.69	509.70	162.99	808783.656	1355.233	8044.657	67.181
Granular carbonaceous chert	D4A	Grain	20	106976.17	1200.96	422.36	188.80	662559.132	1355.671	6024.937	73.847
Granular carbonaceous chert	D4A	Grain	21	122802.80	1198.78	451.34	205.98	712860.129	1356.478	7060.681	67.480
Granular carbonaceous chert	D4A	Grain	22	111949.68	1194.31	396.17	216.10	685300.550	1356.408	7286.141	62.641
Granular carbonaceous chert	D4A	Grain	23	164055.09	1198.60	607.97	203.93	1027530.000	1356.530	10380.126	66.095
Granular carbonaceous chert	D4A	Grain	24	188864.21	1204.81	609.07	241.70	1062840.000	1356.996	12314.596	57.254
Granular carbonaceous chert	D4A	Grain	25	128147.05	1194.82	483.11	199.99	836373.175	1357.060	9241.888	60.162
Granular carbonaceous chert	D4A	Grain	26	92727.16	1195.82	303.11	238.47	508730.144	1356.608	5553.282	60.935
Granular carbonaceous chert	D4A	Grain	27	184386.38	1203.06	633.11	223.60	1046230.000	1356.631	11551.635	60.212
Granular carbonaceous chert	D4A	Grain	28	123427.00	1202.14	524.02	173.17	950268.657	1356.309	9695.531	65.408
Granular carbonaceous chert	D4A	Grain	29	130148.59	1198.61	472.61	207.76	793165.725	1356.291	8307.966	64.510
Granular carbonaceous chert	D4A	Grain	30	141628.83	1198.54	519.02	206.47	862604.259	1356.432	9133.785	63.429

				Gaussian (D3)				Lorentzian (G)			
Facies	Sample	CM microtexture		*A*	ω	*I*	*Γ*	*A*	ω	*I*	*Γ*
Laminated black chert	C2C	Grain	1	57424.90	1550.35	425.41	126.81	222197.93	1605.13	3663.99	40.27
Laminated black chert	C2C	Grain	2	47927.73	1547.03	331.94	135.64	213676.15	1605.58	3403.98	41.75
Laminated black chert	C2C	Grain	3	34193.45	1555.40	214.89	149.49	111638.52	1603.70	1813.47	40.89
Laminated black chert	C2C	Grain	4	54900.97	1552.42	427.78	120.57	211734.95	1604.82	3467.64	40.55
Laminated black chert	C2C	Grain	5	72239.56	1545.23	571.64	118.72	267262.16	1603.91	4248.44	41.83
Laminated black chert	C2C	Grain	6	82246.60	1549.88	668.74	115.54	301891.86	1605.05	4993.08	40.14
Laminated black chert	C2C	Grain	7	68935.51	1542.05	549.55	117.84	279553.01	1604.99	4296.20	43.35
Laminated black chert	C2C	Grain	8	50426.02	1545.38	409.89	115.57	237783.89	1605.86	3714.13	42.62
Laminated black chert	C2C	Grain	9	58923.02	1545.59	408.39	135.54	218816.68	1604.25	3384.91	43.04
Laminated black chert	C2C	Grain	10	77568.48	1551.69	550.87	132.28	237636.14	1606.31	3881.34	40.68
Laminated black chert	C2C	Grain	11	43654.84	1547.69	342.63	119.69	143917.91	1604.75	2345.87	40.75
Laminated black chert	C2C	Grain	12	61687.52	1541.87	472.36	122.69	284379.46	1605.10	4476.24	42.27
Laminated black chert	C2C	Grain	13	53728.40	1548.88	411.19	122.75	214304.64	1606.28	3460.45	41.17
Laminated black chert	C2C	Grain	14	47517.31	1549.49	357.39	124.91	178619.52	1605.56	2845.53	41.75
Laminated black chert	C2C	Grain	15	52047.12	1548.28	359.57	135.98	186046.93	1604.66	3005.98	41.13
Laminated black chert	C2C	Grain	16	28381.21	1550.83	216.29	123.27	114231.68	1605.78	1810.25	41.98
Laminated black chert	C2C	Grain	17	53041.85	1545.11	410.82	121.29	220762.41	1605.37	3474.12	42.28
Laminated black chert	C2C	Grain	18	38229.92	1542.03	282.80	127.00	155102.07	1605.64	2364.22	43.72
Laminated black chert	C2C	Grain	19	44401.31	1543.91	343.72	121.35	205661.75	1605.17	3256.35	42.01
Laminated black chert	C2C	Grain	20	30151.15	1553.44	228.83	123.78	93319.03	1604.91	1650.90	37.42
Laminated black chert	C2C	Grain	21	104506.67	1551.07	708.44	138.58	349428.84	1606.27	5373.31	43.33
Laminated black chert	C2C	Grain	22	54520.37	1545.36	424.97	120.52	237780.54	1606.19	3713.64	42.63
Laminated black chert	C2C	Bituminous-XcV	23	59572.03	1545.90	440.98	126.91	172594.61	1606.11	2698.08	42.59
Laminated black chert	C2C	Bituminous-XcV	24	85844.91	1544.17	554.18	145.52	258827.95	1605.26	3804.51	45.42
Laminated black chert	C2C	Bituminous-XcV	25	58605.44	1539.35	442.50	124.42	230293.18	1607.55	3311.68	46.50

				Gaussian (D3)				Lorentzian (G)			
Facies	Sample	CM microtexture		*A*	ω	*I*	*Γ*	*A*	ω	*I*	*Γ*
Granular carbonaceous chert	D4A	Mats-like network	1	71043.012	1551.989	572.339	116.610	268342.883	1604.438	4350.440	41.002
Granular carbonaceous chert	D4A	Mats-like network	2	46132.207	1542.000	357.015	121.391	243934.215	1605.439	3662.824	44.441
Granular carbonaceous chert	D4A	Mats-like network	3	68845.071	1546.813	584.645	110.624	313333.545	1604.613	4927.163	42.334
Granular carbonaceous chert	D4A	Mats-like network	4	54086.312	1539.703	408.780	124.298	223180.211	1604.646	3389.462	43.907
Granular carbonaceous chert	D4A	Mats-like network	5	50266.088	1543.641	372.083	126.912	206149.985	1605.058	3127.368	43.962
Granular carbonaceous chert	D4A	Mats-like network	6	54479.823	1548.926	406.494	125.907	217591.742	1603.195	3491.812	41.433
Granular carbonaceous chert	D4A	Mats-like network	7	42985.521	1543.143	338.202	119.403	212789.168	1605.035	3316.406	42.734
Granular carbonaceous chert	D4A	Mats-like network	8	65626.905	1546.758	518.453	118.916	296484.821	1605.005	4705.399	41.930
Granular carbonaceous chert	D4A	Mats-like network	9	64340.369	1549.627	509.938	118.532	270806.954	1605.628	4256.366	42.363
Granular carbonaceous chert	D4A	Mats-like network	10	92344.113	1554.299	614.420	141.195	314876.463	1604.299	5025.870	41.675
Granular carbonaceous chert	D4A	Mats-like network	11	61071.182	1551.762	469.700	122.147	243808.063	1604.641	3848.785	42.162
Granular carbonaceous chert	D4A	Mats-like network	12	46003.372	1543.665	316.973	136.344	203145.443	1605.295	3107.317	43.585
Granular carbonaceous chert	D4A	Mats-like network	13	52681.718	1554.449	385.093	128.518	208327.874	1604.879	3311.814	41.856
Granular carbonaceous chert	D4A	Mats-like network	14	52569.655	1544.147	344.377	143.408	251661.191	1604.231	3835.622	43.741
Granular carbonaceous chert	D4A	Mats-like network	15	56977.911	1549.295	474.494	112.809	263226.901	1604.751	4165.325	42.057
Granular carbonaceous chert	D4A	Grain	16	45567.370	1546.651	359.236	119.163	192267.249	1604.073	2915.146	43.979
Granular carbonaceous chert	D4A	Grain	17	60156.018	1535.109	408.153	138.460	258652.523	1603.829	3704.389	46.693
Granular carbonaceous chert	D4A	Grain	18	66468.314	1549.479	388.189	160.875	213719.492	1604.745	3525.799	40.263
Granular carbonaceous chert	D4A	Grain	19	76871.401	1549.984	563.687	128.114	256845.008	1604.748	4038.229	42.342
Granular carbonaceous chert	D4A	Grain	20	57536.831	1543.011	470.361	114.917	215552.674	1605.033	3310.440	43.398
Granular carbonaceous chert	D4A	Grain	21	58076.527	1547.020	461.867	118.128	232568.947	1605.139	3574.589	43.363
Granular carbonaceous chert	D4A	Grain	22	47963.004	1545.858	401.571	112.205	233281.777	1604.765	3585.300	43.363
Granular carbonaceous chert	D4A	Grain	23	59991.091	1531.218	582.320	96.782	331299.774	1603.941	5053.426	43.702
Granular carbonaceous chert	D4A	Grain	24	74098.229	1552.614	611.266	113.879	318733.509	1603.588	4963.220	42.763
Granular carbonaceous chert	D4A	Grain	25	58256.916	1545.262	473.107	115.679	280888.328	1605.319	4359.504	42.924
Granular carbonaceous chert	D4A	Grain	26	39432.916	1548.313	315.918	117.261	166986.626	1605.327	2623.433	42.380
Granular carbonaceous chert	D4A	Grain	27	87637.912	1550.628	705.884	116.634	292558.203	1603.505	4826.251	40.257
Granular carbonaceous chert	D4A	Grain	28	91283.345	1554.219	680.840	125.955	275117.898	1605.193	4447.925	41.126
Granular carbonaceous chert	D4A	Grain	29	58604.140	1544.805	468.824	119.637	250809.079	1604.358	3892.222	42.912
Granular carbonaceous chert	D4A	Grain	30	64575.030	1543.535	516.733	118.507	279831.348	1604.427	4282.226	43.631

Facies	Sample	CM microtexture		Lorentzian (D2)			
				A	ω	*I*	*Γ*
Crinkly laminated chert	D1	Bitumen-like	1	46109.808	1627.318	1212.370	24.915
Crinkly laminated chert	D1	Bitumen-like	2	57608.213	1626.641	1484.149	25.441
Crinkly laminated chert	D1	Bitumen-like	3	81163.559	1625.531	2151.683	24.699
Crinkly laminated chert	D1	Bitumen-like	4	93574.661	1623.625	2067.600	29.801
Crinkly laminated chert	D1	Bitumen-like	5	110950.990	1622.727	2313.182	31.646
Crinkly laminated chert	D1	Bitumen-like	6	101730.116	1624.416	2290.850	29.225
Crinkly laminated chert	D1	Bitumen-like	7	98738.463	1624.010	2188.244	29.710
Crinkly laminated chert	D1	Bitumen-like	8	82641.228	1624.282	1953.575	27.794
Crinkly laminated chert	D1	Bitumen-like	9	118407.196	1623.036	2571.134	30.341
Crinkly laminated chert	D1	Bitumen-like	10	102360.795	1623.556	2216.096	30.437
Crinkly laminated chert	D1	Bitumen-like	11	88126.586	1623.699	2007.864	28.870
Crinkly laminated chert	D1	Bitumen-like	12	95363.448	1623.872	2205.517	28.428
Crinkly laminated chert	D1	Bitumen-like	13	83820.462	1624.025	1888.527	29.207
Crinkly laminated chert	D1	Bitumen-like	14	104491.436	1624.157	2559.427	26.792
Crinkly laminated chert	D1	Bitumen-like	15	82490.853	1626.255	2016.079	26.861
Crinkly laminated chert	D1	Bitumen-like	16	63522.875	1624.909	1528.006	27.301
Crinkly laminated chert	D1	Bitumen-like	17	141881.175	1625.635	3690.129	25.190
Crinkly laminated chert	D1	Bitumen-like	18	78972.189	1626.361	2069.010	25.004
Crinkly laminated chert	D1	Bitumen-like	19	71615.932	1626.869	1890.165	24.817
Crinkly laminated chert	D1	Bitumen-like	20	109813.280	1625.800	2583.016	27.943
Crinkly laminated chert	D1	Bitumen-like	21	77826.145	1627.169	2131.118	23.895
Crinkly laminated chert	D1	Bitumen-like	22	57721.293	1627.481	1618.215	23.325
Crinkly laminated chert	D1	Bitumen-like	23	96221.77	1624.16	2215.88	28.57

Facies	Sample	CM microtexture		Lorentzian (D2)			
				A	ω	*I*	*Γ*
Massive black chert	C9E	Bitumen-like	1	46017.55	1626.46	1221.05	24.67
Massive black chert	C9E	Bitumen-like	2	22150.03	1620.28	434.98	33.65
Massive black chert	C9E	Bitumen-like	3	27970.44	1623.54	598.16	30.82
Massive black chert	C9E	Bitumen-like	4	15035.78	1617.20	293.62	33.83
Massive black chert	C9E	Bitumen-like	5	15179.21	1626.84	414.40	23.97
Massive black chert	C9E	Bitumen-like	6	27292.66	1626.92	698.27	25.63
Massive black chert	C9E	Bitumen-like	7	99472.825	1624.747	2398.142	27.240
Massive black chert	C9E	Bitumen-like	8	11850.523	1627.903	261.296	29.890
Massive black chert	C9E	Bitumen-like	9	37799.193	1623.515	830.879	29.951
Massive black chert	C9E	Bitumen-like	10	18429.284	1625.407	510.800	23.588
Massive black chert	C9E	Bitumen-like	11	41155.769	1628.075	1024.930	26.355
Massive black chert	C9E	Bitumen-like	12	45012.994	1626.634	1280.696	22.974
Massive black chert	C9E	Bitumen-like	13	28412.12	1624.72	713.94	26.97
Massive black chert	C9E	Bitumen-like	14	70858.421	1626.825	1769.482	26.276
Massive black chert	C9E	Interstitial	15	54157.279	1624.787	1364.438	26.020
Massive black chert	C9E	Interstitial	16	14929.826	1627.033	413.200	23.637
Massive black chert	C9E	Interstitial	17	60264.826	1624.690	1327.657	29.902
Massive black chert	C9E	Cloudy	18	14915.711	1628.996	449.751	21.650
Massive black chert	C9E	Cloudy	19	53089.834	1627.620	1832.329	18.844
Massive black chert	C9E	Cloudy	20	141881.175	1625.635	3690.129	25.190
Massive black chert	C9E	Cloudy	21	53712.184	1627.643	1857.415	18.807
Massive black chert	C9E	Cloudy	22	15703.651	1626.691	532.811	19.175
Massive black chert	C9E	Cloudy	23	14123.983	1626.623	479.619	19.158

Facies	Sample	CM microtexture		R_1	$\Gamma_{D1/G}$	$I_{D1}/(I_{D1}+I_G$	A_D/A_G	R_2 (1)	ΔT C° (2)	ΔT C° (3)	ΔT C° (4	R_{D3}	R_{D4}
Crinkly laminated chert	D1	Bitumen-like	1	1.68	1.89	0.6268	3.13	0.7255	318.17	304.85	366.07	0.0947	0.0775
Crinkly laminated chert	D1	Bitumen-like	2	1.74	1.97	0.6356	3.39	0.7306	315.90	304.32	362.51	0.0997	0.0762
Crinkly laminated chert	D1	Bitumen-like	3	1.75	1.92	0.6363	3.31	0.7237	318.97	302.51	367.54	0.0990	0.0809
Crinkly laminated chert	D1	Bitumen-like	4	1.98	1.98	0.6645	3.86	0.7290	316.61	305.49	332.95	0.0955	0.0740
Crinkly laminated chert	D1	Bitumen-like	5	2.00	1.93	0.6664	3.79	0.7317	315.39	302.00	320.44	0.0991	0.0738
Crinkly laminated chert	D1	Bitumen-like	6	1.95	2.05	0.6607	3.92	0.7330	314.79	304.62	336.86	0.1020	0.0723
Crinkly laminated chert	D1	Bitumen-like	7	1.99	2.10	0.6651	4.09	0.7387	312.27	301.80	333.56	0.1073	0.0774
Crinkly laminated chert	D1	Bitumen-like	8	1.90	2.01	0.6556	3.77	0.7382	312.50	302.74	346.56	0.1049	0.0772
Crinkly laminated chert	D1	Bitumen-like	9	2.05	2.04	0.6726	4.12	0.7311	315.65	304.27	329.29	0.0973	0.0747
Crinkly laminated chert	D1	Bitumen-like	10	1.94	1.88	0.6598	3.60	0.7194	320.89	304.99	328.64	0.0836	0.0733
Crinkly laminated chert	D1	Bitumen-like	11	2.02	2.09	0.6692	4.15	0.7400	311.70	304.16	339.26	0.1054	0.0736
Crinkly laminated chert	D1	Bitumen-like	12	1.94	2.03	0.6599	3.88	0.7377	312.73	300.47	342.26	0.1032	0.0774
Crinkly laminated chert	D1	Bitumen-like	13	1.86	1.90	0.6508	3.49	0.7224	319.55	301.09	336.97	0.0893	0.0744
Crinkly laminated chert	D1	Bitumen-like	14	1.85	1.99	0.6493	3.62	0.7328	314.91	301.29	353.35	0.1009	0.0700
Crinkly laminated chert	D1	Bitumen-like	15	1.83	2.00	0.6462	3.60	0.7351	313.87	303.27	352.88	0.1049	0.0751
Crinkly laminated chert	D1	Bitumen-like	16	1.64	1.63	0.6216	2.66	0.6836	336.82	311.29	349.90	0.0874	0.0625
Crinkly laminated chert	D1	Bitumen-like	17	1.97	1.42	0.6632	2.81	0.6943	332.05	341.31	364.21	0.0514	0.0596
Crinkly laminated chert	D1	Bitumen-like	18	1.84	2.07	0.6482	3.74	0.7439	309.98	302.44	365.47	0.1074	0.0826
Crinkly laminated chert	D1	Bitumen-like	19	1.74	1.86	0.6347	3.19	0.7250	318.39	303.55	366.74	0.0842	0.0752
Crinkly laminated chert	D1	Bitumen-like	20	1.92	1.68	0.6570	3.19	0.7047	327.39	320.47	345.55	0.0784	0.0706
Crinkly laminated chert	D1	Bitumen-like	21	1.41	1.73	0.5857	2.42	0.6782	339.20	299.15	372.99	0.1067	0.0831
Crinkly laminated chert	D1	Bitumen-like	22	1.74	1.95	0.6351	3.34	0.7327	314.93	302.79	376.86	0.0966	0.0750
Crinkly laminated chert	D1	Bitumen-like	23	1.81	1.92	0.6440	3.38	0.7189	321.09	302.85	341.27	0.0990	0.0749

Facies	Sample	CM microtexture		R_1	$\Gamma_{D1/G}$	$I_{D1}/(I_{D1}+I_G$	A_D/A_G	R_2 (1)	ΔT C° (2)	ΔT C° (3)	ΔT C° (4	R_{D3}	R_{D4}
Massive black chert	C9E	Bitumen-like	1	1.79	1.63	0.6422	2.91	0.7065	326.59	322.38	367.72	0.0793	0.0761
Massive black chert	C9E	Bitumen-like	2	1.59	1.77	0.6146	2.78	0.6886	334.56	284.18	306.85	0.1205	0.0745
Massive black chert	C9E	Bitumen-like	3	1.71	1.63	0.6316	2.77	0.6832	336.99	322.12	326.07	0.0730	0.0562
Massive black chert	C9E	Bitumen-like	4	1.36	1.55	0.5766	2.10	0.6487	352.35	277.47	305.63	0.1188	0.0825
Massive black chert	C9E	Bitumen-like	5	1.67	1.73	0.6248	2.86	0.7042	327.63	311.91	372.48	0.0847	0.0716
Massive black chert	C9E	Bitumen-like	6	1.56	1.81	0.6088	2.78	0.7004	329.33	301.95	361.24	0.0917	0.0693
Massive black chert	C9E	Bitumen-like	7	1.71	1.80	0.6315	3.05	0.7084	325.75	308.43	350.31	0.0846	0.0705
Massive black chert	C9E	Bitumen-like	8	1.84	1.83	0.6477	3.32	0.7171	321.87	317.74	332.35	0.0817	0.0555
Massive black chert	C9E	Bitumen-like	9	1.96	2.06	0.6619	3.95	0.7378	312.70	296.90	331.93	0.0997	0.0809
Massive black chert	C9E	Bitumen-like	10	1.53	1.82	0.6055	2.75	0.7094	325.34	296.19	375.07	0.0928	0.0850
Massive black chert	C9E	Bitumen-like	11	1.78	1.67	0.6403	2.96	0.7002	329.40	320.56	356.31	0.0775	0.0660
Massive black chert	C9E	Bitumen-like	12	1.66	1.72	0.6241	2.84	0.6969	330.88	319.74	379.24	0.0814	0.0718
Massive black chert	C9E	Bitumen-like	13	1.64	1.75	0.6214	2.82	0.7020	328.60	301.91	352.12	0.0901	0.0755
Massive black chert	C9E	Bitumen-like	14	1.63	1.57	0.6196	2.55	0.6829	337.10	324.19	356.85	0.0692	0.0762
Massive black chert	C9E	Interstitial	15	1.71	1.73	0.6316	2.94	0.6964	331.09	317.89	358.59	0.0844	0.0684
Massive black chert	C9E	Interstitial	16	1.69	1.61	0.6282	2.71	0.6981	330.36	324.34	374.74	0.0717	0.0695
Massive black chert	C9E	Interstitial	17	1.92	1.66	0.6571	3.16	0.6964	331.09	330.00	332.27	0.0768	0.0656
Massive black chert	C9E	Cloudy	18	1.85	1.47	0.6491	2.71	0.7020	328.59	337.56	388.21	0.0625	0.0618
Massive black chert	C9E	Cloudy	19	1.85	1.33	0.6486	2.46	0.6766	339.90	345.93	407.23	0.0608	0.0773
Massive black chert	C9E	Cloudy	20	1.97	1.42	0.6632	2.81	0.6943	332.05	341.31	364.21	0.0514	0.0596
Massive black chert	C9E	Cloudy	21	1.84	1.34	0.6479	2.47	0.6769	339.79	346.52	407.49	0.0636	0.0784
Massive black chert	C9E	Cloudy	22	1.71	1.28	0.6309	2.21	0.6568	348.73	340.96	405.00	0.0635	0.0774
Massive black chert	C9E	Cloudy	23	1.70	1.26	0.6292	2.15	0.6550	349.54	340.50	405.11	0.0620	0.0770

				Lorentzian (D4)				Lorentzian (D1)			
Facies	Sample	CM microtexture		*A*	ω	*I*	*Γ*	*A*	ω	*I*	*Γ*
Laminated black chert	C2C	Grain	1	110888.27	1195.16	401.73	209.69	714507.90	1356.33	8005.59	59.28
Laminated black chert	C2C	Grain	2	133780.70	1186.85	393.05	274.44	642000.06	1356.33	7138.29	59.76
Laminated black chert	C2C	Grain	3	74280.81	1177.52	266.75	213.45	370808.96	1356.60	4479.16	54.81
Laminated black chert	C2C	Grain	4	84303.25	1187.84	369.96	167.13	692698.96	1356.74	8013.66	57.33
Laminated black chert	C2C	Grain	5	141702.82	1195.54	510.81	210.94	903186.90	1356.43	9369.25	64.27
Laminated black chert	C2C	Grain	6	134078.29	1191.95	561.60	176.33	1025870.00	1356.51	10794.74	63.31
Laminated black chert	C2C	Grain	7	148409.62	1197.91	556.18	201.03	886707.92	1356.13	8806.43	67.27
Laminated black chert	C2C	Grain	8	101128.99	1192.61	409.04	183.75	723511.31	1356.60	7848.08	61.33
Laminated black chert	C2C	Grain	9	94040.30	1196.41	412.04	167.03	736152.37	1356.41	7918.25	61.87
Laminated black chert	C2C	Grain	10	91210.73	1193.33	430.02	153.54	781551.46	1356.56	8016.25	65.03
Laminated black chert	C2C	Grain	11	75658.61	1196.05	303.90	185.08	502913.07	1356.75	5286.02	63.39
Laminated black chert	C2C	Grain	12	113570.42	1188.19	490.63	170.22	875042.19	1356.42	9913.66	58.60
Laminated black chert	C2C	Grain	13	81221.90	1204.90	350.32	169.74	615411.84	1356.68	6693.75	61.15
Laminated black chert	C2C	Grain	14	85691.64	1200.56	327.54	196.12	569783.61	1356.55	6492.96	58.25
Laminated black chert	C2C	Grain	15	107487.74	1203.91	374.85	219.05	619027.89	1357.15	6963.57	59.04
Laminated black chert	C2C	Grain	16	55063.12	1188.30	240.78	167.81	376339.21	1357.09	4361.01	57.24
Laminated black chert	C2C	Grain	17	122290.35	1202.73	408.26	231.33	681324.07	1357.00	7698.50	58.76
Laminated black chert	C2C	Grain	18	63959.04	1198.46	273.82	171.53	462545.55	1357.12	5286.24	58.07
Laminated black chert	C2C	Grain	19	112394.81	1190.23	382.53	226.94	637699.27	1357.48	7399.50	57.16
Laminated black chert	C2C	Grain	20	51992.10	1179.28	257.14	145.86	350733.61	1356.92	3908.49	59.62
Laminated black chert	C2C	Grain	21	157322.40	1197.44	643.15	181.17	1074650.00	1356.49	11028.91	64.99
Laminated black chert	C2C	Grain	22	127200.13	1194.63	430.16	228.35	733657.60	1356.95	8193.53	59.49
Laminated black chert	C2C	Bituminous-XcV	23	93552.93	1203.42	370.23	187.97	520298.20	1355.42	4588.67	76.26
Laminated black chert	C2C	Bituminous-XcV	24	105770.04	1203.83	410.28	192.50	660841.26	1355.10	5817.20	76.41
Laminated black chert	C2C	Bituminous-XcV	25	102173.56	1203.21	414.18	182.68	591957.86	1355.23	4685.97	85.55

				Lorentzian (D4)				Lorentzian (D1)			
Facies	Sample	CM microtexture		*A*	ω	*I*	*Γ*	*A*	ω	*I*	*Γ*
Granular carbonaceous chert	D4A	Mats-like network	1	146783.25	1199.64	530.22	210.31	921251.526	1356.435	10782.531	56.653
Granular carbonaceous chert	D4A	Mats-like network	2	94290.10	1193.20	386.52	180.97	664291.674	1356.706	7643.005	57.675
Granular carbonaceous chert	D4A	Mats-like network	3	156880.63	1197.04	571.90	208.17	997801.984	1356.511	11691.717	56.587
Granular carbonaceous chert	D4A	Mats-like network	4	108416.82	1213.15	408.14	199.18	688799.584	1356.628	8041.664	56.802
Granular carbonaceous chert	D4A	Mats-like network	5	83519.13	1198.88	358.46	171.13	621021.756	1356.852	7140.186	57.717
Granular carbonaceous chert	D4A	Mats-like network	6	111076.88	1200.32	412.69	203.18	721823.561	1356.973	8637.836	55.358
Granular carbonaceous chert	D4A	Mats-like network	7	106863.06	1196.18	377.93	216.13	631045.161	1357.015	7448.779	56.155
Granular carbonaceous chert	D4A	Mats-like network	8	144162.04	1195.22	531.29	205.55	914167.588	1357.079	10851.579	55.826
Granular carbonaceous chert	D4A	Mats-like network	9	126868.79	1195.55	474.91	201.66	809623.385	1356.897	9322.197	57.629
Granular carbonaceous chert	D4A	Mats-like network	10	187812.78	1207.98	621.71	233.61	1038100.000	1356.740	12140.436	56.701
Granular carbonaceous chert	D4A	Mats-like network	11	123236.22	1204.10	401.39	238.75	743436.031	1356.852	8872.571	55.514
Granular carbonaceous chert	D4A	Mats-like network	12	90632.40	1202.02	333.03	205.81	592336.070	1357.180	7081.274	55.416
Granular carbonaceous chert	D4A	Mats-like network	13	109637.56	1199.33	378.78	222.20	672528.875	1357.083	7956.220	56.024
Granular carbonaceous chert	D4A	Mats-like network	14	148483.17	1207.82	456.68	256.43	773798.586	1357.150	9522.561	53.768
Granular carbonaceous chert	D4A	Mats-like network	15	135801.09	1201.65	462.04	226.27	848006.545	1357.141	10074.487	55.779
Granular carbonaceous chert	D4A	Grain	16	99741.27	1193.91	357.76	212.58	591926.820	1356.211	6186.134	63.780
Granular carbonaceous chert	D4A	Grain	17	132189.94	1202.52	452.93	224.23	727238.593	1356.294	7760.763	62.398
Granular carbonaceous chert	D4A	Grain	18	109305.09	1199.09	442.35	183.42	728837.847	1355.930	7655.861	63.440
Granular carbonaceous chert	D4A	Grain	19	113713.90	1191.69	509.70	162.99	808783.656	1355.233	8044.657	67.181
Granular carbonaceous chert	D4A	Grain	20	106976.17	1200.96	422.36	188.80	662559.132	1355.671	6024.937	73.847
Granular carbonaceous chert	D4A	Grain	21	122802.80	1198.78	451.34	205.98	712860.129	1356.478	7060.681	67.480
Granular carbonaceous chert	D4A	Grain	22	111949.68	1194.31	396.17	216.10	685300.550	1356.408	7286.141	62.641
Granular carbonaceous chert	D4A	Grain	23	164055.09	1198.60	607.97	203.93	1027530.000	1356.530	10380.126	66.095
Granular carbonaceous chert	D4A	Grain	24	188864.21	1204.81	609.07	241.70	1062840.000	1356.996	12314.596	57.254
Granular carbonaceous chert	D4A	Grain	25	128147.05	1194.82	483.11	199.99	836373.175	1357.060	9241.888	60.162
Granular carbonaceous chert	D4A	Grain	26	92727.16	1195.82	303.11	238.47	508730.144	1356.608	5553.282	60.935
Granular carbonaceous chert	D4A	Grain	27	184386.38	1203.06	633.11	223.60	1046230.000	1356.631	11551.635	60.212
Granular carbonaceous chert	D4A	Grain	28	123427.00	1202.14	524.02	173.17	950268.657	1356.309	9695.531	65.408
Granular carbonaceous chert	D4A	Grain	29	130148.59	1198.61	472.61	207.76	793165.725	1356.291	8307.966	64.510
Granular carbonaceous chert	D4A	Grain	30	141628.83	1198.54	519.02	206.47	862604.259	1356.432	9133.785	63.429

				Gaussian (D3)				Lorentzian (G)			
Facies	Sample	CM microtexture		*A*	ω	*I*	*Γ*	*A*	ω	*I*	*Γ*
Laminated black chert	C2C	Grain	1	57424.90	1550.35	425.41	126.81	222197.93	1605.13	3663.99	40.27
Laminated black chert	C2C	Grain	2	47927.73	1547.03	331.94	135.64	213676.15	1605.58	3403.98	41.75
Laminated black chert	C2C	Grain	3	34193.45	1555.40	214.89	149.49	111638.52	1603.70	1813.47	40.89
Laminated black chert	C2C	Grain	4	54900.97	1552.42	427.78	120.57	211734.95	1604.82	3467.64	40.55
Laminated black chert	C2C	Grain	5	72239.56	1545.23	571.64	118.72	267262.16	1603.91	4248.44	41.83
Laminated black chert	C2C	Grain	6	82246.60	1549.88	668.74	115.54	301891.86	1605.05	4993.08	40.14
Laminated black chert	C2C	Grain	7	68935.51	1542.05	549.55	117.84	279553.01	1604.99	4296.20	43.35
Laminated black chert	C2C	Grain	8	50426.02	1545.38	409.89	115.57	237783.89	1605.86	3714.13	42.62
Laminated black chert	C2C	Grain	9	58923.02	1545.59	408.39	135.54	218816.68	1604.25	3384.91	43.04
Laminated black chert	C2C	Grain	10	77568.48	1551.69	550.87	132.28	237636.14	1606.31	3881.34	40.68
Laminated black chert	C2C	Grain	11	43654.84	1547.69	342.63	119.69	143917.91	1604.75	2345.87	40.75
Laminated black chert	C2C	Grain	12	61687.52	1541.87	472.36	122.69	284379.46	1605.10	4476.24	42.27
Laminated black chert	C2C	Grain	13	53728.40	1548.88	411.19	122.75	214304.64	1606.28	3460.45	41.17
Laminated black chert	C2C	Grain	14	47517.31	1549.49	357.39	124.91	178619.52	1605.56	2845.53	41.75
Laminated black chert	C2C	Grain	15	52047.12	1548.28	359.57	135.98	186046.93	1604.66	3005.98	41.13
Laminated black chert	C2C	Grain	16	28381.21	1550.83	216.29	123.27	114231.68	1605.78	1810.25	41.98
Laminated black chert	C2C	Grain	17	53041.85	1545.11	410.82	121.29	220762.41	1605.37	3474.12	42.28
Laminated black chert	C2C	Grain	18	38229.92	1542.03	282.80	127.00	155102.07	1605.64	2364.22	43.72
Laminated black chert	C2C	Grain	19	44401.31	1543.91	343.72	121.35	205661.75	1605.17	3256.35	42.01
Laminated black chert	C2C	Grain	20	30151.15	1553.44	228.83	123.78	93319.03	1604.91	1650.90	37.42
Laminated black chert	C2C	Grain	21	104506.67	1551.07	708.44	138.58	349428.84	1606.27	5373.31	43.33
Laminated black chert	C2C	Grain	22	54520.37	1545.36	424.97	120.52	237780.54	1606.19	3713.64	42.63
Laminated black chert	C2C	Bituminous-XcV	23	59572.03	1545.90	440.98	126.91	172594.61	1606.11	2698.08	42.59
Laminated black chert	C2C	Bituminous-XcV	24	85844.91	1544.17	554.18	145.52	258827.95	1605.26	3804.51	45.42
Laminated black chert	C2C	Bituminous-XcV	25	58605.44	1539.35	442.50	124.42	230293.18	1607.55	3311.68	46.50

				Gaussian (D3)				Lorentzian (G)			
Facies	Sample	CM microtexture		*A*	ω	*I*	*Γ*	*A*	ω	*I*	*Γ*
Granular carbonaceous chert	D4A	Mats-like network	1	71043.012	1551.989	572.339	116.610	268342.883	1604.438	4350.440	41.002
Granular carbonaceous chert	D4A	Mats-like network	2	46132.207	1542.000	357.015	121.391	243934.215	1605.439	3662.824	44.441
Granular carbonaceous chert	D4A	Mats-like network	3	68845.071	1546.813	584.645	110.624	313333.545	1604.613	4927.163	42.334
Granular carbonaceous chert	D4A	Mats-like network	4	54086.312	1539.703	408.780	124.298	223180.211	1604.646	3389.462	43.907
Granular carbonaceous chert	D4A	Mats-like network	5	50266.088	1543.641	372.083	126.912	206149.985	1605.058	3127.368	43.962
Granular carbonaceous chert	D4A	Mats-like network	6	54479.823	1548.926	406.494	125.907	217591.742	1603.195	3491.812	41.433
Granular carbonaceous chert	D4A	Mats-like network	7	42985.521	1543.143	338.202	119.403	212789.168	1605.035	3316.406	42.734
Granular carbonaceous chert	D4A	Mats-like network	8	65626.905	1546.758	518.453	118.916	296484.821	1605.005	4705.399	41.930
Granular carbonaceous chert	D4A	Mats-like network	9	64340.369	1549.627	509.938	118.532	270806.954	1605.628	4256.366	42.363
Granular carbonaceous chert	D4A	Mats-like network	10	92344.113	1554.299	614.420	141.195	314876.463	1604.299	5025.870	41.675
Granular carbonaceous chert	D4A	Mats-like network	11	61071.182	1551.762	469.700	122.147	243808.063	1604.641	3848.785	42.162
Granular carbonaceous chert	D4A	Mats-like network	12	46003.372	1543.665	316.973	136.344	203145.443	1605.295	3107.317	43.585
Granular carbonaceous chert	D4A	Mats-like network	13	52681.718	1554.449	385.093	128.518	208327.874	1604.879	3311.814	41.856
Granular carbonaceous chert	D4A	Mats-like network	14	52569.655	1544.147	344.377	143.408	251661.191	1604.231	3835.622	43.741
Granular carbonaceous chert	D4A	Mats-like network	15	56977.911	1549.295	474.494	112.809	263226.901	1604.751	4165.325	42.057
Granular carbonaceous chert	D4A	Grain	16	45567.370	1546.651	359.236	119.163	192267.249	1604.073	2915.146	43.979
Granular carbonaceous chert	D4A	Grain	17	60156.018	1535.109	408.153	138.460	258652.523	1603.829	3704.389	46.693
Granular carbonaceous chert	D4A	Grain	18	66468.314	1549.479	388.189	160.875	213719.492	1604.745	3525.799	40.263
Granular carbonaceous chert	D4A	Grain	19	76871.401	1549.984	563.687	128.114	256845.008	1604.748	4038.229	42.342
Granular carbonaceous chert	D4A	Grain	20	57536.831	1543.011	470.361	114.917	215552.674	1605.033	3310.440	43.398
Granular carbonaceous chert	D4A	Grain	21	58076.527	1547.020	461.867	118.128	232568.947	1605.139	3574.589	43.363
Granular carbonaceous chert	D4A	Grain	22	47963.004	1545.858	401.571	112.205	233281.777	1604.765	3585.300	43.363
Granular carbonaceous chert	D4A	Grain	23	59991.091	1531.218	582.320	96.782	331299.774	1603.941	5053.426	43.702
Granular carbonaceous chert	D4A	Grain	24	74098.229	1552.614	611.266	113.879	318733.509	1603.588	4963.220	42.763
Granular carbonaceous chert	D4A	Grain	25	58256.916	1545.262	473.107	115.679	280888.328	1605.319	4359.504	42.924
Granular carbonaceous chert	D4A	Grain	26	39432.916	1548.313	315.918	117.261	166986.626	1605.327	2623.433	42.380
Granular carbonaceous chert	D4A	Grain	27	87637.912	1550.628	705.884	116.634	292558.203	1603.505	4826.251	40.257
Granular carbonaceous chert	D4A	Grain	28	91283.345	1554.219	680.840	125.955	275117.898	1605.193	4447.925	41.126
Granular carbonaceous chert	D4A	Grain	29	58604.140	1544.805	468.824	119.637	250809.079	1604.358	3892.222	42.912
Granular carbonaceous chert	D4A	Grain	30	64575.030	1543.535	516.733	118.507	279831.348	1604.427	4282.226	43.631

Facies	Sample	CM microtexture		Lorentzian (D2)			
				A	ω	*I*	Γ
Laminated black chert	C2C	Grain	1	53975.93	1628.59	1540.26	22.90
Laminated black chert	C2C	Grain	2	45750.31	1629.22	1276.56	23.44
Laminated black chert	C2C	Grain	3	37991.97	1626.56	1001.30	24.84
Laminated black chert	C2C	Grain	4	61724.48	1627.86	1670.15	24.18
Laminated black chert	C2C	Grain	5	102127.76	1625.60	2342.13	28.67
Laminated black chert	C2C	Grain	6	101924.17	1627.08	2552.98	26.18
Laminated black chert	C2C	Grain	7	78021.94	1626.74	1973.40	25.92
Laminated black chert	C2C	Grain	8	53250.64	1628.72	1523.28	22.84
Laminated black chert	C2C	Grain	9	78328.24	1626.54	1787.75	28.82
Laminated black chert	C2C	Grain	10	76531.72	1627.93	1872.32	26.83
Laminated black chert	C2C	Grain	11	55958.17	1626.30	1316.99	27.92
Laminated black chert	C2C	Grain	12	79854.20	1627.52	2033.58	25.74
Laminated black chert	C2C	Grain	13	51437.73	1628.65	1445.74	23.26
Laminated black chert	C2C	Grain	14	50436.91	1627.62	1299.49	25.43
Laminated black chert	C2C	Grain	15	62997.54	1627.23	1556.13	26.56
Laminated black chert	C2C	Grain	16	29374.57	1628.34	765.01	25.16
Laminated black chert	C2C	Grain	17	55938.41	1628.58	1575.09	23.22
Laminated black chert	C2C	Grain	18	37358.17	1628.70	1058.20	23.07
Laminated black chert	C2C	Grain	19	59606.96	1628.32	1565.43	24.94
Laminated black chert	C2C	Grain	20	38649.54	1627.33	954.21	26.58
Laminated black chert	C2C	Grain	21	80041.09	1628.08	2105.88	24.89
Laminated black chert	C2C	Grain	22	57781.75	1628.91	1542.77	24.52
Laminated black chert	C2C	Bituminous-XcV	23	43503.44	1626.51	1068.27	26.72
Laminated black chert	C2C	Bituminous-XcV	24	46346.92	1626.33	1214.56	24.99
Laminated black chert	C2C	Bituminous-XcV	25	35242.59	1627.07	976.77	23.59

Facies	Sample	CM microtexture		Lorentzian (D2)			
				A	ω	*I*	Γ
Granular carbonaceous chert	D4A	Mats-like network	1	84251.654	1627.099	2192.836	25.177
Granular carbonaceous chert	D4A	Mats-like network	2	53498.965	1627.625	1455.017	24.064
Granular carbonaceous chert	D4A	Mats-like network	3	85193.678	1627.538	2211.336	25.249
Granular carbonaceous chert	D4A	Mats-like network	4	69082.625	1627.019	1650.530	27.500
Granular carbonaceous chert	D4A	Mats-like network	5	50455.056	1627.976	1331.472	24.824
Granular carbonaceous chert	D4A	Mats-like network	6	81966.548	1625.870	1989.065	27.058
Granular carbonaceous chert	D4A	Mats-like network	7	56900.244	1627.614	1448.573	25.759
Granular carbonaceous chert	D4A	Mats-like network	8	75440.499	1628.034	2045.143	24.146
Granular carbonaceous chert	D4A	Mats-like network	9	63071.518	1628.269	1770.689	23.293
Granular carbonaceous chert	D4A	Mats-like network	10	103228.710	1626.492	2565.675	26.400
Granular carbonaceous chert	D4A	Mats-like network	11	69043.266	1627.038	1781.196	25.407
Granular carbonaceous chert	D4A	Mats-like network	12	47189.981	1628.316	1272.426	24.280
Granular carbonaceous chert	D4A	Mats-like network	13	59944.481	1627.523	1547.866	25.385
Granular carbonaceous chert	D4A	Mats-like network	14	71595.384	1627.177	1894.054	24.758
Granular carbonaceous chert	D4A	Mats-like network	15	74773.736	1627.596	1992.426	24.576
Granular carbonaceous chert	D4A	Grain	16	49201.862	1626.287	1286.002	25.065
Granular carbonaceous chert	D4A	Grain	17	62843.012	1625.316	1578.037	26.118
Granular carbonaceous chert	D4A	Grain	18	75405.227	1626.796	1699.365	29.212
Granular carbonaceous chert	D4A	Grain	19	69625.113	1626.906	1788.476	25.519
Granular carbonaceous chert	D4A	Grain	20	57883.323	1626.756	1399.943	27.155
Granular carbonaceous chert	D4A	Grain	21	59205.350	1627.054	1528.821	25.382
Granular carbonaceous chert	D4A	Grain	22	58815.018	1627.546	1541.188	25.003
Granular carbonaceous chert	D4A	Grain	23	105505.457	1627.098	2493.124	27.816
Granular carbonaceous chert	D4A	Grain	24	103129.403	1625.887	2483.408	27.274
Granular carbonaceous chert	D4A	Grain	25	65205.076	1627.373	1683.067	25.394
Granular carbonaceous chert	D4A	Grain	26	40821.152	1627.186	1090.512	24.510
Granular carbonaceous chert	D4A	Grain	27	130883.813	1624.996	2878.699	29.949
Granular carbonaceous chert	D4A	Grain	28	93238.443	1626.372	2131.664	28.779
Granular carbonaceous chert	D4A	Grain	29	74990.048	1626.728	1817.172	26.921
Granular carbonaceous chert	D4A	Grain	30	77585.568	1626.606	1925.822	26.251

Legend

A = integrated area

ω = peak position

I = peak intensity

Γ = FWHM (full width half maximum)

(1) $R_2 = A_{D1}/(A_{D1} + A_{D2} + A_G)$ (Beyssac et al., 2002)

(2) T= -445*R2 + 641 (+-50°C) (Beyssac et al., 2002)

(3) T= -2,15 (FWHM-D1)+478 (Kouketsu et al., 2014)

(4) T= -6,78 (FWHM-D2)+535 (Kouketsu et al., 2014)

(5) $R_{D3} = I_{D3}/I_{D1}$ (Sforna et al., 2014)

(6) $R_{D4} = I_{D4}/I_{D1}$ (Sforna et al., 2014)

Facies	Sample	CM microtexture		R_1	$\Gamma_{D1/G}$	$I_{D1}/(I_{D1}+I_G$	A_D/A_G	R_2 (1)	ΔT C° (2)	ΔT C° (3)	T C° (4	R_{D3}	R_{D4}
Laminated black chert	C2C	Grain	1	2.18	1.47	0.6860	3.22	0.7212	320.05	351.54	379.74	0.0531	0.0502
Laminated black chert	C2C	Grain	2	2.10	1.43	0.6771	3.00	0.7122	324.07	350.51	376.11	0.0465	0.0551
Laminated black chert	C2C	Grain	3	2.47	1.34	0.7118	3.32	0.7125	323.94	361.16	366.56	0.0480	0.0596
Laminated black chert	C2C	Grain	4	2.31	1.41	0.6980	3.27	0.7170	321.95	355.73	371.03	0.0534	0.0462
Laminated black chert	C2C	Grain	5	2.21	1.54	0.6880	3.38	0.7097	325.17	340.83	340.60	0.0610	0.0545
Laminated black chert	C2C	Grain	6	2.16	1.58	0.6837	3.40	0.7175	321.69	342.88	357.48	0.0620	0.0520
Laminated black chert	C2C	Grain	7	2.05	1.55	0.6721	3.17	0.7126	323.88	334.36	359.26	0.0624	0.0632
Laminated black chert	C2C	Grain	8	2.11	1.44	0.6788	3.04	0.7131	323.65	347.15	380.13	0.0522	0.0521
Laminated black chert	C2C	Grain	9	2.34	1.44	0.7005	3.36	0.7124	323.97	345.98	339.61	0.0516	0.0520
Laminated black chert	C2C	Grain	10	2.07	1.60	0.6738	3.29	0.7133	323.59	339.18	353.10	0.0687	0.0536
Laminated black chert	C2C	Grain	11	2.25	1.56	0.6926	3.49	0.7156	322.56	342.72	345.72	0.0648	0.0575
Laminated black chert	C2C	Grain	12	2.21	1.39	0.6889	3.08	0.7061	326.79	353.01	360.48	0.0476	0.0495
Laminated black chert	C2C	Grain	13	1.93	1.49	0.6592	2.87	0.6984	330.21	347.52	377.30	0.0614	0.0523
Laminated black chert	C2C	Grain	14	2.28	1.40	0.6953	3.19	0.7133	323.60	353.77	362.56	0.0550	0.0504
Laminated black chert	C2C	Grain	15	2.32	1.44	0.6985	3.33	0.7131	323.67	352.07	354.91	0.0516	0.0538
Laminated black chert	C2C	Grain	16	2.41	1.36	0.7067	3.29	0.7238	318.91	355.94	364.44	0.0496	0.0552
Laminated black chert	C2C	Grain	17	2.22	1.39	0.6891	3.09	0.7112	324.53	352.66	377.60	0.0534	0.0530
Laminated black chert	C2C	Grain	18	2.24	1.33	0.6910	2.98	0.7062	326.75	354.15	378.56	0.0535	0.0518
Laminated black chert	C2C	Grain	19	2.27	1.36	0.6944	3.10	0.7062	326.73	356.11	365.91	0.0465	0.0517
Laminated black chert	C2C	Grain	20	2.37	1.59	0.7030	3.76	0.7266	317.66	350.82	354.82	0.0585	0.0658
Laminated black chert	C2C	Grain	21	2.05	1.50	0.6724	3.08	0.7145	323.06	339.26	366.23	0.0642	0.0583
Laminated black chert	C2C	Grain	22	2.21	1.40	0.6881	3.09	0.7128	323.79	351.11	368.75	0.0519	0.0525
Laminated black chert	C2C	Bituminous-XcV	23	1.70	1.79	0.6297	3.01	0.7065	326.59	315.04	353.83	0.0961	0.0807
Laminated black chert	C2C	Bituminous-XcV	24	1.53	1.68	0.6046	2.55	0.6841	336.58	314.72	365.58	0.0953	0.0705
Laminated black chert	C2C	Bituminous-XcV	25	1.41	1.84	0.5859	2.57	0.6903	333.80	295.08	375.05	0.0944	0.0884

Facies	Sample	CM microtexture		R_1	$\Gamma_{D1/G}$	$I_{D1}/(I_{D1}+I_G$	A_D/A_G	R_2 (1)	ΔT C° (2)	ΔT C° (3)	T C° (4	R_{D3}	R_{D4}
Granular carbonaceous chert	D4A	Mats-like network	1	2.48	1.38	0.7125	3.43	0.7232	319.17	357.20	364.30	0.0531	0.0492
Granular carbonaceous chert	D4A	Mats-like network	2	2.09	1.30	0.6760	2.72	0.6907	333.63	355.00	371.84	0.0467	0.0506
Granular carbonaceous chert	D4A	Mats-like network	3	2.37	1.34	0.7035	3.18	0.7146	323.01	357.34	363.81	0.0500	0.0489
Granular carbonaceous chert	D4A	Mats-like network	4	2.37	1.29	0.7035	3.09	0.7021	328.57	356.88	348.55	0.0508	0.0508
Granular carbonaceous chert	D4A	Mats-like network	5	2.28	1.31	0.6954	3.01	0.7076	326.11	354.91	366.69	0.0521	0.0502
Granular carbonaceous chert	D4A	Mats-like network	6	2.47	1.34	0.7121	3.32	0.7067	326.51	359.98	351.55	0.0471	0.0478
Granular carbonaceous chert	D4A	Mats-like network	7	2.25	1.31	0.6919	2.97	0.7006	329.24	358.27	360.36	0.0454	0.0507
Granular carbonaceous chert	D4A	Mats-like network	8	2.31	1.33	0.6975	3.08	0.7108	324.69	358.97	371.29	0.0478	0.0490
Granular carbonaceous chert	D4A	Mats-like network	9	2.19	1.36	0.6865	2.99	0.7080	325.93	355.10	377.07	0.0547	0.0509
Granular carbonaceous chert	D4A	Mats-like network	10	2.42	1.36	0.7072	3.30	0.7129	323.77	357.09	356.01	0.0506	0.0512
Granular carbonaceous chert	D4A	Mats-like network	11	2.31	1.32	0.6975	3.05	0.7038	327.80	359.65	362.74	0.0529	0.0452
Granular carbonaceous chert	D4A	Mats-like network	12	2.28	1.27	0.6950	2.92	0.7029	328.20	359.86	370.38	0.0448	0.0470
Granular carbonaceous chert	D4A	Mats-like network	13	2.40	1.34	0.7061	3.23	0.7148	322.89	358.55	362.89	0.0484	0.0476
Granular carbonaceous chert	D4A	Mats-like network	14	2.48	1.23	0.7129	3.07	0.7053	327.12	363.40	367.14	0.0362	0.0480
Granular carbonaceous chert	D4A	Mats-like network	15	2.42	1.33	0.7075	3.22	0.7150	322.82	359.08	368.37	0.0471	0.0459
Granular carbonaceous chert	D4A	Grain	16	2.12	1.45	0.6797	3.08	0.7103	324.93	341.87	365.06	0.0581	0.0578
Granular carbonaceous chert	D4A	Grain	17	2.10	1.34	0.6769	2.81	0.6934	332.42	344.84	357.92	0.0526	0.0584
Granular carbonaceous chert	D4A	Grain	18	2.17	1.58	0.6847	3.41	0.7160	322.39	342.60	336.94	0.0507	0.0578
Granular carbonaceous chert	D4A	Grain	19	1.99	1.59	0.6658	3.15	0.7124	323.97	334.56	361.98	0.0701	0.0634
Granular carbonaceous chert	D4A	Grain	20	1.82	1.70	0.6454	3.07	0.7079	326.00	320.23	350.89	0.0781	0.0701
Granular carbonaceous chert	D4A	Grain	21	1.98	1.56	0.6639	3.07	0.7096	325.24	333.92	362.91	0.0654	0.0639
Granular carbonaceous chert	D4A	Grain	22	2.03	1.44	0.6702	2.94	0.7011	328.99	344.32	365.48	0.0551	0.0544
Granular carbonaceous chert	D4A	Grain	23	2.05	1.51	0.6726	3.10	0.7017	328.74	336.90	346.41	0.0561	0.0586
Granular carbonaceous chert	D4A	Grain	24	2.48	1.34	0.7127	3.33	0.7159	322.44	355.90	350.08	0.0496	0.0495
Granular carbonaceous chert	D4A	Grain	25	2.12	1.40	0.6795	2.98	0.7073	326.25	349.65	362.83	0.0512	0.0523
Granular carbonaceous chert	D4A	Grain	26	2.12	1.44	0.6792	3.05	0.7100	325.06	347.99	368.82	0.0569	0.0546
Granular carbonaceous chert	D4A	Grain	27	2.39	1.50	0.7053	3.58	0.7119	324.21	349.54	331.94	0.0611	0.0548
Granular carbonaceous chert	D4A	Grain	28	2.18	1.59	0.6855	3.45	0.7207	320.31	338.37	339.88	0.0702	0.0540
Granular carbonaceous chert	D4A	Grain	29	2.13	1.50	0.6810	3.16	0.7088	325.57	340.30	352.48	0.0564	0.0569
Granular carbonaceous chert	D4A	Grain	30	2.13	1.45	0.6808	3.08	0.7070	326.37	342.63	357.02	0.0566	0.0568